

IADC-04-03

Version 7.2

September 1, 2023

Inter–Agency Space Debris Coordination Committee



PROTECTION MANUAL

Prepared by the IADC WG3 members

Change Record

Issue/ Revision	Date	Ch.	Change(s)	Contributor
4.0 rev.1	13.3.2006		Issue of ver. 4.0	F. Schäfer
4.0 rev. 1	13.3.2006	1	added Chapter 1.1 about IADC PWG and PM updated Chapter 1.2 (Background) moved Chapter 2.7 (Observed effects on S/C) to Chapter 1.3	F. Schäfer, D. Nölke
4.0 rev.1	13.3.2006	2.3	Chinese Risk Assessment Tool MODAOST added (subsection added and first data included) MDPANTO subsection updated (contact, models and BLEs)	D. Nölke
4.0 rev.1	13.3.2006	2.4	Column for MODAOST added in benchmark tables (cube, sphere, simple space station) and inclusion of first benchmarks for NASA91, ORDEM2000 and meteoroid environment MDPANTO benchmarks for first two test modes with ORDEM2000 updated (cube, sphere, simple space station)	D. Nölke
4.0 rev.1	05.7.2007	2.4	Update of MODAOST benchmarks	D. Nölke
4.0 rev.1	23.7.2007	2.3	MDPANTO subsection updated	D. Nölke
4.0 rev.2	1.4.2008	3	Updated chapter 3	D. Nölke
4.0 rev.3	1.4.2008		Completed ver. 4.0 Updated Bumper code meteoroid results for sphere, cube and space station (to reflect constant meteoroid density of 1.0g/cm ³ as required by the calibration case)	E. Christiansen
4.0 rev. 4	15.6.2008	2	Add section 2.4.5 Comparison of Shadowing Algorithms Add section 2.6 STENVI – Standard Environment Interface	D. Nölke
4.0 rev. 5	17.3.2009	6	Entire chapter removed pending revisions	J. Hyde
4.0 rev. 6	22.12.2009	2	Removed references to NASA 96 environment model	J. Hyde
4.0 rev. 7	22.02.2010	3 & 4	Deleted 3.1.2.1.1.3.1 "Impact Damage on Equipment Located behind Whipple Shield Type Structures"	J. Hyde
4.0 rev. 8	12.03.2010	2,4,6	Removed description of PSC risk assessment code Added description of ESABASE2 risk assessment code Updated figure 4.1-2 New chapter 6 "Recommendations and Requirements for Impact Protection of Spacecraft" added	J. Hyde A. Francesconi F. Schäfer H. Stokes
4.0 final	12.04.2011		Updated IADC logo on cover Submitted to steering group	J. Hyde

Issue/ Revision	Date	Ch.	Change(s)	Contributor
5.0 rev. 1	20.09.2010	3	Format corrections Captions added to figure 3.1-16 and table 3.1-8 Removed empty section "3.1.3 MLI" and subsections "3.1.3.1 Combination with Single Wall Structures", "3.1.3.2 Combination with Double Wall Structures" and "3.1.3.3 Combination with other Concepts"	J. Hyde
5.0 rev. 2	14.04.2011	2.3.3 2.3.4 3.1.4	ESABASE2 v3.0 update (IT28-1-1) COLLO update (IT28-1-2) Temp effects on BLEs (IT28-1-9)	A. Francesconi S. Meshcheryakov F. Schäfer
5.0 rev. 3	17.04.2012	Cover intro 1 2 4 7	Updated IADC logo Removed "preliminary note" on pg.2 Updated agency list Added 2.3.9 TURANDOT (IT28-1-3) Added 2.7 Impact Risk Analysis of Unmanned Spacecraft (IT28-1-7) Updated Fig. 4.3-1, -2, -3 (IT28-1-4) Added Table 4.3-2 (IT28-1-4) Added Chapter 7 "MDPS Optimization" (IT28-1-8)	J. Hyde M. Higashide H. Stokes E. Christiansen E. Christiansen H Reimerdes
5.0 rev. 4	15.05.2012	4.3.6 4.3.7 2.3	Add NASA/CNSA facility cross calibration results (IT29-1) Add NASA/CSA facility cross calibration results (IT29-2) Updated figure 2.3-2	B. Pang D. Nikanpour J. Hyde
5.0 rev. 5	18.05.2012	4.3.7 4.4.6	Updated figure 4.3-18 Add "CSA-Canada" to "Test Facilities" section	D. Nikanpour
5.0 rev. 6	22.05.2012	4.3.6 4.4.7	Updated table 4.3-8 and figure 4.3-16 Add "CNSA" to "Test Facilities" section	B. Pang
5.0 final	12.06.2012		Submitted to steering group	

Issue/ Revision	Date	Ch.	Change(s)	Contributor
6.0 rev. 1	24.01.2014	7.5	Add "Benchmark calculations" section	H.G. Reimerdes
6.0 final	07.05.2014		Submitted to steering group	
7.0 rev. 1	08.05.2014		Added section 2.3.10 on PIRAT Added section 3.1.2.2.1 on the SRL ballistic limit equation Updated sections 2.8 References and 3.4 References as required by the two new sections 2.3.10 and 3.1.2.2.1.	R. Putzar
7.0 final	19.09.2014		Submitted to steering group	

Issue/ Revision	Date	Ch.	Change(s)	Contributor
7.1	15.06.2018	2 4 6 8	Updated TURANDOT descriptions (2.3, 2.3.9.2, 2.3.9.3) Updated PIRAT description (2.3.10.3) Updated calibration results of TURANDOT and PIRAT (Tables 2.4.1, 2.4.2, 2.4.3) Deleted NASA/NASDA facility cross calibration (4.3.4) Updated JAXA test facility (4.4.1) Updated ISO standards (6.1.3, 6.3) Updated JAXA standards (6.1.8, 6.3) Added ISO	M. Higashide S. Hasegawa A. Kato, H. Stokes A. Kato H. Stokes
7.2	01.09.2021	2 2 2, 4, 6 2 All	Added benchmark calibration for risk assessment of impact-induced component failures Update ESABASE description (2.3.2 (removed), 2.3.2(new), 2.4.1.2, 2.8) Update SHIELD 3 description (2.3.6, 2.8) Added Risk-Udar (2.3.10, 2.4.1.2, 2.4.1.4.2), Added TSNII Structural Test Center (4.4.8), updated recommendations and requirements (6.1.4) Update BUMPER descriptions (2.3.1, 2.4.1.2, 2.4.1.3.3, 2.8) Updated references to Tables / Figures / Sections / Chapters	M. Schimmerohn K. Bunte, M. Millinger H. Stokes E. Onuchin, B. Pavlov J. Hyde M. Millinger

Table of Contents

1	INTRODUCTION	2-1
1.1	THE IADC PROTECTION WORKING GROUP AND THE PROTECTION MANUAL	2-1
1.2	BACKGROUND	2-2
1.3	OBSERVED EFFECTS OF M/OD IMPACT ON SPACECRAFT	2-3
1.4	REFERENCES	2-4
2	METEOROID/ORBITAL DEBRIS RISK ASSESSMENT.....	2-1
2.1	INTRODUCTION	2-2
2.2	METHODOLOGY	2-4
2.3	IMPACT RISK ASSESSMENT CODES.....	2-7
2.3.1	<i>Bumper 3</i>	2-8
2.3.2	<i>ESABASE2 / DEBRIS</i>	2-11
2.3.3	<i>SHIELD 3</i>	2-15
2.3.4	<i>TURANDOT</i>	2-17
2.3.5	<i>PIRAT</i>	2-18
2.3.6	<i>Risk-Udar</i>	2-20
2.3.7	<i>S³DE</i>	2-22
2.4	VALIDATION OF TOOLS.....	2-24
2.4.1	<i>Calibration of Impact Flux and Penetration Probability</i>	2-24
2.4.2	<i>Calibration of Spacecraft Component Failure Assessment</i>	2-43
2.5	APPLICATIONS OF IMPACT RISK ASSESSMENT CODES.....	2-49
2.5.1	<i>ASI/Alenia</i>	2-49
2.5.2	<i>DLR</i>	2-49
2.5.3	<i>ESA</i>	2-50
2.5.4	<i>NASA</i>	2-51
2.5.5	<i>ROSAVIKOSMOS</i>	2-52
2.5.6	<i>CNSA</i>	2-52
2.6	STENVI - STANDARD ENVIRONMENT INTERFACE	2-53
2.7	IMPACT RISK ANALYSIS OF UNMANNED SPACECRAFT	2-54
2.7.1	<i>Introduction</i>	2-54
2.7.2	<i>Approach for Analysing Unmanned Spacecraft</i>	2-54
2.7.3	<i>Standardized Impact Survivability Assessment Procedure</i>	2-57
2.8	REFERENCES	2-58
3	BALLISTIC LIMIT EQUATIONS	3-65
3.1	BASIC BALLISTIC LIMIT EQUATIONS.....	3-66
3.1.1	<i>Single Wall Structures</i>	3-67
3.1.2	<i>Multiple Wall Structures</i>	3-71
3.1.3	<i>Shape Effects</i>	3-96
3.1.4	<i>Influence of Target Temperature on Impact Damage</i>	3-97
3.2	COMPONENT BALLISTIC LIMIT EQUATIONS.....	3-99
3.2.1	<i>Thermal Protection Systems</i>	3-99
3.2.2	<i>Windows and Glass</i>	3-103
3.2.3	<i>Pressure Vessels</i>	3-108
3.2.4	<i>Tethers</i>	3-111
3.3	SUBSYSTEM BALLISTIC LIMIT EQUATIONS.....	3-125
3.3.1	<i>Propulsion</i>	3-125
3.3.2	<i>Thermal Control System</i>	3-128
3.3.3	<i>Power</i>	3-134
3.3.4	<i>Communications and Data Management</i>	3-139
3.3.5	<i>Attitude Control Subsystem (ACS)</i>	3-140
3.3.6	<i>Inflatable structures</i>	3-141
3.4	REFERENCES	3-144
4	TEST METHODS AND FACILITIES CALIBRATION	4-1

4.1	IMPACT TESTING.....	4-2
4.1.1	<i>Hypervelocity Launchers</i>	4-3
4.2	CALIBRATION PROCEDURES.....	4-12
4.3	HYPERVELOCITY LAUNCHERS AND CALIBRATION.....	4-13
4.3.1	NASA.....	4-13
4.3.2	ESA – NASA Calibration	4-13
4.3.3	NASA JSC-Houston and Khrunichev Space Center GOSINAS Calibration	4-15
4.3.4	NASA JSC and CNES	4-16
4.3.5	NASA JSC and CNSA Test Calibration.....	4-22
4.3.6	NASA JSC and CSA Test Calibration	4-29
4.4	TEST FACILITIES	4-35
4.4.1	JAXA Two-Stage Light Gas Guns.....	4-35
4.4.2	ROSAVIKOSMOS.....	4-36
4.4.3	Russian Federal Nuclear Center VNIIEF (RFNC-VNIIEF, Sarov).....	4-36
4.4.4	ASI-CISAS	4-39
4.4.5	Ernst-Mach-Institute	4-41
4.4.6	CSA-Canada.....	4-43
4.4.7	CNSA.....	4-46
4.4.8	TSNIIMASH Structural Test Center	4-47
4.4.9	CNES	4-48
4.5	REFERENCES	4-49
5	NUMERICAL MODELLING.....	5-1
5.1	INTRODUCTION	5-2
5.1.1	<i>Spatial Discretisation</i>	5-2
5.1.2	<i>Time Integration Scheme</i>	5-7
5.1.3	<i>Equations of State</i>	5-8
5.1.4	<i>Deviatoric Stress Rate and Strength Models</i>	5-8
5.1.5	<i>Failure Criteria</i>	5-9
5.2	VALIDATION OF HYDROCODES	5-10
5.2.1	<i>Definition of Benchmark Cases</i>	5-10
5.2.2	<i>Validation Results</i>	5-15
5.3	CODES USED BY THE PWG	5-22
5.3.1	ROSAVIKOSMOS.....	5-22
5.3.2	NASA.....	5-22
5.3.3	ALENIA.....	5-22
5.3.4	JAXA.....	5-23
5.3.5	NAL/CRC	5-24
5.3.6	CDL	5-24
5.4	DEVELOPMENT OF MATERIAL MODELS FOR NEXTEL AND KEVLAR EPOXY RESIN	5-25
5.5	SIMULATION OF HVI ON PRESSURE VESSELS	5-27
5.5.1	<i>CNES Simulations</i>	5-27
5.5.2	<i>ESA Simulations</i>	5-33
5.6	SIMULATION OF ORBITAL DEBRIS IMPACT PROBLEMS USING A HYBRID PARTICLE – FINITE ELEMENT METHOD	5-36
5.7	REFERENCES	5-40
6	RECOMMENDATIONS AND REQUIREMENTS FOR IMPACT PROTECTION OF SPACECRAFT	6-1
6.1	GUIDELINES AND STANDARDS.....	6-1
6.1.1	<i>Europe</i>	6-1
6.1.2	<i>Europe – ESA</i>	6-2
6.1.3	<i>International Organization for Standardization</i>	6-2
6.1.4	<i>Russia</i>	6-3
6.1.5	<i>United Nations</i>	6-3
6.1.6	<i>U.S. – Government</i>	6-3
6.1.7	<i>U.S. – NASA</i>	6-4
6.1.8	<i>Japan – JAXA</i>	6-5
6.2	IADC PROTECTION WORKING GROUP	6-7

6.2.1	<i>Spacecraft Design and Operations</i>	6-7
6.2.2	<i>Shielding Design Considerations</i>	6-8
6.3	REFERENCES	6-9
7	MASS OPTIMIZATION OF METEOROID/SPACE DEBRIS PROTECTION SYSTEMS	7-1
7.1	INTRODUCTION	7-1
7.2	OPTIMIZATION OF PROTECTION SYSTEMS	7-1
7.2.1	<i>Optimization Algorithm</i>	7-2
7.2.2	<i>Optimization Criteria and Restrictions</i>	7-3
7.3	BALLISTIC LIMIT EQUATIONS FOR OPTIMIZATION.....	7-4
7.3.1	<i>Optimization Variables</i>	7-4
7.3.2	<i>Other Parameters</i>	7-5
7.4	MASS DESIGN EQUATIONS	7-5
7.4.1	<i>Single Wall Mass Analysis</i>	7-5
7.4.2	<i>Double Wall Mass Analysis</i>	7-5
7.5	BENCHMARK CALCULATIONS	7-7
7.5.1	<i>Definition of the Optimization Runs</i>	7-7
7.5.2	<i>Optimization Results</i>	7-8
7.5.3	<i>References</i>	7-10
8	LIST OF ACRONYMS	8-1
9	NOTATIONS	9-1
10	APPENDIX	10-1
10.1	RISK ANALYSIS EXAMPLE: AUTOMATED TRANSFER VEHICLE (ATV)	10-1
10.1.1	<i>Mission Parameters</i>	10-1
10.1.2	<i>ATV Model Geometry</i>	10-1
10.1.3	<i>The Stuffed Whipple Shield</i>	10-2
10.1.4	<i>Equations used in the Computation of the PNP for the ATV</i>	10-3
10.1.5	<i>Total Fluxes on the ATV</i>	10-5
10.1.6	<i>Results</i>	10-7
10.1.7	<i>Conclusions</i>	10-14
10.2	REFERENCES	10-16

List of Figures

Figure 1.1-1: IADC Protection Working Group Activities: Calibrated Databases and Analysis Codes	2-2
Figure 1.3-1: Meteoroid/Debris impact damage on Service Module Window #7	2-4
Figure 1.3-2: Perforation of MPLM aluminium bumper after Flight 5A.1. Hole inside diameter is 1.4 mm, outside diameter is 2.5 mm.....	2-4
Figure 2.2-1: Standard Process for Assessing Spacecraft Meteoroid/Orbital Debris Risks.....	2-4
Figure 2.3-1: Bumper analysis methodology	2-10
Figure 2.3-2: Finite Element Model (FEM) of the International Space Station (ISS).	2-10
Figure 2.3-3: SHIELD 3 impact risk assessment procedure	2-15
Figure 2.3-4: Example SHIELD 3 result: flux of debris/meteoroid penetrators in the size range 0.1 – 1.0 mm on the external surfaces of a radar satellite	2-16
Figure 2.3-5: Example SHIELD 3 result: number of penetrations of equipment on an optical satellite from debris/meteoroids in the 1.0 – 10.0 mm size range.....	2-16
Figure 2.3-6: Risk-Udar HW&SWS Interface	2-21
Figure 2.4-1: Geometry of the Box	2-24
Figure 2.4-2: Geometry of the simple Space-Station Model	2-25
Figure 2.4-3: Geometry of the Sphere (1m ² cross-sectional area, 1.1284m diameter)	2-25
Figure 2.4-4: Spacecraft geometry for shadowing algorithm benchmark	2-38
Figure 2.4-5: Debris impacts on surfaces (consisting of 1 element per surface)	2-40
Figure 2.4-6: Debris impacts on surfaces (consisting of 25 elements per surface)	2-40
Figure 2.4-7: Debris impacts on surfaces (consisting of 100 elements per surface)	2-41
Figure 2.4-8: Debris impacts on surfaces (consisting of 400 elements per surface)	2-41
Figure 2.4-9: Meteoroid impacts on surfaces (consisting of 1 element per surface)	2-41
Figure 2.4-10: Meteoroid impacts on surfaces (consisting of 25 elements per surface).....	2-42
Figure 2.4-11: Meteoroid impacts on surfaces (consisting of 100 elements per surface)	2-42
Figure 2.4-12: Meteoroid impacts on surfaces (consisting of 400 elements per surface)	2-42
Figure 2.4-13: Geometry of the spacecraft (left) and components (middle and right for different test cases, dimensions in millimeter).....	2-43
Figure 2.4-14: Positioning of component relative to the spacecraft: the Electronics box is centered (Case #1), shifted in flight direction (+X) or in lateral direction (+Y), respectively. Dimensions in millimeter.....	2-44
Figure 2.4-15: Positioning of components relative to the spacecraft for Case #4 (Dimensions in millimeter, perspective view with component identification).....	2-44
Figure 2.5-1: ERA Basic End Effectors attached to the ISS in hibernation position.	2-49
Figure 2.5-2: ERA Basic End Effectors	2-50
Figure 2.5-3: ATV Debris impact flux	2-51
Figure 2.7-1: Failure probability curves as a function of d/dc for an electronics box (with no internal redundancy) subjected to impact in the low velocity (LV) range of 3.3 – 4.7 km/s and the high velocity (HV) range of 5.2 – 7.7 km/s [Putzar et al., 2006]	2-56
Figure 3.1-1: CFRP filament wound structure concepts [Taylor et al., 2001]	3-68
Figure 3.1-2: Cross-section of damage to 40 mm thick shield structure (1.0 mm Al2017 sphere at 5.11 km/s) [Taylor et al., 2001].....	3-68
Figure 3.1-3: Whipple shield	3-71
Figure 3.1-4: Typical SRL configuration.....	3-79
Figure 3.1-5: Stuffed Whipple shield configuration and equations (NASA).....	3-80
Figure 3.1-6: Multi-Shock shield configuration and equations (NASA).....	3-81
Figure 3.1-7: Mesh double bumper shield configuration and equations (NASA)	3-82
Figure 3.1-8: Standard Single-Honeycomb Panel Structure with MLI	3-83
Figure 3.1-9: Typical impact damage on honeycomb core sandwich.....	3-84
Figure 3.1-10: Double-Honeycomb Panel Structure with MLI	3-88
Figure 3.1-11: Baseline and double honeycomb shield designs and MLI designs	3-89
Figure 3.1-12: Double honeycomb (right) and Double honeycomb + toughened MLI (left)	3-90
Figure 3.1-13: General view of ISS	3-92
Figure 3.1-14: NCSC BLC calculation procedure.....	3-93
Figure 3.1-15: Verification of BLC _{NCSC} calculation	3-95

Figure 3.1-16: BLE shape factor coefficients (y-axis) as a function of velocity (x-axis)	3-96
Figure 3.2-1: RCC damage modes	3-99
Figure 3.2-2: RCC impact test data	3-100
Figure 3.2-3: Solar cell schematic	3-106
Figure 3.2-4: Damage morphology observed on space-exposed targets	3-106
Figure 3.2-5: Large impact on HST solar cell	3-107
Figure 3.2-6: Experimental results from impact testing of unshielded Al 5754 vessels	3-109
Figure 3.2-7: Experimental results from impact testing of unshielded Ti 99.6% vessels	3-110
Figure 3.2-8: Tether impact damage morphology	3-114
Figure 3.2-9: Tether test set-up	3-115
Figure 3.2-10: Tether penetration efficiency factor	3-117
Figure 3.2-11: Tape tether reference geometry	3-118
Figure 3.2-12: Piecewise BLE for Al-1100	3-119
Figure 3.2-13: Tether orbital lifetime as a function of the altitude and orbit inclination	3-123
Figure 3.3-1: Shuttle radiator panels after “doubler” modification	3-129
Figure 3.3-2: ISS radiator panel schematic	3-129
Figure 3.3-3: Impact damage on MLI-top and rear side [Lambert et al., 2001]	3-132
Figure 3.3-4: Post-test photo of a single primary-power cable impacted by a 3.57 mm diameter aluminium sphere at 6.6 km/s and a 45 degree impact angle	3-138
Figure 3.3-5: High speed cinema image of primary-power cable arcing during test shown in Figure 3.3-4. The arcing lasted a total of 179 ms.	3-138
Figure 3.3-6: Embedded protection design	3-141
Figure 3.3-7: Protection mock-up for impact tests	3-142
Figure 3.3-8: Results of the inflatable protection development tests	3-143
Figure 3.3-9: Ballistic limit equation of inflatable module protection	3-143
Figure 4.1-1: The role of HVI experiments	4-2
Figure 4.1-2: Performance ranges of hypervelocity launchers	4-4
Figure 4.1-3: Schematic of a simple two-stage light-gas gun [Canning]	4-6
Figure 4.1-4: Deformable piston two-stage light gas gun [Canning]	4-6
Figure 4.1-5: Working principle of a two-stage light gas gun.	4-7
Figure 4.1-6: Schematic of a Conical Shaped Charge launcher	4-8
Figure 4.1-7: Battelle Shaped Charge	4-9
Figure 4.1-8: Battelle shaped charge assembly	4-10
Figure 4.1-9: Rail Gun working principle	4-11
Figure 4.3-1: JSC HITF and WSTF test articles for WSTF 1" calibration with JSC 0.5" launcher	4-13
Figure 4.3-2: 1992 ESA-NASA calibration tests	4-14
Figure 4.3-3: NASA JSC and KhSC calibration tests	4-15
Figure 4.3-4: CNES and NASA JSC calibration tests	4-16
Figure 4.3-5: Numerical model using spatial mesh resolution of 2 elements / mm	4-17
Figure 4.3-6: Test 1 @ 200 μ s	4-18
Figure 4.3-7: Test 2 @ 250 μ s	4-18
Figure 4.3-8: Test 3 @ 400 μ s	4-18
Figure 4.3-9: Test 4 @ 400 μ s	4-18
Figure 4.3-10: Test 2 @ 8 μ s	4-20
Figure 4.3-11: Test 2 @ 7.4 μ s	4-20
Figure 4.3-12: Test 2 @ 18 μ s	4-21
Figure 4.3-13: Test 2 @ 17.4 μ s	4-21
Figure 4.3-14: CNSA and NASA calibration test article	4-22
Figure 4.3-15: Photographs of NASA and CNSA test articles	4-28
Figure 4.3-16: CSA and NASA test articles	4-29
Figure 4.3-17: Photographs of NASA and CSA test articles	4-34
Figure 4.4-1: JAXA two-stage light gas guns: (left) the horizontal accelerator, (right) the vertical accelerator.	4-35
Figure 4.4-2: Sabot for the acceleration of individual projectiles (left) and projectiles having a diameter of a fraction of a millimeter (right)	4-41
Figure 4.4-3: Medium two-stage light-gas gun (6.5-15 mm launch tube and 40 mm pump tube diameter) at EMI ..	4-42
Figure 4.4-4: Performance diagram of EMI's light-gas guns (total mass versus velocity)	4-42

Figure 4.4-5: Performance diagram of all EMI facilities.....	4-43
Figure 4.4-6: Video capture of the projectile in flight, showing the integrity of projectile prior to target impact.	4-44
Figure 4.4-7: Syn-shot framing camera sequence (16 frames). Start top left image and step down to next row and move left to right for sequence. Last image is bottom-right, two outer plates shown only.....	4-45
Figure 4.4-8: Two-stage light-gas gun at HIT	4-46
Figure 4.4-9: HERMES launcher	4-48
Figure 4.4-10: HERMES 's impact chamber.....	4-48
Figure 4.4-11: example of hypervelocity impact	4-49
Figure 5.1-1: Grid based and meshless discretization of an impact situation.	5-5
Figure 5.1-2: Particle interaction and interpolation function W with first and second derivative	5-6
Figure 5.2-1: Image of rear wall back surface damage including attached spall.	5-10
Figure 5.2-2: <i>Image of rear wall back surface damage including attached spall.</i>	5-11
Figure 5.2-3: Debris cloud at 1 μ s interframe rate	5-12
Figure 5.2-4: <i>Image of front wall and rear wall (front and back surface) damage</i>	5-12
Figure 5.2-5: <i>Debris cloud at 1 μs interframe rate</i>	5-13
Figure 5.2-6: <i>Image of front wall and rear wall (front and back surface) damage</i>	5-14
Figure 5.2-7: <i>Comparison of the simulated debris cloud evolution with obtained videographs at 1 μs interframe rate</i>	5-16
Figure 5.2-8: <i>Density contour of the simulated damage at the front surface view of the rear wall</i>	5-17
Figure 5.2-9: <i>Comparison back surface rear wall hole from experiment and simulation</i>	5-18
Figure 5.2-10: <i>Comparison of the simulated debris cloud evolution with obtained videographs at 1 μs interframe rate</i>	5-19
Figure 5.2-11: <i>Density contour of the simulated damage at the front surface view of the rear wall</i>	5-20
Figure 5.2-12: <i>Comparison back surface rear wall hole from experiment and simulation</i>	5-21
Figure 5.4-1: Spacecraft shielding configuration for the Columbus module.	5-25
Figure 5.4-2: AUTODYN-2D Simulation using the AMMHIS model.	5-26
Figure 5.5-1: 3D axisymmetric simulation	5-28
Figure 5.5-2: Tank rupture scenarios	5-29
Figure 5.5-3: Helium 30 Mpa	5-30
Figure 5.5-4: Helium 300 Mpa	5-31
Figure 5.5-5: Phase diagram – Helium 30 Mpa	5-31
Figure 5.5-6: Xenon – 15 Mpa.....	5-32
Figure 5.5-7: Phase diagram – Xenon 15 Mpa	5-32
Figure 5.5-8: Results of HVI simulation on pressure vessels.....	5-33
Figure 5.5-9: Shadowgraph pictures of fragment cloud at different pressures and numerical results	5-35
Figure 5.5-10: Position of centre tip fragment and radial expansion of the shock wave in gas	5-35
Figure 5.6-1: ESA Benchmark Case Number 4	5-37
Figure 5.6-2: Particle Plot at 150 Microseconds	5-38
Figure 5.6-3: Element Plot at 150 Microseconds	5-38
Figure 5.6-4: Element Plot at 150 Microseconds, Alternate View	5-39
Figure 5.6-5: Element Plot at 150 Microseconds, Alternate View	5-39
Figure 6.1-1: JAXA document system related to space debris impact assessment.	6-6
Figure 7.2-1: Optimization Algorithm	7-2
Figure 7.2-2: Structural diagram of a combined genetic algorithm/sensitivity analysis optimization process	7-3
Figure 7.4-1: Whipple Shield.....	7-6
Figure 7.4-2: Spacing.....	7-6
Figure 7.5-1: Geometry of the box	7-7
Figure 10.1-1: ATV Geometry	10-2
Figure 10.1-2: Configuration of the stuffed Whipple shield	10-3
Figure 10.1-3: ATV Debris impact flux	10-6
Figure 10.1-4: ATV Meteoroid impact flux.....	10-6
Figure 10.1-5: Example of ATV shielding configuration.....	10-8
Figure 10.1-6: Summary of the results for all configurations for a 135 day mission	10-15

List of Tables

Table 1-1: Predictions of MPLM bumper perforation rate	2-3
Table 2-1: Calibration results for the cube	2-28
Table 2-2: Calibration results for the simple space-station model	2-30
Table 2-3: Calibration results for the sphere	2-32
Table 2-4: Comparison of meteoroid results in COLLO.....	2-33
Table 2-5: Number of impacts/penetrations for “cube” calibration	2-35
Table 2-6: Number of impacts/penetrations for “simple space station” calibration	2-37
Table 2-7: Spacecraft geometry input for shadowing algorithm benchmark.....	2-38
Table 2-8: Debris (D#) Benchmarks - No. of impacts by 0.1mm particles	2-39
Table 2-9: Meteoroid (M#) Benchmarks - No. of impacts by 0.1mm particles.....	2-39
Table 2-10: Flux and penetration calibration results for the component failure assessment.....	2-46
Table 2-11: Calibration results for the component failure assessment for benchmark Cases #1 through #3.....	2-47
Table 2-12: Calibration results for the component failure assessment for benchmark Cases #4	2-48
Table 3-1: Material property data for a typical composite sandwich panel.....	3-69
Table 3-2: Performance of Whipple shield with no MLI included.	3-77
Table 3-3: Performance of Whipple shield with MLI included.....	3-78
Table 3-4: Shielding options for sandwich panel structures.....	3-87
Table 3-5: Shielding requirements for unmanned spacecraft	3-88
Table 3-6: Damage equation terms	3-90
Table 3-7: Typical parameter values for the generic multiple wall ballistic limit equation	3-90
Table 3-8: Preliminary risk assessment results with BLE shape factors.....	3-97
Table 3-9: Tether penetration efficiency factor.....	3-118
Table 3-10: Statistical estimate of encounters/year between a 20 km tether and a catalogued object.....	3-121
Table 3-11: MLI shielding options.....	3-132
Table 3-12: Summary of MLI and enhanced MLI hypervelocity impact data	3-133
Table 3-13: Protection mock-up configuration.....	3-142
Table 4-1: Summary of EMI test results for shields with 1mm Al 2024 T3 back-walls	4-14
Table 4-2: Summary of NASA - KhSC test results	4-15
Table 4-3: CNES and NASA JSC calibration tests	4-16
Table 4-4: Experimental and calculation results.....	4-19
Table 4-5: Physical characteristics of cloud fragments	4-19
Table 4-6: Summary of NASA JSC test results	4-22
Table 4-7: Summary of CNSA test results	4-23
Table 4-8: Summary of NASA JSC test results	4-30
Table 4-9: Summary of CSA test results.....	4-30
Table 4-10: Achieved range of BAS acceleration parameters.....	4-37
Table 4-11: Main parameters of stationary X-ray units.....	4-37
Table 4-12: Main parameters of high frame-rate cameras.....	4-38
Table 4-13: Main parameters of apparatus for plasma parameters measuring.....	4-38
Table 4-14: CISAS LGG – main functional parameters	4-40
Table 4-15: Instrumentation available.....	4-40
Table 4-16: Summary of HVI tests including diagnostics (MDB = Mesh Double Bumper).....	4-45
Table 4-17: Two-stage LGG-main functional parameters	4-46
Table 4-18: Main parameters of X-ray system.....	4-47
Table 4-19: Instrumentation	4-49
Table 5-1: Simulation Parameters, ESA Benchmark Case Number 4	5-37
Table 7-1: Coefficients of spacer mass function	7-7
Table 7-2: Optimization Results-Single Wall Design	7-9
Table 7-3: Optimization Results-Double Wall Design: All Faces equal	7-9
Table 7-4: Optimization Results-Double Wall Design	7-9
Table 10-1: Mission and analysis parameters.....	10-1
Table 10-2: ATV Geometry.....	10-2
Table 10-3: Summary of all shielding configurations.....	10-7
Table 10-4: Configuration 1 (ATV baseline), 135 days attached to the ISS.....	10-9

Table 10-5: ATV configuration 2, 135 days attached to the ISS.....	10-10
Table 10-6: ATV configuration 3, 135 days attached to the ISS.....	10-11
Table 10-7: ATV configuration 4, 135 days attached to the ISS.....	10-12
Table 10-8: ATV configuration 5, 135 days attached to the ISS.....	10-13
Table 10-9: ATV configuration 6, 135 days attached to the ISS.....	10-14

Scope

The aim of this document is to provide a synthesis of the knowledge and experience available among the contributors with respect to spacecraft protection against orbital debris and micro-meteoroids. The primary objective of the Protection Manual (PM) is to capture results of interchange and cooperative activities among members of the Protection Working Group (PWG) of the Interagency Space Debris Coordination Committee (IADC). The PM provides the framework that allows comparable meteoroid/orbital debris (M/OD) risk assessments across the spectrum of member agencies. In particular, the PM provides a standard methodology for meteoroid/debris risk assessments, a means to cross-calibrate risk assessment tools, documentation of reliable ballistic limit equations, procedures and results used to calibrate member hypervelocity impact test facilities, and description of validation activities for hypervelocity impact simulation codes.

This document is regularly updated to reflect the evolution of the acquired experience. It is intended to provide, in the frame of the IADC activities, guidelines and eventually standards related to spacecraft meteoroid/orbital debris protection design, testing, characterization and verification.

1 Introduction

This chapter provides a brief introduction to the space debris problem, its effect on space missions, and the need to implement protection in spacecraft. In addressing these issues, the activities of the IADC Protection Working Group (PWG) are set out, and the focus of this Protection Manual is stated.

1.1 The IADC Protection Working Group and the Protection Manual

The primary objective of the Protection Working Group (PWG) of the IADC is to exchange results of national and cooperative activities among its member space agencies on the most critical topics related to spacecraft protection from hypervelocity impacts:

- impact risk assessment
- damage laws for most common materials and configurations
- system aspects of impact damage
- performances and limitations of available hypervelocity impact test techniques, and
- verification of the damage laws in the velocity regime > 10 km/s by numerical simulation.

The PWG presently consists of representatives of the following space agencies:

- ASI (Agenzia Spaziale Italiana)
- CNES (Centre National d'Etudes Spatiales)
- CNSA (China National Space Administration)
- CSA (Canadian Space Agency)
- DLR (German Aerospace Center)
- ESA (European Space Agency)
- ISRO (Indian Space Research Organisation)
- JAXA (Japan Aerospace Exploration Agency)
- NASA (National Aeronautics and Space Administration)
- NSAU (National Space Agency of Ukraine)
- ROSCOSMOS (Russian Federal Space Agency)
- UKSpace (UK Space Agency)

The aim of this Protection Manual (PM) is to provide a synthesis of the knowledge and experience available among the members of the Protection Working Group (PWG). In particular, the PM provides a standard methodology for meteoroid/debris risk assessments, a means to cross-calibrate risk assessment tools, documentation of reliable ballistic limit equations, procedures and results used to calibrate member hypervelocity impact test facilities, and description of validation activities for hypervelocity impact simulation codes.

The contents of the PM reflect the activities carried out by the meteoroid/debris Protection Working Group of the IADC. Activities of the PWG are illustrated in **Figure 1.1-1**.

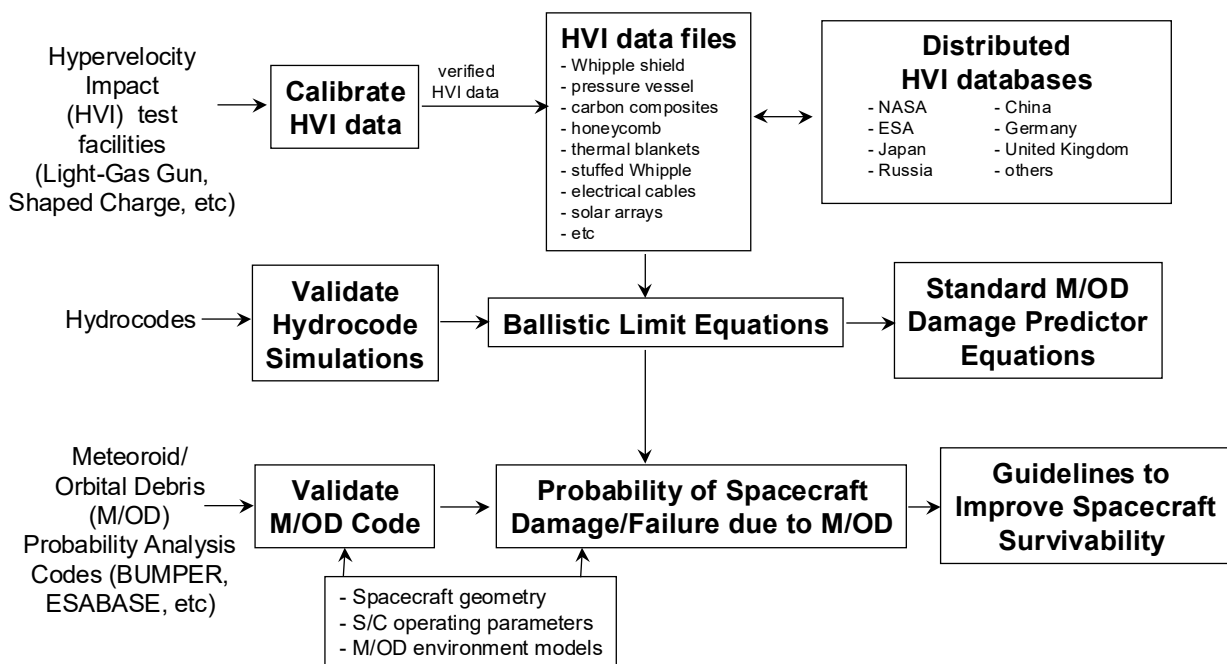


Figure 1.1-1: IADC Protection Working Group Activities: Calibrated Databases and Analysis Codes

1.2 Background

Human enthusiasm for exploring space has resulted in the launch of many payloads over the years, leading to the creation of orbital debris around the Earth in addition to the meteoroid hazard. Since the beginning of the space age and the launch of Sputnik-1 on 4 October 1957, there have been thousands of satellite launches, leading to tens of thousands of satellites and catalogued debris objects in Earth orbit. Most recent statistics can be found in [ODQN], [ESA-AR]. For each satellite launched, several other objects are also injected into orbit, including rocket upper stages, instrument covers, etc. Accidental, and sometimes deliberate, collisions between or explosions of such objects have created a very large number of fragments of varying sizes over the years.

The naturally occurring meteoroid environment, both in the neighbourhood of the Earth and further afield, was considered for space programmes like NASA's Apollo missions in the 1960s [NASA, 1969], Soviet Salyut and Mir space stations in the seventies and later [Nazarenko et al., 1996], and ESA's Giotto mission to Comet Halley in the eighties [Lainé et al., 1982].

Risk analysis studies have indicated that space debris or meteoroid impact damage can have a wide range of effects on spacecraft [Lambert, 1990; Drolshagen, 2001; Christiansen, 2003]. A simple impact on an electronics box cover can generate internal fragments (i.e., spall particles) which can fatally degrade sensitive electronic equipment. Pressure vessels can leak or burst and lead to the premature termination of the mission with possible creation of more debris. Designers need data to build spacecraft able to cope with the space debris threat. It is thus imperative to define a coherent set of damage laws addressing the various effects of hypervelocity impacts.

However, it has to be recognised there are a huge number of spacecraft configurations, each one with various and peculiar exposed surfaces. In addition, the penetration of an external wall does not necessarily mean the loss of the mission.

1.3 Observed Effects of M/OD Impact on Spacecraft

There has been clear evidence of hypervelocity impacts on spacecraft in various missions, e. g. on surfaces of EURECA [Drolshagen, 1994], LDEF [Love et al., 1995], the Hubble Space Telescope HST [Drolshagen et al., 2003], and the Space Shuttle [Hyde et al., 2001a]. ISS has weathered reasonably well through 7.4 years of exposure to the meteoroid/orbital debris (M/OD) environments (FGB launch on 20.11.98, through March 2005), with no hardware failures reported due to M/OD impact. Nevertheless, substantial evidence of hypervelocity impact damage to ISS external surfaces from meteoroid/debris strikes have been identified in down-linked video and photographs [NASA JSC ISAG, 2001], by examining the surfaces of returned ISS hardware such as the Mini-Pressurized Logistics Module (MPLM) [Hyde & Christiansen, 2001], as well as direct observations by the crew. For instance, the crew reported 3 impacts (one “thumbnail-sized”) to a DC-DC Converter Unit (DDCU) heat pipe during an EVA on 20 February 2002, and **Figure 1.3-1** shows an impact crater (3mm-5mm diameter) on a Service Module window transmitted to the ground in January 2002 [NASA JSC ISAG, 2002]. Other direct evidence of M/OD impacts has been evident on MPLM surfaces. MPLM pressurised modules have been used 5 times (through 2004) to carry supplies to ISS, with approximately 6 days each mission exposed to the M/OD environment while docked to ISS (the MPLM is much less exposed to M/OD during the remainder of each mission by virtue of being in the payload bay of the Space Shuttle Orbiter). Over the 5 MPLM missions to ISS, 26 hypervelocity impacts have been observed on MPLM exterior surfaces, with 2 of these completely penetrating the outer 0.8 mm thick aluminium “bumper” shield of the module (**Figure 1.3-2**) [Hyde et al., 2001b]. Predictions of perforation rates have been made of the MPLM, using JSC BUMPER code [Lear & Christiansen, 1999] with the NASA standard meteoroid model and the latest debris model (ORDEM2000) [Lear, 2001; Liou *et al.*, 2002; Prior, 2002]. As **Table 1-1** demonstrates, BUMPER predictions with ORDEM2000 match the MPLM bumper perforation history.

Predictions	Risk of MPLM bumper perforation each flight	Frequency of bumper perforations
ORDEM2000 & std. Meteoroids	55%	1 every 1.8 flights

(Actual perforation rate is 1 every 2 flights for 4 flight history)

Table 1-1: Predictions of MPLM bumper perforation rate



Figure 1.3-1: Meteoroid/Debris impact damage on Service Module Window #7

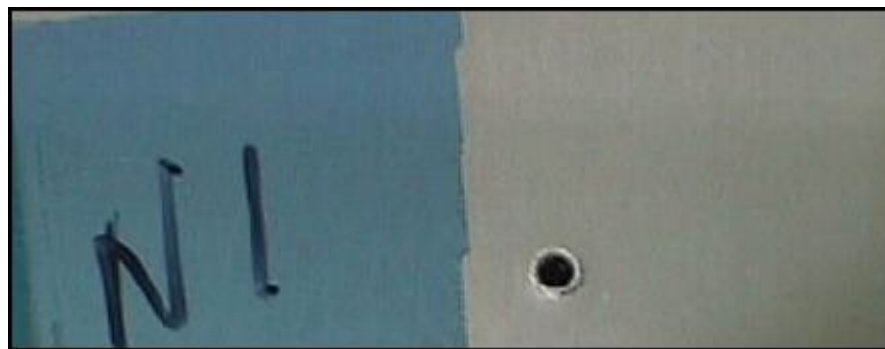


Figure 1.3-2: Perforation of MPLM aluminium bumper after Flight 5A.1. Hole inside diameter is 1.4 mm, outside diameter is 2.5 mm

1.4 References

Christiansen E.L., Meteoroid/Debris Shielding, NASA TP-2003-210788, 2003.

Drolshagen G., EURECA Meteoroid/Debris Impact Analysis, in: EURECA - The European Retrievable Carrier, Technical Report, ESA WPP-069, ISSN 1022-6656, April 1994.

Drolshagen G., Hypervelocity Impact Effects on Spacecraft, Proceedings of the Meteoroids 2001 Conference (ESA SP-495, November 2001), Swedish Institute of Space Physics, Kiruna, Sweden, 6-10 August 2001

Drolshagen G., McDonnell J. A. M., Mandeville J.-C., Moussi A., Impact Studies of The HST Solar Arrays Retrieved in March 2002, IAC-03-IAA.5.1.02, Intern. Astr. Congr., Bremen, Germany, 29 Sep. – 3 Oct. 2003

Christiansen E.L., et al., Space Station MMOD shielding, <https://doi.org/10.2514/6.IAC-06-B6.3.05>, Nov 2012

Hyde J., Christiansen E. L., Bernhard R. P., Kerr J. H., Lear D. M., A history of meteoroid and orbital debris impacts on the space shuttle, Proceedings of the Third European Conference on Space Debris, ESA SP-473, 2001a.

Hyde, J., and E. Christiansen, Meteoroid and Orbital Debris Impact Analysis of Returned International Space Station Hardware, NASA report JSC-29456, May 2001, 2001b.

Kessler, D., J. Zhang, M.J. Matney, P. Eichler, R.C. Reynolds, P.D. Anz-Meador and E.G. Stansbery, A Computer Based Orbital Debris Environment Model for Spacecraft Design and Observations in Low Earth Orbit, NASA TM 104825, November 1996.

Lambert, M., Shielding against orbital debris - a challenging problem, *Proceedings of the ESA Symposium on "Space applications of advanced structural materials"*, 21-21 March 1990, ESTEC, ESA SP-303, 1990.

Lear, D., and E. Christiansen, ISS Debris Risk Assessment Process, Orbital Debris Quarterly Newsletter, Vol.4, Issue 1, Jan.1999.

Lear, D., NASA JSC-29629, Verification of ORDEM2000 BUMPER-II Implementation and Comparison with ORDEM96 Impact Calculations, Oct. 2001.

Lainé R. and Felici F., The Giotto Dust Protection System, ESA Bulletin 32, November 1982

Liou, J.-C., *et al.*, NASA TP-2002-210780, The New NASA Orbital Debris Engineering Model ORDEM2000, May 2002.

Love S. G., Brownlee D. E., King N. L., and Horz F., Morphology of Meteoroid and Debris Impact Craters Formed in Soft Metal Targets on the LDEF Satellite, *Int. J. Impact Engng*, Vol. 16, No. 3, pp. 405-418, 1995.

NASA SP-8013, Meteoroid Environment Model – 1969 [Near Earth to Lunar Surface], NASA Space Vehicle Design Criteria (Environment), 1969.

Nazarenko A.I., Romanchenkov V.P., Sokolov V.G. and Gobenko A.V., Analysis of the Characteristics of Orbital Debris and the Vulnerability of an Orbital Station's Structural Elements to Puncture, *Space Forum: The International Journal of Space Policy, Science and Technology for Industrial Applications*, Dr. Peter Kleber (editor in chief), ISBN 90-5699-072-1, Vol. 1, pp. 285-295, 1996.

Orbital Debris Quarterly Newsletter (ODQN), NASA JSC,
<http://orbitaldebris.jsc.nasa.gov/newsletter/newsletter.html>

ESA's Annual Space Environment Report (ESA-AR), ESA Space Debris Office,
https://www.sdo.esoc.esa.int/environment_report/Space_Environment_Report_latest.pdf

Prior, T., *et al.*, JSC-29648, ITA-10, International Space Station Meteoroid and Debris Integrated Threat Assessment No.10, NASA Johnson Space Center Hypervelocity Impact Technology group (HITF), Nov. 2001.

2 Meteoroid/Orbital Debris Risk Assessment

To ensure that appropriate protection measures are implemented in spacecraft, it is necessary first to assess the debris / meteoroid impact risks. This chapter describes the standard methodology and the principal software codes that are currently available to quantify these risks. Validation of the codes is an important activity of the PWG which is documented in some detail here. Typical applications of the codes are also presented, including an example assessment of the Automated Transfer Vehicle (ATV). The chapter concludes by summarising some of the observed effects of impacts on the International Space Station (ISS) mission. These provide an opportunity to compare code predictions with reality.

2.1 Introduction

There are two types of particles constituting a hypervelocity-impact (HVI) risk to spacecraft: naturally occurring meteoroids and man-made orbital debris objects. Meteoroids are cometary or asteroidal fragments in orbit about the Sun. Orbital debris objects are characterised as either larger, trackable pieces or smaller, non-trackable particles in orbit about Earth.

Debris objects larger than about 10 cm in LEO and larger than about 1 m in GEO are typically tracked by ground-based radar and optical sensor systems. Trackable orbiting objects, whose orbital elements are known, can be propagated along their orbit and their chance of a future collision with another spacecraft or object can be assessed. This deterministic approach provides the opportunity for some spacecraft operators to implement orbit-change manoeuvres to avoid a potential collision if assessed risks are deemed to be too high.

Trackable orbiting objects are too large for shielding measures. The only viable protection measures against these particles are evasive manoeuvres, which are performed if the particles are predicted to come dangerously close to operating spacecraft.

For meteoroids and space debris particles which cannot be tracked, statistical flux models, impact risk assessment tools, and shield or other means to control risks are implemented.

Meteoroid and debris are specified by their number density $n(t, \bar{r}, \bar{V}, \delta)$ in the phase space $(t, \bar{r}, \bar{V}, \delta)$, i.e. (time, space, velocity, size). Also usually used function $f = n|\bar{V}|$, which is a differential flux. The time-averaged flux F_r against a single-sided randomly tumbling surface is calculated by the formula:

$$F_r = F_r(t, \bar{r}, \delta_{min}) = \frac{1}{4\pi} \iint_{4\pi} \left(\int_{\delta > \delta_{min}} (\iiint n * (\bar{V} \cdot \bar{v}) d\bar{V}) d\delta \right) d\bar{v}, \quad [2.1-1]$$

Where \bar{v} is a surface normal unit vector and δ_{min} is a ballistic limit size. Note that the integral over 4π steradians must have a factor that is set to zero (i.e., flux is zero) for impact directions from the back of a single-sided plate. This formula applies for randomly tumbling plates, and not oriented surfaces as considered in the BUMPER code and other probability analysis codes.

Meteoroid and debris fluxes are usually specified as a time-averaged flux, F_r , against a single sided, randomly tumbling surface. Flux is defined as number of intercepted objects per unit time and area. The relevant area for F_r is the outer surface area of the spacecraft. One may also define a "cross sectional area flux", F_c , for a randomly tumbling satellite, where the relevant area is the time averaged cross-sectional area. For randomly tumbling objects with no concave surfaces (no self-shielding):

$$F_c = 4F_r. \quad [2.1-2]$$

For spacecraft which fly with a fixed orientation, the meteoroid and orbital debris fluxes have to be treated as vector quantities and the effects of directionality must be carefully evaluated. Most impacts from meteoroids and space debris will occur on forward-, side-, and space-facing surfaces

with the forward-surface defined as the leading surface in the direction of motion of the spacecraft, i.e., the velocity direction or “ram” direction.

The number of impacts (N), from particles larger than a given diameter, increases linearly with exposed area (A), flux (F), and exposure time (T):

$$N = F A T \quad [2.1-3]$$

where F is the cumulative number of impacts (of a given diameter and larger) per unit area and time.

The numbers of impacts from meteoroids and space debris can be summed to obtain the total number of impacts:

$$N_{\text{tot}} = N_{\text{met}} + N_{\text{deb}} \quad [2.1-4]$$

Once N has been determined, the probability of exactly n impacts occurring in the corresponding time interval is given by Poisson statistics:

$$P_n = (N^n)/n! \ e^{-N} \quad [2.1-5]$$

The probability for no impacts, P_0 is thus given by:

$$P_0 = e^{-N} \quad [2.1-6]$$

The probability for exactly one impact, P_1 is given by:

$$P_1 = N e^{-N} \quad [2.1-7]$$

For values of $N \ll 1$ the probability, Q, for at least one impact ($Q = 1 - P_0$) is approximately equal to N:

$$Q = 1 - e^{-N} \approx 1 - (1 - N) = N \quad [2.1-8]$$

and the probability for no impacts P_0 is:

$$P_0 = e^{-N} \approx 1 - N \quad [2.1-9]$$

The same equations apply if N is the number of failures rather than the number of impacts. The number of failures depends on the impact fluxes and the failure criterion which is determined by the shielding thickness and effectiveness as expressed by a damage equation. A widely used failure criterion is the complete penetration (that is, “perforation”) of the structural wall. But other failure criteria are possible as well, such as creation of a hole larger than a given critical size, penetration depth that exceeds an allowable amount, or the creation of an impact plasma larger than a specified value, etc.

If the failure criterion is 'no penetration' the probability for no penetration, P_0 , is also denoted PNP.

More information on the meteoroid and debris flux models and their application can be found in [Anderson (ed.), 1994; ECSS, 2000; NASA JSC HVIT website].

2.2 Methodology

The standard M/OD risk assessment methodology for spacecraft is illustrated in **Figure 2.2-1**.

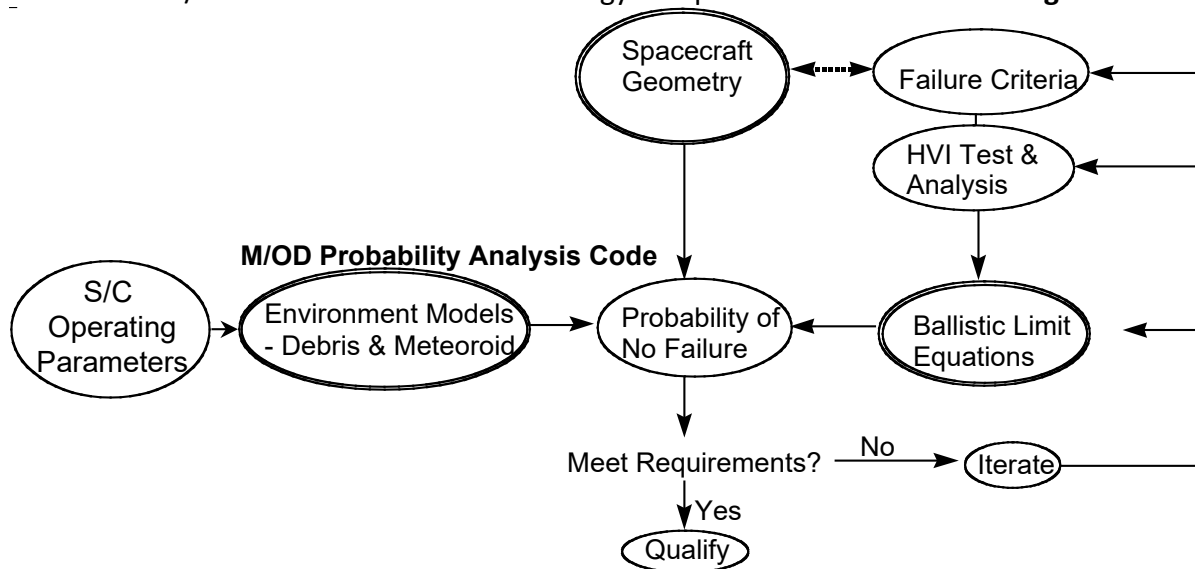


Figure 2.2-1: Standard Process for Assessing Spacecraft Meteoroid/Orbital Debris Risks

The procedure for assessing and reducing spacecraft risks from M/OD impact is an iterative one. Specific steps in the procedure are listed below.

1. Identify vulnerable spacecraft components/subsystems:

The M/OD analyst must know many details of the spacecraft design, operation, failure modes and effects, to properly perform a spacecraft M/OD risk assessment. The Spacecraft geometry should be well known, including materials and allocation of critical subsystems. The systems and components that are exposed to M/OD are identified and their criticality for the mission is assessed.

2. Assess HVI damage modes:

Hazards to be assessed in the M/OD risk assessment are defined for each exposed system and component.

3. Determine failure criteria:

A very clear failure criterion is defined from the many potential hypervelocity impact damage modes for each spacecraft system. The Protection Manual (PM) defines many potential

damage modes for different spacecraft systems. The failure mode is explicitly defined for each ballistic limit equation.

4. Perform HVI test/analysis to define “ballistic limits”:

Ballistic limit equations (BLE) are analytical equations that define the particle on the threshold of “failure” of the spacecraft system/component. Failure is defined by the failure criterion selected in step 3. BLEs relate projectile diameter to the impact speed, angle, projectile density, and target parameters. BLEs must span the impact velocity range of on-orbit impacts (1-16 km/s for debris and 1-72 km/s for meteoroids). These equations are needed in the M/OD risk/probability codes described in Section 2.3, which assess the probability of impact from particles that are of the ballistic limit particle size and greater.

Hypervelocity impact (HVI) tests are necessary to anchor and verify the ballistic limit equations within the testable range. Two-stage light-gas guns (LGG) typically achieve velocities from 2 km/s to 7 km/s using hydrogen driver gas in the second stage. However, to verify BLEs at possible M/OD impact velocities, higher velocities than these are necessary. As such, ultra high-speed launchers are being developed and used by the various agencies to assess spacecraft protection performance. These launchers include explosively launched projectiles, 3-stage launchers, and other techniques.

Hydrocodes, analytical models, semi-empirical approaches and other analysis techniques are used to formulate and/or verify the BLEs.

5. Conduct probability analysis of failure due to meteoroid/orbital debris:

The probability of M/OD failure is assessed using the spacecraft geometry, ballistic limit equations and M/OD environment models. Typically, computer codes are used to perform the probability calculations for complex spacecraft. They have been developed to conduct this analysis in a reliable manner, including the effects of shadowing and/or semi-shadowing from other spacecraft components. The output of the analysis is a Probability of No Failure for the different components of the spacecraft geometry.

The probability of no-failure (PNF) is sometimes referred to as the probability of no-penetration (PNP). These probabilities are determined using Poisson statistics. Poisson statistics are used for statistical assessment of random events and is suited to M/OD assessments. The PNP is assessed by the following equation (see discussion above):

$$\text{PNP} = \exp(-N) = \exp(-\text{Flux} * \text{Area} * \text{Time}) \quad [2.2-1]$$

Where N is the average number of expected M/OD impact penetrations or failures over a given time period. N is assessed from the flux (number per unit area per unit time) of M/OD particles that exceed the BLE, the exposed area, and the exposure time.

The Risk (in percent) of M/OD failure in this case is assessed simply as:

$$\text{Risk} = (1 - \text{PNP}) * 100 \quad [2.2-2]$$

6. Compare M/OD analysis results with goal or requirement:

The analysis results (PNP or PNF) are compared to the goal or requirement for the spacecraft system or component, which is defined by the reliability and/or safety community. If PNF is greater than the required survival probability, then the analysis can be considered complete, otherwise the analysis continues with step 7.

7. Consider updates to design, operations, analysis, test, or failure criteria:

If the analysis results do not meet the requirements, iteration of the analysis is necessary. Revising analysis assumptions in terms of failure criteria and/or improved spacecraft modelling is typically the least expensive option, as it has the least effect on the spacecraft design. Additional testing may be necessary to validate the ballistic limit equations. It is often possible to remove engineering conservatism in the BLEs after additional testing is conducted. Other options include changes to the spacecraft design. It is the goal of the M/OD analyst to identify the “risk drivers” of the spacecraft. Those areas with the greatest risk of failure are the first areas that should be considered for design modification to meet requirements. These modifications may include changes in the wall thickness, materials, shielding structure or even re-location of critical sub-systems. Another option is to orient the spacecraft in ways to minimize M/OD hazards. Within operational constraints, the most vulnerable spacecraft surface can be oriented toward Earth where M/OD impacts are fewest, and the least vulnerable or hardest surface of the spacecraft oriented into the velocity vector where M/OD impacts are greatest.

8. Update/iterate as necessary to meet requirement:

Typically, many updates to a spacecraft’s M/OD risk assessment are necessary to reflect changes in the spacecraft, BLEs, and M/OD environment models. These updates are achieved after each iteration of the previous steps.

2.3 Impact Risk Assessment Codes

Several statistical impact analysis tools have been developed for a detailed impact risk assessment of non-trackable particles. These tools allow a fully three-dimensional numerical analysis, including directional and geometrical effects and spacecraft shielding considerations. They normally support the application of different environment and particle/wall interaction models. The tools allow a 3-D display of the results.

Typical user specified input parameters for these tools are:

- the orbit and mission parameters,
- spacecraft attitude, geometry and shielding,
- the particle type, size, mass density and velocity range to be analysed,
- the damage equations and related parameters to be applied.

The computed output typically includes:

- the number of impacts for the specified particle range,
- the resulting number of damaging impacts (failures) taking into account the spacecraft shielding and damage assessment equations,
- the mean particle impact velocity (amplitude and direction),
- the numbers of craters of specified size,
- the probability of no failure.

Computer codes used by the PWG members to assess the risk from M/OD impacts include:

- Bumper3: NASA
- ESABASE2/DEBRIS: ESA
- SHIELD3: UKSA
- TURANDOT: JAXA
- PIRAT: EMI
- Risk-Udar: ROSCOSMOS
- S³DE: CNSA

The main features of the specific codes are described in the following sections. Descriptions of deprecated computer codes can be found in respective PM version:

- COLLO – PM version 7.1
- BUFFER – PM version 7.1
- MDPANTO – PM version 7.1
- MODAOST – PM version 7.1

2.3.1 Bumper 3

The Bumper code has been the standard in use by NASA and contractors to perform meteoroid/debris risk assessments since 1990. It has undergone extensive revisions and updates [NASA JSC HVIT website; Christiansen *et al.*, 1992, 1997]. NASA Johnson Space Center (JSC) has applied Bumper to risk assessments for Space Station, Shuttle, Mir, Extravehicular Mobility Units (EMU) space suits, Orion MPCV, Deep Space Gateway and other spacecraft (e.g., LDEF, Iridium, TDRS, and Hubble Space Telescope). The Bumper change board processes three or more requests a month to update the ballistic limit equations describing failure threshold of various spacecraft components, and every few years processes a request to update the meteoroid and debris environment models. The change engineers verify each code change and at regular intervals, they validate Bumper by benchmarks with other meteoroid/debris risk assessment codes.

Bumper 3 is a refactored version of Bumper II. The goal of the refactoring was improved maintenance, performance and flexibility. The architecture now separates the frequently updated ballistic limit equations from the relatively stable common core functions of the program. These updates allow NASA to produce specific editions of the Bumper 3 tailored for specific customer requirements. The core consists of common code necessary to process the MMOD environment models, assess shadowing and calculate MMOD risk. The library of target response subroutines includes a broad range of different types of MMOD shield ballistic limit equations as well as equations describing damage to various spacecraft subsystems or hardware (thermal protection materials, windows, radiators, solar arrays, cables, etc.). Bumper 3 is under configuration control. NASA no longer maintains or distributes Bumper II.

2.3.1.1 References

[Christiansen *et al.*, 1992, 1997; Prior *et al.*, 2001; Bjorkman *et al.*, 2014]

2.3.1.2 Procedure

Figure 2.3-1 illustrates the analysis methodology implemented in Bumper. A finite element model (FEM) describing the spacecraft geometry is created in Siemens NX. In conducting International Space Station (ISS) risk assessments, a number of FEMs are required to describe the geometry of each assembly stage. **Figure 2.3-2** illustrates the ISS FEM for an assembly complete configuration. This model has over 1,000,000 finite elements and nearly 1,000 different shield types.

Bumper calculates the number of failures by determining the number of meteoroid/debris particles that exceed the ballistic limits for each element of the FEM, then summing failures over all elements and/or particular regions of interest in the FEM. The number of failures is determined by assigning environment specific threat directions for each element of the FEM. Each threat direction has a distribution of velocities, and a unique impact angle for each element is determined for each threat direction. The environment models define the fraction of total flux that impacts at each threat direction/velocity combination. Those threat directions that are shadowed by other elements in the FEM are removed from the calculation. The calculation of number of particles that exceed the ballistic limit is done at the element level.

The probability of no failure (PNF) is determined from Poisson statistics, i.e., $PNF = \exp(-N)$, where N is the number of failures. PNF is equivalent to PNP (Probability of No Penetration) when the ballistic limits used in the assessment define shield threshold penetration. Failure criteria and risk calculations are made for functional failures, system degradation, or spacecraft mission abort cases. Bumper is also used to assess probability of no impact from certain size meteoroid/debris particles and larger.

Bumper outputs the number of failures (and risk of failure) for the entire FEM or pieces of the FEM as desired by the user. Risk per unit area can be produced as an output from Bumper, which can be used to produce contour plots where colors are used to highlight high risk and low risk areas on the spacecraft. Relative meteoroid/debris risks as a function of impact angle and velocity can also be plotted from Bumper output. This feature is particularly important for planning the most likely impact angle and velocity, which can be used in designing hypervelocity impact tests.

2.3.1.3 Flux Models Implemented

Note, MEM R2 and ORDEM 3 are the current NASA MMOD environments for risk assessment. The use of older environments should be avoided, unless dictated by program requirements.

Meteoroids

- NASA 91 [NASA SSP-30425, Rev. B, 1994]
- MEM R2 (includes EarthMEM, LunarMEM and Interplanetary MEM) [Cooke, et al, 2013]

Space Debris

- NASA 91 [NASA SSP-30425, Rev.B, 1994]
- NASA ORDEM 2 [Liou *et al.*, 2002]
- MASTER 2009, via STENVI files [Institute for Aerospace Systems, 2011]
- NASA ORDEM 3 [Stansbery et al, 2014]

2.3.1.4 Damage Equations Implemented

Parameter equations are included for single walls, multiple walls and crater/hole sizes. Any damage or hole size equation can be specified in the form of a subroutine. Most of the damage/ballistic limit equations included in Bumper have been documented in the IADC Protection Manual and in NASA reports [Christiansen, et al. 2009; Christiansen, 2003; Ryan and Christiansen 2009].

2.3.1.5 Special Features/Comments

Probabilistic risk assessments may be performed using environment and ballistic limit equation uncertainty distributions. Partial shadowing from solar arrays, radiators or other “thin”, non-conformal hardware can be assessed using a 3-part method.

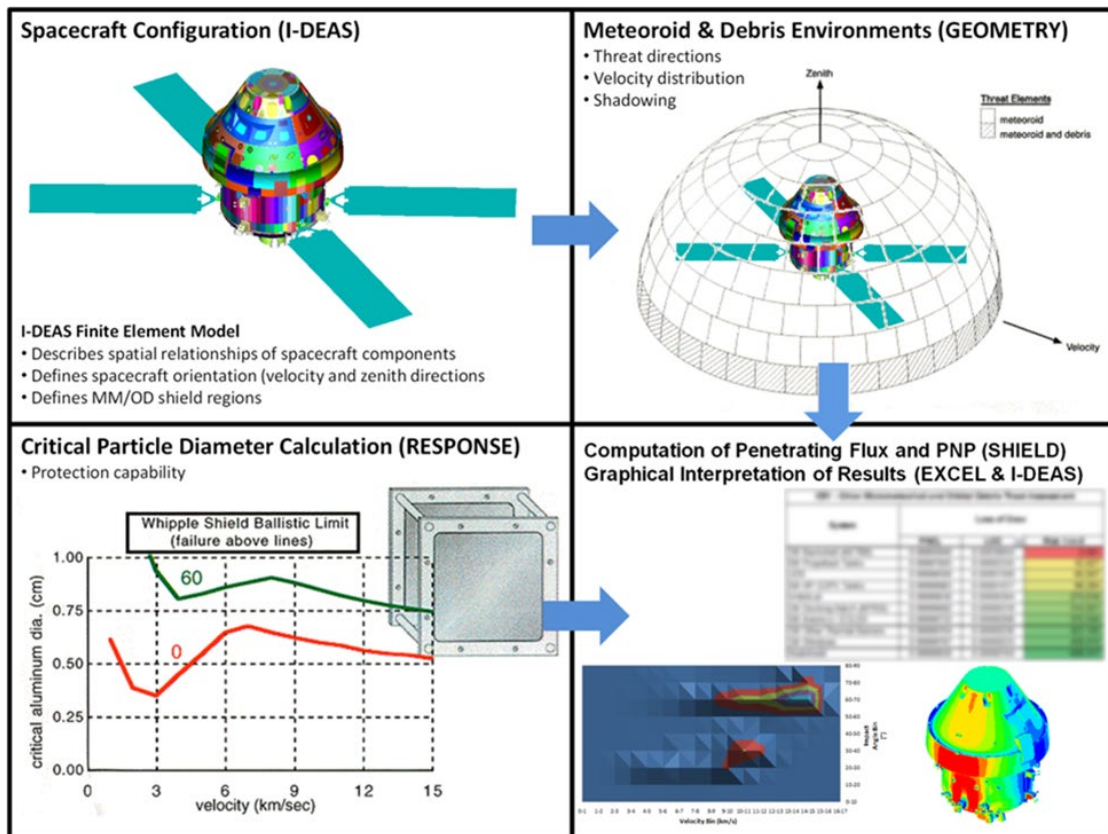


Figure 2.3-1: Bumper analysis methodology

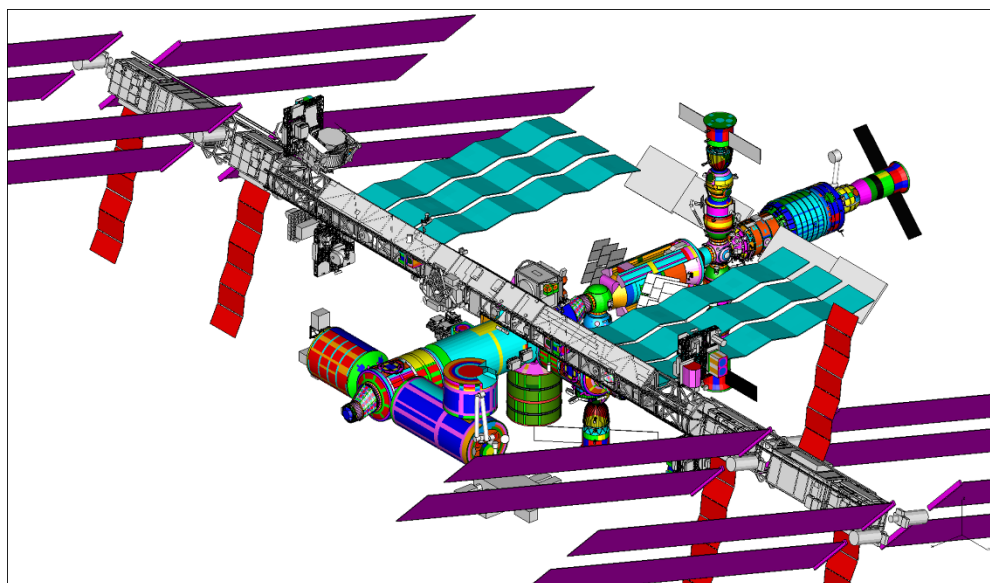


Figure 2.3-2: Finite Element Model (FEM) of the International Space Station (ISS).

2.3.2 ESABASE2 / DEBRIS

2.3.2.1 References

[Bunte *et al.*, 2009, Langwost *et al.*, 2005, Miller., 2021, Ruhl *et al.*, 2021]

2.3.2.2 Procedure

The development of ESABASE2 was undertaken by etamax space GmbH under the European Space Agency contract No. 16852/02/NL/JA to migrate ESABASE/Debris and its framework/user interface to the PC platform (Microsoft Windows) [Bunte *et al.*, 2009]. Meanwhile, ESABASE2/Debris is also available for Linux platforms.

The ESABASE2 tool enables the user to establish a 3-dimensional geometrical spacecraft model [Langwost *et al.*, 2005] of any level of detail. Such model can also be imported from a STEP (AP203/214/242), STEP-SPE or GDML file. The software provides different possibilities to define the mission parameters. If the orbit is defined by means of orbital elements, a numerical orbit propagator, which can take into account various orbit perturbations (gravitational field, aerodynamic drag, solar radiation pressure, 3rd body perturbations), calculates the required trajectory points. Alternatively, the user may provide a trajectory via a trajectory file for orbits around Earth and Moon or via SPICE kernels. A 3D analysis can be performed using the geometrical model of the system including material and/or shielding properties, body kinematics and pointing information. The application of a ray tracing algorithm ensures the proper consideration of self-shielding effects.

ESABASE2/Debris solvers can perform space debris and/or meteoroids impact and damage analyses by applying the selected particle environment models. Currently (May 2021), the models specified below are available.

The software allows to specify shield wall characteristics (e.g., wall configuration, thicknesses, spacing and material properties) for each geometrical object. The risk analysis is then performed under consideration of the space environment model selection, and with failure and damage equation specifications.

The failure equation determines whether a particle penetrates the wall configuration, while the damage equation determines the size of the crater or hole on the first wall or shield [Ruhl *et al.*, 2021]. A set of up-to 15 different wall-configurations can be defined in the debris section, based on several pre-defined single- and multi-wall equations, using user parameter sets, or even a user created UserSubroutine, which can be linked to ESABASE2/Debris.

The 3D geometry is meshed, resulting in a compilation of planar surface elements, which approximate the surfaces of the objects. The ray tracing-based analysis calculations are performed for each planar surface element of S/C 3D model.

The individual element results are combined and the results for individual elements, individual objects of the 3D model and the complete S/C model are provided to the user, where the user can specify the level of result details.

M/OD analysis main results are:

- Number of impacts
- Impact directions and velocities
- Number of damage events (holes, craters)

- Probability of no damage

Results are stored in ASCII files and are also provided as graphical 2D and 3D-colored outputs.

2.3.2.3 Flux Models Implemented

Meteoroids

- Gruen Model [Gruen *et al.*, 1985; Anderson (ed.), 1994]
- Meteoroid stream model [Jenniskens, 1994; McBride, 1997]
- Divine Staubach Model [Divine, 1993; Staubach *et al.*, 1996]
- MEM Model [McNamara *et al.*, 2005]
- LunarMEM (Tailored MEM)
- MEMR2 [NASA MEM Release 2.0, 2013]
- MEM 3 [Moorhead *et al.*, 2019]
- IMEM [Dikarev *et al.*, 2002]
- IMEM2 [Soja *et al.*, 2019]

Space Debris

- NASA 90 [Anderson, 1991]
- ORDEM 2000 [Liou *et al.*, 2002]
- ORDEM 3.0 [NASA ORDEM 3.0, 2014]
- MASTER2001 [Wegener *et al.*, 2002]
- MASTER2005 [Stabroth *et al.*, 2006]
- MASTER2009 [Flegel *et al.*, 2011]
- MASTER 8 [Horstmann *et al.*, 2019]

The use of old environments should be avoided, unless dictated by program requirements.

2.3.2.4 Damage Equations Implemented

Particle/wall interactions are described by some parametric equations giving ballistic limit or damage size. In the first case, damage equations give the critical impacting particle size above which the structure fails [Miller, 2021]. Different equations are used for single and multiple wall structures and are mostly derived from experimental tests.

In the second case, the crater size of semi-infinite targets and the hole diameter of punctured targets (generally thin walls) are computed.

The parametric formulation of ballistic limit equation is:

Single Wall

$$d_{p,\text{lim}} = \left[\frac{t_t}{K_f \cdot K_1 \cdot \rho_p^\beta \cdot v^\gamma (\cos \alpha)^\xi \cdot \rho_t^\kappa} \right]^{\frac{1}{\lambda}} \quad [2.3-1]$$

Multiple Wall

$$d_{p,\text{lim}} = \left[\frac{t_B + K_2 \cdot t_S^\mu \cdot \rho_S^{v_2}}{K_1 \cdot \rho_p^\beta \cdot v^{\gamma \cdot (\cos \alpha)^\xi} \cdot \rho_B^\kappa \cdot S^\delta \cdot \rho_S^{v_1}} \right]^{\frac{1}{\lambda}} \quad [2.3-2]$$

While crater size equation is:

$$D = K_1 \cdot K_c \cdot d_p^\lambda \cdot \rho_p^\beta \cdot v^{\gamma \cdot (\cos \alpha)^\xi} \cdot \rho_t^\kappa \quad [2.3-3]$$

and hole diameter is given by:

$$D = \left\{ K_0 \cdot \left(\frac{t_S}{d_p} \right)^\lambda \cdot \rho_p^\beta \cdot v^{\gamma \cdot (\cos \alpha)^\xi} \cdot \rho_S^v + A \right\} \cdot d_p \quad [2.3-4]$$

where:

t_t, t_B, t_S is the thickness of Target, Back-up wall, Shield [cm]

K, A represent characteristic factor

d_p is the particle diameter [cm]

$\rho_t, \rho_p, \rho_S, \rho_B$ is the density of Target, Particle, Shield, Back-up wall [g/cm³]

v is the impact velocity [km/s]

α is the impact angle

S is the spacing between shielding and back-up wall [cm]

D is the crater or hole diameter [cm]

Coefficients and exponents vary depending on different authors formulation. Further details can be found in the ESABASE2/Debris technical documentation [Miller, 2021]

2.3.2.5 Special Features/Comments

Besides the “Debris” application (module), ESABASE2 includes further space environment analysis tools:

- Atomic Oxygen, for atmosphere and ionosphere,
- Sunlight, including illumination, UV degradation and stray-light,
- COMOVA interface for contamination, outgassing and venting analyses.

ESABASE2/Debris can also be used in batch mode and allows to regularly vary certain analysis parameters via its “Scripting” module.

The results of large numbers of ESABASE2/Debris runs can be analysed using the “Postprocessing” module.

In summary, ESABASE2/Debris has the following special features:

- It is possible to point different parts of the spacecraft in different directions (kinematics and pointing module).
- The tool includes a non-geometrical version to assess the impacts and failures for an oriented or randomly tumbling plate for environment model testing.
- The tool includes a ground test section for BLE testing.

- Secondary debris impacts can be analysed (ejecta module).
- Large and updated pool of usable environment models
- Orbits around Earth, Moon, Mercury, Venus and Mars can be defined and analysed.
- Meteoroid impact assessments can be performed for interplanetary orbits (ESABASE2/Debris interplanetary module) using trajectories provided by means of SPICE kernels.
- Large pool of pre-defined failure and damage equations and the possibility to apply a set of user parameters to define a failure/damage equation.
- Interface for a user subroutine, which can be used to define any special failure and damage equation that cannot be realised by a set of user parameters.

2.3.2.6 Settings for ESABASE2/DEBRIS v3.0 validation

Referring to the validation of this tool (see section 2.3.6), some settings for calibration runs have been applied in addition to those presented in section 2.4.1.1:

- The simulated mission starts on 01 January 2002 and ends on 01 January 2003.
- 36 orbital points for one orbit calculation have been considered, as suggested by ETAMAX (K.D. Bunte, ETAMAX, private communication).
- Analysis using MASTER2005 [Stabroth *et al.*, 2006] debris model has been added.
- Single wall and Double wall analysis results have been obtained using debris with diameter greater than 0.1 mm.
- Debris maximum diameter has been set to 100 cm as ESABASE2 default.
- To obtain craters with a minimum depth of 1 mm, as a desired output of calibration runs (see 2.4.1.3.1), crater minimum diameter has been set to 0.2 cm, assuming a diameter to depth ratio of 2, acceptable for metal targets.
- For meteoroids analysis, the NASA90 model has been used for general velocity distribution in the range 9-50 km/s, while a constant value of 16.5 km/s has been set for algorithm convergence exceptions.
- Ray-tracing technique has been configured with 1000 points.
- Secondary ejecta have not been taken into account.
- Failure equations selected, referring to target geometry are:
 - Single Wall with user parameters set suitable to [Christiansen, 1993],
 - Multi-Wall NASA ISS.
- Failure coefficient in the single wall ballistic limit equation (see section 2.3.2.4) has been set to $K_f = 1.8$ (occurrence of detached spall)
- Damage equation for crater size selected, referring to target geometry, is a generic one with user parameters set suitable to [Christiansen, 1993].

2.3.3 SHIELD 3

2.3.3.1 References

[Stokes *et al.*, 1997, 1999, 2000, 2004, 2005, 2012, 2013; Ryan *et al.*, 2010]

2.3.3.2 Procedure

SHIELD 3 is the latest incarnation of a model that has been in development since the mid-1990s. It uses a variety of modelling techniques to establish the impact-induced probability of no failure (PNF) of each equipment on a spacecraft, and hence the overall spacecraft PNF. **Figure 2.3-3** illustrates the impact risk assessment procedure that SHIELD 3 follows to calculate the PNF.

In the first step of the procedure a 3D representation of the spacecraft is constructed. The geometry of the entire spacecraft structure, including external panels and internal walls and shelves, is modelled, and material properties are assigned to each of these structural elements. Each equipment item on the spacecraft is defined in terms of its geometry, material properties, function, redundancy, mission criticality, interfaces with other equipment, and location on the spacecraft.

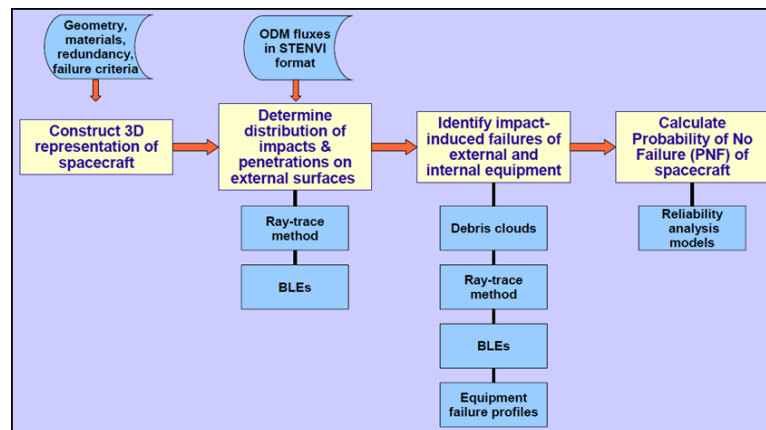


Figure 2.3-3: SHIELD 3 impact risk assessment procedure

For the next step in the methodology the software simulates impact and penetration distributions on the spacecraft. An impact distribution is derived by sampling target-centred directional flux data generated by a debris/meteoroid environment model. SHIELD 3 can accept flux data from any environment model provided the data files comply with the IADC's STENVI format. Test particles are then created and fired at the 3D geometry using a standard ray-trace method to find the precise impact points. Having obtained the impact distribution, appropriate ballistic limit equations (BLEs) are called up to ascertain which of the impacting particles penetrate external surfaces of the spacecraft structure or external equipment. In order to derive a statistically meaningful distribution of penetrating particles on the spacecraft geometry, the entire simulation is repeated many thousands of times. From this dataset, it is a straightforward matter to calculate the probability of no penetration (PNP) of the external surfaces of the spacecraft.

In the final part of the methodology, the damage inside the spacecraft is assessed. SHIELD 3 has a number of proprietary algorithms for analysing penetrative impact damage inside a spacecraft. The code also contains empirically derived models published in the open literature, such as debris fragmentation models, as well as a wide range of ballistic limit equations. Each of the particles that penetrate inside a spacecraft creates a secondary debris cloud that can interact with one or

more equipment items, harnessing, and internal structures. A combination of ray-trace and geometrical methods is used to identify the intersection of the cloud with these interior elements. Depending on the configuration of the interaction, one of the damage assessment routines is utilised to determine which items are penetrated. For some scenarios a multi-wall BLE is suitable. However, for more complex scenarios, the interaction of individual elements of the cloud with internal surfaces can be modelled.

The response of an equipment item to an impact is not simple. In some instances, it is possible for a non-penetrative impact to cause an item to fail. Conversely, it is also possible that an item may survive a marginally penetrating impact. To cater for both of these cases, SHIELD 3 samples failure probability curves to determine whether each impacted item fails. In the event of an item failure, the consequences for the mission are determined using the reliability analysis module within SHIELD 3. For example, if the equipment is not essential to the mission or has a redundant unit, then it is conceivable that the mission may continue largely unaffected. Essentially, mission success or failure is determined by the equipment's criticality and redundancy.

Finally, when each of the thousands of penetrative debris clouds has been analysed, the PNFs of individual equipment items (both internal and external) and groups of redundant items are calculated. Thus, the PNF of the whole spacecraft is derived. This is a measure of the impact survivability of the spacecraft design.

The above methodology can be used to quantify and compare the effectiveness of different protection solutions on a spacecraft. As an example, SHIELD 3 was used within a European Commission FP7-funded project called ReVuS to analyse a range of shielding designs for two different types of LEO spacecraft – a radar satellite (**Figure 2.3-4**) and an optical satellite (**Figure 2.3-5**) – operating over the 2020-2030 timeframe (Stokes, 2012) (Stokes, 2013).

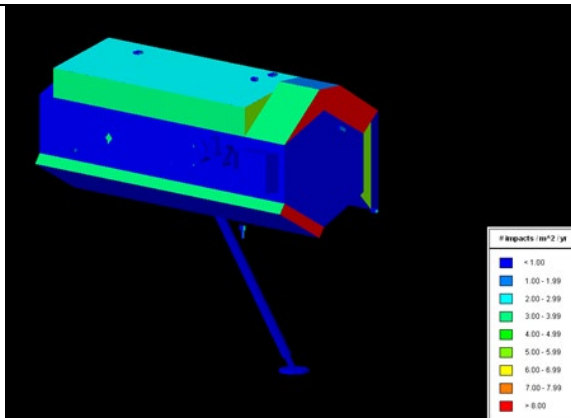


Figure 2.3-4: Example SHIELD 3 result: flux of debris/meteoroid penetrators in the size range 0.1 – 1.0 mm on the external surfaces of a radar satellite

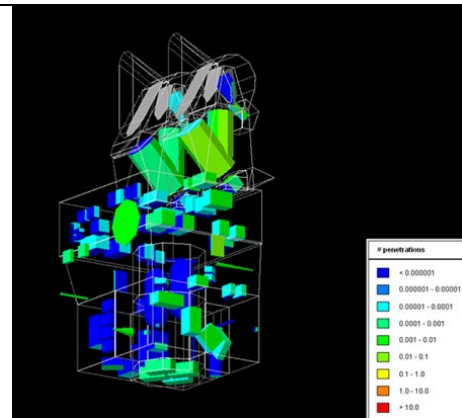


Figure 2.3-5: Example SHIELD 3 result: number of penetrations of equipment on an optical satellite from debris/meteoroids in the 1.0 – 10.0 mm size range

2.3.3.3 Flux Models Implemented

Meteoroids

- Any model that provides meteoroid flux data files in the IADC STENVI format.

Space Debris

- Any model that provides debris flux data files in the IADC STENVI format.

2.3.3.4 Damage Equations Implemented

SHIELD 3 contains a wide range of damage equations listed in the IADC Protection Manual and elsewhere in the literature, e.g., Ryan, 2010. The model also allows new user-defined equations to be input.

2.3.3.5 Special Features/Comments

SHIELD 3 can assess impact damage to equipment inside a spacecraft. SHIELD 3 can also use stochastic search routines to help identify the optimum shielding and layout of equipment on a spacecraft.

2.3.4 TURANDOT

2.3.4.1 References

[Kawamoto et al., 2007]

2.3.4.2 Procedure

Turandot (Tactical Utility for Rapid ANalysis of Debris on Orbit Terrestrial) is a debris collision risk analysis tool developed by JAXA to calculate the probability of damage by MMOD collision for each surface of a space system considering its shape, attitude and the shielding effect. The user can construct a model of the space system by mouse manipulations using a 3D user interface based on the JAVA3D library. The tool can also read STEP format files exported by CAD software. The debris flux is calculated by the ESA MASTER 2009 cell passage events (CPE) dump function and NASA ORDEM 3.0 igloo debris population flux data. The user can define any damage mode and ballistic limit equation by FORTRAN. Defined damage modes are mapped to spacecraft model, and then the collision frequency and damage probability for each part are calculated.

2.3.4.3 Flux Models Implemented

Meteoroids

- Models available in MASTER-8.0.3
- MEM3

Space Debris

- MASTER-2009
- MASTER-8.0.3
- ORDEM 3.2

2.3.4.4 Damage Equations Implemented

In addition to the typical damage equations implemented in advance, the user can add any new damage equation. A user can define new BLEs using FORTRAN code via a graphical user interface.

2.3.5 PIRAT

PIRAT is an acronym for Particle Impact Risk and Vulnerability Assessment Tool.

2.3.5.1 References

[Kempf *et al.*, 2013; Welty *et al.*, 2013]

2.3.5.2 Procedure

PIRAT calculates the statistically independent failure rates of internal components, which are shielded by structure panels. The software is based on the methodology developed in [Welty *et al.*, 2013] and applies primarily the Schäfer-Ryan-Lambert (SRL) triple-wall ballistic limit equation (BLE) [Schäfer *et al.*, 2008], cf. section 3.1.2.2.1 on page 3-79.

The first step in the analysis is the development of a 3D satellite model including external and internal components. Mission and orbit parameters are defined, and a debris model is chosen (see 2.3.5.3 for available models).

Following the calculation of relevant debris fluxes, the geometric analysis of the satellite physical architecture is performed. By discretizing potential threat directions based on a geodesic sphere, a database of impact angle based vulnerable projected areas for individual components and structure panels is created. “Visible” components are those which are exposed to the given threat direction (having a vulnerable projected area greater than zero) either directly, or through a single structure panel.

Using the output of the chosen debris flux models and the geometric analysis of the satellite physical architectures, the individual incoming fluxes are mapped to threat directions, whereby penetration and failure of visible structure panels and components are calculated using the appropriate BLE. Failure and penetration counts are aggregated based on flux (1/m²/yr), projected vulnerable area (m²) and mission duration (yr). Failure and penetration probabilities are determined based on failure rates using the equation derived from the discrete probability function in [Welty *et al.*, 2013]:

$$P(\lambda > 0) = 1 - e^{-\lambda}$$

where λ is the expected number of events.

In order to maintain statistical independence, during the survivability assessment phase, the debris fluxes generated by the debris flux models are evaluated individually. It is possible to define the mass of the satellite (kg) and a catastrophic threshold (J/g). Fluxes exceeding the catastrophic threshold are labeled as such and are added to the overall catastrophic failure rate. Fluxes determined to be non-catastrophic are further assessed for structure panel penetration and external component failure. Penetrating fluxes are further assessed for internal component failure.

For each component, it is possible to specify whether the component should be analyzed for penetration, cratering (external components only), none or both. Non-analyzed components are ignored during the survivability assessment, except with regard to shadowing effects on other

active components. Cratering failures are defined as individual impacts resulting in a proportion of damaged to total surface areas greater than a configurable threshold. Cratering is only assessed if no penetration failure has occurred, or if penetration has been disabled. Cascading conditions (such as multiple craters resulting in component failure) are precluded from the methodology.

Following the completed aggregation of all failures for individual components, the resulting probabilities can be applied to the assessment of system or function vulnerability, using a Boolean logic model representing the satellite functional architecture [Welty *et al.*, 2013].

2.3.5.3 Flux Models Implemented

Meteoroids

- Divine Staubach Model [Divine *et al.*, 1993; Staubach *et al.*, 1996] as implemented in MASTER

Space Debris

- MASTER-2005 [Oswald *et al.*, 2005]
- MASTER-2009 [Flegel *et al.*, 2011]
- MASTER-8.0.3 [Space Debris User Portal]
- ORDEM2000 [Liou *et al.*, 2002]
- ORDEM 3.0 [NASA ORDEM 3.0, 2014]
- ORDEM 3.2 [NASA ORDEM 3.2, 2022]

2.3.5.4 Damage Equations Implemented

PIRAT evaluates damage to structure panels as well as functional damage to spacecraft components. To predict structural damage, the following damage equations are currently implemented:

- single bumper: Cour-Palais Al single wall [Christiansen, 1993], SRL equation [Schäfer *et al.*, 2008]
- double bumper: Al Whipple shield [Christiansen, 1993], SRL equation, modified SRL equation for CFRP [Ryan *et al.*, 2008]
- surface cratering: Schäfer cratering equation [Schäfer *et al.*, 2001]

To predict component survivability, the following damage equations are currently implemented:

- external components: Cour-Palais Al single wall, SRL equation
- MLI only: SRL equation
- single bumper: SRL equation
- double bumper: SRL equation, modified SRL equation for CFRP

2.3.5.5 Special Features/Comments

Besides predicting penetration of the outer structure wall, PIRAT predicts also the survivability of internal components.

2.3.6 Risk-Udar

Risk-Udar (Russian for “Impact Risk”) Hardware and Software System (HW&SWS), designed by FGUP TSNII MASH and RSC Energia, is designated for integrated assessment of risks related to impact of particles of fragment-meteoroidal environment on Orbital Stations (OS).

2.3.6.1 References

2.3.6.2 Procedure

The computing system performs the tasks on determination of Ballistic Limit Equations (BLER) of OS structures with protection shields, on particles trajectory tracing based on the values obtained for particle flows on the basis of the current industrial and meteoroidal environment models, as well as determination of probabilistic characteristics of interaction in between meteoroidal and industrial environments and OS under consideration.

The structure of the software system comprises two computing modules: Ballistic Limit Equations (BLE) and Probability of No Penetration (PNP) interacting to each other via database of pre-defined and pre-estimated protection shield structures performance characteristics.

BLE estimation software program is designed for computation of ballistic limit relations of the protection shield structures defined by the following input data:

1. Protection shield design.
2. Protection shield structure geometric and physical characteristics.
3. Protection shield structure location on OS.

Protection shield structure is developed based on the single-layer structure templates of the most frequently used types.

BLE estimation data for the structure under consideration is transferred in the common data base which provides access to the next system module – PNP being a software program designed for determination of probabilistic characteristics of interaction in between meteoroidal and industrial environments and OS.

PNP estimation software program performs the following functions:

Decomposition of a complex-form 3D object achieved by splitting the complex-form 3D objects to get a set of program-defined primitives.

The software system ensures two ways of OS design model generation:

out of text files prepared in advance and model design constructor; or out of geometrical model components – 3D primitives.

The full OS model can be specified with the help of Object Constructor application. The application interface (see **Figure 2.3-6**) comprises 3 principal areas: structure image representation area, structure description area and project selection area, that ensure:

1. Selection of module to be edited and estimated by clicking on the graphic image of the module.
2. Selection of a specific module area from the object tree.
3. Adding of a specific primitive either to the tree or in the image representation.
4. Manipulation of primitive within the image representation area.
5. Changing of primitive characteristics.
6. Manipulation of image.

The model generated in the Object Constructor application is to be estimated.

Particles trajectory tracing based on values obtained for particle flows on the basis of the current industrial and meteoroidal environment models can be performed. The module ensures

assignment of particle flows to separate elements of OS surface taking into account mutual overlapping of structure elements.

Particles tracing uses backtracing algorithm based on analogy to the interaction of light beams and 3D objects surfaces. The principle used makes determination of conditions of particle bombarding of the station way more effective in terms of computation efforts in comparison with performing analysis of potential bombarding trajectories using a “direct” tracing method.

Taking into account the following particles movement tracing peculiarities in comparison with the optical beams:

- Replacement of laws on optical interaction of light beams and surfaces for laws on impact interaction.
- Possibility of fragments formation after the collision of particles with the surface, use of standard backtracing algorithms is unfeasible, thus development of a new algorithm is required.

The probabilistic characteristics of the interaction in between meteoroidal and industrial environments and 3D object are the software program outcome.

This outcome includes probability for OS pressure-tight protection penetration with the pre-defined parameters of the protection shield of individual structure elements, estimation of OS outer surface damaged area caused by crater formation due to particles bombardment, estimation of probability for catastrophic consequences of penetration damage to manned space station pressure-tight protection.

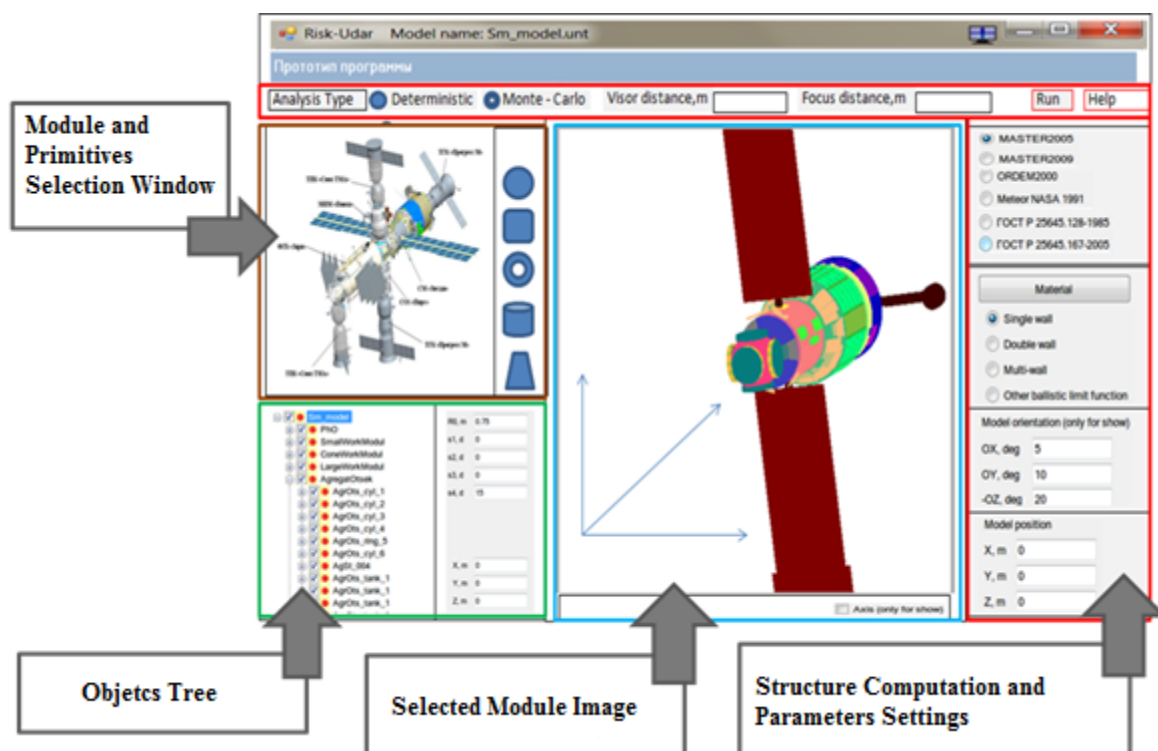


Figure 2.3-6: Risk-Udar HW&SWS Interface

2.3.6.3 Flux Models Implemented

The current software version ensures application of the following meteoroidal and industrial environments models: ORDEM2000, ORDEM 3.0, MEM, MASTER2009.

2.3.6.4 Damage Equations Implemented

The BLE computation is performed based on the integrated computation methodology developed by TSNIIMASH. The methodology allows for analysis of BLE for one- and multi-layered shield protection structures with inter-layer non-metallic shields of various composition and configuration.

2.3.6.5 Special Features/Comments

Risk-Udar HW&SWS ensures PNP estimation using two approaches:

- Deterministic
- Monte-Carlo method

The current program version ensures evaluation of catastrophic consequences risks of the following types:

- inability of any further station operation (LOM, Loss of Mission)
- station destruction (LOV, Loss of Vehicle)
- loss of at least one crew member (LOC, Loss of Crew).

The list given will be extended in the next program version.

On the current stage Risk-Udar is used only in ISS but its capabilities ensure analysis of random-configuration OS PNP.

Comparison of calculation data using Risk-Udar and BUMPER programs suggests that relative difference in industry-related particles calculation using NASA model (1991) does not exceed 2.58%, using ORDEM2000 model – 3.49%, using meteoroidal model – 2.44%.

2.3.7 S³DE

2.3.7.1 References

[Hu, Pang, Chi, Song, Wu, 2021; Hu, Chi, Liu, Pang, 2021]

2.3.7.2 Procedure

Survivability of Spacecraft in Space Debris Environment, abbreviated as S³DE, have been developed by HIT in 2021. S³DE can be used to calculate the survivability of orbiting spacecraft in a space debris and meteoroid environments. Where the survivability is the probability that the spacecraft components/system does not fail under MM/OD impact. Survivability analysis includes a sensitivity analysis, which means the probability of being impacted by MM/OD.

The S³DE is composed of three modules: input module, computational module and output module. In the input module, users can determine the input data according to the requirements, including: 1) the MM/OD environment model data supported in the latter section, 2) a grid geometrical model in required format of any level of detail, 3) material properties of spacecraft components, 4) attitude parameters of spacecraft (S³DE considering two attitude mode including: a three axis stabilized mode and spin-stabilized mode), 5) structural properties of spacecraft components, such as: wall configuration, thicknesses, spacing and failure mode, 6) the functional properties of the spacecraft, which covers the functional logic relationship between the components and systems).

The computational module is composed of a sensitivity module, a vulnerability module, and a survivability module. The sensitivity analysis is performed using the shielding algorithm [Hu, Chi, Liu, Pang, 2021]. And the vulnerability module relies on the construction of the ballistic limit equations (BLE). The survivability module contains the aforementioned PNF/PNP calculation method and the model construction of the relationship between components and system. It is worth mentioning that the PNF here is not only used to calculate the non-failure probability of the spacecraft, but users can also calculate the functional order reduction probability of the spacecraft in the MM/OD environment with the customized failure mode.

In addition, the S³DE covers ray method and the panel method. Ray method means using rays represent the MM/OD to impact spacecraft. This method employs a model from CARDIC which described the shape of the cloud and the distribution of mass and velocity. While the panel method considering the shadowing relationship between the panels and using SRL-BLE to determine whether an MM/OD impactor can cause the spacecraft external structure and internal equipment wall to fail.

Finally, the S³DE can give the data results of the sensitivity and survivability of all components and the survivability of the spacecraft system. For the detailed and vivid representation, S³DE also gives a sensitivity pseudo-color 3D map and a survivability pseudo-color 3D map.

2.3.7.3 Flux Models Implemented

Meteoroids

- Meteoroids output from MASTER-8 [Horstmann *et al.*, 2019]
- Meteoroids output from MASTER2009 [Flegel *et al.*, 2011]
- Model from [NASA SSP-30425, Rev. B, 1994]
- Meteoroids output from SDEEM2019 [Wang *et al.*, 2019; Pang *et al.*, 2019]

Space Debris

- ORDEM2000 [Liou *et al.*, 2002]
- MASTER-8 [Horstmann *et al.*, 2019]
- MASTER2009 [Flegel *et al.*, 2011]
- SDEEM2015 [Pang *et al.*, 2017]
- SDEEM2019 [Wang *et al.*, 2019; Pang *et al.*, 2019]

2.3.7.4 Damage Equations

Presently, damage equations for the following configurations are implemented:

- Single wall [Cour-Palais, Christiansen]
- Single bumper [Christiansen]
- Double bumper [Schäfer *et al.*, 2008]
- Honeycomb sandwich wall [Ryan *et al.*, 2008]

2.3.7.5 Special Features/Comments

In 2021, S³DE added a protection optimization module and a debris cloud module. The protection optimization module can give the optimized structural parameters that meet the mass constraints and survivability requirements user given. And the protection structure should have its BLE. The debris cloud module uses the debris cloud equation [Huang *et al.*, 2013] to carry out simulation calculation and realize the visualization animation process.

2.4 Validation of Tools

The impact risk assessment tools can be validated in different ways. For some simple test cases, like a flat plate and fixed impact velocity, the results can be compared to calculations done by hand. This method is no longer feasible when the full directional and velocity distribution of the impacting particles is included. For these cases the tools can be validated to some extent by comparing the results of different codes for well-defined test cases. The results from “benchmark” cases are useful to calibrate results obtained and reported by different agencies using different codes.

Two basic functions of risk assessment tools are cross calibrated below: 1) the impact fluence on outer surfaces and the resulting probability of structural penetration, and 2) the assessment of spacecraft component failures induced by hypervelocity impacts.

2.4.1 Calibration of Impact Flux and Penetration Probability

The above presented impact risk assessment tools differ in terms of scope and applied methodology. The basic outcome of all tools is the computation of meteoroid and debris impact fluxes on the surfaces of an object in space and the penetration probability as a function of its wall configuration.

2.4.1.1 Definition of Calibration Runs for Impact Flux and Penetration Probability Analysis

Three generic spacecraft geometries were defined for the validation of the M/OD risk assessment tools:

- a simple box (**Figure 2.4-1**) with edge length of 1m.
- a simple space station (**Figure 2.4-2**).
- a sphere with 1 square meter cross section (**Figure 2.4-3**).

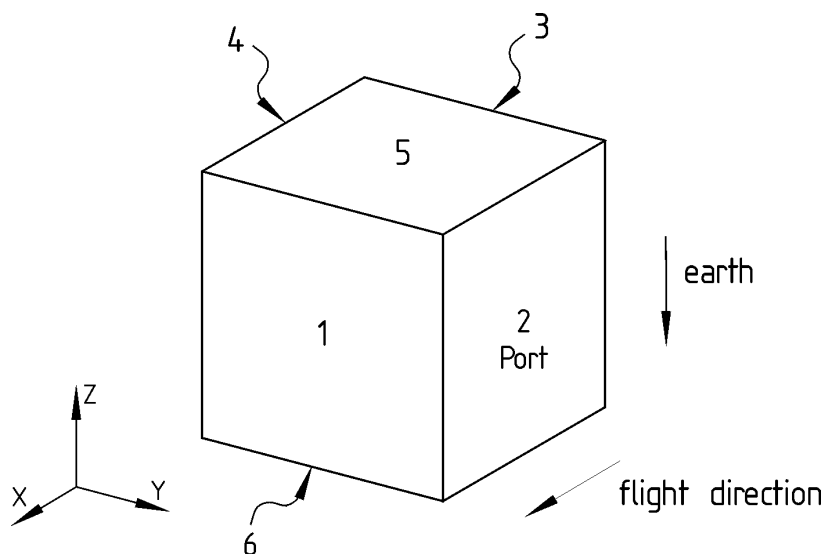
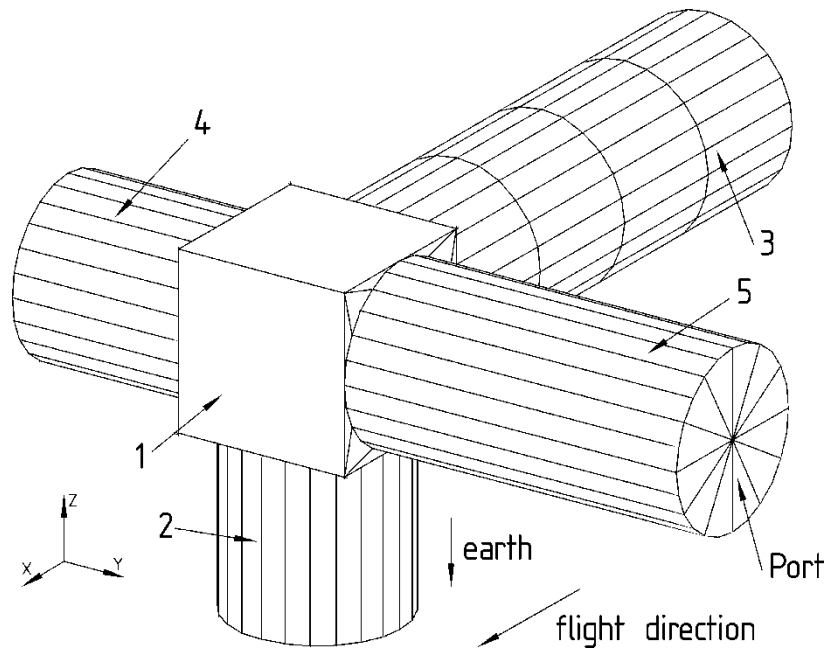


Figure 2.4-1: Geometry of the Box



Note: The edge length of the cubical box (#1) and diameter of all cylindrical modules are 1m. Cylinders #2 and #4 are 1m long, cylinder #5 is 2m long, cylinder #3 is 3m long.

Figure 2.4-2: Geometry of the simple Space-Station Model

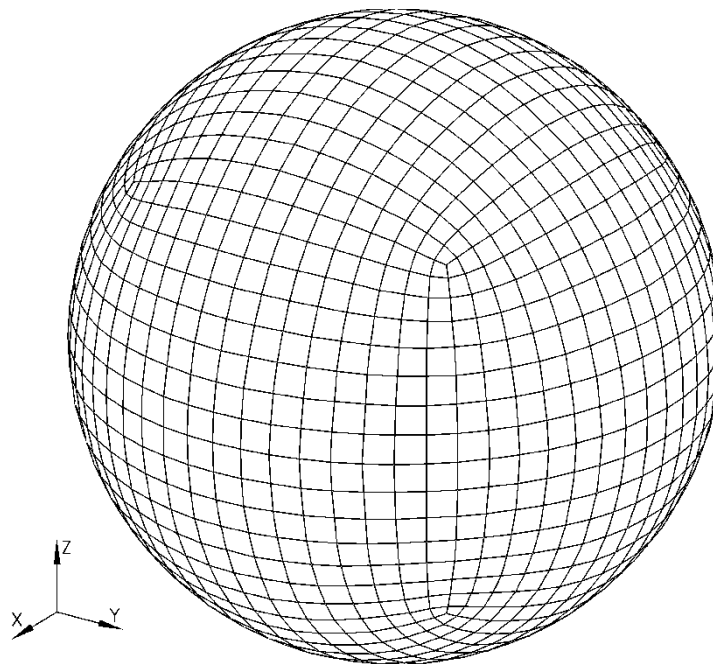


Figure 2.4-3: Geometry of the Sphere (1m^2 cross-sectional area, 1.1284m diameter)

2.4.1.2 Environment Models and Mission Parameters

The environment models to be applied are:

- NASA debris '91 [NASA SSP-30425, Rev.B, 1994]
- NASA debris 2000 (ORDEM2000) [Liou *et al.*, 2002]
- Meteoroid model (i.e., NASA SSP-30425, Rev. B, 1994, for BUMPER; Gruen model [Anderson (ed.), 1994] for ESABASE2/DEBRIS)

The environment/mission parameters are:

- Altitude = 400 km; Inclination = 51.6 deg; Launch 2002, 1 year duration
- NASA '91: $S=70$, $p=0.05$, $q=0.02$
- meteoroid density is model specific, in case user-specified = 1 g/cm^3 (for all particle masses)
- debris density is model specific, in case user-specified = 2.8 g/cm^3

2.4.1.3 Ballistic Limit Equations and Material Properties

Ballistic limit equation to be used:

- Single wall and Whipple shield equations given in [Christiansen, 1993].

Material Properties for Al 6061-T6 single wall and first layer in double wall structure:

- Brinell hardness = 95,
- density = 2.713 g/cm^3 ,
- speed of sound = 5.1 km/s

Material Properties for rear wall in double wall structure (Al 2024-T3):

- yield strength = 47 ksi

2.4.1.3.1 Desired Output of the Calibration Runs

For each geometry, five runs are defined in order to investigate its behaviour in the M/OD-environment:

- number of impacts by particles with $d \geq 0.1 \text{ mm}$
- number of impacts by particles with $d \geq 1.0 \text{ cm}$
- number of impacts resulting in craters with depth $p \geq 1.0 \text{ mm}$
- "Single": number of penetrations in single wall structure: 1mm wall thickness
- "Double": number of penetrations in double wall structure: 2mm shield thickness, 4 mm backwall thickness, 10 cm spacing.

2.4.1.4 Impact Flux and Penetration Probability Calibration Results

Calibration runs were performed by different agencies, using their codes. A summary of available results are presented in **Table 2-1** for the cube, in **Table 2-2** for the Space Station, and in **Table 2-3** for the Sphere. More detailed results for each face of the cube case, for each element of the space station case (cylinders and cube) are generally available. Detailed results for some of the codes are presented in Section 2.4.1.6.

CUBE		BUMPER 3	ESABASE2 / Debris	MDPANTO	COLLO	MODAOST	TURANDOT	PIRAT	Risk-Udar
NASA 91	d > 0.1 mm	4.464E+00	4.516E+00	4.473E+00	4.52E+00	4.476E+00			4.472E+00
	d > 1.0 cm	5.689E-05	6.110E-05	5.702E-05	6.27E-05	5.706E-05			5.700E-05
	p > 1.0 mm	8.053E-02	8.116E-02	8.094E-02	8.23E-02	8.051E-02			8.065E-02
	single	3.240E-01	3.364E-01	3.256E-01	3.19E-01	3.239E-01			3.245E-01
	double	2.025E-04	2.060E-04	2.034E-04	2.12E-04	2.081E-04			2.028E-04
NASA 2000	d > 0.1 mm	2.131E+01	2.096E+01	2.139E+01	2.16E+01	2.143E+01			2.137E+01
	d > 1.0 cm	2.874E-06	2.667E-06	2.872E-06	2.87E-06	2.873E-06			2.882E-06
	p > 1.0 mm	3.445E-01	1.654E-01	3.360E-01	4.00E-01	3.368E-01			3.453E-01
	single	1.669E+00	7.829E-01	1.642E+00	1.90E+00	1.639E+00			1.672E+00
	double	2.330E-05	3.016E-05	2.257E-05	1.62E-05	2.303E-05			2.336E-05
MASTER2005	d > 0.1 mm		5.069E+00				6.145E+00		
	d > 1.0 cm		1.681E-05				1.358E-05		
	p > 1.0 mm		1.053E-02						
	single		1.530E-01				2.043E-01		
	double		5.076E-05				1.273E-04		
MASTER2009	d > 0.1 mm						6.367E+00	6.359E+00	
	d > 1.0 cm						1.501E-05	1.535E-05	
	p > 1.0 mm								
	single						2.105E-01	6.334E-01 ^{*3}	
	double						4.633E-05	4.051E-05 ^{*3}	
ORDEM 3.0^{*2}	d > 0.1 mm	1.943E+01	1.953E+01					1.881E+01	
	d > 1.0 cm	3.412E-06	3.411E-06					3.331E-06	
	p > 1.0 mm	3.902E-01 ^{*3}	2.522E-01 ^{*3}						
	single	1.408E+00 ^{*3}	1.101E+00 ^{*3}					3.924E-01 ^{*3}	
	double	1.744E-05 ^{*3}	1.895E-05 ^{*3}					7.484E-06 ^{*3}	

Meteoroid ^{*1}	d > 0.1 mm	2.342E+01	2.124E+01	2.164E+01	3.50E+01	2.164E+01	1.105E+01	1.080E+01	1.172E+01
	d > 1.0 cm	1.474E-06	1.336E-06	1.360E-06	2.21E-06	1.362E-06	8.922E-07	8.837E-07	3.424E-06
	p > 1.0 mm	1.003E-01	8.595E-02	9.064E-02	1.67E-01	8.812E-02			8.696E-02
	single	6.725E-01	6.164E-01	6.204E-01	1.04E+00	6.018E-01	3.009E-01	1.158E+00 ^{*3}	5.943E-01
	double	1.354E-05	1.146E-05	1.142E-05	2.47E-05	1.142E-05	6.306E-06	2.170E-05 ^{*3}	2.814E-05
MEM R2	d > 0.1 mm	1.920E+01	1.935E+01 ^{*4}						
	d > 1.0 cm	1.283E-06	1.268E-06						
	p > 1.0 mm	1.301E-01	1.278E-01						
	single	8.274E-01	8.084E-01						
	double	1.982E-05	1.928E-05						

*1 See Section 2.4.1.5.2 for discussion of these results

*2 Launch 2018

*3 Use particle density from the environment model (not constant)

*4 Scaled to 0.1 mm (~0.124 mm minimum for MEM)

Table 2-1: Calibration results for the cube

SPACE STATION		BUMPER 3	ESABASE2 /Debris	MDPANTO	COLLO	MODAOST	TURANDOT	PIRAT	Risk-Udar
NASA 91	d > 0.1 mm	1.758E+01	1.769E+01	1.761E+01	1.77E+01	1.763E+01			1.759E+01
	d > 1.0 cm	2.240E-04	2.394E-04	2.245E-04	2.45E-04	2.247E-04			2.241E-04
	p > 1.0 mm	2.858E-01	2.849E-01	2.920E-01	2.91E-01	2.855E-01			2.861E-01
	single	1.150E+00	1.181E+00	1.175E+00	1.13E+00	1.149E+00			1.151E+00
	double	7.595E-04	7.477E-04	7.654E-04	7.87E-04	7.861E-04			7.636E-04
NASA 2000	d > 0.1 mm	9.176E+01	9.167E+01	9.165E+01	9.09E+01	9.193E+01			9.184E+01
	d > 1.0 cm	1.150E-05	1.094E-05	1.149E-05	1.13E-05	1.151E-05			1.152E-05
	p > 1.0 mm	1.149E+00	5.586E-01	1.148E+00	1.48E+00	1.125E+00			1.150E+00
	single	5.725E+00	2.699E+00	5.787E+00	7.95E+00	5.629E+00			5.733E+00
	double	8.586E-05	1.213E-04	9.054E-05	5.98E-05	8.581E-05			8.619E-05
MASTER2005	d > 0.1 mm		2.107E+01				2.550E+01		
	d > 1.0 cm		6.790E-05				5.450E-05		
	p > 1.0 mm		3.686E-02						
	single		5.386E-01				6.826E-01		
	double		2.034E-04				5.176E-04		
MASTER2009	d > 0.1 mm						2.472E+01	2.484E+01	
	d > 1.0 cm						6.013E-05	6.181E-05	
	p > 1.0 mm								
	single						6.890E-01	1.848E+00 ^{*3}	
	double						1.847E-04	1.615E-04 ^{*3}	
ORDEM 3.0^{*2}	d > 0.1 mm		7.908E+01					7.481E+01	
	d > 1.0 cm		1.385E-05					1.323E-05	
	p > 1.0 mm		8.725E-01 ^{*3}						
	single		3.895E+00 ^{*3}					1.421E+00 ^{*3}	
	double		7.310E-05 ^{*3}					2.766E-05 ^{*3}	

Meteoroid	d > 0.1 mm	7.771E+01	8.991E+01	9.247E+01	7.21E+01	9.246E+01	4.657E+01	4.558E+01	5.018E+01
	d > 1.0 cm	1.361E-05	5.656E-06	5.820E-06	1.02E-05	5.819E-06	3.727E-06	3.681E-06	1.467E-05
	p > 1.0 mm	1.406E+00*	3.521E-01	3.732E-01	7.28E-01	3.639E-01			3.600E-01
	single	5.037E+00*	2.534E+00	2.564E+00	4.50E+00	2.495E+00	1.229E+00	4.759E+00 ^{*3}	2.470E+00
	double	6.309E-	4.659E-05	4.657E-05	1.09E-04	4.660E-05	2.481E-05	8.549E-05 ^{*3}	1.150E-04
MEM R2	d > 0.1 mm	8.234E+01	8.372E+01 ^{*4}						
	d > 1.0 cm	5.503E-06	5.485E-06						
	p > 1.0 mm	5.515E-01	5.489E-01						
	single	3.513E+00	3.476E+00						
	double	8.348E-05	8.262E-05						

*2 Launch 2018

*3 Use particle density from the environment model (not constant)

*4 Scaled to 0.1 mm (~0.124 mm minimum for MEM)

Table 2-2: Calibration results for the simple space-station model

SPHERE		BUMPER 3	ESABASE2 /Debris	MDPANTO	COLLO	MODAOST	TURANDOT	PIRAT	Risk-Udar
NASA 91	d > 0.1 mm	3.307E+00	3.341E+00	3.302E+00	3.34E+00	3.314E+00			3.310E+00
	d > 1.0 cm	4.215E-05	4.520E-05	4.209E-05	4.63E-05	4.225E-05			4.220E-05
	p > 1.0 mm	5.201E-02	5.270E-02	5.355E-02	8.23E-02	5.201E-02			5.204E-02
	single	2.093E-01	2.160E-01	2.154E-01	3.19E-01	2.092E-01			2.094E-01
	double	1.393E-04	1.360E-04	1.394E-04	2.12E-04	1.440E-04			1.400E-04
NASA 2000	d > 0.1 mm	1.705E+01	1.696E+01	1.699E+01	1.71E+01	1.698E+01			1.707E+01
	d > 1.0 cm	2.145E-06	2.019E-06	2.141E-06	2.14E-06	2.143E-06			2.149E-06
	p > 1.0 mm	2.044E-01	9.624E-02	2.050E-01	2.41E-01	2.009E-01			2.045E-01
	single	1.019E+00	4.680E-01	1.033E+00	1.20E+00	1.005E+00			1.020E+00
	double	1.504E-05	2.093E-05	1.607E-05	1.08E-05	1.509E-05			1.509E-05
MASTER2005	d > 0.1 mm		3.725E+00				4.373E+00		
	d > 1.0 cm		1.233E-05				9.537E-06		
	p > 1.0 mm		6.864E-03						
	single		9.282E-02				1.165E-01		
	double		3.809E-05				9.004E-05		
MASTER2009	d > 0.1 mm						4.279E+00	4.658E+00	
	d > 1.0 cm						1.017E-05	1.136E-05	
	p > 1.0 mm								
	single						1.159E-01	4.511E-01 ^{*3}	
	double						3.228E-05	2.937E-05 ^{*3}	
ORDEM 3.0^{*2}	d > 0.1 mm		1.442E+01					1.397E+01	
	d > 1.0 cm		2.528E-06					2.478E-06	
	p > 1.0 mm		1.533E-01 ^{*3}						
	single		6.971E-01 ^{*3}					2.721E-01 ^{*3}	
	double		1.142E-05 ^{*3}					4.852E-06 ^{*3}	

Meteoroid	d > 0.1 mm	1.494E+01	1.416E+01	1.457E+01	2.37E+01	1.461E+01	6.739E+00	7.206E+00	7.939E+00
	d > 1.0 cm	9.400E-07	8.910E-07	9.200E-07	1.50E-06	9.196E-07	5.453E-07	5.892E-07	2.320E-06
	p > 1.0 mm	6.463E-02	5.426E-02	5.779E-02	1.07E-01	5.647E-02			5.586E-02
	single	4.365E-01	3.913E-01	3.976E-01	6.66E-01	3.878E-01	1.765E-01	7.567E-01 ^{*3}	3.840E-01
	double	8.532E-06	7.145E-06	7.180E-06	1.56E-05	7.210E-06	3.717E-06	1.381E-05 ^{*3}	1.778E-05
MEM R2	d > 0.1 mm	1.297E+01	1.288E+01 ^{*4}						
	d > 1.0 cm	8.667E-07	8.440E-07						
	p > 1.0 mm	8.475E-02	8.120E-02						
	single	5.409E-01	5.158E-01						
	double	1.279E-05	1.215E-05						

*2 Launch 2018

*3 Use particle density from the environment model (not constant)

*4 Scaled to 0.1 mm (~0.124 mm minimum for MEM)

Table 2-3: Calibration results for the sphere

2.4.1.5 Discussion of Impact Flux and Penetration Probability Calibration Results

2.4.1.5.1 BUMPER – ESABASE / DEBRIS - MDPANTO Comparison

The results presented in **Table 2-1**, **Table 2-2** and **Table 2-3** give a good impression of the inherent accuracy of the three models and the differences between them. The predicted numbers can be very sensitive to a correct treatment of the damage equation and of the full directional and velocity distribution of impacting particles. In general, agreement is very good on debris predictions (within a few %), and fairly close between BUMPER and ESABASE, MDPANTO on meteoroids (within about 10%). The causes for meteoroid discrepancies are related to differences in the meteoroid velocity and directionality models considered as demonstrated by closeness for the simple spherical case and particle fluxes (number of particles >0.1mm and >1cm) and larger differences in penetration fluxes. Further effort to clarify the differences in meteoroid models is underway and will be reported in a future issue of the Protection Manual. Some discrepancies arise in damage calculation by ESABASE2 v3.0 when using ORDEM2000 debris model (within about 50%), while the number of impacts is in good agreement (within 10%). These differences can be due to the dependency of damage equations on specific impact direction and velocity distribution of debris particle in the case of ORDEM2000 model. Furthermore, this model revealed to be also very sensitive to orbital points settings affecting debris impact flux.

2.4.1.5.2 Comparison of Gruen and McBride/Taylor models

The model by McBride/Taylor uses the same mass distribution as the Gruen one. But velocity distributions (angular and speed) are different. The model by Gruen based on an even angular distribution but the model by McBride/Taylor considers a more complicated radiant distribution and the speed distribution depends on radiant.

In the table below there are given the fluxes of particles with sizes greater than 0.1 mm impacting an oriented cube. In both cases gravitational focusing and interception by the Earth and its atmosphere is considered. Model by McBride/Taylor gives the higher fluxes because the lower speeds of meteoroid are used. The most challenging increase (up to ten times) is for the Earth oriented surface. If we define the particles after they change the half-space during their motion as dispersed ones. Then, by Gruen model, the fluxes of such particles at the altitude of 400 km are zero. But, by McBride/Taylor model, the input of dispersed particles is about 5-10%. It is due availability of lower speed particles which isn't intercepted by the Earth and its atmosphere, and which experience the greater focusing effects. The dispersed particles give the sharp increase in fluxes on Earth oriented surfaces.

	Front	Starboard	Port	Back	Space	Earth	Total
Gruen	0.509E+01	0.253E+01	0.295E+01	0.963E+00	0.401E+01	0.281E+00	0.158E+02
McBride/Taylor	0.140E+02	0.511E+01	0.475E+01	0.109E+01	0.730E+01	0.281E+01	0.350E+02

Table 2-4: Comparison of meteoroid results in COLLO

2.4.1.5.3 Additional Details of Calibrations

The following tables provide detailed results of the calibration runs.

Case 1: Cube								
MDPANTO								
		Fwd	Stbd	Port	Back	Space	Earth	Total
NASA 91	d>0.1 mm	2.327E+00	1.073E+00	1.073E+00	0.000E+00	0.000E+00	0.000E+00	4.473E+00
	d>1 cm	2.966E-05	1.368E-05	1.368E-05	0.000E+00	0.000E+00	0.000E+00	5.702E-05
	p>1 mm	5.506E-02	1.294E-02	1.294E-02	0.000E+00	0.000E+00	0.000E+00	8.094E-02
	single	2.215E-01	5.207E-02	5.207E-02	0.000E+00	0.000E+00	0.000E+00	3.256E-01
	double	1.198E-04	4.178E-05	4.178E-05	0.000E+00	0.000E+00	0.000E+00	2.034E-04
NASA 2000	d>0.1 mm	5.284E+00	7.757E+00	7.785E+00	5.643E-01	0.000E+00	0.000E+00	2.139E+01
	d>1 cm	1.306E-06	7.733E-07	7.743E-07	1.824E-08	0.000E+00	0.000E+00	2.872E-06
	p>1 mm	5.232E-02	1.433E-01	1.399E-01	4.711E-04	0.000E+00	0.000E+00	3.360E-01
	single	2.729E-01	6.903E-01	6.749E-01	3.985E-03	0.000E+00	0.000E+00	1.642E+00
	double	3.189E-06	9.557E-06	9.716E-06	1.047E-07	0.000E+00	0.000E+00	2.257E-05
Meteoroid $\rho = 1.0$	d>0.1 mm	7.692E+00	3.626E+00	3.626E+00	9.851E-01	5.177E+00	5.313E-01	2.164E+01
	d>1 cm	4.840E-07	2.282E-07	2.282E-07	6.198E-08	3.257E-07	3.343E-08	1.360E-06
	p>1 mm	5.247E-02	1.047E-02	1.047E-02	7.178E-04	1.370E-02	1.064E-04	8.794E-02
	single	3.515E-01	7.770E-02	7.770E-02	5.938E-03	1.025E-01	5.095E-03	6.204E-01
	double	7.063E-06	1.275E-06	1.275E-06	8.077E-08	1.658E-06	7.030E-08	1.142E-05
BUMPER 3								
		Fwd	Stbd	Port	Back	Space	Earth	Total
NASA 91 2002	d>0.1 mm	2.320E+00	1.072E+00	1.072E+00	0.000E+00	0.000E+00	0.000E+00	4.464E+00
	d>1 cm	2.957E-05	1.366E-05	1.366E-05	0.000E+00	0.000E+00	0.000E+00	5.689E-05
	p>1 mm	5.500E-02	1.276E-02	1.276E-02	0.000E+00	0.000E+00	0.000E+00	8.053E-02
	single	2.213E-01	5.135E-02	5.135E-02	0.000E+00	0.000E+00	0.000E+00	3.240E-01
	double	1.197E-04	4.142E-05	4.142E-05	0.000E+00	0.000E+00	0.000E+00	2.025E-04
NASA ORDEM 2 2002	d>0.1 mm	5.162E+00	7.901E+00	7.790E+00	4.570E-01	0.000E+00	0.000E+00	2.131E+01
	d>1 cm	1.315E-06	7.721E-07	7.698E-07	1.724E-08	0.000E+00	0.000E+00	2.874E-06
	p>1 mm	5.195E-02	1.480E-01	1.445E-01	8.291E-05	0.000E+00	0.000E+00	3.445E-01
	single	2.591E-01	7.123E-01	6.964E-01	9.071E-04	0.000E+00	0.000E+00	1.669E+00
	double	8.550E-06	7.354E-06	7.354E-06	4.707E-08	0.000E+00	0.000E+00	2.330E-05
NASA ORDEM 3.0 2018	d>0.1 mm	9.303E+00	4.954E+00	4.954E+00	7.719E-02	7.267E-02	7.267E-02	1.943E+01
	d>1 cm	1.661E-06	8.419E-07	8.419E-07	4.149E-08	1.263E-08	1.263E-08	3.412E-06
	p>1 mm	2.190E-01	8.507E-02	8.507E-02	2.077E-04	4.078E-04	4.078E-04	3.902E-01
	single	8.574E-01	2.739E-01	2.739E-01	7.354E-04	1.184E-03	1.184E-03	1.408E+00
	double	7.984E-06	4.655E-06	4.655E-06	1.176E-07	1.357E-08	1.357E-08	1.744E-05
NASA 91	d>0.1 mm	8.769E+00	3.842E+00	3.842E+00	9.637E-01	5.445E+00	5.574E-01	2.342E+01
	d>1 cm	5.518E-07	2.418E-07	2.418E-07	6.064E-08	3.426E-07	3.507E-08	1.474E-06
	p>1 mm	5.715E-02	1.248E-02	1.248E-02	1.933E-03	1.619E-02	9.606E-05	1.003E-01
	single	3.777E-01	8.508E-02	8.508E-02	1.295E-02	1.109E-01	7.710E-04	6.725E-01
	double	7.910E-06	1.690E-06	1.690E-06	2.993E-07	2.158E-06	7.945E-08	1.383E-05
NASA MEM R2	d>0.1 mm	6.534E+00	3.188E+00	3.241E+00	1.135E+00	4.678E+00	4.201E-01	1.920E+01
	d>1 cm	4.367E-07	2.131E-07	2.166E-07	7.584E-08	3.127E-07	2.808E-08	1.283E-06
	p>1 mm	5.194E-02	2.088E-02	2.135E-02	7.918E-03	2.783E-02	2.359E-04	1.301E-01
	single	3.285E-01	1.330E-01	1.359E-01	4.976E-02	1.784E-01	1.746E-03	8.274E-01
	double	7.869E-06	3.165E-06	3.244E-06	1.248E-06	4.199E-06	9.498E-08	1.982E-05
MODAOST								
		Fwd	Stbd	Port	Back	Space	Earth	Total
NASA 91	d>0.1 mm	2.328E+00	1.074E+00	1.074E+00	0.000E+00	0.000E+00	0.000E+00	4.476E+00
	d>1 cm	2.968E-05	1.369E-05	1.369E-05	0.000E+00	0.000E+00	0.000E+00	5.706E-05
	p>1 mm	5.503E-02	1.274E-02	1.274E-02	0.000E+00	0.000E+00	0.000E+00	8.051E-02
	single	2.214E-01	5.124E-02	5.124E-02	0.000E+00	0.000E+00	0.000E+00	3.239E-01
	double	1.223E-04	4.288E-05	4.288E-05	0.000E+00	0.000E+00	0.000E+00	2.081E-04
NASA 2000	d>0.1 mm	5.311E+00	7.731E+00	7.843E+00	5.402E-01	0.000E+00	0.000E+00	2.143E+01
	d>1 cm	1.307E-06	7.732E-07	7.742E-07	1.826E-08	0.000E+00	0.000E+00	2.873E-06
	p>1 mm	5.432E-02	1.394E-01	1.430E-01	9.303E-05	0.000E+00	0.000E+00	3.368E-01
	single	2.713E-01	6.755E-01	6.915E-01	1.068E-03	0.000E+00	0.000E+00	1.639E+00
	double	8.430E-06	7.322E-06	7.229E-06	4.446E-08	0.000E+00	0.000E+00	2.303E-05
Meteoroid $\rho = 1.0$	d>0.1 mm	7.699E+00	3.598E+00	3.598E+00	1.025E+00	5.186E+00	5.325E-01	2.164E+01
	d>1 cm	4.845E-07	2.265E-07	2.265E-07	6.451E-08	3.264E-07	3.351E-08	1.362E-06
	p>1 mm	5.242E-02	1.052E-02	1.052E-02	7.271E-04	1.383E-02	1.146E-04	8.812E-02
	single	3.491E-01	7.416E-02	7.416E-02	5.534E-03	9.794E-02	9.105E-04	6.018E-01
	double	7.049E-06	1.275E-06	1.275E-06	8.391E-08	1.668E-06	7.028E-08	1.142E-05

COLLO								
		Fwd	Stbd	Port	Back	Space	Earth	Total
NASA 91	d>0.1 mm	2.35E+00	1.09E+00	1.09E+00	0.000E+00	0.000E+00	0.000E+00	4.52E+00
	d>1 cm	3.26E-05	1.51E-05	1.51E-05	0.000E+00	0.000E+00	0.000E+00	6.27E-05
	p>1 mm	5.58E-02	1.32E-02	1.32E-02	0.000E+00	0.000E+00	0.000E+00	8.23E-02
Debris ρ = 2.8	single	2.16E-01	5.13E-02	5.13E-02	0.000E+00	0.000E+00	0.000E+00	3.19E-01
	double	1.24E-04	4.38E-05	4.38E-05	0.000E+00	0.000E+00	0.000E+00	2.12E-04
NASA 2000	d>0.1 mm	5.33E+00	7.78E+00	7.91E+00	5.33E-01	0.000E+00	0.000E+00	2.16E+01
	d>1 cm	1.30E-06	7.73E-07	7.72E-07	1.83E-08	0.000E+00	0.000E+00	2.87E-06
	p>1 mm	5.53E-02	1.69E-01	1.75E-01	4.05E-04	0.000E+00	0.000E+00	4.00E-01
Debris ρ = 2.8	single	2.91E-01	7.91E-01	8.16E-01	4.26E-03	0.000E+00	0.000E+00	1.90E+00
	double	6.02E-06	5.07E-06	5.02E-06	5.60E-08	0.000E+00	0.000E+00	1.62E-05
Meteoroid ρ = 1.0	d>0.1 mm	1.40E+01	5.11E+00	4.75E+00	1.09E+00	7.30E+00	2.81E+00	3.50E+01
	d>1 cm	8.84E-07	3.22E-07	3.00E-07	6.87E-08	4.61E-07	1.77E-07	2.21E-06
	p>1 mm	9.14E-02	1.76E-02	1.94E-02	8.61E-03	2.44E-02	5.94E-03	1.67E-01
	single	5.62E-01	1.11E-01	1.20E-01	4.94E-02	1.55E-01	4.09E-02	1.04E+00
	double	1.37E-05	2.54E-06	2.88E-06	1.55E-06	3.40E-06	6.47E-07	2.47E-05

Table 2-5: Number of impacts/penetrations for “cube” calibration

Case 2: Simple Space Station							
MDPANTO							
		Box	Stbd	Port	Trailing	Earth	Total
NASA 91	d>0.1 mm	2.569E+00	3.042E+00	5.367E+00	3.325E+00	3.309E+00	1.761E+01
	d>1 cm	3.275E-05	3.878E-05	6.841E-05	4.239E-05	4.217E-05	2.245E-04
	p>1 mm	5.796E-02	4.942E-02	8.980E-02	2.792E-02	6.688E-02	2.920E-01
	single	2.332E-01	1.988E-01	3.613E-01	1.123E-01	2.691E-01	1.175E+00
	double	1.293E-04	1.229E-04	2.165E-04	1.324E-04	1.643E-04	7.654E-04
NASA 2000	d>0.1 mm	7.276E+00	1.098E+01	1.652E+01	3.989E+01	1.698E+01	9.165E+01
	d>1 cm	1.485E-06	1.834E-06	3.149E-06	2.878E-06	2.140E-06	1.149E-05
	p>1 mm	8.616E-02	1.496E-01	1.881E-01	4.549E-01	2.689E-01	1.148E+00
	single	4.372E-01	7.462E-01	9.615E-01	2.344E+00	1.298E+00	5.787E+00
	double	5.672E-06	9.915E-06	1.275E-05	4.280E-05	1.940E-05	9.054E-05
Meteoroid ρ = 1.0	d>0.1 mm	1.410E+01	1.386E+01	2.527E+01	2.782E+01	1.142E+01	9.247E+01
	d>1 cm	8.870E-07	8.722E-07	1.590E-06	1.750E-06	7.183E-07	5.820E-06
	p>1 mm	7.046E-02	5.912E-02	1.105E-01	7.639E-02	5.672E-02	3.732E-01
	single	4.773E-01	4.048E-01	7.546E-01	5.421E-01	3.849E-01	2.564E+00
	double	9.098E-06	7.439E-06	1.398E-05	8.775E-06	7.281E-06	4.657E-05
BUMPER 3							
		Box	Stbd	Port	Trailing	Earth	Total
NASA 91 2002 Debris ρ = 2.8	d>0.1 mm	2.556E+00	3.048E+00	5.366E+00	3.302E+00	3.306E+00	1.758E+01
	d>1 cm	3.258E-05	3.885E-05	6.839E-05	4.209E-05	4.213E-05	2.240E-04
	p>1 mm	5.780E-02	4.825E-02	8.717E-02	2.648E-02	6.610E-02	2.858E-01
	single	2.325E-01	1.941E-01	3.507E-01	1.065E-01	2.660E-01	1.150E+00
	double	1.289E-04	1.221E-04	2.145E-04	1.300E-04	1.640E-04	7.595E-04
NASA ORDEM 2 2002 Debris ρ = 2.8	d>0.1 mm	7.154E+00	1.087E+01	1.631E+01	4.038E+01	1.704E+01	9.176E+01
	d>1 cm	1.489E-06	1.849E-06	3.174E-06	2.844E-06	2.144E-06	1.150E-05
	p>1 mm	8.641E-02	1.458E-01	1.827E-01	4.600E-01	2.738E-01	1.149E+00
	single	4.264E-01	7.155E-01	9.069E-01	2.366E+00	1.310E+00	5.725E+00
	double	1.032E-05	1.166E-05	1.776E-05	2.692E-05	1.920E-05	8.586E-05
NASA ORDEM 3.0 2018 Debris 5 populations	d>0.1 mm	1.053E+01	1.280E+01	2.219E+01	1.768E+01	1.451E+01	7.771E+01
	d>1 cm	1.872E-06	2.278E-06	3.980E-06	2.943E-06	2.542E-06	1.361E-05
	p>1 mm	2.395E-01	2.233E-01	3.832E-01	2.478E-01	3.120E-01	1.406E+00
	single	9.225E-01	8.064E-01	1.409E+00	7.574E-01	1.142E+00	5.037E+00
	double	9.126E-06	9.523E-06	1.558E-05	1.531E-05	1.355E-05	6.309E-05
NASA 91 Meteoroid ρ = 1.0	d>0.1 mm	1.545E+01	1.516E+01	2.767E+01	2.914E+01	1.263E+01	1.001E+02
	d>1 cm	9.723E-07	9.541E-07	1.741E-06	1.833E-06	7.948E-07	6.296E-06
	p>1 mm	7.706E-02	6.560E-02	1.221E-01	8.814E-02	6.285E-02	4.157E-01
	single	5.139E-01	4.408E-01	8.197E-01	6.024E-01	4.194E-01	2.796E+00
	double	1.058E-05	8.944E-06	1.666E-05	1.184E-05	8.674E-06	5.670E-05
NASA MEM R2 Meteoroid ρ = 1.0	d>0.1 mm	1.230E+01	1.227E+01	2.240E+01	2.528E+01	1.009E+01	8.234E+01
	d>1 cm	8.221E-07	8.198E-07	1.497E-06	1.690E-06	6.744E-07	5.503E-06
	p>1 mm	8.679E-02	8.193E-02	1.492E-01	1.588E-01	7.479E-02	5.515E-01
	single	5.516E-01	5.221E-01	9.507E-01	1.015E+00	4.735E-01	3.513E+00
	double	1.315E-05	1.238E-05	2.255E-05	2.399E-05	1.141E-05	8.348E-05
MODAOST							
		Box	Stbd	Port	Trailing	Earth	Total
NASA 91	d>0.1 mm	2.583E+00	3.044E+00	5.371E+00	3.318E+00	3.308E+00	1.763E+01
	d>1 cm	3.292E-05	3.881E-05	6.846E-05	4.230E-05	4.217E-05	2.247E-04
	p>1 mm	5.803E-02	4.803E-02	8.698E-02	2.653E-02	6.594E-02	2.855E-01
	single	2.335E-01	1.932E-01	3.499E-01	1.067E-01	2.653E-01	1.149E+00
	double	1.326E-04	1.262E-04	2.223E-04	1.370E-04	1.681E-04	7.861E-04
NASA 2000	d>0.1 mm	7.401E+00	1.106E+01	1.650E+01	3.998E+01	1.698E+01	9.193E+01
	d>1 cm	1.495E-06	1.836E-06	3.152E-06	2.880E-06	2.142E-06	1.151E-05
	p>1 mm	8.970E-02	1.454E-01	1.783E-01	4.424E-01	2.689E-01	1.125E+00
	single	4.437E-01	7.166E-01	8.915E-01	2.287E+00	1.290E+00	5.629E+00
	double	1.029E-05	1.150E-05	1.768E-05	2.725E-05	1.908E-05	8.581E-05
Meteoroid ρ = 1.0	d>0.1 mm	1.414E+01	1.384E+01	2.525E+01	2.784E+01	1.140E+01	9.246E+01
	d>1 cm	8.898E-07	8.710E-07	1.589E-06	1.752E-06	7.176E-07	5.819E-06
	p>1 mm	6.939E-02	5.776E-02	1.080E-01	7.323E-02	5.550E-02	3.639E-01
	single	4.692E-01	3.947E-01	7.364E-01	5.189E-01	3.759E-01	2.495E+00
	double	9.106E-06	7.439E-06	1.397E-05	8.802E-06	7.281E-06	4.660E-05

COLLO							
		Box	Stbd	Port	Trailing	Earth	Total
NASA 91	d>0.1 mm	2.55E+00	3.05E+00	5.37E+00	3.36E+00	3.32E+00	1.77E+01
	d>1 cm	3.53E-05	4.23E-05	7.45E-05	4.65E-05	4.60E-05	2.45E-04
	p>1 mm	5.71E-02	4.91E-02	8.95E-02	2.85E-02	6.69E-02	2.91E-01
Debris $\rho = 2.8$	single	2.21E-01	1.90E-01	3.47E-01	1.11E-01	2.59E-01	1.13E+00
	double	1.30E-04	1.26E-04	2.22E-04	1.39E-04	1.69E-04	7.87E-04
NASA 2000	d>0.1 mm	7.27E+00	1.13E+01	1.69E+01	3.84E+01	1.71E+01	9.09E+01
	d>1 cm	1.47E-06	1.85E-06	3.18E-06	2.66E-06	2.12E-06	1.13E-05
	p>1 mm	1.02E-01	1.98E-01	2.40E-01	5.78E-01	3.59E-01	1.48E+00
Debris $\rho = 2.8$	single	5.60E-01	1.05E+00	1.31E+00	3.22E+00	1.82E+00	7.95E+00
	double	7.26E-06	8.48E-06	1.32E-05	1.76E-05	1.32E-05	5.98E-05
Meteoroid $\rho = 1.0$	d>0.1 mm	1.01E+01	1.07E+01	1.92E+01	2.31E+01	9.05E+00	7.21E+01
	d>1 cm	1.50E-06	1.56E-06	2.82E-06	2.83E-06	1.45E-06	1.02E-05
	p>1 mm	1.27E-01	1.18E-01	2.11E-01	1.60E-01	1.13E-01	7.28E-01
	single	7.83E-01	7.29E-01	1.31E+00	9.88E-01	6.93E-01	4.50E+00
	double	1.91E-05	1.74E-05	3.15E-05	2.44E-05	1.71E-05	1.09E-04

Table 2-6: Number of impacts/penetrations for “simple space station” calibration

2.4.1.6 Comparison of Shadowing Algorithms

Damage prediction tools have to consider, that some elements are shadowed by other elements of a spacecraft and thus can't be hit by impacting particles. Each tool presented above has its own algorithm, which computes this shadowing effect.

The following benchmark is performed in order to demonstrate the performance of the shadowing algorithm of the different damage prediction tools.

2.4.1.6.1 Benchmark Settings

- Mission parameters and environment models as defined in section 2.4.1.1.
- The spacecraft geometry is simply described by three surfaces with the dimension shown in **Figure 2.4-4**. The surfaces are oriented parallel to velocity direction. Each surface should consider impacts only from one side. Thus, two surfaces are partially hidden by the first surface. If the shadowing algorithm works properly, the two hidden surfaces should have the same number of impacts but fewer impacts than the first surface.

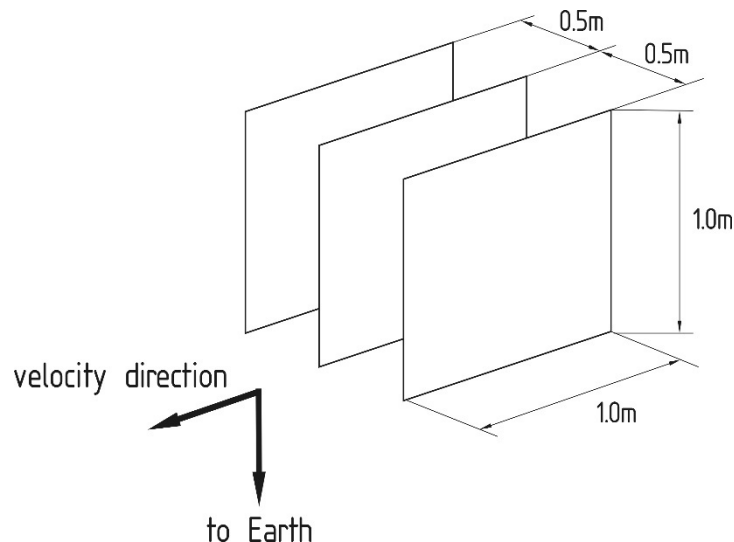


Figure 2.4-4: Spacecraft geometry for shadowing algorithm benchmark

- For both environments, the debris (D1-D4) and meteoroid (M1-M4) environment, four test cases can be defined. They differ in the number of vertical and horizontal elements on each of the three surfaces.

	Test Case D1/M1	Test Case D2/M2	Test Case D3/M3	Test Case D4/M4
No. vertical/horizontal elements	1	5	10	20

Table 2-7: Spacecraft geometry input for shadowing algorithm benchmark

- Number of impacts ($dp \geq 0.1\text{mm}$) shall be computed for all elements and summarized for the three surfaces.

2.4.1.6.2 Benchmark Results

The shadowing algorithms used in the different damage prediction tools have been tested with the described benchmark. The total number of impacts should be the same for the 2nd and 3rd surface and should be independent on the number of idealized elements.

The results are given in the following table:

Tool	BMK	Surface 1	Surface 2	Surface 3	Total
MDPANTO	D1	1.073E+00	5.442E-01	5.442E-01	2.162E+00
	D2	1.073E+00	5.442E-01	5.442E-01	2.162E+00
	D3	1.073E+00	5.442E-01	5.442E-01	2.162E+00
	D4	1.073E+00	5.442E-01	5.442E-01	2.162E+00
BUMPER	D1	1.072E+00	4.9990E-01	4.9990E-01	2.0717E+00
	D2	1.072E+00	5.4166E-01	5.4166E-01	2.1553E+00
	D3	1.072E+00	5.4212E-01	5.4212E-01	2.1562E+00
	D4	1.072E+00	5.4735E-01	5.4735E-01	2.1667E+00
MODAOST	D1	1.074E+00	5.467E-01	5.467E-01	2.168E+00
	D2	1.074E+00	5.467E-01	5.467E-01	2.168E+00
	D3	1.074E+00	5.467E-01	5.467E-01	2.168E+00
	D4	1.074E+00	5.467E-01	5.467E-01	2.168E+00
COLLO	D1	1.08E+00	5.78E-01	5.78E-01	2.23E+00
	D2	1.08E+00	5.78E-01	5.78E-01	2.23E+00
	D3	1.08E+00	5.78E-01	5.78E-01	2.23E+00
	D4	1.08E+00	5.78E-01	5.78E-01	2.23E+00
Risk-Udar	D1	1.072E+00	5.457E-01	5.460E-01	2.164E+00
	D2	1.072E+00	5.457E-01	5.460E-01	2.164E+00
	D3	1.072E+00	5.457E-01	5.460E-01	2.164E+00
	D4	1.072E+00	5.457E-01	5.460E-01	2.164E+00

Table 2-8: Debris (D#) Benchmarks - No. of impacts by 0.1mm particles

Tool	BMK	Surface 1	Surface 2	Surface 3	Total
MDPANTO	M1	3.626E+00	2.132E+00	2.132E+00	7.890E+00
	M2	3.626E+00	2.132E+00	2.132E+00	7.890E+00
	M3	3.626E+00	2.132E+00	2.132E+00	7.890E+00
	M4	3.626E+00	2.132E+00	2.132E+00	7.890E+00
BUMPER	M1	3.6198E+00	1.5871E+00	1.5871E+00	6.7940E+00
	M2	3.6198E+00	2.0980E+00	2.0974E+00	7.8152E+00
	M3	3.6198E+00	2.1095E+00	2.1095E+00	7.8388E+00
	M4	3.6198E+00	2.1073E+00	2.1073E+00	7.8344E+00
MODAOST	M1	3.598E+00	2.409E+00	2.409E+00	8.416E+00
	M2	3.598E+00	2.116E+00	2.116E+00	7.831E+00
	M3	3.598E+00	2.111E+00	2.111E+00	7.820E+00
	M4	3.598E+00	2.110E+00	2.110E+00	7.818E+00
COLLO	M1	3.54E+00	1.96E+00	1.96E+00	7.45E+00
	M2	3.54E+00	1.96E+00	1.96E+00	7.45E+00
	M3	3.54E+00	1.96E+00	1.96E+00	7.45E+00
	M4	3.54E+00	1.96E+00	1.96E+00	7.45E+00

Table 2-9: Meteoroid (M#) Benchmarks - No. of impacts by 0.1mm particles

The results achieved show that more or less the number of impacts on surface 2/3 are equal and less than on surface 1 in the different test cases. This is as expected, because the 2nd surface hides the 3rd one as the 1st one does with the 2nd. This effect is the same for the debris and meteoroid environment test cases. Only BUMPER and MODAOST show differences in the number of impacts on the 2nd and 3rd surface in the meteoroid benchmarks, BUMPER as well in the debris benchmarks.

The fact that the number of elements on each surface doesn't influence the total number of impacts on a surface leads to the conclusion that a low number of elements on each surface

are enough to compute a correct number of impacts. For this geometry (a planar surface) one element per surface is sufficient.

The flux concentration for each test case can be seen in the following figures as an example output of the damage prediction tool MDPANTO.

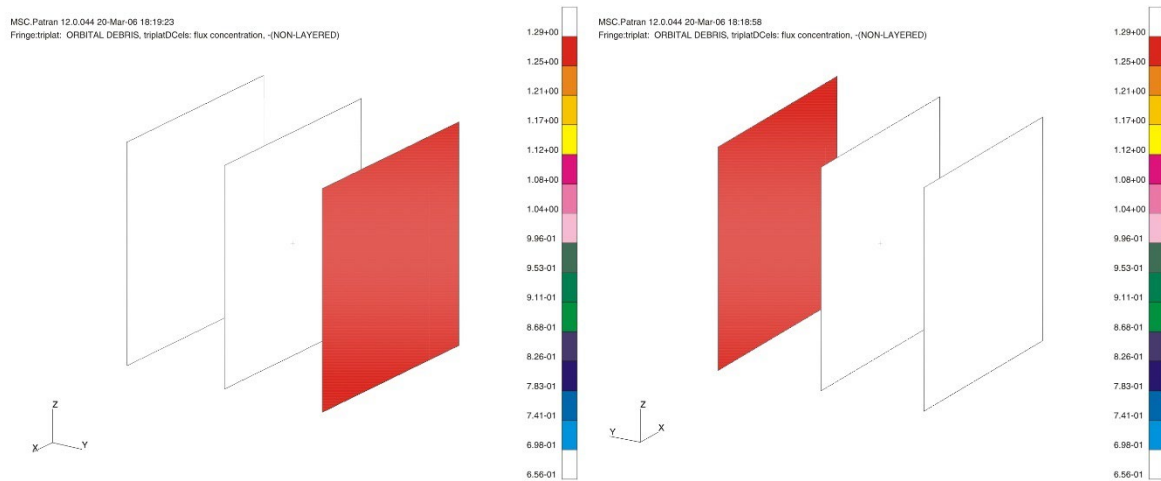


Figure 2.4-5: Debris impacts on surfaces (consisting of 1 element per surface)

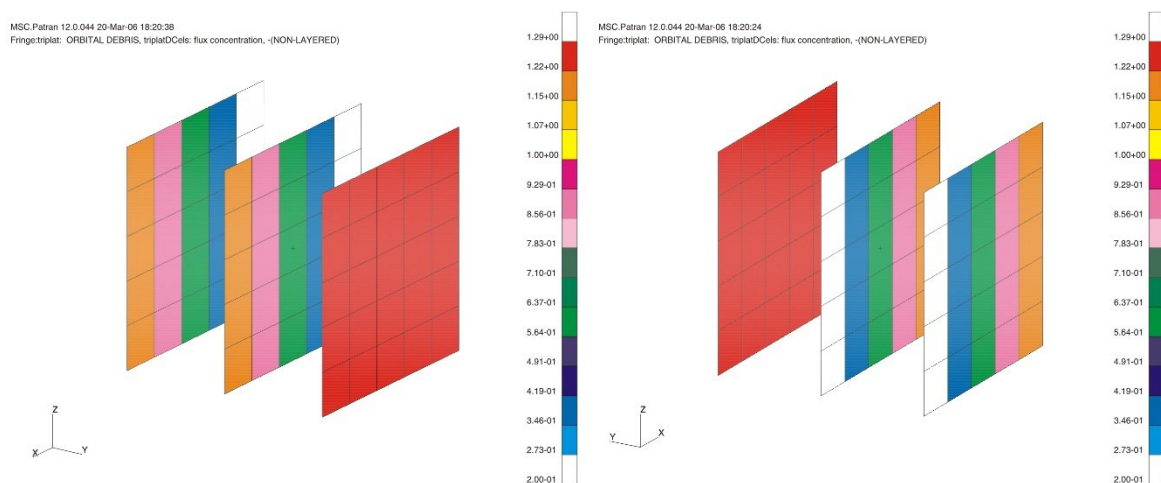


Figure 2.4-6: Debris impacts on surfaces (consisting of 25 elements per surface)

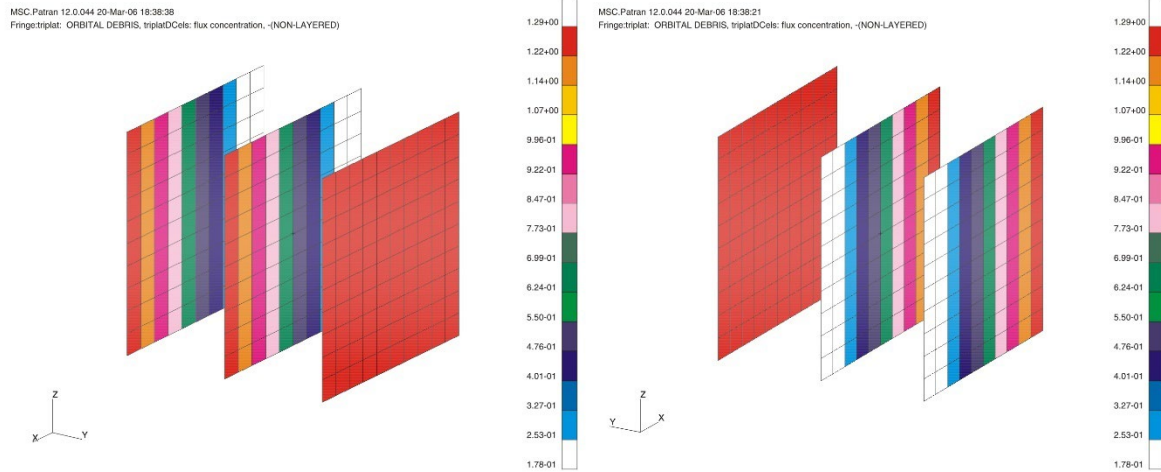


Figure 2.4-7: Debris impacts on surfaces (consisting of 100 elements per surface)

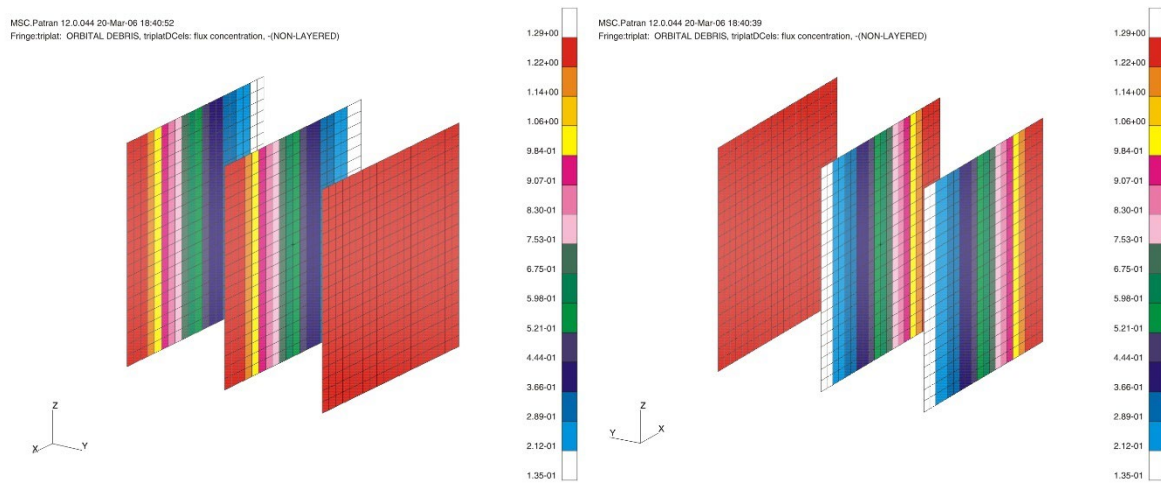


Figure 2.4-8: Debris impacts on surfaces (consisting of 400 elements per surface)

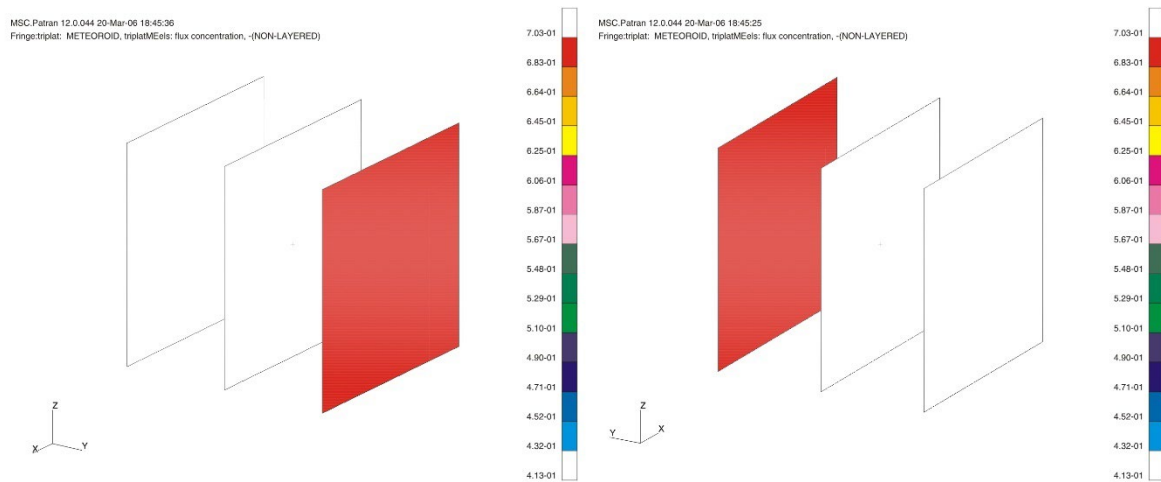


Figure 2.4-9: Meteoroid impacts on surfaces (consisting of 1 element per surface)

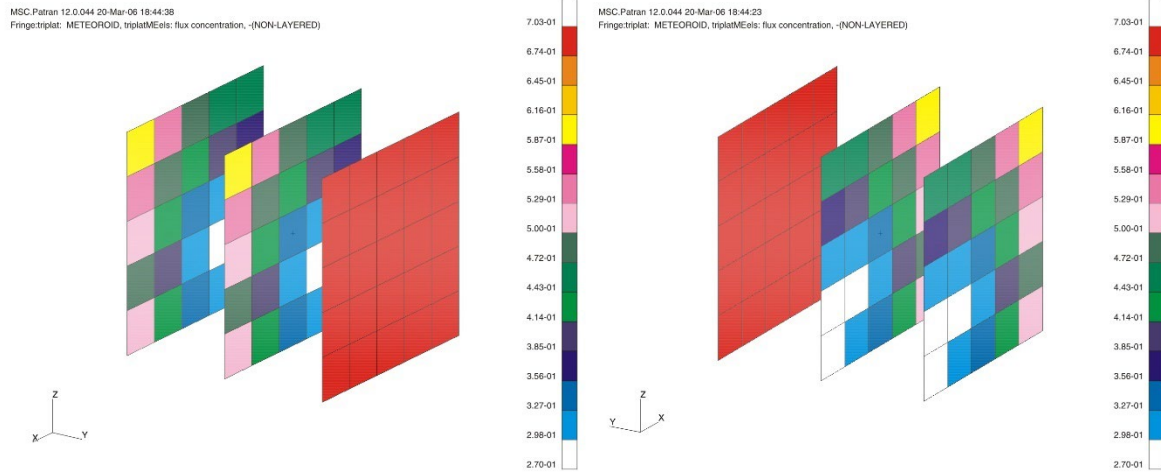


Figure 2.4-10: Meteoroid impacts on surfaces (consisting of 25 elements per surface)

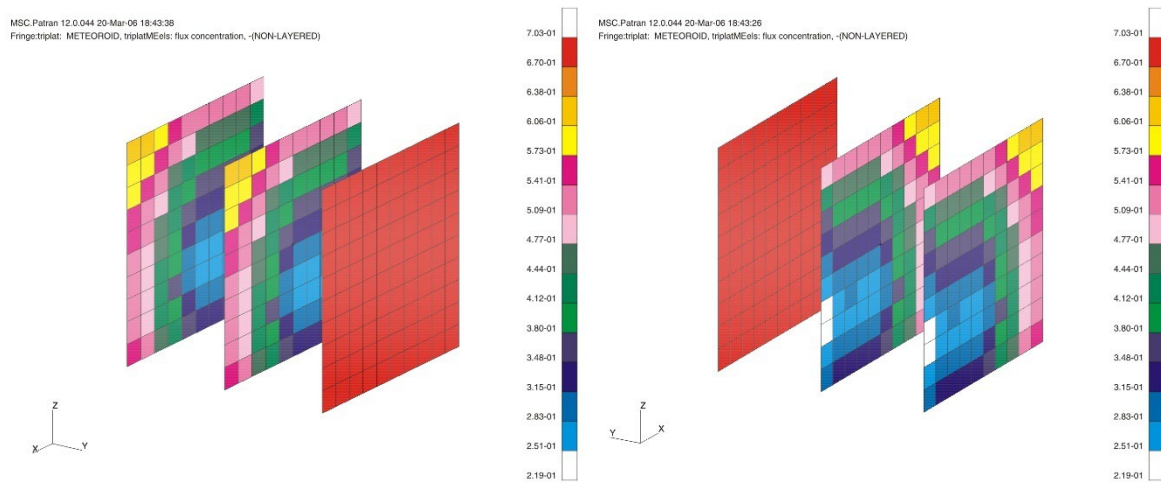


Figure 2.4-11: Meteoroid impacts on surfaces (consisting of 100 elements per surface)

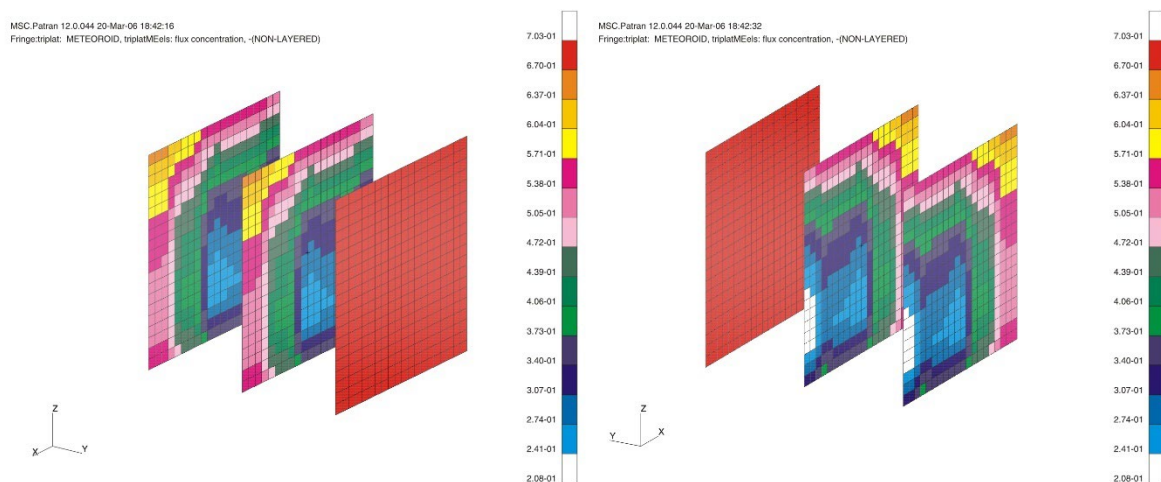


Figure 2.4-12: Meteoroid impacts on surfaces (consisting of 400 elements per surface)

2.4.2 Calibration of Spacecraft Component Failure Assessment

Some of the current risk assessment tools not only compute impact fluxes and their penetration capabilities on the outer hull of a spacecraft but also assess the probability of internal spacecraft component failure induced by impacts that have penetrated into the inside of the spacecraft.

2.4.2.1 Definition of Calibration Runs for Component Failure Assessment

Four generic spacecraft geometries are defined for the component failure benchmark calibration. All cases share a cube-shaped spacecraft inside of which different equipment configurations are implemented.

The spacecraft geometry is defined by:

- Cube-shape with 1000 mm outer edge length
- Honeycomb sandwich panel structural walls with
 - 0.4 mm face-sheet thickness
 - 35 mm honeycomb core thickness

Two geometries of equipment are defined for test cases #1-#3 and test case #4, respectively.

- Cube-shaped electronics boxes
- 1.5 mm equipment wall thickness
- Two equipment sizes
 - 328.4 mm outer edge length (Electronics Box 1, Case #1-#3)
 - 200 mm outer edge length (Electronics Box 2, Case #4)

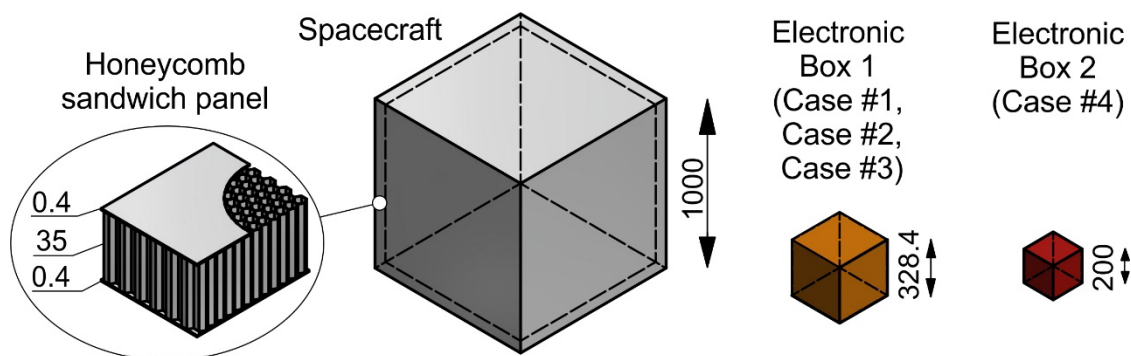


Figure 2.4-13: Geometry of the spacecraft (left) and components (middle and right for different test cases, dimensions in millimeter)

The equipment position inside the spacecraft includes four benchmark cases:

- Case #1: One Electronics box 1, centered position with 300 mm stand-off in each direction.
- Case #2: One Electronics Box 1, shifted from centered position in +X direction (RAM) with 100 mm stand-off to +X inner wall.
- Case #3: One Electronics Box 1, shifted from centered position in +Y direction with 100 mm stand-off to +Y inner wall.
- Case #4: Four Electronics Boxes 2, distributed in the center plane of the S/C with even spacing in the center plane with 100 mm stand-off to +X inner wall.

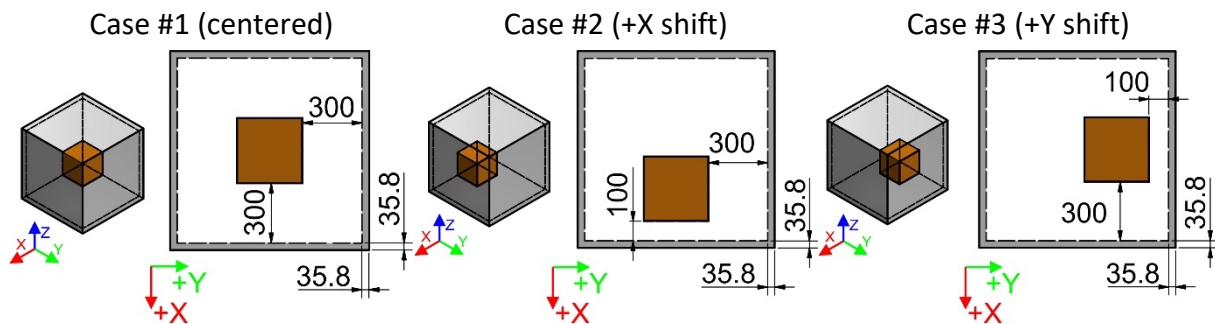


Figure 2.4-14: Positioning of component relative to the spacecraft: the Electronics box is centered (Case #1), shifted in flight direction (+X) or in lateral direction (+Y), respectively. Dimensions in millimeter.

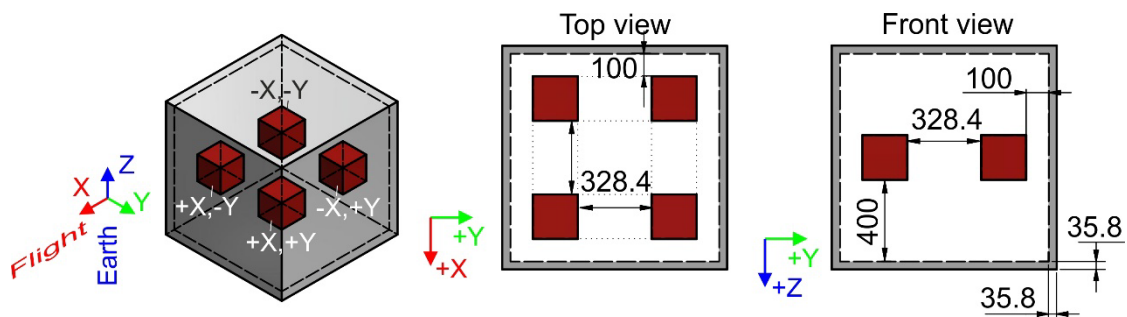


Figure 2.4-15: Positioning of components relative to the spacecraft for Case #4 (Dimensions in millimeter, perspective view with component identification).

2.4.2.1.1 Environment Models and Mission Parameters

The influence of the environment model is reflected in the impact flux calibration presented in Section 2.4.1. In order to reduce the parameter space for the calibration of component failure assessment, only one model is to be applied:

ESA MASTER 2009 v7.02 (Oct. 5, 2012)

Tick: all (human-made) condensed debris sources, Grün Taylor/HRMP model

The environment/mission parameters are:

- Semi-major axis = 7200 km
- Eccentricity = 0.0
- Inclination = 98.0 deg
- Right Ascension of the Ascending Node (RAAN) = 0.0 deg
- Argument of perigee 0.0 deg
- Launch 01/01/2009, 1 year duration.

2.4.2.1.2 Failure Type, Ballistic Limit Equations and Material Properties

Equipment failure criteria shall be one of the two following:

- any damage equal to or exceeding spall detachment from the rear side of the box cover plate (i.e. „light-tight“, but contamination of the box interior with spalled-off metallic fragments occurred) or
- complete perforation of the box cover plate (i.e. material from the perforation hole in the cover plate is ejected into the box interior; in other words: the cover is not „light-tight“ any more)

If the risk assessment tool uses ballistic limit equations for calculating the component failure, the following shall be used:

- Equation for electronics boxes given in [Schäfer et al. 2008] with the update fit parameters from [Rudolph et al. 2012].

Any method other than ballistic limit equation shall be specified along with the parameters applied.

The applied material properties for the honeycomb sandwich panel are:

- Face-sheets are both made from Al 2024-T3
 - Face sheet density: 2.780 g/cm³
 - Face sheet yield strength: 324 MPa (47 ksi)
- Honeycomb core type: 2.0-3/16-07P-5056 MIL-C-7438G
 - Honeycomb areal weight: 0.4 g/cm²

Material Properties for the electronics box walls:

- Al 2024-T3 with 324 MPa (47 ksi) yield strength

2.4.2.1.3 Desired Output of the Calibration Runs

For Case #1 (the results should be the same for the other test cases) the impact fluxes and their consequences on the spacecraft walls shall outputted:

- Number of impacts by particles with $d \geq 0.1$ mm for each surface of the spacecraft
- Number of impacts by particles with $d \geq 1.0$ cm for each surface of the spacecraft
- Total number of impacts by particles with $d \geq 0.1$ mm on all spacecraft surfaces
- Total number of impacts by particles $d \geq 1.0$ cm on all spacecraft surfaces
- Number of penetrations for each surface of the spacecraft
- Total number of penetrations for all spacecraft surfaces

For Case #1, Case #2, and Case #3, the component failures shall be outputted in terms of:

- Number of failures in each surface of the electronics box
- Total number of failures in all electronics box surfaces

For Case #4, the component failures shall be outputted in terms of:

- Total number of failures in each surface of each of the four electronics boxes
- Total number of failures (= summing up of all faces) in each of the four electronics boxes

2.4.2.2 Component Failure Assessment Calibration Results

		Surface	PIRAT	SHIELD	BUMPER3	ESABASE2
Number of impacts on spacecraft structure	d ≥ 0.1 mm	+X				
		-X				
		+Y				
		-Y				
		+Z				
		-Z				
S/C total		All surfaces				
Number of impacts on spacecraft structure	d ≥ 1.0 cm	+X				
		-X				
		+Y				
		-Y				
		+Z				
		-Z				
S/C total		All surfaces				
Number of penetrations in spacecraft structure		+X				
		-X				
		+Y				
		-Y				
		+Z				
		-Z				
S/C total		All surfaces				

Table 2-10: Flux and penetration calibration results for the component failure assessment

MASTER2009		Surface	PIRAT	SHIELD3	BUMPER3	ESABASE2
Number of failures per E-Box side	Case #1	+X				
		-X				
		+Y				
		-Y				
		+Z				
		-Z				
		All faces				
E-Box total						
Number of failures per E-Box side	Case #2	+X				
		-X				
		+Y				
		-Y				
		+Z				
		-Z				
		All faces				
E-Box total						
Number of failures per E-Box side	Case #3	+X				
		-X				
		+Y				
		-Y				
		+Z				
		-Z				
		All faces				
E-Box total						

Table 2-11: Calibration results for the component failure assessment for benchmark Cases #1 through #3

MASTER2009		Component	Face	PIRAT	SHIELD3	BUMPER3	ESABASE2
Number of failures per E-Box side	Case #4	+X, +Y	+X				
			-X				
			+Y				
			-Y				
			+Z				
			-Z				
E-Box total		All faces					
Number of failures per E-Box side		+X, -Y	+X				
			-X				
			+Y				
			-Y				
			+Z				
			-Z				
E-Box total		All faces					
Number of failures per E-Box side		-X, +Y	+X				
			-X				
			+Y				
			-Y				
			+Z				
			-Z				
E-Box total		All faces					
Number of failures per E-Box side		-X, -Y	+X				
			-X				
			+Y				
			-Y				
			+Z				
			-Z				
E-Box total		All faces					

Table 2-12: Calibration results for the component failure assessment for benchmark Cases #4

2.5 Applications of Impact Risk Assessment Codes

2.5.1 ASI/Alenia

ASI/Alenia is involved in the design and construction of different modules of the ISS (Columbus, MPLM, Node 2, Node 3, Cupola 1, Cupola 2, and ATV C/C). For this activity, a damage prediction methodology based upon the ESABASE code is used. Key inputs for the analyses are as follows: the geometrical and structural configuration of modules, meteoroid and debris population models, and empirical damage equations. These formulae describe the damage caused by an impacting projectile (of known mass, dimension, velocity, impact angle, etc.) on a known structure. The NASA code Bumper II is also used in the assessment.

Damage equations are derived from analytical, numerical and experimental considerations of HVI phenomenon.

The accuracy of damage predictions is strongly dependent on the accuracy of M/OD population models and damage formulas. The latter have to be modified for different shield designs.

2.5.2 DLR

MDPANTO was used to investigate the probability of no critical impact for the ERA Basic End Effectors in the micrometeoroid/orbital debris environment. To take shielding by the International Space Station into account, its structure was idealised, as shown in **Figure 2.5-1**. The idealisation of the ERA Basic End Effectors and one of its hibernation positions is shown in **Figure 2.5-2**. The requirement of $P_0 \geq 0.976$ over a 10 year-period could only be fulfilled when the shielding by the ISS-structure was considered.

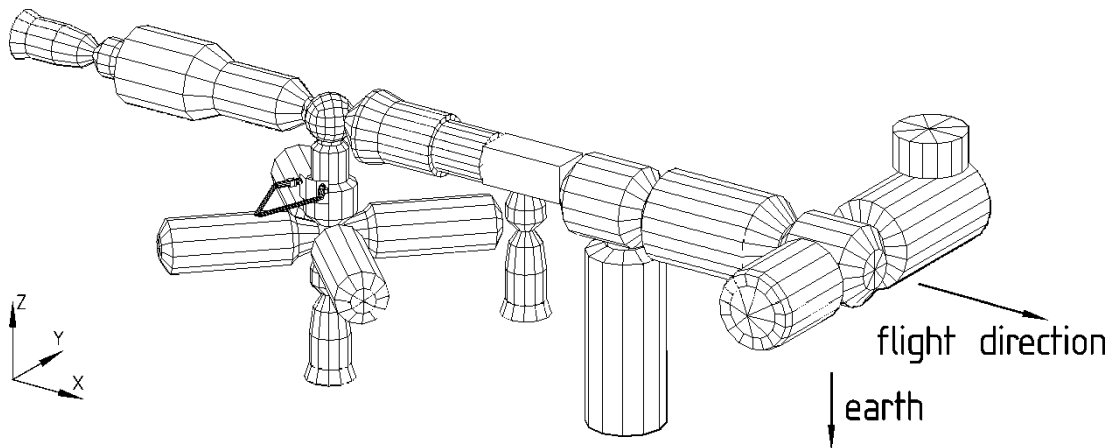


Figure 2.5-1: ERA Basic End Effectors attached to the ISS in hibernation position.

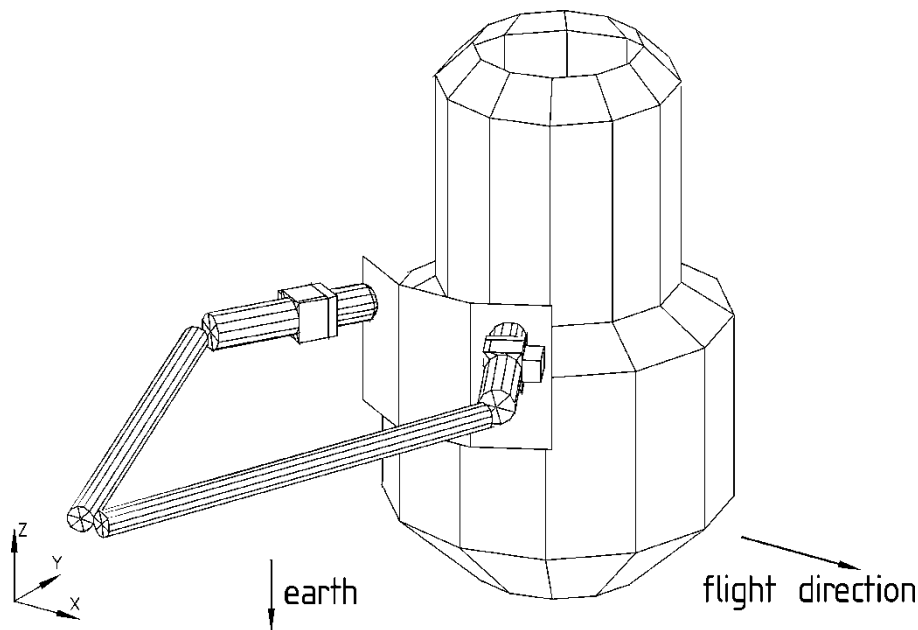


Figure 2.5-2: ERA Basic End Effectors

2.5.3 ESA

ESA uses the ESABASE2/DEBRIS tool on a regular basis to identify potential impact risks, to analyse protective measures, and to verify the implemented shielding design. The specific application depends on the request of the project.

ESABASE2/DEBRIS has been applied *inter alia* to the following missions/systems: ISS elements Columbus, ATV, ERA, CRV, scientific missions ISO, XMM, Rosetta, XEUS, and the PPF/ENVISAT Earth observation mission. The tool has also been applied to LDEF, EURECA and the Hubble Space Telescope solar arrays as part of the related post-flight impact investigations. ESA initiates updates of the tool as new models or user requirements appear.

In **Figure 2.5-3** a typical result of an ESABASE2/DEBRIS analysis for the Automated Transfer Vehicle (ATV) is presented. A more detailed description of the assessment of the probability of no penetration and the investigation of the mass penalty for different shielding concepts for ATV, performed with the precursor version ESABASE/DEBRIS, is given in appendix 10.1. The complete analysis is reported in [Beltrami, 2000].

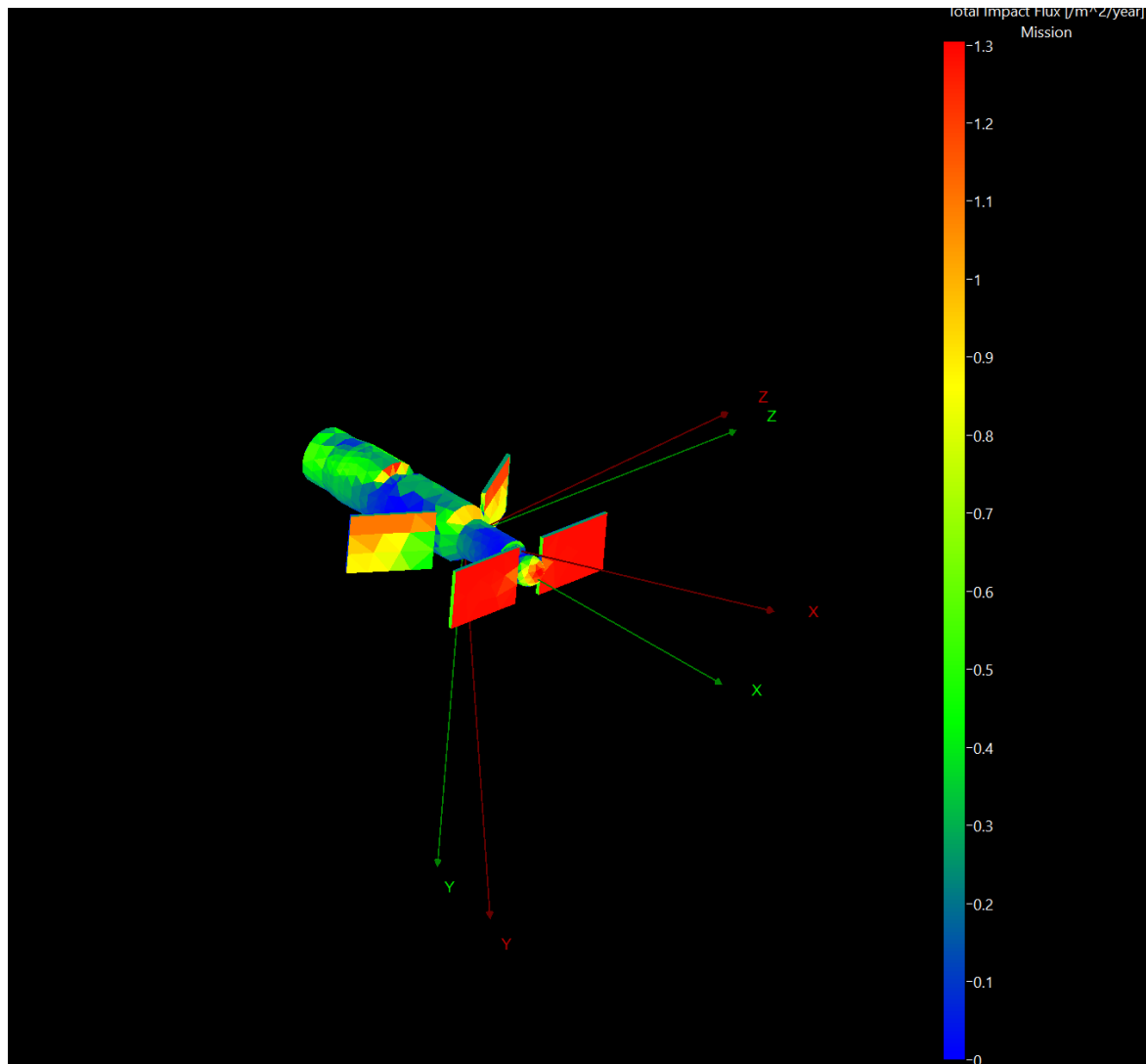


Figure 2.5-3: ATV Debris impact flux

2.5.4 NASA

NASA uses the PWG M/OD risk assessment methodology and the BUMPER code in performing risk assessments for Shuttle, the International Space Station (ISS), Extravehicular Activity (EVA) Mobility Units (EMU or Space Suits), crew return vehicle, reusable launch vehicle, Hubble Space Telescope, and other spacecraft.

2.5.4.1 Assessment of the Space Shuttle

Before each Shuttle flight, M/OD risks are calculated for the following types of damage: (1) critical penetrations (i.e., impacts that potentially endanger the vehicle or crew), (2) mission terminating impacts (e.g., radiator cooling loop puncture), and (3) impact damage to window debris panes that are deep enough to require replacement. After each Shuttle flight, observed M/OD impact damage is compared to the results of M/OD assessments of external damage to radiators, windows, and other Shuttle exposed surfaces.

2.5.4.2 Assessment of the International Space Station

NASA Johnson Space Center assesses ISS Probability of No Penetration (PNP) using the BUMPER code [NASA JSC HVIT website; Christiansen *et al.*, 1992]. Critical elements on ISS are all pressurised modules, external pressure vessels, and stored energy devices (such as control moment gyros and gyrodynes). Integrated Threat Assessment (ITA) number 10 was published in November 2001 [Prior *et al.*, 2001]. PNPs are based on ballistic limit equations derived from several thousand hypervelocity impact tests and hydrocode calculations. The PNP for the overall ISS for a 10 year period following First Element Launch (FEL) in November 1998 is assessed as 0.78 [Prior *et al.*, 2001] using standard meteoroid and the 1996 debris (ORDEM96) models. The requirement for ISS is to meet or exceed 0.76 PNP for 10 years following FEL.

The Probability of No Catastrophic Failure (PNCf) is determined using PNP and the “R-factor”, R, for each element: $PNCf_{\text{element}} = PNP_{\text{element}} \times R$. Catastrophic failure is defined as loss of one or more crew members, or loss of the entire station. PNP for each element is derived from BUMPER assessment. R is the ratio of catastrophic failure to penetration. The R-factors for each element are determined using the NASA Marshall Space Flight Center (MSFC) MSC-Surv code. Catastrophic failure modes assessed in the R-factor assessment include catastrophic rupture of the modules and pressure vessels, hypoxia, thrust loss, catastrophic failure of critical/hazardous internal equipment, and death to crew by penetration products such as fragments [Evans]. PNCf for ISS is determined from the product of the PNCf for each element: $PNCf_{\text{overall}} = \prod (PNCf_{\text{element}})$ for all ISS critical elements.

2.5.5 ROSAVIAKOSMOS

ROSAVIAKOSMOS has used the Bumper code to perform a risk analysis of the first two ISS modules. Specifically:

- A damage analysis of the Zarya module was performed by the Khrunichev Center and GOSNIIAS (using the ORDEM96 debris model).
- An analysis of the Zvezda module was made by RSC “Energia” and TSNIIMASH (using the NASA 91 debris model).

2.5.6 CNSA

Protection structures will be implemented in Chinese next generation manned spacecraft. During preliminary design phase, MODAOST was used to assess the impact risk and the result was used to guide the protection design. PNP risk has been calculated many times in order to meet the requirement and two specific ballistic limited curves achieved by HVI tests have been integrated into MODASOT system.

2.6 STENVI - Standard Environment Interface

Current environment models contain information like flux, impact velocity, impact direction of particles encountering the spacecraft in its orbit and much more. This information differs not only in the values between the models but also in the structure and the content of the result files. Because of this, a damage prediction tool must use a separate interface for each environment model which is adapted. Environment models are updated regularly and become more and more complex. A fact, which makes it complicated for developers of damage prediction tools, to access the relevant data from environment models. The consequence is massive coding effort when adapting future environment models. Without a defined standard, the inaccuracy in data conversion and data transfer is high, which impacts directly the quality of the damage prediction results.

Therefore, it is recommended to use the standard environment interface (STENVI) between orbital debris environment models and damage prediction tools. A main advantage is that different environment models can be adapted easily to the damage prediction tools without much effort. This guarantees a fast use of new environment models. Furthermore, it helps to avoid failure and to reduce inaccuracy in data conversion and data transfer due to a defined format.

For more information on STENVI please refer to [IADC-23-03, 2023]

2.7 Impact Risk Analysis of Unmanned Spacecraft

2.7.1 Introduction

During the design of a spacecraft a requirement may be specified for the survivability of the spacecraft against Meteoroid / Orbital Debris (M/OD) impacts. Typically, for an unmanned spacecraft, the requirement may state that the Probability of No Penetration (PNP) of the primary structure must be greater than a certain value. Thus, it is implicitly assumed that penetration of the primary structure is an appropriate failure criterion for an unmanned spacecraft. A logical consequence of this specification is that engineers will concentrate on applying any necessary impact protection to the external primary structure whilst giving little consideration to the equipment inside the spacecraft. There are a number of advantages to this approach:

- The impact risk analysis is relatively simple.
- Protection enhancements can be implemented quite easily by the addition of shielding to the primary structure.
- It is not necessary to know anything about the design, operation or location of the underlying equipment. Such information can also be difficult to identify early in the spacecraft design process.

For a crewed spacecraft, one can see that this approach is entirely reasonable since the perforation of a pressurised module would have serious consequences for the safety of the crew. However, the same is not necessarily true for an unmanned spacecraft. It is plausible that an unmanned spacecraft will survive an M/OD particle penetrating its primary structure for a variety of reasons:

- The resulting penetrative fragmentation cloud does not impact any sensitive or critical equipment. This may be because of the integration density of the equipment inside the spacecraft or its particular layout.
- If an equipment item is impacted, the cloud particles may not penetrate its casing.
- If perforation of the equipment casing occurs, there is a possibility that the resulting damage inside the equipment is insufficient to cause its failure.
- A penetrated equipment item may not fail if it has in-built redundancy.
- If the equipment item does fail, then this does not necessarily mean the mission will terminate. For example, a back-up unit may be located elsewhere in the spacecraft.

Thus, by focusing protection enhancement on the primary structure of an unmanned spacecraft, and ignoring the inherent robustness of the spacecraft design, it is likely that the primary structure will be heavier and bulkier than is strictly necessary. This suggests that, for unmanned spacecraft, an alternative approach should be adopted when analysing the impact risk and implementing protection.

2.7.2 Approach for Analysing Unmanned Spacecraft

Currently, most risk analysis codes utilise a ray-tracing routine to identify the points of impact of M/OD particles on external surfaces of a spacecraft. Ballistic Limit Equations (BLEs) are then called up to calculate if the particles penetrate the surfaces. The end result of this computation is a PNP

for each external surface, and hence the entire spacecraft primary structure. To perform an accurate evaluation of the M/OD impact risk on an unmanned spacecraft, a higher fidelity analysis than this is needed. As a minimum, the analysis should include the following five additional steps:

- 1) If an M/OD particle has penetrated the primary structure calculate the trajectory angles and spread angles of the two components of its fragmentation cloud. It should be noted that any penetrating oblique hypervelocity impact on a structure wall will be split into a cloud comprising two components, one of which propagates approximately in line with the flight direction of the impactor, and the other which propagates in a direction approximately normal to the structure wall. The combination of trajectory angle and spread angle provides a cone-shaped boundary for each component of the cloud, such that each cone defines a region of vulnerability inside the spacecraft. Relationships for the trajectory angles and cone spread angles of both components can be found in the literature, e.g. [Schonberg *et al.*, 1991], and adapted where necessary.
- 2) Determine which equipment items inside the spacecraft are impacted by the fragmentation cloud from a penetrating M/OD particle. Two different techniques that can be considered for this assessment are:
 - a) For all internal equipment, calculate the probability that it is impacted by a fragment from the cloud. This requires a consideration of the geometry of intersection of the two cone-shaped components of the cloud (as calculated in Step 1) with each equipment item. One possible method for calculating the equipment impact probability is available in [Putzar *et al.*, 2006]. This relies on a number of assumptions, such as the fragment mass within a cone being distributed homogeneously. However, the method is relatively simple to implement, and the computation is quick. Once the impact probability on each equipment item is known, then random sampling can be applied to determine which of the equipment items have been impacted by the cloud.
 - b) Consider the cloud as a set of fragments. Then, ray-trace each individual fragment to identify the surfaces of all internal equipment items that are impacted. This requires the trajectory information from Step 1 and the use of a fragmentation model. An analytical fragmentation model, such as the one described in [Schäfer *et al.*, 2006], which provides mass and velocity distribution functions that can be randomly sampled, is ideally suited to generate the individual fragments. Although the method is computationally more intensive than that in Step 2a) it should enable a more accurate modelling of the intersection of the cloud with internal equipment.
- 3) Determine the interaction of the fragmentation cloud with each internal equipment item that is impacted. This can be performed in one of two ways depending on which of the methods in Step 2 is used, i.e.:
 - a) If the method in Step 2a) is followed, then it is possible to use a specially adapted Ballistic Limit Equation (BLE), such as the SRL equation, to calculate the critical diameter of M/OD particle, d_c , that penetrates the entire configuration of primary spacecraft structure plus front wall of a particular internal equipment item. This must be done for each of the impacted equipment surfaces that are identified in Step 2a).
 - b) If the method in Step 2b) is followed, then it is possible to use any one of a number of single wall BLEs that are available in the literature, e.g., those listed in [Ryan *et al.*, 2010],

to determine whether or not each individual cloud fragment will penetrate the front wall of the equipment item that it impacts.

- 4) For each equipment item that is impacted or penetrated, establish if it fails. In the absence of any data, one might simply assume that failure occurs when there is a penetration, otherwise the equipment continues to operate. For some types of equipment, such as pipes and pressure vessels, this assumption can be considered reasonable if the criterion for failure is leakage. However, it is not valid if the failure mode is rupture. Neither is it valid for other types of equipment, such as electronics boxes. In 2006, Ernst Mach Institute, with support from QinetiQ and OHB-System, completed an ESA-funded study which demonstrated, amongst other results, that penetrated equipment does not necessarily cease to function [Putzar *et al.*, 2006]. Thus, for a given type of equipment, there is a quantifiable probability of impact-induced failure that can be defined in terms of the ratio of particle diameter, d , to critical particle diameter, d_c . This can be characterised by a failure probability curve, an example of which is shown in **Figure 2.7-1**.

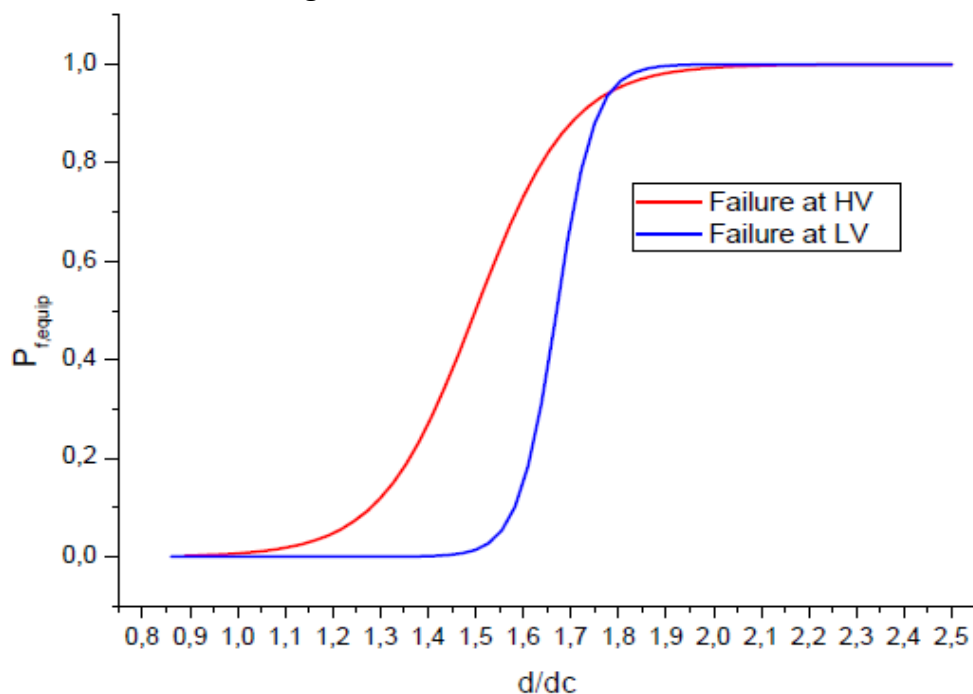


Figure 2.7-1: Failure probability curves as a function of d/d_c for an electronics box (with no internal redundancy) subjected to impact in the low velocity (LV) range of 3.3 – 4.7 km/s and the high velocity (HV) range of 5.2 – 7.7 km/s [Putzar *et al.*, 2006]

It should be noted that the shape of a failure probability curve for a particular type of equipment will vary depending on factors such as the precise point of impact on the equipment, the internal design of the equipment (including the amount of any redundancy), and the characteristics of the fragment cloud. Therefore, to establish an accurate probability function for a particular equipment item, an impact test programme must be undertaken. If this is not feasible, then consideration should be given to using one of the probability functions available in the literature, e.g. [Putzar *et al.*, 2006], although this will only give an approximate answer. Once a function has been identified, random sampling can be used to determine whether or not the equipment fails.

- 5) The consequences to the mission if the equipment fails. For example, this should take into account whether the equipment performs a function that is essential for the success of the mission. Consideration also needs to be given to the presence of redundancy located elsewhere in the spacecraft, as this might enable the mission to continue if an equipment item should fail.

By following this process for every M/OD particle that penetrates the spacecraft primary structure, it should be possible to quantify the impact-induced Probability of No Failure (PNF) of each equipment and hence the whole spacecraft. This will be a different figure to its PNP. Scrutiny of the distribution of PNF on a spacecraft enables engineers to identify which areas of the design are weakest. Therefore, attention can be focused on implementing protection where it is most needed.

2.7.3 Standardized Impact Survivability Assessment Procedure

The above approach fits well with an impact survivability assessment procedure that is currently being drafted for a new standard to be published by the International Organization for Standardization (ISO) [ISO 16126]. This recognises the need to calculate PNF during the design of an unmanned spacecraft. At the time of writing (January 2011), the draft standard contains the following high-level clauses:

Specify a requirement for the survivability of the spacecraft against space debris and meteoroid impacts for the purpose of achieving successful post-mission disposal.

Express the survivability requirement in terms of a minimum allowable value of impact-induced Probability of No Failure, PNF_{min} , over the operational phase of the spacecraft.

Perform an impact risk analysis to determine and compare the impact-induced Probability of No Failure of the spacecraft, $PNF_{s/c}$, with the minimum allowable value, PNF_{min} .

The draft standard then describes two possible procedures for analysing PNF and reducing impact risk, i.e., a “simple” analysis and a “detailed” analysis. It is worth noting that the approach described in the previous sub-section could be followed during the performance of the detailed analysis.

2.8 References

- Anderson, B.J., Review of Meteoroids / Orbital Debris Environment, NASA SSP 30425, Revision A, 1991.
- Anderson B.J., (editor), and R.E. Smith, (compiler), Natural Orbital Environment Guidelines for Use in Aerospace Vehicle Development, NASA TM 4527, chapter 7, June 1994.
- Beltrami, P., and G. Drolshagen, Assessment of the Probability of No Penetration and mass penalty for different shield configurations of the ATV, ESA internal report, ref. EMA/00-058/GD/ATV, June 2000.
- Bjorkman M.D., E.L. Christiansen, D.M. Lear, Bumper 3 Software User Manual, NASA TM-2014-218559, October 2014.
- Bryksin, E., S. Meshcheryakov, and M. Yakovlev, Preliminary evaluation of orbital debris collision danger for the Service Module, *15th Inter-Agency Space Debris Coordination Meeting Proceedings*, NASA Johnson Center, Houston, Texas, December 9-11, 1997.
- Bunte, K.D., Destefanis, R., Drolshagen, G., Spacecraft shielding layout and optimisation using ESABASE2/Debris. Proceedings of the 5th European Conference on Space Debris. ESA SP-672, 2009.
- Bunte, K.D., Miller, A., Hake, P., Milke, O., Drolshagen, G., Impact Risk Assessment for Lunar Missions, Proceedings of the 6th European Conference on Space Debris. ESA 4a.P-8, 2013.
- Christiansen, E.L., *et al.*, Spacecraft Survivability in the Meteoroid and Debris Environment, AIAA Paper No. 92-1409, 1992.
- Christiansen, E., Design and Performance Equations for Advanced Meteoroid and Debris Shields, *International Journal of Impact Engineering*, Vol.14, pp.145-156, 1993.
- Christiansen, E.L., J.L. Hyde, and D. Lear, Meteoroid/Debris Impact Damage Predictions for the Russian Space Station Mir, ESA SP-393, *Proceedings of the Second European Conference on Space Debris*, pp.503-508, March 1997.
- Christiansen, E.L., Meteoroid/Debris Shielding, NASA TP-2003-210788, 2003.
- Christiansen, E.L., et al., Handbook for Designing MMOD Protection, NASA TM-2009-214785, 2009.
- Cour-Palais, B., Meteoroid Environment Model -- 1969. [Near Earth to Lunar Surface], NASA SP-8013, 1969.
- Dikarev, V., et al., "Towards a New Model of the Interplanetary Meteoroid Environment", *Adv. Space Res.* 29 (28) pp. 1171-1175, 2002.

Divine, N., Five Populations of Interplanetary Meteoroids, *J. Geophys. Res.*, Vol. 98, No. E9, 1993.

Divine, N., E. Grün, P. Staubach, Modeling the meteoroid distribution in interplanetary space and near Earth, ESA SD-1, *Proceedings of the First European Conference on Space Debris*, pp 245-250, 1993.

Drolshagen, G., and J. Borde, ESABASE/DEBRIS, Meteoroid/Debris Impact Analysis, Technical Description, ref. *ESABASE--GD--01/1*, 1992.

ECSS (European Cooperation for Space Standardization), Space engineering, Space environment, *ECSS-E-10-04A*, January 2000.

ESABASE/DEBRIS release 2, Final Report, *ESA report, CR (P) 4214*, 1998.

Evans, S., NASA MSFC, personal communication.

Flegel, S.; Gelhaus, J.; Möckel, M.; Wiedemann, C.; Kempf, D.; Krag, H. Maintenance of the ESA MASTER Model, Final Report of ESA contract 21705/08/D/HK, M09/MAS-FR, 2011.

Grün, E., H.A. Zook, H. Fechtig, and R.H. Giese, Collisional Balance of the Meteoritic Complex, *Icarus*, Vol. 62, p.244, 1985.

Horstmann, A.; Hesselbach, S.; Kebschull, C.; Lorenz, J.; Wiedemann, C. Software User Manual - MASTER, M2018/MAS-SUM, May 2019.

Hu, D., Pang, B., Chi, R., Song, Z., Wu, H., 2021. Survivability assessment of spacecraft impacted by orbit debris. *Defence Technology*, 2021, 17(3): 961–970.
<https://doi.org/10.1016/j.dt.2020.06.003>

Hu, D., Chi, R., Liu, Y., Pang, B., 2021. Sensitivity analysis of spacecraft in micrometeoroids and orbital debris environment based on panel method. *Defence Technology* S2214914721001999.
<https://doi.org/10.1016/j.dt.2021.11.001>

Huang, J., Ma, Z., Ren, L., Li, Y., Zhou, Z., Liu, S., 2013. A new engineering model of debris cloud produced by hypervelocity impact. *International Journal of Impact Engineering* 56, 32–39.
<https://doi.org/10.1016/j.ijimpeng.2012.07.003>

Hyde, J., et al., JSC-66630, ITA-14, International Space Station Micrometeoroid and Orbital Debris Integrated Threat Assessment 14 (ITA-14), NASA Johnson Space Center Hypervelocity Impact Technology group (HITF), Sept. 2013.

IADC WG3 members, Standard Environment Interface, IADC-23-03, Apr 2023

ISO 16126:—, Space Systems — Assessment of Survivability of Unmanned Spacecraft against Space Debris and Meteoroid Impacts, International Organization for Standardization, to be published.

Jenniskens, P., Meteor Stream Activity, *Astron. Astrophys.*, Vol. 287, pp 990-1013, 1994.

Kawamoto, S., Narumi, T., Hanada, T., Kato, A. Space Debris Modeling in Japan, IAC-07-A6.2.04, 2007.

Kempf, S., F. Schäfer, M. Rudolph, N. Welty, T. Donath, R. Destefanis, L. Grassi, R. Janovsky, L. Evans, and A. Winterboer, Risk and vulnerability analysis of satellites due to MM/SD with PIRAT, *Proceedings of the 6th European Conference on Space Debris*, ESA SP-723; ESA/ESOC, Darmstadt, Germany, 2013.

Kessler, D.J., NASA JSC-20001, Orbital Debris Environment for Space Station, 1984.

Kessler, D., J. Zhang, M.J. Matney, P. Eichler, R.C. Reynolds, P.D. Anz-Meador and E.G. Stansbery, A Computer Based Orbital Debris Environment Model for Spacecraft Design and Observations in Low Earth Orbit, *NASA TM 104825*, November 1996.

Langwost, A.; Sdunnus, H.; Gunia, D.; Drolshagen, G.; Sørensen, J.; Hauptmann, S.; Presentation of the PC Version of the ESABASE/Debris Impact Analysis Tool; *Proceedings of the 4th European Conference on Space Debris*, ESA SP-587; ESA/ESOC, Darmstadt, Germany; p.619; 2005.

Lear, D., and E. Christiansen, ISS Debris Risk Assessment Process, Orbital Debris Quarterly Newsletter, Vol.4, Issue 1, <https://orbitaldebris.jsc.nasa.gov/quarterly-news/pdfs/odqnv4i1.pdf>, Jan.1999.

Lear, D., NASA JSC-29629, Verification of ORDEM2000 BUMPER-II Implementation and Comparison with ORDEM96 Impact Calculations, Oct. 2001.

Liou, J.-C., *et al.*, NASA TP-2002-210780, The New NASA Orbital Debris Engineering Model ORDEM2000, May 2002.

Space Debris User Portal, MASTER-8.0.3, <https://sdup.esoc.esa.int/master/>, April 2022.

McBride, N., The importance of the annual meteoroid streams to spacecraft and their detectors, *Adv. in Space Res.*, 20, pp1513-1516, 1997.

McNamara, H., Suggs, R.; Kauffman, B.; Jones, J.; Cooke, W.; Smith, S.; Meteoroid Engineering Model (MEM): A Meteoroid Model for the Inner Solar System; *Earth, Moon and Planets* (2004); 95, 123 -139; Springer 2005.

Meshcheryakov, S., Modelling and Analyses of Collision Risk of the International Station with Space Debris Fragments. *16th IADC Meeting. Proceedings*. Toulouse. October 9-11, 1998.

Meshcheryakov, S., About the ISS Protection Problem Against Orbital Debris; *In Collected Papers, Near Earth Astronomy and the Problems of Investigations of small Bodies in the Solar System*, Obninsk, 1999.

Meshcheryakov, S., The Orbital Impact Risk Analysis Methods. The COLLO System. *Third European Conference on Space Debris*, Darmstadt, Germany, 2000.

Miller, A., Zaake, M., Großman-Ruh, F., Bunte, K.B., Millinger, M., Drolshagen, G., Recent Extensions of the ESABASE2/Debris Impact Risk Assessment Tool, Proceedings of the 7th European Conference on Space Debris, Darmstadt, Germany, 2017.

Miller, A., ESABASE2 – Debris Release 12.0: Technical Description, ESA Contract No.16852/02/NL/JA "PC Version of DEBRIS Impact Analysis Tool", 2021.

Moorhead, A.V., et al., "NASA Meteoroid Engineering Model (MEM) version 3", July 22, 2019.

NASA SSP 30425, Rev. B, Space Station Program Natural Environment Definition for Design, 1994.

NASA Meteoroid Engineering Model Release 2.0 – User's Guide, Meteoroid Environment Office, George C. Marshall Space Flight Center, Huntsville, January 2013.

NASA ORDEM 3.0, NASA Orbital Debris Engineering Model 3.0 – User's Guide, Orbital Debris Program Office, NASA/TP-2014-217370, April 2014.

NASA ORDEM 3.2, NASA Orbital Debris Engineering Model 3.2, MSC-25457-1, <https://orbitaldebris.jsc.nasa.gov/modeling/ordem.html> .

NASA Johnson Space Center Hypervelocity Impact Technology group web site, <https://hvit.jsc.nasa.gov/>

Pang, B., Xiao, W., Peng, K., Wang, D. , The Space Debris Environment Engineering Model SDEEM 2015, Proc. 7th European Conference on Space Debris, Darmstadt, Germany, 18–21 April 2017, published by the ESA Space Debris Office.

Pang, B., Space Debris Environment Engineering Model SDEEM 2019, <https://www.eventi.polimi.it/events/space-debris-environment-engineering-model-sdeem-2019/> (Last access date: August,3,2020)

Prior, T., *et al.*, JSC-29648, ITA-10, International Space Station Meteoroid and Debris Integrated Threat Assessment No.10, NASA Johnson Space Center Hypervelocity Impact Technology group (HITF), Nov. 2001.

Prior, T., NASA JSC-29751, Validation of ORDEM2000 into BUMPER-II Risk Analysis Code and Impact on ISS, 2002.

Putzar, R.; Schäfer, F., Vulnerability of Spacecraft Equipment to Space Debris and Meteoroid Impacts, Final Report of ESA Contract 16483/02/NL/PA, 2006.

Reimerdes, H.-G., K.-H. Stecher, and M. Lambert, Ballistic Limit Equations for the Columbus-Double Bumper Shield Concept, *ESA SD-01, Proceedings of the First European Conference on Space Debris*, Darmstadt, Germany, 1993.

Reimerdes, H.-G., and W. Wohlers, Optimization of Micrometeoroid and Space Debris Protection Systems, ESA SP-473, *Proc. Third European Conference on Space Debris*, Darmstadt, Germany, 2001.

Rudolph, M., Welty, N., Putzar, R., Schäfer, F.K. et al., Extending the applicable range of the SRL ballistic limit equation to oblique hypervelocity impacts. 12th European Conference on Spacecraft Structures, Materials & Environmental Testing, ESA SP-691, Noordwijk, The Netherlands, 2012.

Ruhl, K., Bunte, K.D., Gäde, A., Miller, A., Zaake, M., Großmann-Ruh, F., ESABASE2 – Debris: Software User Manual, ESA Contract No.16852/02/NL/JA "PC Version of DEBRIS Impact Analysis Tool", 2021

Ryan, S. and Christiansen, E.L., Micrometeoroid and Orbital Debris (MMOD) Shield Ballistic Limit Analysis Program, NASA TM–2009–214789, 2009.

Ryan, S., Christiansen, E., A Ballistic Limit Analysis Program for Shielding against Micrometeoroids and Orbital Debris, presented at the 61st International Astronautical Congress, Prague, 2010.

Ryan, S., and Christiansen, E.L., "Micrometeoroid and Orbital Debris (MMOD) Shield Ballistic Limit Analysis Program", NASA/TM-2009-214789, 2010.

Ryan, S., F. Schäfer, and R. Destefanis, A ballistic limit equation for hypervelocity impacts on composite honeycomb sandwich panel satellite structures, *Advances in Space Research*, 41, pp 1152-1166, 2008.

Schäfer, F., T. Geyer, E. Schneider, M. Rott, E. Igenbergs, Degradation and destructions of optical surfaces by hypervelocity impact, *International Journal of Impact Engineering*, 26, pp 683-698, 2001.

Schäfer, F.K., An Engineering Fragmentation Model for the Impact of Spherical Projectiles on Thin Metallic Plates, *International Journal of Impact Engineering*, 33, p745-762, 2006.

Schäfer, F. K., S. Ryan, M. Lambert, R. Putzar, Ballistic limit equation for equipment placed behind satellite structure walls, *International Journal of Impact Engineering*, 35, No. 12, pp 1784-1791, 2008.

Sdunnus, H., K.D. Bunte, P. Beltrami, and A. Langwost, Upgrade of ESABASE /DEBRIS, Final Report of ESA/ESTEC contract 15206/01/NL/ND, eta_max space, Braunschweig, August 2002.

Soja, R. et al., IMEM2: A meteoroid environment model for the inner solar system. *Astronomy & Astrophysics*. 628. 10.1051/0004-6361/201834892, 2019.

Stabroth, S., Wegener, P., Klinkrad, H., MASTER 2005, Software User Manual, M05/MAS-SUM, 2006.

Staubach, P., E. Grün, and R. Jehn, The meteoroid environment of the Earth, 31st COSPAR Sci. Assembly, Birmingham/UK, July 1996.

Stokes, P.H., Swinerd, G.G., Crowther, R., Marsh, V., and Walker, R.J., “A New Approach for Optimising Satellite Shielding and Configuration using Genetic Algorithms”, *Presented at the Second European Conference on Space Debris*, ESOC, Darmstadt, Germany, March 1997.

Stokes, H., G. Swinerd, R. Walker, and J. Wilkinson, SHIELD: A New Model to identify Optimum Debris Protection for Unmanned Spacecraft, IAA-99-IAA.6.5.02, *presented at the 50th International Astronautical Congress*, Amsterdam, The Netherlands, 4-8 October 1999.

Stokes, H., G. Swinerd, R. Walker, J. Wilkinson, and C. Martin, Achieving Cost-Effective Debris Protection of Unmanned Spacecraft using SHIELD, IAA-00-IAA.6.5.06, *presented at the 51st International Astronautical Congress*, Rio de Janeiro, Brazil, 2-6 October 2000.

Stokes, P.H. and Swinerd, G.G., “The Implementation of Cost Effective Debris Protection in Unmanned Spacecraft”. *Advances in Space Research*, 34: p. 1090-1096, 2004.

Stokes, P.H. and Swinerd, G.G., “Debris Protection Optimisation of a Realistic Unmanned Spacecraft using SHIELD”, *Presented at the 4th European Conference on Space Debris*, ESOC, Darmstadt, Germany, 18 – 20 April, 2005.

Stokes, H., Cougnet, C., Gelhaus, J., Oswald, M., Schaefer, U., and Theroude, C., “A Detailed Impact Risk Assessment of Two Low Earth Orbiting Satellites”, IAC-12-A6.3.2, *63rd International Astronautical Congress*, Naples, Italy, 2012.

Stokes, H., Cougnet, C., David, M., Gelhaus, J., and Röthlingshöfer, M., “A detailed impact risk assessment of possible protection enhancements to two LEO spacecraft”, *Presented at the 6th European Conference on Space Debris*, ESOC, Darmstadt, Germany, April 2013.

Sun, Z., G. Yuan, J., G. Han, Z., Y. Development and Calibration of Structural Optimization Software for Debris Protection Systems, IAC-07-A6.4.04, *58th International Astronautical Congress*, Hyderabad, India, 2007.

Wang, D., Pang, B., Xiao, W., Unexpected Breakup Events Analysis Based on SDEEM 2019, *Space Debris Research*, 2019, 19, (2), pp.25-31.

Wegener, P., J. Bendisch, K. Bunte, S. Hauptmann, and H. Sdunnus, Upgrade of the ESA MASTER Space Debris and Meteoroid Environment Reference Model, Final Report of ESOC/TOS-GMA contract 14710/00/D/HK, Aug 2002.

Welty, N., M. Rudolph, F. Schäfer, J. Apeldoorn, and R. Janovsky, Computational methodology to predict satellite system-level effects from impacts of untrackable space debris, *Acta Astronautica*, 88, pp 35–43, 2013.

Zheng, S., G. Han, Z. Y. Yan, J. Fan, J. Y. Qu, G. J. Calibration and Application of Meteoroid/Debris Failure Probability Assessment Code, Proc. 4th European Conference on Space Debris, Darmstadt, Germany, 2005.

3 Ballistic Limit Equations

This chapter provides a description of typical spacecraft components and subsystems, their impact-related failure mechanisms, and associated ballistic limit equations.

Ballistic limit equations (BLEs) are developed to define impact conditions (i.e., particle size, particle density, impact velocity, and impact angle) that results in threshold failure of specific spacecraft components or subsystems. The PWG uses a combination of hypervelocity impact test results and analyses to determine the BLEs.

The chapter defines specific characteristics for each BLE:

- the relevant spacecraft system, subsystem or component (name, use, materials, thickness, gaps, etc),
- the damage mode or failure mode of the subsystem/component,
- the specific ballistic limit equations with appropriate nomenclature defined,
- limits of applicability, and references.

3.1 Basic Ballistic Limit Equations

The structure of a spacecraft is designed to ensure its integrity during the launch, throughout the mission, and if it is reusable during descent, re-entry, and landing. In addition, the structure has to provide required stiffness in order to allow for e.g. exact positioning of experiments and antennas, and it has to protect the payload against the space environment. The structural mass should be as low as possible allowing a maximum amount of payload. Therefore, a spacecraft represents a light-weight-design, made out of thin walled structural elements which may be stiffened locally or may be sandwich plates or shells. Structures for manned spacecraft are addressed in Sections 3.2 and 3.3

Typical structural materials, used in spacecraft design are Aluminium alloys and fibre reinforced plastics. To insulate the structure against heat, it may be covered by thermal insulation like MLI (multi layer insulation), silica felt or ceramic tiles. The structural parts may be connected by brackets and mechanism are needed to allow required movements of structural parts.

In addition to the inertial loads resulting from accelerations and to pressure loads in pressurised parts of the spacecraft structure (pressure vessels or pressurised modules) the structure has to protect the payload against hypervelocity impacts which can be either from micro-meteoroids or from orbital debris particles. The complexity of this problem represents a serious technical challenge for manned missions and is becoming an important consideration in the design of unmanned spacecraft. This means, the structure has to give sufficient impact protection both to man and equipment. Catastrophic failure of loaded structures (pressure vessels, pressurised modules) has to be avoided as well as the generation of new orbital debris.

When a projectile impacts on a structure, high pressures and temperatures are generated, which may melt or even vaporise the material and produce a crater. If the projectile is large enough perforation of a single wall structure (thin structure) and initiation of cracks will occur.

The impact behaviour of thin-walled structures can be considerably improved by use of a so-called Whipple shield or bumper shield. This shield is located in a certain distance in front of the structure to protect. If a particle hits and passes the thin shield, the pressure and the heat produced lead to fragmentation, melting or even vaporisation of the particle. A debris cloud is produced, which will spread over a large surface area of the protected structure and is thus less detrimental. Multiple wall structures such as Whipple shields and triple shields also in combination with MLI were investigated. The presence of MLI seems to reduce the protection ability of the multiple wall structure. E. g., it has been experimentally observed that for Whipple shield configurations including Multi-Layer Insulation on top of the bumper, the shielding performance can be degraded.

Advanced concepts have been developed in order to further improve the protection against impacts. These concepts incorporate Sandwich structures, composite structures and e. g. additional layers of Nextel or Kevlar for multiple wall structures.

3.1.1 Single Wall Structures

Behaviour under Hypervelocity Impact

Ductile Metallic Targets

Upon impact of a projectile on a structure, high pressures and temperatures are generated, which may melt or even vaporise the material and produce a crater, the volume of which is much larger than the particle volume. If the particle is large enough (about 10 – 15% of the wall thickness for a particle velocity around 7 km/s [Cour-Palais, 1987]) perforation of the thin structure and initiation of cracks will occur. The particle will be fragmented, and the fragments will enter the spacecraft and produce further damage. In the case of loaded structures, the generated cracks may exceed the critical crack length, resulting in catastrophic rupture.

Brittle Targets (Glass, Ceramic)

In brittle targets like glass (windows, solar cells) or ceramic tiles, the particle will also create craters, the volume of which is much larger than in case of ductile material. This results from spallation due to the low tensile strength of these materials.

Fibre Reinforced Plastics

If targets made of fibre reinforced plastics are impacted, craters or holes are created, too. Contrary to metallic targets, the shape of the crater or the hole is much more irregular due to the disintegration of fibre and matrix material. As the wall is typically made out of several layers, delamination of the layers will happen, resulting in a damage area which is much larger than the crater or the hole.

Improvement of the Impact Behaviour

The impact behaviour of thin-walled structures can be considerably improved by use of a so-called Whipple shield or bumper shield. This shield is located in a certain distance in front of the structure to protect. If a particle hits and passes the thin shield, the pressure and the heat produced lead to fragmentation, melting or even vaporisation of the particle. A debris cloud is produced, which will spread over a large surface area of the protected structure and is thus less detrimental.

3.1.1.1 Composite Wall Panels

A composite wall structure has been developed and tested by Taylor *et al.*, 2001, as a low-cost alternative for unmanned spacecraft. It comprises filament wound carbon fibre HMA 2236 (with Epon 9405 resin and Epon 9470 cure agent ("G50 fibre")). The structure can also be combined with shielding layers of Kevlar fabric prepreg (120 style weave, Kevlar 49 prepreg and Fiberite 934 resin) + Scotch-Weld film adhesive for enhanced protection, as shown in **Figure 3.1-1**.

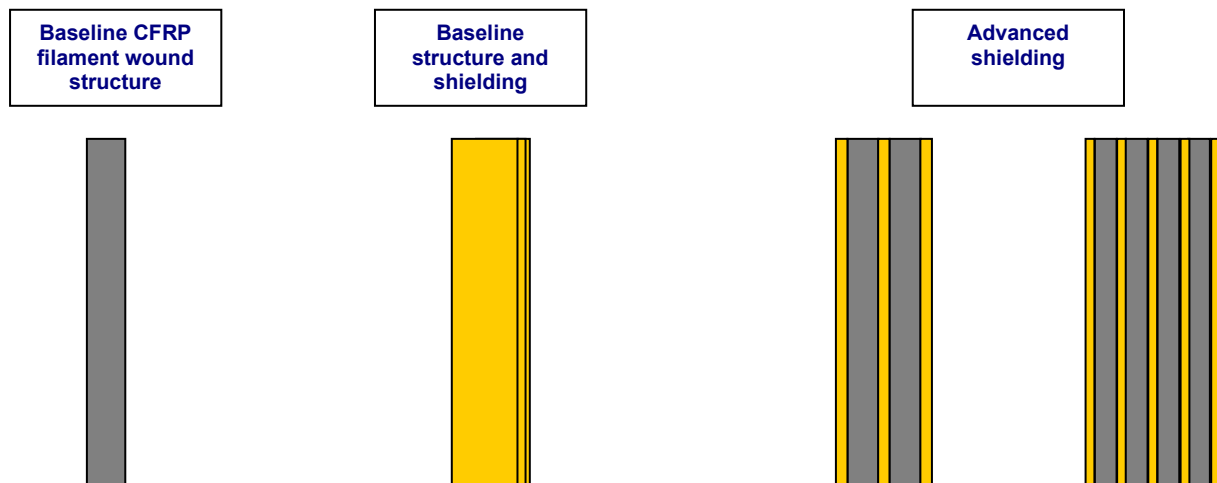


Figure 3.1-1: CFRP filament wound structure concepts [Taylor et al., 2001]

Flat plate samples (comprising four plies of Kevlar 49 + one ply adhesive) were manufactured (0/90 orientation) and impact tested using the University of Kent's Light Gas Gun. Shots were performed using Aluminium (Al2017) projectiles at $\sim 6\text{ km/s}$ and 0 degree incidence. An example of the resulting damage on one of the targets is shown in **Figure 3.1-2**.

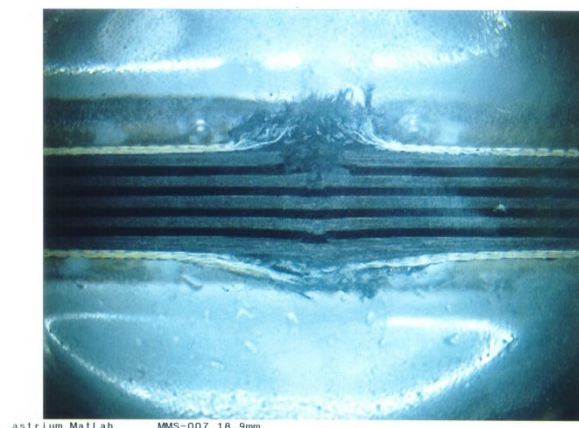


Figure 3.1-2: Cross-section of damage to 40 mm thick shield structure (1.0 mm Al2017 sphere at 5.11 km/s) [Taylor et al., 2001]

Results from the test programme have revealed that:

- The Kevlar shield option minimises delamination.
- A 2-mm projectile perforating the shielded structure (areal density = 0.77 g/cm^2) at $\sim 5.6\text{--}5.7\text{ km/s}$ was shown to produce a widely dispersed debris cloud, which would not subsequently perforate a 1.5 mm thick witness plate located 10 cm behind the target. Thus, from this result, it was surmised that equipment boxes located inside a spacecraft would not be severely damaged in this circumstance.

3.1.1.2 Composite Sandwich Panels

3.1.1.2.1 Design

Composite sandwich panels are an alternative to the traditional metallic sandwich structures. **Table 3-1** shows an example design for a composite sandwich panel.

Face-sheet / core	Design
Prepreg matrix	4-ply satin woven carbon fibre epoxy, HMF371-7714B
Fibre orientation	0°/90°/90°/0°
Thickness	1.62 mm
Density	1800-1850 kg/m ³
Mod. of Elasticity	69.1-69.5 kN/mm ²
Section type	Aeroweb
Material	Al Alloy 3003
Core density	83 kg/m ³
Cell size	6.4 mm
Cell foil thickness	0.06 mm
Core thickness	45 mm
Film adhesive	Redux 609 or 312

Table 3-1: Material property data for a typical composite sandwich panel

3.1.1.2.2 Behaviour under Hypervelocity Impact

The behaviour under impact of a composite sandwich panel is very dependent upon the chemical composition of the material, the size of the strands, and its conditioning (unidirectional lay-up, fabrics). The distribution of the various components of the structure is also important. Three modes of impact damage have been observed for CFRP / Al honeycomb structures [Taylor *et al.*, 1997a]. These are primary and internal damage; debris cloud damage; and contamination.

Primary and Internal Damage

This damage refers to the point of impact of a projectile, and the consequential damage to the front and rear face-sheets and internal honeycomb core. The hole can show signs of fibre and lay-up delamination around its periphery. Internal damage is typically much larger than the face-sheet hole. Damage to individual honeycomb cells can range from bulging (no cell perforation), through to bursting (cell perforation), and finally blasting (cell disintegration). Failure of the entire structure occurs when there is perforation of the rear CFRP face-sheet. The combined effect of perforated face-sheets and honeycomb cell voids creates local stress concentrations. These could induce further crack propagation and delamination, particularly when exposed to thermal cycling, possibly resulting in local buckling of the face-sheets.

Debris Cloud Damage

This damage refers to the cloud of high and low velocity ejecta particles produced when there is perforation. These ejecta typically comprise elongated carbon fibres. Debris clouds formed by impacts on composite face-sheets are irregular and difficult to characterise, compared to clouds produced from aluminium face-sheet impacts.

Contamination

Post impact contamination, caused by unattached fragments of carbon fibre and aluminium honeycomb, can occur in the structure.

3.1.1.2.3 Damage Equations and Ballistic Limit Equations

As noted for non-composite sandwich structures, ballistic limits are in general poorly defined with the impactor parameters lying in a broad range of particle diameters and velocities. This prevents comparison of the relative performance of different configurations. Therefore, caution has to be exercised before extrapolating data to untested materials or configurations [Taylor *et al.*, 1997a, 1997b, 1999]. Some composite materials have however demonstrated their efficiency in specific conditions [Hayhurst, 1998; Lambert, 1995; Shiraki, 1996; Hiermaier, 1999]. The need for in-depth consideration of composites' characteristics like orthotropy and compaction has also been demonstrated [Hiermaier, 1999].

Taylor *et al.*, 1999, have applied the modified Cour-Palais equation [Christiansen, 1993] to characterise the ballistic limit of an Envisat-type CFRP / Al single-honeycomb panel. The equation can be applied conservatively to particles impacting at angles of incidence greater than 15°. However, because of the increased channelling effect at near-normal incidence angles (i.e., < 15°) and the low tensile failure strength of the rear composite face-sheet, the rear wall thickness term in the equation was modified by a scaling factor of 0.5.

3.1.1.3 Glass

In brittle targets like glass (windows, solar cells) or ceramic tiles, the particle will also create craters, the volume of which is much larger than in case of ductile material. This results from spallation due to the low tensile strength of these materials.

3.1.2 Multiple Wall Structures

Shields are protection techniques intended to achieve very low rates of penetration of the main structure. They are typical of manned spacecraft with long duration missions.

3.1.2.1 Double Wall

3.1.2.1.1 Whipple Shields

Whipple shields are named after Fred Whipple who invented a standoff bumper shield system for protecting spacecraft from meteoroid impacts in the 1940's [Whipple, 1947]. These shields consist of a single bumper, standoff, and the spacecraft structure that is to be protected.

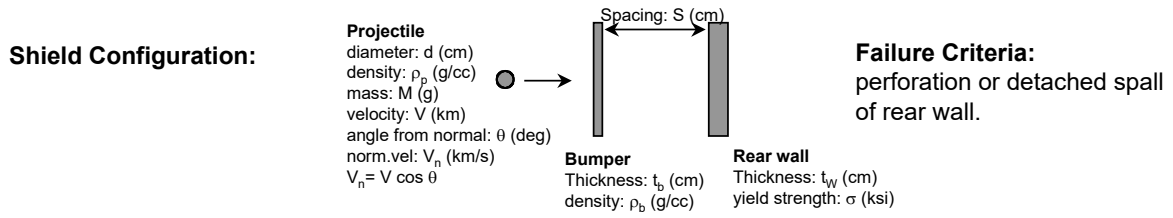


Figure 3.1-3: Whipple shield

3.1.2.1.1.1 NASA

Whipple Shield Sizing Equations

The following equations were provided in earlier work [Christiansen, 1993], and represent equations that can be used for preliminary design of MMOD protection using Whipple shields. Additional analyses supported by tests will be necessary to show preliminary shield designs meet or exceed MMOD protection requirements. Bumper and rear wall thickness to defeat a given threat particle are determined by the following equations (assuming $V_n \geq 7$ km/s).

$$t_b = c_b m_p / \rho_b = c_b d \rho_p / \rho_b \quad [3.1-1]$$

Where

c_b = coefficient 0.25 when $S/d < 30$, and $c_b = 0.2$ when $S/d \geq 30$

d = projectile diameter (cm)

m_p = projectile areal density (g/cm²)

ρ_p = projectile density (g/cm³)

ρ_b = bumper density (g/cm³)

S = overall spacing between outer bumper and rear wall (cm)

t_b = bumper thickness (cm)

$$t_w = c_w d^{0.5} (\rho_p \rho_b)^{1/6} (M_p)^{1/3} V_n / S^{0.5} (70/\sigma)^{0.5} \quad [3.1-2]$$

Where

c_w = coefficient 0.16 cm²-sec/(g^{2/3} km)

d = projectile diameter (cm)

M_p = projectile mass (g)
 ρ_p = projectile density (g/cm³)
 ρ_b = bumper density (g/cm³)
 S = overall spacing between outer bumper and rear wall (cm)
 σ = rear wall yield stress (ksi)
 t_w = rear wall thickness (cm)
 V = projectile velocity (km/s)
 V_n = normal component of projectile velocity (km/sec)

Whipple Shield Performance Equations

The following equations [Christiansen, 1993] define the protection capability limits for a Whipple shield in terms of a critical particle size (d_c) that causes failure (complete penetration or detached spall of the rear wall). These equations assume that the bumper thickness is adequate to disrupt the projectile at high velocities. If the bumper is too thin, then the following equations over-estimate the performance of the shield. If the bumper is too thick, then the extra bumper mass is not effective, i.e., shield performance will not suffer, but the extra bumper mass will not improve shielding performance (unless the bumper becomes very thick, i.e., the thickness is greater than the diameter of the projectile at the shield's ballistic limit).

At higher velocities, the debris cloud impacting the rear wall will contain various amounts of solid, liquid and vapor components of the projectile depending on impact conditions (projectile size, impact speed, obliquity, projectile density, shape and bumper thickness). The critical particle size for $V_n \geq 7$ km/s is given by:

$$d_c = 3.918 t_w^{2/3} \rho_p^{-1/3} \rho_b^{-1/9} (V \cos \theta)^{-2/3} S^{1/3} (\sigma/70)^{1/3} \quad [3.1-3]$$

Where

d_c = critical projectile diameter at shield failure threshold (cm)
 ρ_p = projectile density (g/cm³)
 σ = rear wall yield stress (ksi)
 S = standoff distance from back of bumper to front of rear wall (cm)
 t_w = rear wall thickness (cm)
 θ = impact angle from target normal (deg); note impact at $\theta = 0$ deg is normal to the target.
 V = projectile velocity (km/s)
 V_n = normal component of projectile velocity (km/sec) = $V \cos \theta$

At low velocities, below 3 km/s, impact shock pressures are low, and the projectile remains essentially intact after impact on the bumper. The shield's rear wall is then impacted by a deformed or slightly fragmented projectile. The critical particle size for $V_n \leq 3$ km/s is given by:

$$d_c = [(t_w(\sigma/40)^{0.5} + t_b) / (0.6(\cos^{5/3} \theta) \rho_p^{0.5} V^{2/3})]^{(18/19)} \quad [3.1-4]$$

Where

d_c = critical projectile diameter at shield failure threshold (cm)

ρ_p = projectile density (g/cm³)

σ = rear wall yield stress (ksi)

t_b = bumper thickness (cm)

t_w = rear wall thickness (cm)

θ = impact angle from target normal (deg); note impact at $\theta = 0$ deg is normal to the target.

V = projectile velocity (km/s)

V_n = normal component of projectile velocity (km/sec) = $V \cos\theta$

The projectile is more damaging as velocity increases in the low velocity regime, resulting in the critical particle size decreasing as velocity increases. At velocities above $V_n=3$ km/s, projectile fragmentation during the collision with the bumper becomes significant. Above 5.5 km/s, the projectile will begin to melt for aluminum on aluminum impacts. A fragmenting or partially molten projectile is less damaging to the rear wall than a substantially intact projectile, thus critical particle size increases in the intermediate velocity range: $3 \text{ km/s} < V_n \leq 7 \text{ km/s}$:

$$d_c = \left[(t_w(\sigma/40)^{0.5} + t_b) / (1.248\rho_p^{0.5} \cos\theta) \right]^{(18/19)} \times [1.75 - (V_n/4)] + [1.071t_w^{2/3}\rho_p^{-1/3}\rho_b^{-1/9}S^{1/3}(\sigma/70)^{1/3}] \times (V_n/4 - 0.75) \quad [3.1-5]$$

Where

d_c = critical projectile diameter at shield failure threshold (cm)

ρ_b = bumper density (g/cm³)

ρ_p = projectile density (g/cm³)

σ = rear wall yield stress (ksi)

S = standoff distance from back of bumper to front of rear wall (cm)

t_b = bumper thickness (cm)

t_w = rear wall thickness (cm)

θ = impact angle from target normal (deg); note impact at $\theta = 0$ deg is normal to the target.

V = projectile velocity (km/s)

V_n = normal component of projectile velocity (km/sec) = $V \cos\theta$

For highly oblique impacts ($\theta \geq 65^\circ$), bumper fragments contribute the majority of damage to the rear wall. Thus, the critical particle size for impact angles over 65° should be set to the critical particle size for 65° (to prevent over-prediction of the critical projectile diameter) as given by

$$d_c^{\theta > 65} = d_c^{\theta = 65} \quad (3.1-6)$$

3.1.2.1.1.2 DLR

Under ESA/ESTEC-contract, the following modifications of the Whipple Shield Equations were developed [Reimerdes *et al.*, 1993]. They are based on equations developed by Cour-Palais, 1979, and Christiansen, 1993. The equations are applicable to aluminium shields and aluminium particles. The velocity domain is divided into three regions:

- ballistic region: $0 < v \leq v_L$
- shatter region: $v_L < v \leq 7 \text{ km/s}$
- hypervelocity region: $v > 7 \text{ km/s}$

The limit-velocity, v_L (km/s), between ballistic and shatter regions depends on the shield thickness t_b :

$$v_L = 1.6 + 0.44 \left(\frac{t_b}{d} \right)^{-0.59} \quad [3.1-7]$$

Sizing Equations

Ballistic Region:

$$t_W = (p_\infty - t_b)k \quad [3.1-8]$$

with:

$$p_\infty = K_\infty m_p^{0.352} \rho_p^{1/6} v^{2/3} \quad [3.1-9]$$

K_∞ depends on the material. For aluminium alloys:

$$K_\infty = 0.42 \quad [3.1-10]$$

k depends on the type of damage:

$k \geq 1.8$	no perforation,
$k \geq 2.2$	no detached spall,
$k \geq 3.0$	no spall.

Hypervelocity region:

$$t_W = F_2^* 0.167 m_p^{1/2} \rho_b^{1/6} v \sqrt{\frac{482}{S \sigma_y}} \quad [3.1-11]$$

with yield strength σ_y in (N/mm²). The factor F_2^* depends on the shield thickness to particle diameter –ratio:

$$\begin{aligned}
 F_2^* &= 1 & ; \left(\frac{t_b}{d}\right) &\geq 0.2 \\
 F_2^* &= 5 - 40\left(\frac{t_b}{d}\right) + 100\left(\frac{t_b}{d}\right)^2 & ; \left(\frac{t_b}{d}\right) &< 0.2
 \end{aligned}
 \tag{3.1-12}$$

Ballistic-Limit Equations

Ballistic region:

$$d = \left(\frac{\frac{t_w}{k} + t_b}{0.796 K_\infty \rho_p^{0.519} v^{2/3}} \right)^{0.947}
 \tag{3.1-13}$$

Hypervelocity region:

$$d = \left(\frac{8.29 t_w}{F_2^* \rho_b^{1/6} \rho_p^{1/2} v} \sqrt{\frac{S \sigma_y}{482}} \right)^{2/3}
 \tag{3.1-14}$$

F_2^* depends on the computed critical particle diameter d . If the t_b/d -ratio falls below 0.2, an iteration procedure is needed to compute this factor.

Shatter region:

A linear interpolation between the limit velocities v_L and 7 km/s gives:

$$d(v) = d(v_L) - \frac{d(v_L) - d(7 \text{ km/s})}{7 \text{ km/s} - v_L} (v - v_L)
 \tag{3.1-15}$$

3.1.2.1.1.3 ESA

It has been experimentally observed that for Whipple shield configurations including Multi-Layer Insulation on top of the bumper, the shielding performance can be degraded [Schäfer & Günther, 2001]. For a configuration made of a 1.2 mm Al 5083 bumper with 596 g/m² of MLI on top of it, a backwall of Al 2219-T851 3 mm thickness located 128 mm behind the bumper shows a small perforation with a 4.7 mm aluminium projectile at 6.92 km/s normal impact. To match the experiment, equation (3.1-4) above needs to have a coefficient of 2.9754.

3.1.2.1.1.4 JAXA

The effect of the location of MLI has been studied experimentally by JAXA in the frame of the Space Station JEM development. For a Whipple shield, the expansion of the debris cloud is hindered by the presence of MLI between the bumper and the backwall [Shiraki & Harada, 2000]. Further work on Stuffed Whipple shields has shown that it is detrimental to place the MLI on top of the second bumper [Shiraki *et al.*, 1997].

3.1.2.1.1.5 Energia

The effect of MLI located behind the first bumper is illustrated in **Table 3-2** and **Table 3-3**.

Test protocol


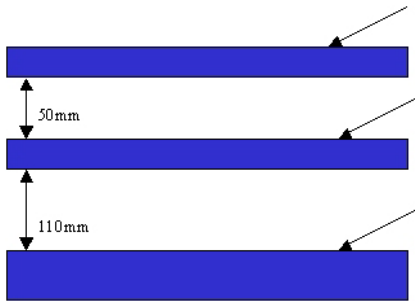
No	Test No	dp mm	Projectile form	Projectile material and mass	α grad	V km/s	P ₆ mm Hg	
	1021	3,17	sphere	Al 2017 0,046g	0°	6,0	18	
Sample description and test results								
Elem No	Element descrip.	Element material	Element thickness	Elem. Mass kg/m ²	Sample configuration	Failure description		
1	bumper	Al alloy AMG-6	$\delta=0,95$	2,57		1	1 – hole with D=6,9mm	
2	wall	AMG-6	$\delta=1,43$	3,86		2	2 – hole 2,2*1.2mm with crack, 3 microholes,	
3	witness plate	AMG-6	$\delta=3,0$	6,43		3	3 – 1 microcrater	

Table 3-2: Performance of Whipple shield with no MLI included.

Test protocol

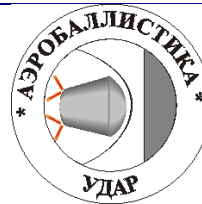
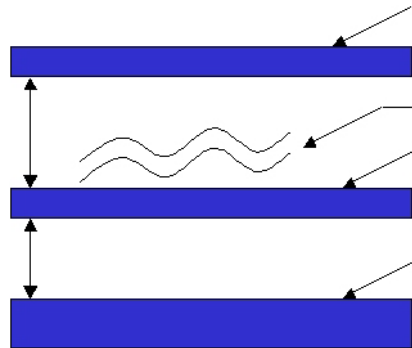
No	Test No	dp mm	Projectile form	Projectile material and mass	α grad	V km/s	P ₆ mm Hg	
	1021	3,17	sphere	Al 2017 0,046g	0°	6,05	32	
Sample description and test results								
Elem No	Element descrip.	Element material	Element thickness	Elem. Mass kg/m ²	Sample configuration	Failure description		
1	bumper	Al alloy AMG-6	$\delta=0,95$	2,57		1	1 – hole D=7,0mm	
2	MLI			0,64		2	2 – hole D _{exter} =45mm	
3	wall	AMG-6	$\delta=1,42$	3,76		3	3 – no penetration, bulge D=25mm, h=4mm	
4	witness plate	AMG-6	$\delta=3,0$	6,97		4	4 – no traces	

Table 3-3: Performance of Whipple shield with MLI included

3.1.2.2 Triple Wall

3.1.2.2.1 The SRL Ballistic Limit Equation

The SRL triple-wall BLE [Schäfer *et al.*, 2008] can be used for the analysis of the vulnerability of internal satellite components placed behind double panel structure walls to micrometeoroids and space debris (MM/SD). The applicability to internal satellite components for unmanned missions is due to the inclusion of the third wall, which represents the equipment cover plate located behind the satellite's outer structure and accounts for the inherent shielding capability of the internal components. The first two walls represent the satellite's outer structure, typically as aluminum honeycomb sandwich panels (H/C SP) or Whipple shields. Based on the Christiansen-Whipple BLE [Christiansen 1993], the SRL BLE defines ballistic, shatter and hypervelocity regimes (3.0 and 7.0 km/s threshold velocities for aluminum). As with the Christiansen-Whipple BLE, the SRL BLE calculates the critical diameter d_c necessary to produce a component failure (via penetration or detached spall from the inner side of the component cover plate) based on the material characteristics and spacing of the structure panel and cover plate, as well as the characteristics of the impacting particle. The material characteristics are given as the multi-layer insulation (MLI) areal density $\rho_{AD,MLI}$, outer bumper thickness t_{ob} , and density ρ_{ob} , inner bumper thickness t_b , and internal component cover plate thickness t_w and yield strength $\sigma_{y,ksi}$. The spacing is given between the outer and inner bumpers s_1 as well as between the inner bumper and the component cover plate s_2 . The impacting particle characteristics include the impact velocity v and angle ϑ , and the particle density ρ_p .

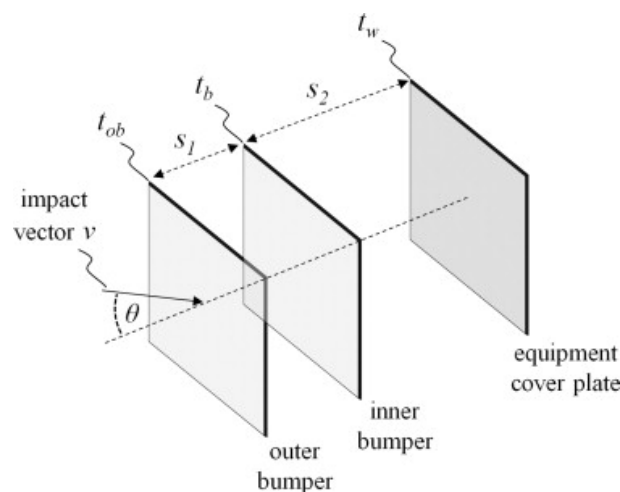


Figure 3.1-4: Typical SRL configuration

Because the SRL BLE is designed to be applicable for a variety of internal component types, the results are moderately conservative and assume that the generation of spall or penetration definitively result in component failure. The typical SRL configuration is demonstrated in **Figure 3.1-4**. Additionally, for the application of internal components behind varying structure panels from the described honeycomb panel or Whipple shield, the SRL provides special cases, specifically for stand-alone MLI (with or without stand-off to equipment) and single wall shielding.

The SRL BLE was developed, calibrated and validated via a series of test campaigns both during and preceding the before noted ESA project [Schäfer, Ryan, *et al.*, 2008; Schäfer, Putzar, *et al.*, 2008; Putzar *et al.*, 2005; Putzar, Schäfer, Stokes, Chant, Lambert, 2006; Putzar *et al.*, 2008].

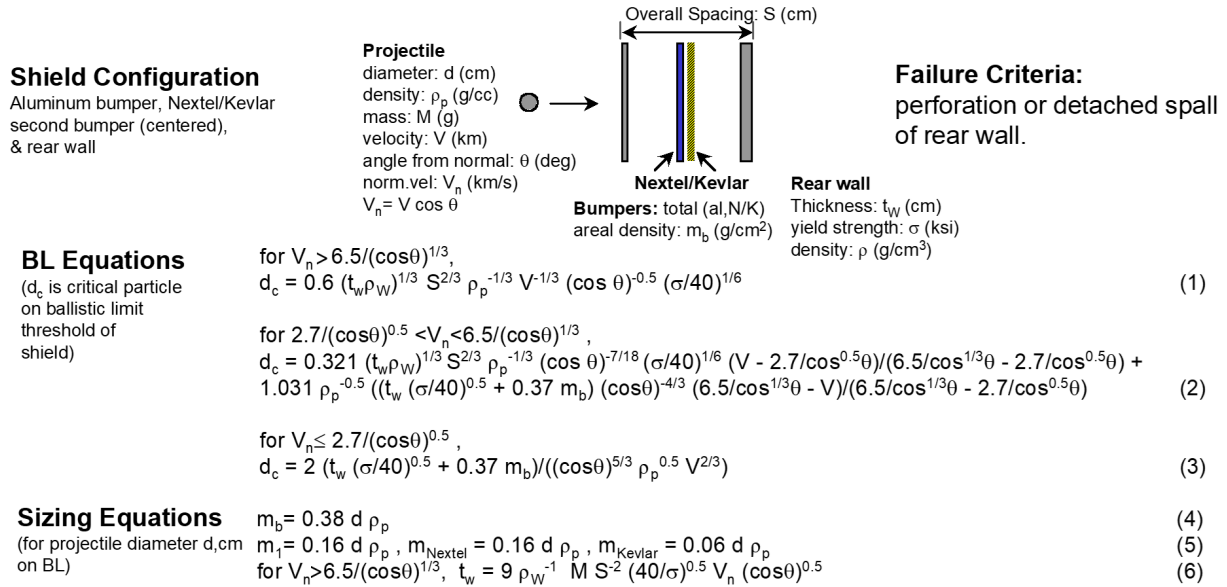
3.1.2.3 Advanced Concepts

3.1.2.3.1 Stuffed Whipple Shields

Stuffed Whipple shields consist of a Whipple shield with an intermediate bumper consisting of advanced materials, e.g., ceramic cloth (Nextel™) backed up by high-strength cloth (Kevlar™), or cloth-epoxy panels. In some cases, metal mesh is included in front of the intermediate layers.

3.1.2.3.1.1 NASA

In the frame of the Space Station program, NASA has developed various high-performance shields [Christiansen, 1993; Christiansen & Kerr, 1993; Christiansen *et al.*, 1995]. Ballistic limit equations for the indicated failure criteria are given below.



Constraints/Discussion: Valid for metallic rearwalls. No impact angle constraint.

Ref. E.L. Christiansen, *et al.* "Enhanced Meteoroid and Orbital Debris Shielding," *International Journal of Impact Engineering*, Vol.17, pp. (1995).

Figure 3.1-5: Stuffed Whipple shield configuration and equations (NASA)

3.1.2.3.1.2 JAXA

JAXA has developed specific shields for the Japanese Module [Shiraki *et al.*, 1997; Shiraki & Noda, 1998].

3.1.2.3.1.3 ESA

ESA has developed, via Alenia Aerospazio and EADS-LV, a directional Meteoroid and Debris Protection System for the Columbus Module (APM). Alenia Aerospazio has gained dedicated experience in the protection of pressure modules. Different test campaigns have been completed to evaluate the performance of a shield based upon a Whipple structure plus an intermediate wall made of layers of Nextel™, placed on top of a Kevlar™ composite with epoxy resin. This shield configuration reported excellent ballistic performance against aluminium spherical projectiles impacting with velocities up to 7 km/s and angles between 0 and 60 degrees [Beruto *et al.*, 1997; Destefanis *et al.*, 1998].

3.1.2.3.1.4 RSC Energia

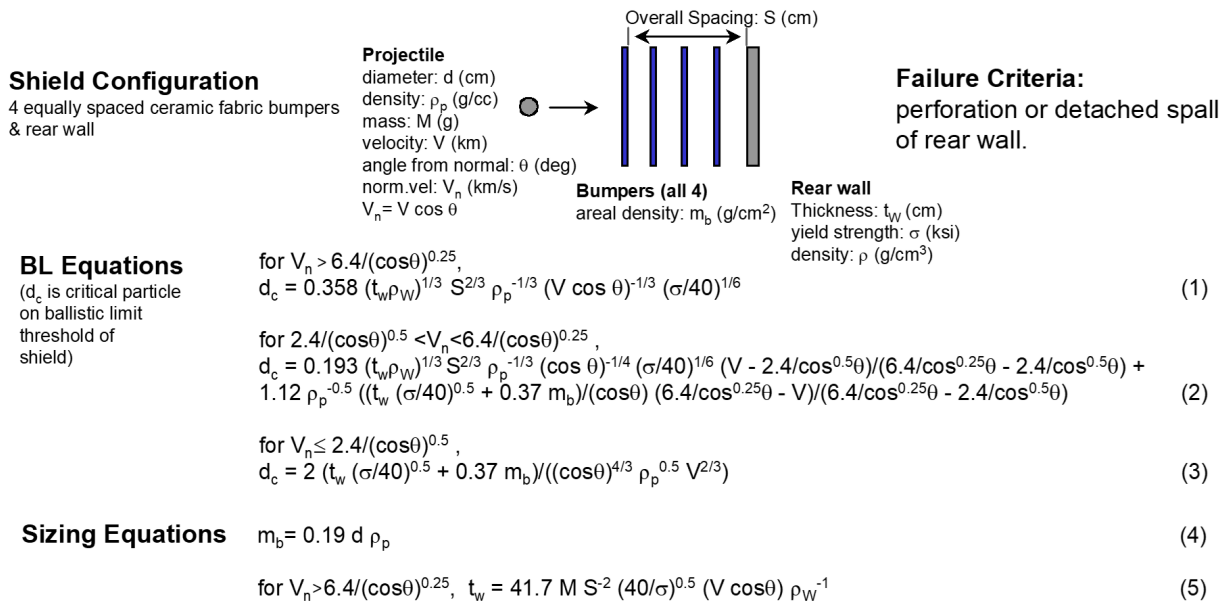
RSC Energia is developing innovative protection for the Russian Segment of the Space Station [Sokolov, 1998].

3.1.2.3.2 Multi-Shock Shields

Multi-Shock Shields consist of 3 or more bumpers followed by a rear wall.

3.1.2.3.2.1 NASA

Ballistic limit equations for a Multi-Shock shield consisting of Nextel™ (ceramic cloth) bumpers followed by a rear wall are given below.



Constraints/Discussion: Valid for ceramic bumpers and metallic rearwalls. No impact angle constraint. At 6.4 km/s normal impact, when $S/d < 30$, the high-velocity equations (1 and 2) tend to over-estimate critical diameter.

Ref. B.G.Cour-Palais and J.L. Crews, "A Multi-Shock Concept for Spacecraft Shielding," *International Journal of Impact Engineering*, Vol.10, pp.135-146 (1990).

E.L. Christiansen, "Design and Performance Equations for Advanced Meteoroid and Debris Shields," *International Journal of Impact Engineering*, Vol.14, pp.145-156 (1993), Proceedings of the 1992 HVIS, November 1992.

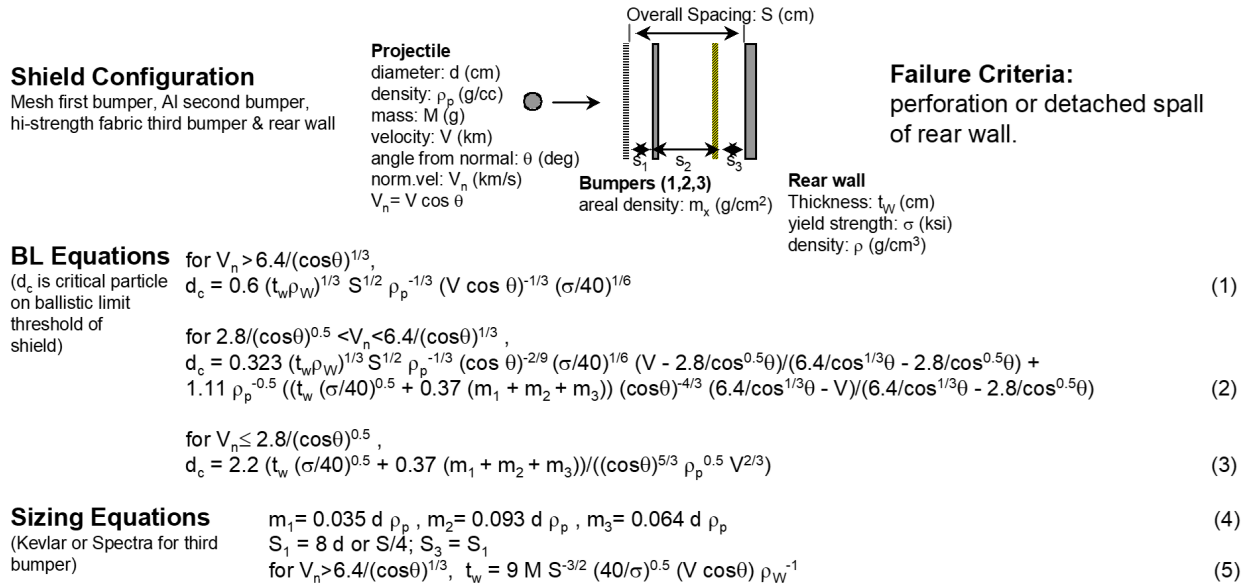
Figure 3.1-6: Multi-Shock shield configuration and equations (NASA)

3.1.2.3.3 Mesh Double-Bumper Shields

There are numerous examples of shields on the International Space Station that contain metal meshes. The JAXA configuration of the Stuffed Whipple shield uses a metal mesh on top of the Nextel/Kevlar blanket. This section provides ballistic limit equations, failure criteria and references for other types of bumper shields using metallic meshes.

3.1.2.3.3.1 NASA

NASA mesh-double bumper shielding includes an outer mesh bumper and a high-strength cloth layer (Kevlar™, Spectra™, etc.) near, but not on, the rear wall.



Constraints/Discussion: Valid for metallic rearwalls. No impact angle constraint.
Ref. E.L. Christiansen, Advanced Meteoroid and Debris Shielding Concepts, AIAA Paper No. 90-1336, 1990.
 E.L. Christiansen and J.H. Kerr, "Mesh Double-Bumper Shield: A low-weight alternative for spacecraft meteoroid and orbital debris protection," *International Journal of Impact Engineering*, Vol.14, pp.169-180, (1993)

Figure 3.1-7: Mesh double bumper shield configuration and equations (NASA)

3.1.2.3.4 Sandwich

3.1.2.3.4.1 Design

Sandwich structures are two thin facesheets bonded to a low weight core. The core separates the sheets and carries shear loads, while the sheets take bending loads very efficiently. With respect to impact loads, the two face sheets work similar to a shielded structure. They are less effective, as the core channels the debris cloud.

Unmanned spacecraft usually employ a sandwich plate structure, i.e., face-sheets bonded to honeycomb core (**Figure 3.1-8**). Aluminium or CFRP are the most commonly used material for both face-sheets and honeycomb. Typically, face-sheet thickness can range from 0.25 mm to 2 mm, with cell sizes anywhere from 3 mm to 25 mm. Overall thickness of the honeycomb core can vary between 5 and 50 mm.

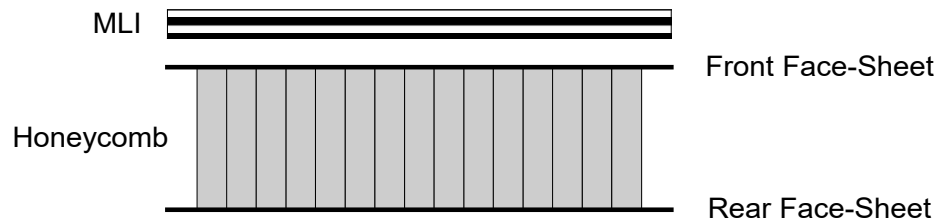


Figure 3.1-8: Standard Single-Honeycomb Panel Structure with MLI

The purpose of each face-sheet in a structure panel is to:

- Carry the direct (tensile and compressive) loads that cause extension and contraction.
- Carry the in-plane shear loads and bending that cause face-sheet distortion.

The core of a structure panel is introduced to:

- Stabilise the face-sheets at the spacing to produce the desired strength to weight ratio and rigidity.
- Provide a transverse shear load path to resist out of plane distortions.

In order to attach equipment, the following basic requirements must be met:

- Mechanical attachment to the structure using metallic inserts.
- Electrical interfacing and electromagnetic screening.
- A means of conducting and radiating heat using a thermal control subsystem, which may incorporate active heater lines mounted on the internal face of the structure.

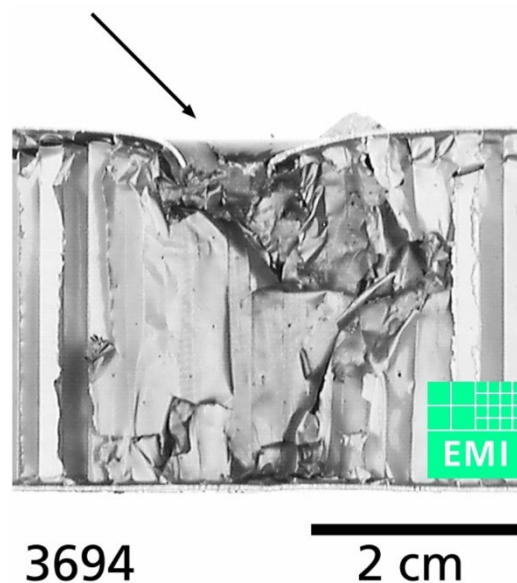
For thermal control purposes, materials such as multi-layer insulation (MLI) or coatings such as Teflon can cover the face-sheets. Typically, MLI comprises 10 to 25 layers of Mylar interleaved with Dacron net and covered with a layer of Kapton or Teflon-impregnated Beta-cloth.

3.1.2.3.4.2 Behaviour under Hypervelocity Impact

Several modes of impact damage have been observed for aluminium alloy honeycomb structures.

Primary and Internal Damage

This damage refers to the point of impact of a projectile, and the consequential damage to the front and rear face-sheets and internal honeycomb core. Internal damage is typically much larger than the face-sheet hole (**Figure 3.1-9**). Damage to individual honeycomb cells can range from bulging (no cell perforation), through to bursting (cell perforation), and finally blasting (cell disintegration). Failure of the entire structure occurs when there is perforation of the rear face-sheet. The combined effect of perforated face-sheets and honeycomb cell voids creates local stress concentrations. A random distribution of impact cell voids may contribute to the local dimensional stability of the structure being compromised, which can be crucial for maintaining instrument pointing accuracy. Honeycomb blast damage may lead to loss of structural integrity of the epoxy potting compound of nearby metallic inserts. This could result in mounted equipment becoming detached.



METOP sample with Nextel - MLI removed. Impact damage.
1.74 mm projectile, 7.2 km/s, 45 degrees.

Figure 3.1-9: Typical impact damage on honeycomb core sandwich

Debris Cloud Damage

This damage refers to the cloud of high and low velocity ejecta particles produced when there is perforation of the rear face-sheet.

The cloud of high and low velocity ejecta particles produced when there is perforation of the structure presents the highest risk of mechanical damage to payload equipment located inside the spacecraft body. This is particularly the case for equipment mounted directly on or near to vulnerable body faces. For externally mounted equipment, debris cloud damage is possible from ricochet ejecta generated by a particle impacting a nearby surface at an oblique angle. The effect of a low energy cloud impact is to blast and abrade the surface of the equipment, whereas a higher energy cloud impact may penetrate the equipment's aluminium walls.

Contamination

If an impactor strikes a structure wall at a sufficiently oblique angle, then secondary ejecta (ricochet) fragments may be released, which could impact other parts of the spacecraft or contaminate payloads and subsystems.

3.1.2.3.4.3 Damage Equations and Ballistic Limit Equations

Ballistic limits for sandwich panels are in general poorly defined with the impactor parameters lying in a broad range of particle diameters and velocities. This prevents comparison of the relative performance of different configurations. However, the key damage mechanisms can be identified, as follows:

- Significant delamination of the honeycomb core from the face-sheets occurs above the ballistic limit [Frate & Nahra, 1996].
- The debris cloud is channelled for both normal and oblique impact angles [Taylor, 1999; Lambert, 1997; Jex, 1970].
- Internal honeycomb damage can be at least an order of magnitude greater than the original projectile diameter [Taylor, 1997].
- The type of aluminium alloy used in the honeycomb core does not affect the channelling [Sennett & Lathrop, 1968].
- No strong dependence of the ballistic limit on the spacing was found (above a minimum spacing \approx twice the cell diameter) [Sennett & Lathrop, 1968].
- There is a strong dependence of the ballistic limit with impact angle [Jex, 1970; Taylor, 1997].
- MLI increases the ballistic limit of the overall structure.

The ballistic limit of a sandwich panel is a function of face-sheet thickness, cell dimensions and cell wall thickness, core depth, and the materials used. No equations currently exist that combine these parameters. Instead, an equation such as the modified Cour-Palais (Christiansen-Cour-Palais) Whipple bumper equation (see below) can be compared with experimental impact test data, and its parameters adjusted accordingly. This approach, however, means that the influence of the honeycomb core is not represented in the equation. For some honeycomb configurations, this equation may be consistent with the normal incidence data; the use of either equivalent spacing [Sennett & Lathrop, 1968] or equivalent rear facesheet thickness [Taylor *et al.*, 1999].

For $v_n \leq 3$ km/s:

$$d_c(v_n) = \left(\frac{\frac{t_w}{K_{3S}} \left(\frac{\tau}{40000} \right)^{0.5} + t_b}{0.6 \cos \theta_n^{0.667} \rho_p^{0.5}} \right)^{0.947} \quad [3.1-16]$$

For $v_n \geq 7$ km/s:

$$d_c(v_n) = 1.155 K_{3D}^{-0.667} t_w^{0.667} \rho_p^{-0.333} \rho_b^{-0.111} v_n^{-0.667} \left(\frac{\tau S}{70000} \right)^{0.333} \quad [3.1-17]$$

For $3 \leq v_n \leq 7$ km/s:

$$d_c(v_n) = d_c(v_n = 3) \left(1.75 - \frac{v_n}{4} \right) + d_c(v_n = 7) \left(\frac{v_n}{4} - 0.75 \right) \quad [3.1-18]$$

where,

K_{3S}	1 (baseline)
K_{3D}	0.16 (baseline)
d_c	particle diameter at ballistic limit (cm)
v	velocity (km/s)
v_n	normal component of velocity (km/s)
θ	impact angle measured from surface normal (deg.)
t_b	thickness of bumper (cm)
t_w	thickness of rear wall (cm)
ρ_p	projectile density (g/cm ³)
ρ_w	rear wall density (g/cm ³)
ρ_b	bumper density (g/cm ³)
τ	rear wall yield stress (in lb/inch ²)
S	spacing between bumper and rear wall (cm)

Due to the influence of the impact angle on the honeycomb structure shielding performance, the Christiansen-Cour-Palais equation cannot be used to represent the impact angle dependence for honeycomb structure targets. For oblique incidence impacts, the projectile line of flight intersects with multiple thin aluminum sheets (the honeycomb core). The honeycomb core can be considered to act as a “multi-shock shield”. The ballistic limit of a target as a function of impact energy can be used to identify the increase in shielding performance as a function of impact energy. Experimental data from Jex, 1970, show that, at 45 degrees incidence, ~2.3 times the impact energy is required to reach the ballistic limit compared with at 0 degrees. This is for a honeycomb core depth of 22 mm. For a honeycomb core depth of 45 mm (i.e., twice the honeycomb core), ~4.6 times the impact energy is required to reach the ballistic limit. An impact traversing a 45 mm deep core “sees” twice as much honeycomb material as an impact traversing a 22 mm deep core; the doubling in impact energy required to reach the ballistic limit is consistent with this visualisation [Taylor *et al.*, 1999].

3.1.2.3.4.4 Enhanced Impact Damage Tolerance

Techniques to augment the existing spacecraft honeycomb structure and/or the multi-layer insulation has previously been applied to unmanned spacecraft [Terrillion, 1991; Christiansen, 1999]. These have primarily involved enhancement of the MLI with fabrics and materials such as Nextel, wire mesh and Beta cloth. Using the baseline structure, as defined for a low Earth orbiting platform, a range of unmanned spacecraft shielding strategies have been identified by Turner *et al.*, 2000, as listed in **Table 3-4**.

Shield type		Expected shielding benefit
1	Change thickness of HC cell walls	Alter the debris cloud channelling effect. Angle dependency
2	Change HC cell size	Alter the debris cloud channelling effect. Angle dependency
3	Increase HC depth	Increase debris cloud dispersion
4	Vary outer face-sheet thickness	Increased projectile disruption
5	Vary inner face-sheet thickness	Increased tolerance to debris cloud loading
6	Use multiple HC layers	Similar effect to multiple wall shield
7	HC+laminate	Different shock impedances to increase projectile disruption
8	MLI+Nextel/Kevlar/Beta-cloth front layer	Multi-shock shield effect & increased projectile disruption
9	MLI+Nextel/Kevlar/Beta-cloth rear layer	Multi-shock shield effect & increased debris cloud containment
10	MLI+Nextel/Kevlar/Beta-cloth mid layer	Multi-shock shield effect & increased debris cloud disruption
11	MLI+spacer rods	Multi-shock shield effect
12	HC+Nextel/Kevlar inside spacecraft	Protects sensitive internal spacecraft equipment
13	HC+spaced bumper	Whipple bumper shield effect

Table 3-4: Shielding options for sandwich panel structures

These “cost effective debris shields for unmanned spacecraft” were defined according to the unmanned spacecraft shielding requirements given in **Table 3-5**.

Requirement	Compliance
Be affordable.	Yes , Cost per square metre is typically less than 2,000 Euro for the double honeycomb and less than 200 Euro for Beta-cloth toughened MLI.
Impose minimum weight penalty.	Yes , the mass increase per square metre is approximately 1.2kg for double honeycomb and 0.8kg for Beta-cloth toughened MLI.
Be amenable to simple design and construction.	Yes , the manufacture of single honeycomb and Beta-cloth toughened MLI present no problems and uses current processes.
Provide ‘second hit’ capability, i.e. minimise the sacrificial aspects.	Partially , there is destruction of the shield materials at the point of impact but the chances of a second large particle (>1mm) hitting the same place are small.
Produce non-damaging secondary ejecta and spall.	Partially , the CEDS shields produce no more secondary ejecta and spall than manned shields and for the MLI covered areas, a lot of this material is contained within the MLI after impact.
Provide means of melting and/or vaporising meteoroid and debris particles over a large range of projectile mass, size and velocity.	Yes , the design is essentially a Whipple type shield. The CEDS shielding will stop particles of around 1mm at 12 km/s.
Provide a degree of thermal and radiation protection.	Yes , all shielding materials are used underneath existing thermal control finishes.
Be resistive to the effects of atomic oxygen (a requirement for low-Earth orbits only).	Yes , all shielding materials are used underneath existing thermal control finishes.
The shield when impacted, ideally should not add to the orbital debris by creating more debris.	Partially , the radiator areas should produce no more additional orbital debris than manned shields but for the MLI covered areas a great deal of the potential debris created is trapped within the MLI.
Ideally the shield should trap any resulting spall inside the spacecraft.	Yes , Resulting spall and debris cloud material inside the spacecraft can only escape through venting holes.
It must be capable of surviving the normal launch and in-orbit vibration environments.	Yes , with one possible question mark over the support of the Beta-cloth toughened MLI.
It should meet spacecraft system requirements such as having a conductive external surface, electrically grounded to the spacecraft structure and acceptable thermo-optical properties.	Yes , all shielding materials are used underneath existing thermal control finishes. The Beta-cloth cannot be grounded but it is used in between grounded layers.
Any resulting debris, spall or dust from the shield should not cause subsequent failures	Not tested , particles greater than the ballistic limit of the shield will result in the debris cloud entering the spacecraft interior. No tests have been

of spacecraft equipment or unacceptable deterioration in performance (jamming of mechanisms, coating of optics etc).	performed to establish the effect of this debris cloud on other spacecraft equipments. By not using Nextel it is believed that the amount of dust has been minimised.
It should not interfere with the normal operation of the spacecraft such as deployment sequences, observation and taking measurements, communication and telecommand etc	Yes , no part of the shielding can interfere with the normal operation of the spacecraft. The use of the toughened MLI and more layers will extend the envelope of the MLI closer to the launch vehicle interface envelope but by only a small amount (max 10 mm).

Table 3-5: Shielding requirements for unmanned spacecraft

The options listed in **Table 3-4** are constrained by a number of engineering factors. The optimum structure with respect to strength is a deep honeycomb, thick walls, and small cell sizes. Where inserts have to be mounted in the structure, their spacing and loading is a function of the cell size. The honeycomb depth is also governed by the inserts as well as buckling considerations.

A particularly interesting option in the table is the replacement of a standard single-honeycomb structure with a multiple (e.g. double) honeycomb layer design (**Figure 3.1-10**).

The baseline and augmented spacecraft honeycomb and multi-layer insulation from [Terrillion, 1991; Christiansen, 1999] are shown in **Figure 3.1-11**.

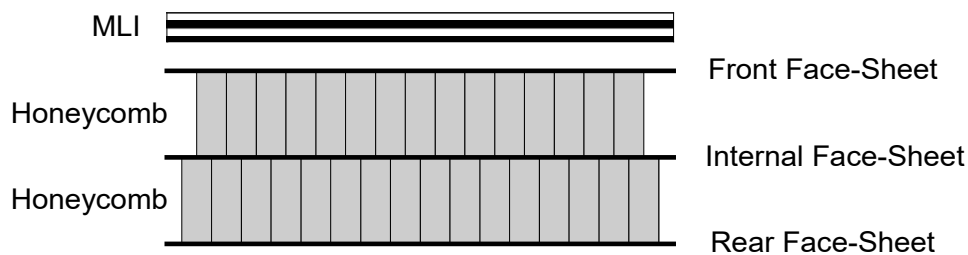


Figure 3.1-10: Double-Honeycomb Panel Structure with MLI

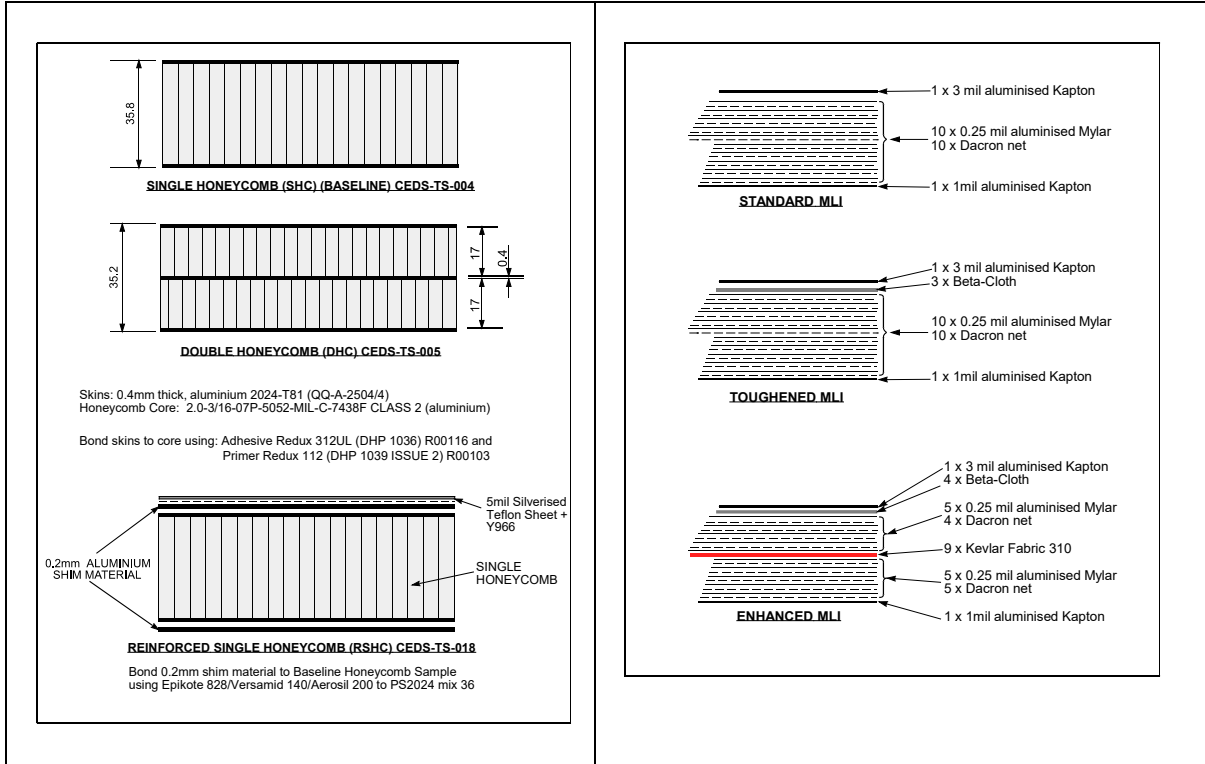


Figure 3.1-11: Baseline and double honeycomb shield designs and MLI designs

Turner *et al.*, 2000, have investigated this option and particularly recommend it for the most vulnerable spacecraft surfaces, e.g. those facing the velocity direction. The double-honeycomb structure is effective at disrupting the debris cloud channelling effect and reducing the size of the largest fragments in the cloud. However, it should be borne in mind that the use of a double-honeycomb structure might introduce additional engineering issues compared to the single honeycomb configuration. For example, thermal control may be reduced. Also, it might not be possible to use laminates due to warping during manufacture.

A damage equation was developed to predict the shielding performance of the double honeycomb shields. The equation was based on the modified Cour-Palais (Christiansen-Cour-Palais) Whipple bumper equation, with constants modified to represent double aluminium bumper shields (equivalent to double honeycomb structures). A general form of the multiple wall equation is given below [Lemcke *et al.*, 1998a]:

$$d_{p_{crit}} = \left[\frac{t_w + K_2 \cdot t_b^\mu \cdot \rho_b^{\nu 2}}{K_1 \cdot \rho_p^\beta \cdot v^\gamma \cdot (\cos \alpha)^\epsilon \cdot \rho_w^\kappa \cdot S^\delta \cdot \rho_b^{\nu 1}} \right]^{\frac{1}{\lambda}} \quad [3.1-19]$$

For impact velocities in the transition region, i.e. between v_l and v_u , linear interpolation is used to calculate the ballistic limit, as follows:

$$d_{p_{crit}} = d_{p_{crit}, v_n = v_l} \cdot \left(\frac{v_u - v_n}{v_u - v_l} \right) + d_{p_{crit}, v_n = v_u} \cdot \left(\frac{v_n - v_l}{v_u - v_l} \right) \quad [3.1-20]$$

The various terms in the equation [Lemcke *et al.*, 1998a] are defined in **Table 3-6**.

Symbol	Unit	Description
t_w, t_b	cm	Thickness of rear wall, bumper
t_{Equiv}	cm	Equivalent aluminium single wall thickness
K_1, K_2		Equation specific characteristic factors.
d_p	cm	Particle (impactor) diameter
ρ_p, ρ_b, ρ_w	$g\ cm^{-3}$	Density of particle, bumper, rear wall
v	$km\ s^{-1}$	Impact velocity
α	degrees	Impact angle (with respect to surface normal)
S	cm	Space between bumper and rear wall
τ_1^*	$lb\ in^{-2}$	Yield stress of reference material, i.e. 40,000 $lb\ in^{-2}$ (= 276 x 10 ⁶ Pa)
τ_2^*	$lb\ in^{-2}$	Yield stress of reference material, i.e. 70,000 $lb\ in^{-2}$ (= 483 x 10 ⁶ Pa)
τ	$lb\ in^{-2}$	Yield stress of rear wall
σ_w	$k\ lb\ in^{-2}$	Yield stress of rear wall

Table 3-6: Damage equation terms

Values for the terms in the formulation of this multiple wall equation are given in **Table 3-7** [Lemcke *et al.*, 1998b].

Equation	v (km/s)	K_1	K_2	λ	β	γ	κ	δ	ξ	v_1, v_2	μ
ESA triple*	$v < 3$	$0.312 \left[\frac{\tau_1^*}{\tau} \right]^{0.5}$	$1.667 \cdot K_1$	1.056	0.5	2/3	0	0	5/3	0, 0	1
	$v > 7$	$0.107 \left[\frac{\tau_2^*}{\tau} \right]^{0.5}$	0	1.5	0.5	1	0	-0.5	1	0.167, 0	0
Modified Cour-Palais	$v < 3$	$0.6 \left[\frac{\sigma_w}{40} \right]^{0.5}$	$1.667 \cdot K_1$	1.056	0.5	2/3	0	0	5/3	0, 0	1
	$v > 7$	$0.129 \left[\frac{\sigma_w}{70} \right]^{0.5}$	0	1.5	0.5	1	0	-0.5	1	0.167, 0	0

* This is the modified Cour-Palais equation with ESA constants

Table 3-7: Typical parameter values for the generic multiple wall ballistic limit equation

For Al / Al single- and double-honeycomb panels that would be applicable to the METOP and ERS satellites, Turner *et al.*, 2000, have adapted the formulation of the equation (shown in **Table 3-7**). For velocities below 3 km/s, the ξ term is changed from 5/3 to 8/3 (if v is input) or 6/3 (if v_n is input). For velocities above 7 km/s, Turner *et al.* suggest replacing the rear wall (i.e. rear face-sheet) thickness term, t_w , in the equation with an equivalent thickness of aluminium, t_{Equiv} , for the entire panel.

Figure 3.1-12 provides an example of impact damage on double honeycomb sandwich panels. The enhanced protection offered by toughened MLI is also illustrated.

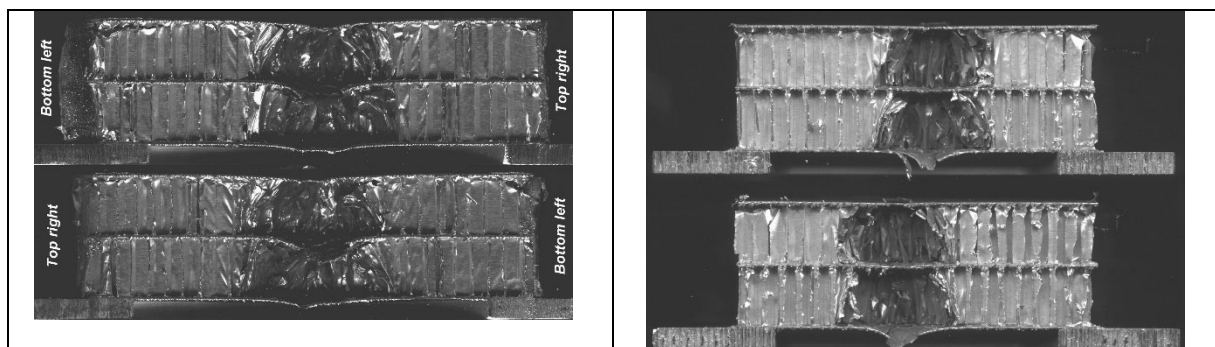


Figure 3.1-12: Double honeycomb (right) and Double honeycomb + toughened MLI (left)

3.1.2.4 Non-Conformal Shields

This section describes a new shield concept – the “non-conformal” shield. The author is V. Sokolov (RSC-Energia).

3.1.2.4.1 Introduction

The usual shielding practice deals with so-called conformal shields, that is, shields which conform to the shape of protected pressure walls.

The term “non-conformal shield” refers to a shield that is separated from the structure it protects. In this case, mechanical impulse loads generated by the impact cloud on the main structure are not sufficiently large to be taken into consideration. So, the main cause of structural failure is the largest fragment in the cloud of secondary particles spreading behind the shield. This largest fragment defines the ballistic limit of the construction protected.

Practical examples of non-conformal shielding in the International Space Station configuration are illustrated in **Figure 3.1-13** and include:

- shield constructions in the form of deployed vertical “wings”, shadowing the Service Module from space debris;
- solar panels and thermal radiators of the US segment which serve as “semi-transparent” barriers partially protecting some modules of the Russian segment from space debris.

The combination of non-conformal shields and the structure they protect will be called “non-conformal shielding construction” (NCSC) further in the text.

The characteristics of NCSC are not as thoroughly investigated as those of conformal shields. So, a new methodology of obtaining ballistic limit curves (BLC’s) for NCSC is presented below.

3.1.2.4.2 Non-Conformal Shielding Construction BLC Calculation

One can calculate the BLC of NCSC by using the BLC of the construction without the non-conformal shield (that is, the baseline BLC), and using an equation of projectile fragmentation (EPF). The EPF for a compact projectile can be obtained on the basis of experimental data in the following normalised form:

$$\frac{d_f}{d_p} = f(V_{p0}, V_p) \quad [3.1-21]$$

where

d_f – size of the projectile’s largest fragment.

d_p – size of the original projectile.

V_p – projectile velocity.

V_{p0} – projectile velocity critical value, at which fragmentation begins, and which is dependent on the value of t/d_p , where t is a shield thickness.

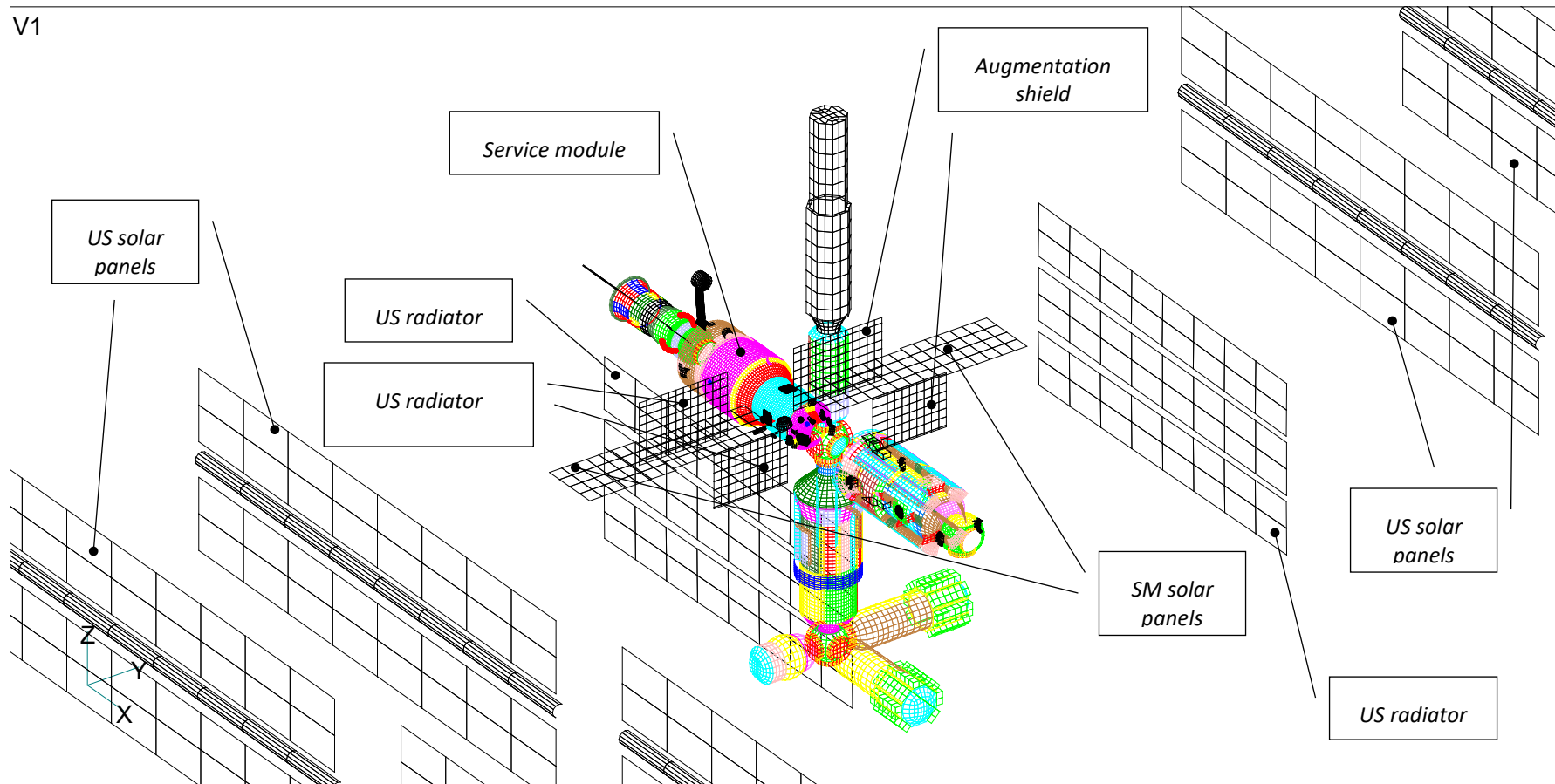


Figure 3.1-13: General view of ISS

To obtain a BLC for NCSC, one can modify the baseline BLC by applying the following procedure illustrated in Figure 3.1-14.

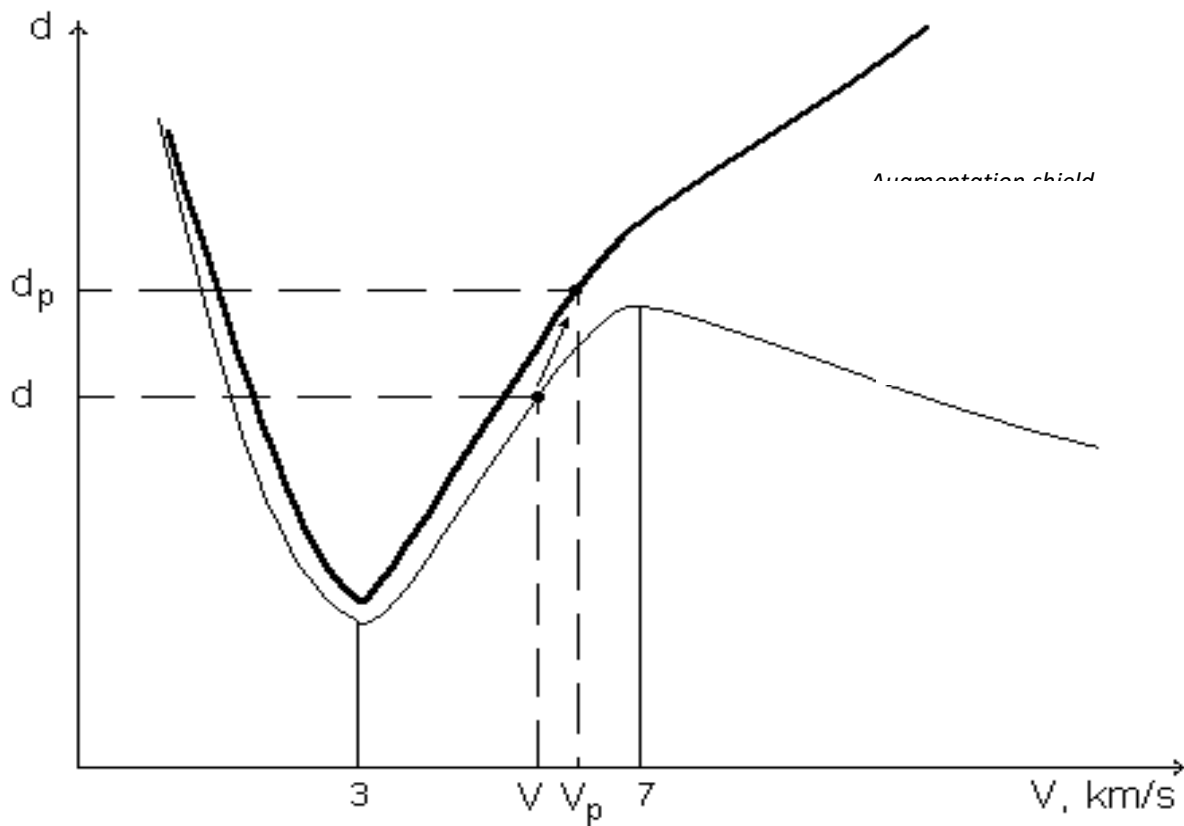


Figure 3.1-14: NCSC BLC calculation procedure

At arbitrary velocity V , the diameter of the largest fragment, d_f , which can penetrate the pressure wall, can be found from the baseline BLC. Then the projectile diameter, d_p , can be found from the EPF by applying an iterative procedure, taking into account the relation between projectile velocity V_p and the velocity of the largest fragment, V . For thin shields ($t/d_p < 0.2$), this relation can be found from the momentum conservation law:

$$V_p = \left(1 + \frac{1.5}{\cos \alpha} \frac{\rho_s}{\rho_p} \frac{t}{d_p} \right) \quad [3.1-22]$$

where

- ρ_s, ρ_p – density of the shield and projectile materials, respectively.
- α - angle of incidence.
- t - shield thickness.

For thick or composite non-conformal shields, such relations have to be determined experimentally.

For constructions shadowed by several non-conformal shields, distanced from each other, this procedure must be iterated in order to obtain a resulting BLC which accounts for all semi-transparent barriers, as is illustrated in **Figure 3.1-14**.

3.1.2.4.3 EPF Experimental Verification

The most fundamental experimental studies of aluminium projectile fragmentation on thin aluminium bumpers were performed by A.J. Piekutowski [Piekutowski, 1994, 1997]. He found that the ratio of largest fragment size to particle diameter does not simply depend on particle size. His first study provides the rationale for a unified formula for largest fragment size.

In order to get the relation between largest fragment size and impact parameters, a joint experimental program was performed both in Russia at the TSNIIMASH test facility and in the USA at the White Sands test facility.

The analysis of experimental data for aluminium barriers obtained in these experiments has shown that the formula for largest fragment size, best fitted to experimental data, has the following exponential form [Christiansen *et al.*, 2000]:

$$\frac{d_f}{d_p} = \exp \left[- \left(\frac{V_p}{0.85 V_{p0}} - 1 \right) \right] \quad [3.1-23]$$

where the critical velocity V_{p0} is determined by the equation:

$$V_{p0} = \frac{1.675}{\cos \alpha} \left(\frac{t}{d_p} \right)^{-0.294} \text{ km / s} \quad [3.1-24]$$

3.1.2.4.4 Experimental Verification of NCSC BLC Calculation Methodology

Two high-velocity impact tests [Burt *et al.*, 2001] were performed at NASA's White Sands Test Facility for verification of the BLC calculation method described above. The test scheme, presented in **Figure 3.1-15**, simulates shadowing of the Service Module by US solar arrays and radiators, as well as by the Service Module solar array (aluminium plates of equivalent thickness were used to simulate real materials). The first shot was performed with a 1.27 cm diameter aluminium ball at an impact velocity $V \approx 7$ km/s and an incidence angle $\alpha = 0^\circ$; the wall was not penetrated. The second shot was performed with the same size ball at the same velocity and an incidence angle $\alpha = 45^\circ$; this time the wall failed.

The test results are presented in **Figure 3.1-15**, where an experimental point for the test projectile size and velocity is plotted, together with calculated BLC's for two values of incidence angle ($\alpha = 0^\circ, 45^\circ$). As can be seen from the graph, there is a good agreement between calculated and experimental results for $V = 7$ km/s.

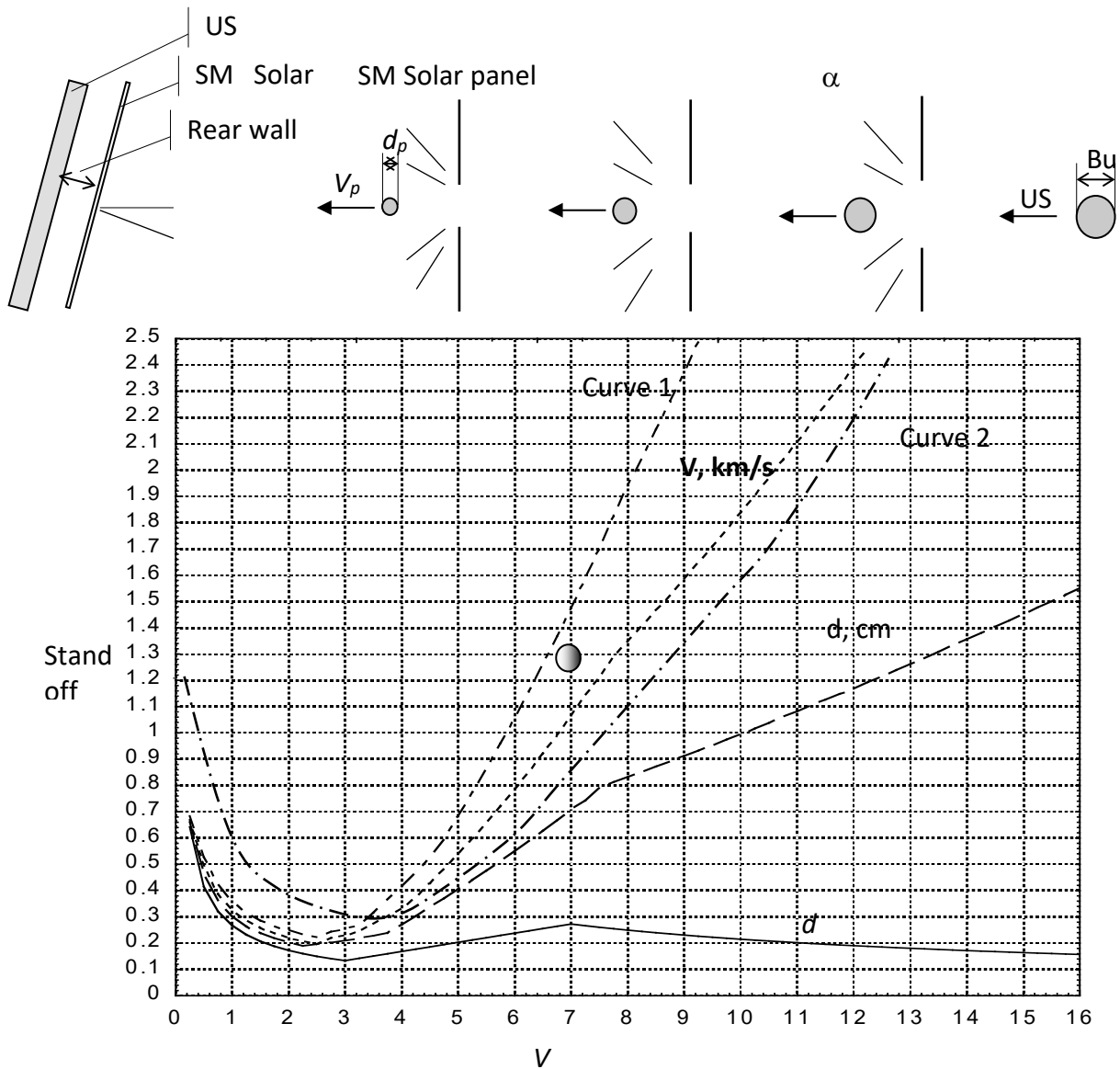


Figure 3.1-15: Verification of BLC_{NCSC} calculation

Designation of curves in **Figure 3.1-15**:

- Curve 1 – baseline BLC ($\alpha = 0^\circ$)
- Curve 2 – BLC_{NCSC} accounting for US solar panel ($\alpha = 0^\circ$)
- Curve 3 – BLC_{NCSC} accounting for US solar panel, plus US radiator ($\alpha = 0^\circ$)
- Curve 4 – BLC_{NCSC} accounting for US panel, US radiator, and SM panel ($\alpha = 0^\circ$)
- Curve 5 – BLC_{NCSC} accounting for US panel, US radiator, and SM panel ($\alpha = 45^\circ$)

3.1.3 Shape Effects

EMI has recently introduced BLE's for considering projectile shape effect. Therefore, ellipsoids are taken as projectiles.

The BLE's are based on Christiansen's double wall equations. A shape factor f is introduced:

$$f = (c/a) \quad [3.1-25]$$

$$d_p = 3.918 t_w^{2/3} \rho_p^{-1/3} \rho_s^{-1/9} v_n^{-2/3} S^{1/3} \left(\frac{\sigma_w}{70} \right) b 3^{-\frac{(f-1)^2}{b^2}} f^{b1} \quad \text{for} \quad v_n > v_{G2} \quad [3.1-26]$$

$$d_p = \left(\left(t_w \frac{\sigma_w}{40} \right)^{0.5} + t_s \right) / (0.6(\cos \alpha) \rho_p^{0.5} v_n^{2/3} f^{a2})^{18/19} \quad \text{for} \quad v_n < v_{G1} \quad [3.1-27]$$

The critical particle mass is:

$$m_p = \rho_p \frac{\pi}{6} d_p^3 \quad [3.1-28]$$

For shape factors $f = 0.42$ (black); 1.00 (red), 1.53 (blue) one gets the following graph:

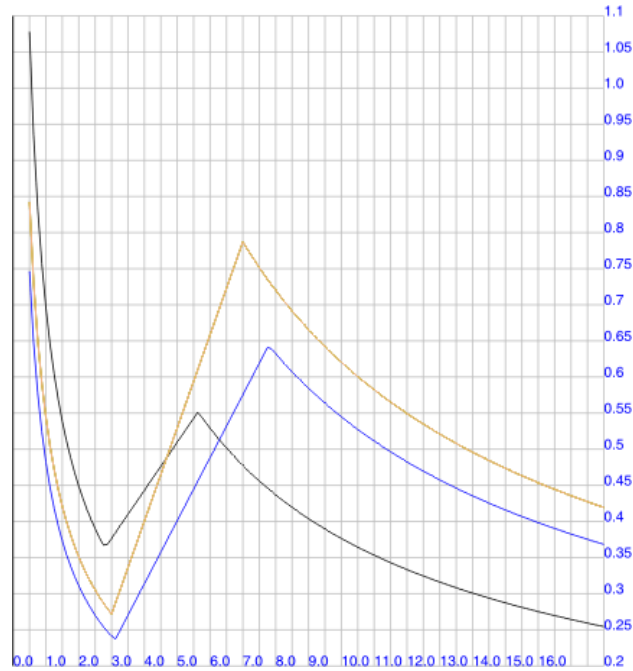


Figure 3.1-16: BLE shape factor coefficients (y-axis) as a function of velocity (x-axis)

A first risk analysis with MDPANTO for the above-mentioned shape factors was performed with the cube and the simple space station (benchmarks of section 2.3.7).

	f=0.42	f=1.0	f=1.53
CU-debris	1.989E-04	2.546E-04	5.116E-04
CU-meteoroid	5.058E-05	7.046E-06	1.185E-05
SS-debris	6.994E-04	1.269E-03	1.792E-03
SS-meteoroid	2.063E-04	2.873E-05	4.833E-05

Table 3-8: Preliminary risk assessment results with BLE shape factors

3.1.4 Influence of Target Temperature on Impact Damage

3.1.4.1 Motivation

In the laboratory, shielding systems for manned modules and structure walls of satellites are typically submitted to hypervelocity impact tests at ambient temperature. This ambient temperature does not represent the actual large temperature extremes caused by solar radiation and the near vacuum of space as experienced by International Space Station modules and unmanned Satellites. However, none of the damage prediction equations and Ballistic Limit Equations (BLE) contains temperature as parameter. As materials become more brittle at lower temperature and increase ductility at elevated temperature, it is reasonable to assume that temperature effects also damage type and -extensions in spacecraft structures.

Purpose of the following review of published articles is to analyze the existing knowledge regarding the influence of target temperature on the damage caused by a hypervelocity impact and to reach a preliminary conclusion on the relevance concerning the need of quantitatively considering this effect.

3.1.4.2 Literature Review

In [Tanaka *et al.*, 2003], the authors examined the low velocity penetration of steel rods in thick carbon steel plates at room temperature and at liquid nitrogen temperature. Impact velocities ranged. The observation was that the crater diameter was about 20 % larger at the lower temperature over the whole velocity range of between 1.0 km/s and 2.1 km/s. The penetration depths were about 30 % lower at the low temperature (over the whole velocity range). While the target behaved ductile at room temperature, at low temperature, the target behaved very brittle. In [Myers *et al.*, 2003], the authors investigate the influence of the bumper temperature on the hole size. They analyzed a set of 18 impact tests performed on 1.6 mm thick Al-bumpers at impact velocities between 2 and 7 km/s. Projectile diameter was constant 3.18 mm. Three different temperatures were considered: Room temperature (RT), 110°C and 210°C. The hole size data suggest that for constant impact parameters, there is an increase of hole size of between 5 and 10 % at elevated temperature.

[Francesconi *et al.*, 2004] Performed impact tests on two different aluminium alloy bumper plates and on thin CFRP plates at room temperature (RT) and about -110°C. Projectiles were 1.5 and 2.3 mm diameter Al-spheres impacting at around 5 km/s. At the lower temperatures, the hole diameter was less than 5% smaller than at RT in the aluminium alloys. The authors noted some qualitative difference in the damage on the backwall: At lower temperature, there seemed to be more and smaller craters compared to the RT case. Concerning the crater diameters in CFRP they

noted a 10% lower diameter at low temperature but could not see any significant difference in backwall damage.

In [Schäfer *et al.*, 2004] the influence of the target temperature on the position of the ballistic limit curve was investigated experimentally. The target consisted of a Whipple shield with a 1 mm thick Al-bumper and a 3 mm thick Al-backwall. The temperature of both plates was changed between about -150°C, RT, and about +150°C. The whole Whipple shield was cooled down at once. Impact tests concerned Al-projectiles with diameters of between 4.5 - 5 mm and impact velocities around 5 km/s. Their finding was that the curve that provides the ballistic limit diameter at low temperature takes values that are about 10% higher than those at room temperature. The BL curve at elevated temperature is 10% below the BL curve at RT. An explanation of the temperature dependence of the BL curve was provided based on the temperature dependence of the yield stress.

In [Reimerdes *et al.*, 2004] the influence of temperature on the hole size in a bumper plate and the impact damage in the backup wall was investigated. Target was a double bumper shielded backwall, Bumper 1: Al 6061-T6, 0.8mm, Bumper 2: Al 6061-T6, 0.8mm, backwall 3.2 mm Al 2219-T851, spacing each 60 mm. Impact conditions were Al-sphere 5 mm at around 5.4 km/s and 7.4 km/s, normal impact. Six impact tests were performed. The temperature was varied in the range RT to -73°C. Within the range of tested temperatures, the variation of hole sizes was on the order of a few percent which is in the order of measurement uncertainties. Also, the extension of the cratered areas on the backwall did not exhibit a clear trend with regards to influence of temperature. Just the measured maximum penetration depth in the backwall decreased continuously as a function of temperature (from 0.7 mm at RT to 0.3 mm at -75 °C).

3.1.4.3 Conclusions

The temperature effect on hole sizes in bumper plates is in the range of below 10 %. At low temperature, the hole sizes tend to be smaller than at RT, at elevated temperature, the hole sizes tend to increase. One paper dealing with rod penetration indicated that the penetration depth in thick plates decreased considerably at lower temperature. While there is generally a small effect of temperature on the hole sizes, it was noted that the crater pattern on backwalls of Whipple shields shows clear differences with regards to the temperature: At low bumper temperature, the projectile seems to fragment more efficiently and hence the craters in the backwalls generally seem to be shallower compared to the room temperature reference cases. This is also substantiated by the reported finding that the ballistic limit curve of Whipple shields is shifted to higher projectile diameters at low target temperature.

3.2 Component Ballistic Limit Equations

3.2.1 Thermal Protection Systems

Thermal protection systems (TPS) have been evaluated with respect to meteoroid and orbital debris impact damage in the frame of re-entry vehicle projects as NASA Space Shuttle and ESA Huygens [Christiansen *et al.*, 1993; Christiansen & Friesen, 1997; Lambert & Schäfer, 1998].

3.2.1.1 NASA

3.2.1.1.1 Reinforced Carbon-Carbon (RCC)

Ballistic limit equations for Reinforced-Carbon Carbon (RCC) penetration and hole size are provided below. Additional details are found in [Christiansen *et al.*, 1993; Christiansen & Friesen, 1997; Friesen *et al.*, 1996; Lyons, 1998; NASA JSC HVIT web sites].

TPS Description

Targets consist of silicon-carbide (SiC) coated reinforced carbon-carbon composite. Nominal thickness of the targets is 6.3mm, SiC coating thickness is 0.8mm (+/-0.2mm) on each side, and the carbon substrate is 4.7mm (+/-0.4mm) thick. The substrate has a density of 1.44 g/cm³ to 1.6 g/cm³.

Damage Modes

1. Coating Damage
2. Penetration to Carbon Substrate (see **Figure 3.2-1**)
3. Detached Spall from Back
4. Complete Penetration (see **Figure 3.2-1**)

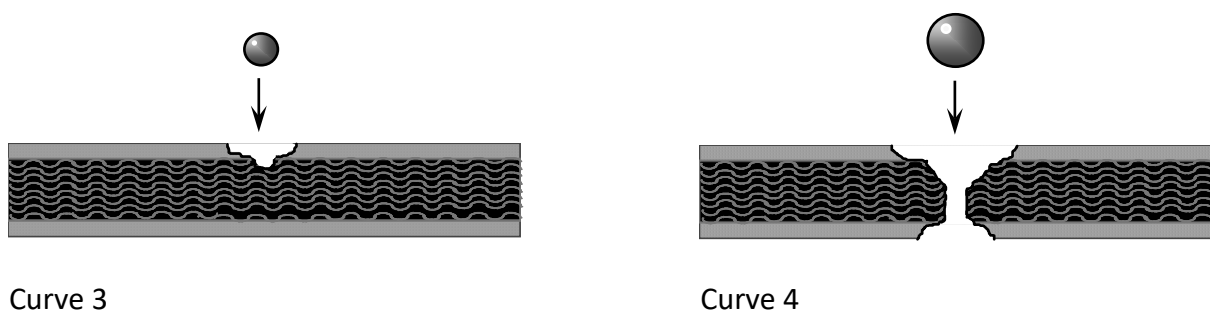


Figure 3.2-1: RCC damage modes

Projectile and TPS parameters

- | | |
|----------------|---|
| d | projectile diameter (cm) |
| D _H | through-hole diameter (cm) |
| ρ _p | projectile density (g/cm ³) |

ρ_t	target density (g/cm ³)
M	projectile mass (g)
P	penetration depth (cm) from original surface
t	target thickness (cm)
V	impact velocity (km/s)
V_n	normal component of velocity (km/s) = $V \cos\theta$
θ	impact angle from surface normal (deg)

RCC Damage Equations

The equations below are based on an analysis of over 50 hypervelocity impact tests on RCC samples as well as hydrocode simulation results [Christiansen *et al.*, 1993].

Penetration Depth (P):

$$P = 0.61 d V_n^{2/3} (\rho_p/\rho_t)^{0.5} \quad [3.2-1]$$

Thickness to prevent complete penetration:

$$t = 2.3 P \quad [3.2-2]$$

Thickness to prevent detached spall:

$$t = 4.5 P \quad [3.2-3]$$

Through-hole diameter (D_H):

$$D_H = 2.2 d \rho_p^{1/3} V_n^{1/3} - 0.36 \quad [3.2-4]$$

Figure 3.2-2 illustrates impact data on RCC and correlation of impact parameters with hole size.

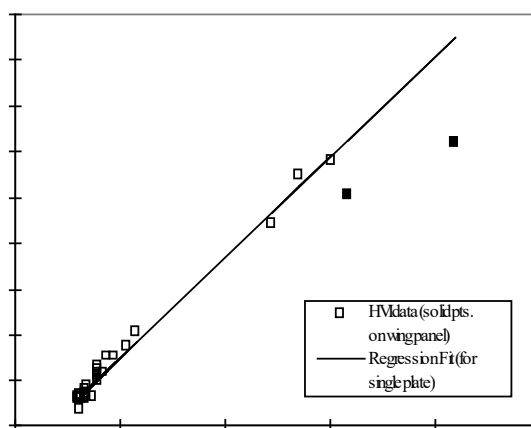


Figure 3.2-2: RCC impact test data

3.2.1.2 ESA

3.2.1.2.1 Flexible External Insulation

The Flexible External Insulation (FEI) material is a thermal protection for re-entry spacecraft parts submitted to moderate heat fluxes. Typical applications are the upper fuselage of winged re-entry vehicles or the conical part of capsules. The material is a laminate that contains felt blankets made of silica fibre. The outer cover of the laminate is made of ceramic fabric (Nextel®) while the inner cover is made of glass fabric. The various components are held together by a squared sewing pattern which uses glass as sewing thread. A thin, high emissivity silica-based coating is applied on the outer fabric. This laminate (0.36 g/cm²) is subsequently bonded to the structure (Aluminium Al-7075 T6 1.9 mm) of the vehicle by a silicone adhesive. A reinforced version of the material includes three intermediate layers of Nextel fabric embedded between each of the felt blankets (0.58 g/cm²).

Impact Damage

Between 1 and 3 km/s, the impact pressure is not sufficient to fragment or melt the incoming projectile. In this case the damage is driven by the capability of the target at decelerating and eroding the projectile. This process leads to localised damage with a deep hole in the low-density target and craters, spall and possibly cracks of limited extent in the denser material at the rear of the target.

In the low velocity regime, for an equal surface density, test results show the FEI configuration is more effective by a significant margin than the single aluminium plate. The gain is approximately 20 percent in terms of kinetic energy or projectile mass if the velocity is kept constant.

At impact velocities at or above 6 km/s, the contact pressure is sufficiently high to generate projectile shock and heat. According to the characteristics of the target material, ellipsoidal or quasi-spherical cavities are formed during the dissipation of the projectile energy.

In the high velocity regime, the penetration depth is given by:

$$P/d = 1.25 (\rho_p/\rho_t)^{1/2} (V \cos(\theta))^{2/3} \quad [3.2-5]$$

For the reinforced FEI the coefficient is reduced to 0.83.

The front hole diameter is given by:

$$D_h/d = 0.51 (V(1+\sin(\theta)))^{2/3} \quad [3.2-6]$$

Hypervelocity impacts produce, in low-density materials like FEI, an ovoid cavity. A correlation between the cavity diameter and the impact conditions has been established for the whole set of available data:

$$D_c/d = 3.15 (V(1+\sin(\theta)))^{2/3} \quad [3.2-7]$$

The high emissivity coating covering the front fabric layer is detached by the impact process in the vicinity of the hole. The affected area appears quite irregular in shape. Data shows a large scatter. Observed damage is assimilated to a circle. The following expression provides an idea of the damage extent:

$$D_s/d = 1.86 (V(1+\sin(\theta)))^{2/3} \quad [3.2-8]$$

Test results show that the FEI configuration performs better than a single Aluminium plate of the same surface density. This advantage is very marked in the high velocity regime.

3.2.1.2.2 AQ60

AQ60 is a thermal protection for re-entry spacecraft parts subjected to significant heat fluxes. A typical application is the front shield of capsules. AQ60 is a felt made of short fibres. It is obtained by vacuum processing of an aqueous suspension of silica fibres. The material is then reinforced by impregnation and polymerization of phenolic resin (representing 30 % of the total mass). The final density is 0.3, total porosity is 84 %, the volumic percentages are 10 % and 6 % for silica and resin respectively. This material (0.3 g / cm³) is similar in some aspects to the STS shuttle tile material, but it is not reusable because its non-mineral bonding agent is pyrolyzed at temperature between 100 and 1000 °C. However, following pyrolysis, the material is still self-supporting and becomes a very efficient insulator with quite high ablation temperature. AQ60 front side is coated with a thin layer made of a silicone-based product. The samples (0.75 g/cm²) are 25 mm thick. Some samples are bonded to a 2.9 mm aluminium substrate as per envisaged spacecraft configuration.

Impact Damage

For velocities above 6 km/s, the penetration depth is given by:

$$P/d = 1.35 (\rho_p/\rho_t)^{1/2} (V \cos(\theta))^{2/3} \quad [3.2-9]$$

The impact hole diameter is given by:

$$D_h/d = 0.39 (\rho_p/\rho_t)^{1/2} (V(1+\sin(\theta)))^{2/3} \quad [3.2-10]$$

Hypervelocity impacts produce, in low-density materials like AQ60, an ovoid cavity. A correlation between the cavity diameter and the impact conditions has been established for the available data:

$$D_c/d = 0.78 (\rho_p/\rho_t)^{1/2} (V(1+\sin(\theta)))^{2/3} \quad [3.2-11]$$

Test results indicate that, even for energies well below the ballistic limit of the AQ60/ aluminium configuration, AQ60 is debonded from the aluminium substrate on a large area. This severe damage for the thermal protection is due to shock waves reflections at the interface between AQ60 and the aluminium plate.

3.2.2 Windows and Glass

Windows, also called viewports, are required to support external activities of manned missions. They are important to crew comfort as well as providing ports for scientific experiments and observations. They have the capability of deep space, sun and earth viewing for photographic use in the normal human visual spectral range [Alwes, 1988].

3.2.2.1 Fused-Silica Glass Windows

Window ports on spacecraft typically consist of multiple, separate glass panes. NASA practice for Shuttle and ISS windows is to use a 3-pane window system, with the outer window a sacrificial debris pane and two inner pressure-panes (primary and redundant pressure panes). Typically, only the inner, primary pressure pane is carrying the load from differential pressure across the window, while the other 2 panes are unloaded since the cavities between windows are vented to space. Fused silica (99% silica glass) is typically used as the outer window debris pane material. Due to its brittle nature, glass is more susceptible to hypervelocity impact damage than strong, ductile materials such as aluminium.

Hypervelocity impact damage equations for fused silica glass have been defined by NASA [Cour-Palais, 1982; NASA, 1985; Christiansen *et al.*, 1997]. Penetration depth (P , cm) in semi-infinite glass is determined from:

$$P = 0.53 \rho^{0.5} d_i^{1.06} V_n^{(2/3)} \quad [3.2-12]$$

$$d_i = (1.89 P \rho^{-0.5} V_n^{-2/3})^{0.94} \quad [3.2-13]$$

where d_i is the diameter or length (perpendicular to the target surface) of the projectile (cm), ρ is projectile density (g/cm^3) and V_n is the normal component of the projectile impact velocity (km/s), $V_n = V \cos\theta$ where θ is impact angle measured from the normal to the target.

Thickness of fused-silica glass to prevent incipient spall (cracks) at back of target:

$$t = 7P \quad [3.2-14]$$

Thickness of fused silica to prevent detached spall at back of target:

$$t = 4P \quad [3.2-15]$$

Thickness of fused silica to prevent complete perforation of target:

$$t = 2P \quad [3.2-16]$$

Thickness to prevent complete shattering of target:

$$t = 0.14P V^{1.28} \quad [3.2-17]$$

Diameter of crater, D_c , (cm) and diameter of projectile, d , (cm) parallel to target surface are given in the following equations:

$$D_c = 31 d^{1.33} \rho^{0.44} V_n^{0.44} \quad [3.2-18]$$

$$d = 0.076 D_c^{0.75} \rho^{-0.33} V_n^{-0.33} \quad [3.2-19]$$

A limited amount of hypervelocity impact data exists for impacts on multi-pane window systems [Schneider, 1990; Sanchez *et al.*, 1998]. The failure criterion for loss of ISS windows (i.e., for the NASA design) is complete penetration of the outer debris pane and detached spall from the back of the redundant pressure pane. A conservative approach in assessing ballistic limits for this type of failure definition is to conservatively add the thickness of the two outer panes, using the penetration equation and perforation factor as described above.

3.2.2.1.1 Shutter Protected Glass Windows

Glass windows are in some cases protected by a cover or “shutter” which can be opened and closed. The simplest shutters are single sheets of aluminium from 0.1cm to 0.2cm thick, usually also including a thermal blanket, that are spaced a distance (5cm to 10cm) from the outer glass surface. Some hypervelocity impact data is available on shutter-protected windows [Sanchez *et al.*, 1998]. More complex, multi-layer shutters are under development for ISS application, and hypervelocity impact tests on multi-layer shutters followed by fused-silica glass windows are also available [Burt & Christiansen, 2001a, 2001b].

3.2.2.1.2 Alternative Glass Material Studies

Hypervelocity impact tests on clear polycarbonate plates have been conducted, and ballistic limit equations have been developed [Burt & Christiansen, 2001c]. Compared to fused-silica glass, polycarbonate provides superior resistance to meteoroid/debris damage, especially cracking and shattering. The clear polycarbonate plates are currently used to provide transparent covers for ISS hatch windows. They are also under consideration as a material candidate for glass substitution in future vehicles.

Penetration depth in polycarbonate (Hyzod AR hard-coated), for $P > 0.1$ cm:

$$P = 3.0 \rho^{1/3} d^{1.2} V^{2/3} \cos^{0.75} \theta - 1.38 \quad [3.2-20]$$

where P is penetration depth (cm), d is projectile diameter (cm), ρ is projectile density (g/cm^3), V is impact velocity (km/s), and θ is the impact angle measured from the normal to the target.

3.2.2.2 Glass and Optics

Optical instrument surfaces are particularly susceptible to degradation from multiple small impacts. These can dramatically increase the light scattered from an optic. Small debris impacts in telescope tubes or optical baffles can also degrade optical components by releasing large amounts of particulates or contaminants. Particulates can temporarily confuse or blind optical sensors, whereas contaminants can affect the light scattering of an optical sensor.

The following damage equations have been derived by least-squares fits to experimental data. Different brittle materials (quartz versus basaltic rocks) may produce differing hypervelocity impact response. Hydrocode modelling of hypervelocity impact onto soda-lime glass does not support the depth of penetration $\propto v^{2/3}$ and suggests that the ratio may be closer to $v^{1/3}$ [Taylor *et al.*, 1999].

Gault, 1973, has derived the following for basaltic rocks (units in cgs, velocity in km/s):

$$T_c = 0.54 d_p^{1.071} \rho_p^{0.524} V^{0.714} \quad [3.2-21]$$

For fused silica (units in cgs, velocity in km/s), McHugh & Richardson, 1974, give:

$$T_c = 0.64 d_p^{1.2} \rho_p^{0.5} V^{0.67} \quad [3.2-22]$$

The equation (units in cgs, velocity in km/s) for fused quartz [Cour-Palais, 1982] is:

$$T_c = 0.53 d_p^{1.06} \rho_p^{0.5} V^{0.67} \quad [3.2-23]$$

The conchoidal diameter on brittle materials represents the maximum radius of damage for semi-infinite targets. Damage equations derived for one brittle material type should not be applied to different brittle material types; as defined by the different shock material response characterisation.

For basaltic rocks (units in cgs, velocity in km/s) [Gault, 1973]:

$$D_{co} = 5.92 \times 10^{-4} d_p^{1.11} \rho_p^{0.54} \rho_t^{-0.5} V^{0.74} \cos \Theta^{0.86} \quad [3.2-24]$$

Fechtig, 1974, modified the Gault equation to give:

$$D_{co} = 5 \times 10^{-4} d_p^{1.13} \rho_p^{0.71} \rho_t^{-0.5} V^{0.754} \quad [3.2-25]$$

More recently, Taylor *et al.*, 1999, define the following for borosilicate glass and soda-lime glass (d_p in microns, ρ_p in g/cm³, v in km/s):

$$D_{co} = 10^{-0.21} d_p^{1.28} \rho_p^{0.44} V^{0.66} \cos \Theta^{0.62} \quad [3.2-26]$$

3.2.2.3 Solar Cells

Micrometeoroid and debris hypervelocity impact on the Hubble Space Telescope solar arrays produces a complex impact feature due to their multi-layer structure (**Figure 3.2-3**). As the overall thickness is less than a millimetre, impacts onto both the front and the rear surface show damage on the glass surface side (**Figure 3.2-4**). One of the largest impact features observed is shown in **Figure 3.2-5**.

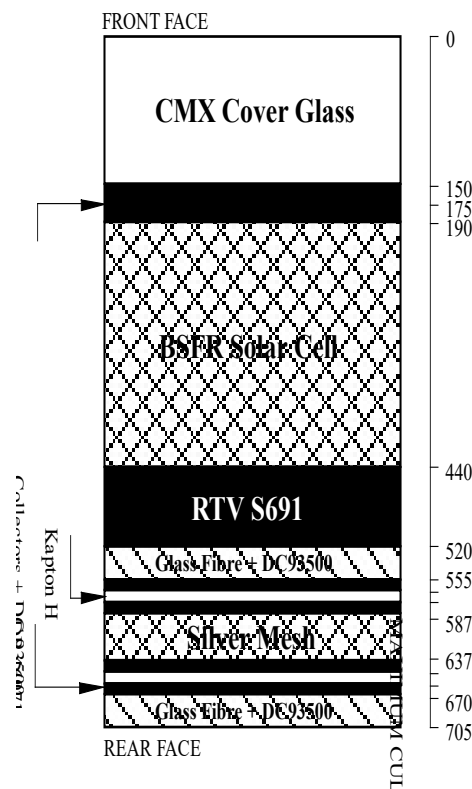


Figure 3.2-3: Solar cell schematic

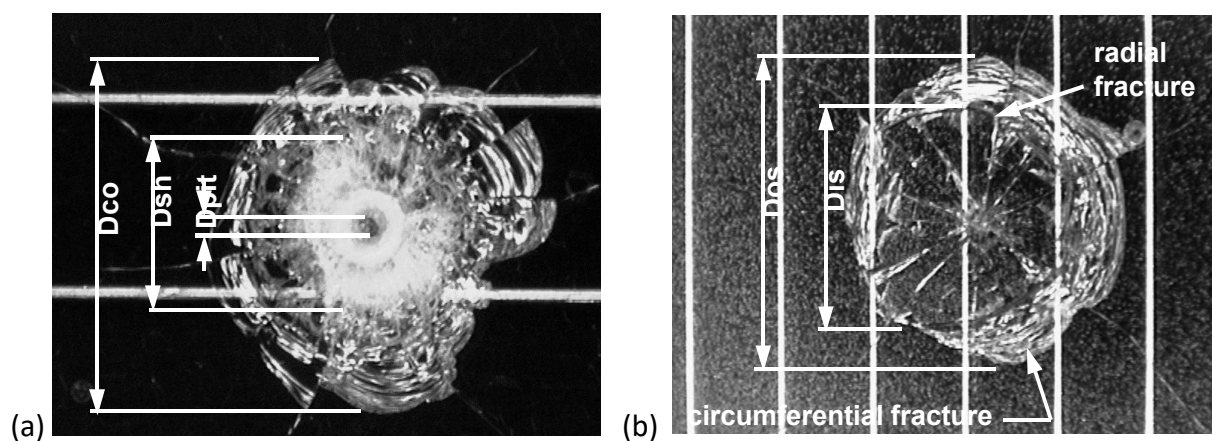


Figure 3.2-4: Damage morphology observed on space-exposed targets
(a) front surface, (b) rear surface

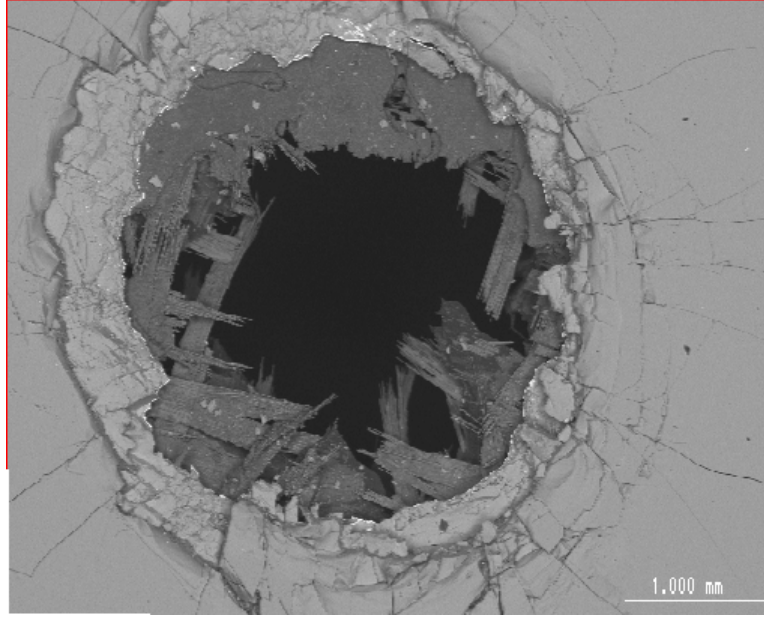


Figure 3.2-5: Large impact on HST solar cell

A damage equation linking D_{co} and d_p is the *McDonnell-Taylor* [Unispace Kent, 1998] solar cell damage equation. It was derived from extensive calibration of HST impact data and may be applied within the calibrated regime $0.1 < d_p < 4.5$ mm:

$$D_{co} = g(\log_{10}(d_p)) f_1(d_p) f_2(d_p) / [f_1(d_p) + f_2(d_p)] \quad [3.2-27]$$

Where the component terms are as follows:

$$f_1(d_p) = f_3(d_p) \cdot 10^{-0.21} d_p^{1.28} \rho_p^{0.44} V^{0.66} \quad [3.2-28]$$

$$f_2(d_p) = 1.0798 d_p + k_{Dco} \quad [3.2-29]$$

$$f_3(d_p) = (2d_p + d_0) / (d_p + d_0) \quad [3.2-30]$$

$$g(\log_{10}(d_p)) = 1 - k / (2\pi \log_{10}(\sigma) \exp[-(\log_{10}(d_p/x_0))^2 / 2(\log_{10}(\sigma))^2]) \quad [3.2-31]$$

$$d_0 = 0.1, \quad \text{mm} \quad [3.2-32]$$

$$k_{Dco} = 12, \quad \text{mm} \quad [3.2-33]$$

$$k = 0.8 \quad [3.2-34]$$

$$x_0 = 0.1, \quad \text{mm} \quad [3.2-35]$$

$$\sigma = 4 \quad [3.2-36]$$

Additional HVI tests and analysis on Hubble solar cells are provided elsewhere [Burt & Christiansen, 2001d]. The through-hole diameter, D_h (mm), was related to normal component kinetic energy of the projectile, KE_n (J), by the following equation:

$$D_h = 0.926 KE_n^{1/3} - 0.169 \quad [3.2-37]$$

Examples of impact damage on solar cells can be found at: <https://space-env.esa.int/madweb/>.

Finally, ESA has performed experimental work to assess the origins of the impact damage on the Hubble Space Telescope (HST) solar cells [Graham *et al.*, 2001].

3.2.3 Pressure Vessels

A Pressure Vessel, as defined by Military Standards, 1986, is a component of a pressurised system designed primarily as a container that stores pressurised fluids and:

1. Contains stored energy of 19,310 joules or greater.
2. Contains a gas or liquid which will create an accident if released.
3. Will experience a design limit pressure greater than 0.7 MPa.

Pressure Vessels store large amounts of energy which under determined conditions can lead to burst. Liquid filled vessels are particularly prone to burst. The process by which projectiles penetrating liquid-filled vessels transfer kinetic energy to the structure is termed hydrodynamic ram. In this process, pressure is induced in the liquid by both impact shock and projectile drag [Rosenberg *et al.*, 1987].

The impact damage on pressure vessels filled with liquid and gas has been experimentally investigated [Poe & Rucker, 1993]. Impacts on gas-filled pressure vessels have been looked at experimentally [Whitney, 1993; Schäfer *et al.*, 1997], numerically [Kamoulakos *et al.*, 1997; Salomé *et al.*, 2001] and theoretically [Telitchev *et al.*, 1999].

3.2.3.1 Damage Modes

Assessment of all possible failure / damage modes is dependent on a number of factors, such as:

- Hole size.
- Blow-down rates.
- Physical characteristics of the fluid released after perforation or burst.
- Location of hole.
- Size and momentum of the debris generated by the projectile and the target.
- Crew action and procedures for manned missions.

A puncture of a pressurised vessel or module will produce a thrust [Celestian & Schonberg, 1993], which can result in failure to maintain spacecraft attitude control. Loss of attitude control can lead to loss of power and other systems. In the case of manned spacecraft, loss of attitude control will affect the ability for safe evacuation if this is necessary.

The thrust from a pressure vessel puncture can also induce structural failures. The thrust may be large enough to fail the mounting structure of the pressure vessel [Poe & Rucker, 1993], allowing the pressure vessel to be released. Or the thrust may be strong enough to break or buckle weaker joints on the spacecraft.

3.2.3.2 Technological Work on Pressure Vessels

Impacts on unshielded and shielded vessels were investigated experimentally, analytically and numerically in a systematic manner to generate a large database of impact results and enable a better understanding of the processes that occur upon impact of hypervelocity particles on gas filled pressure vessels [Schäfer & Schneider, 2001].

The impact tests were performed on unshielded and shielded cylindrical pressure vessels (as in Whitney, 1993) made of Al 5754 (**Figure 3.2-6**), Al 2219, unalloyed titanium (Ti 99.6%) (**Figure 3.2-7**), and Ti6Al4V.

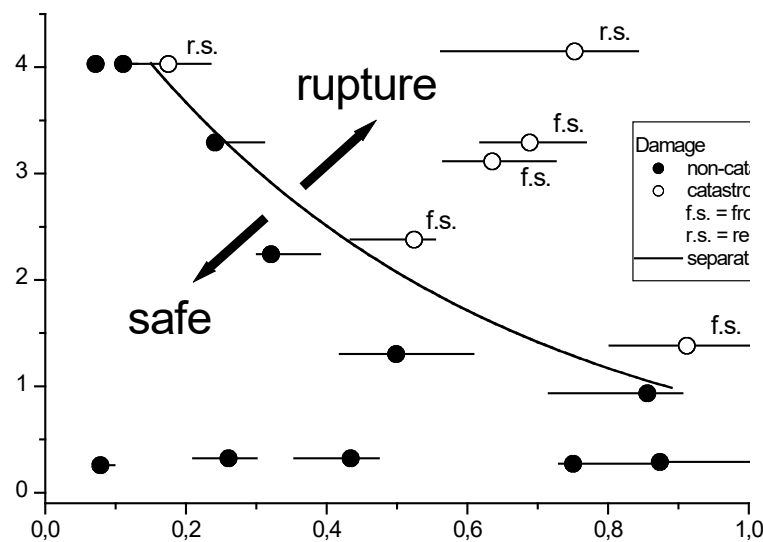


Figure 3.2-6: Experimental results from impact testing of unshielded Al 5754 vessels

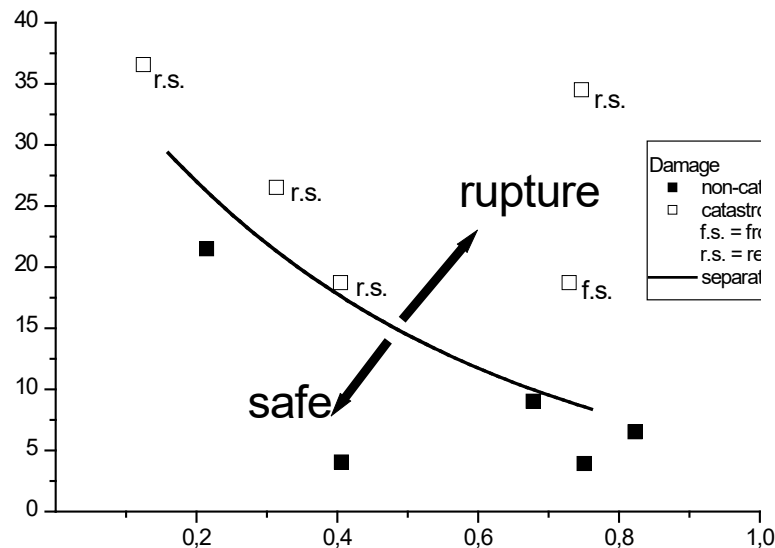


Figure 3.2-7: Experimental results from impact testing of unshielded Ti 99.6% vessels

Most of the cylindrical vessels had a wall thickness of 1 mm, a diameter of 150 mm, and a length of 350 mm. A few tests were performed on 1:1.5 upscaled - and 1:0.5 downscaled Al 2219 vessels for investigation of scaling effects. The fluid was gaseous nitrogen. In some impact tests on shielded vessels made of Al 2219 and Ti6Al4V, the vessels were filled up to a level of 3/4 by water and pressurised with nitrogen to investigate the behaviour of impacts on liquid filled vessels compared to gas-filled vessels. One spherical vessel - a fully integrated gas-filled unshielded Ariane 5 SCA tank from Ti6Al4V - was also impact-tested during the study. The majority of tests was performed at normal incidence. The impact velocity in all tests was chosen to be around 7 km/s, except for the Ariane 5 SCA tank, which was impacted at 8.8 km/s. Projectiles were spheres from aluminium. The shields were 0.5 mm and 1.0 mm thick plates from aluminium, MLI, reinforced MLI, and an all-aluminium double-bumper shield with various spacings.

It is worth noting that for gas-filled aluminium vessels (**Figure 3.2-6**) the kinetic energy of the projectile to burst the vessel at half its maximum operating pressure is 2 KJ while the critical kinetic energy for liquid filled vessels [Poe & Rucker, 1993] is 1 KJ.

The major conclusions of this work are:

- Catastrophic rupture of unshielded gas-filled vessels can be avoided when the impact energy is less than a certain limit value. The energy needed to rupture a vessel depends strongly on the vessel material and vessel pressure.
- Shielding reduces the risk of catastrophic rupture.
- When small particles impact on shielded vessels, the vessel will not leak gas until a certain limit projectile energy is exceeded; the vessel wall tolerates a certain amount of damage before leakage occurs.
- Impacts of particles on shielded water-filled vessels will not lead to catastrophic rupture until a certain impact energy is exceeded; small perforation holes in the vessel wall do not lead to burst.

- Standard and reinforced MLI are very efficient shielding materials when placed at a moderate spacing from the vessel surface.

3.2.3.3 Design Guidelines

Critical impact conditions for liquid filled vessels have been addressed by Rosenberg *et al.*, 1987. Interestingly, the proposed model has been satisfactorily correlated with test results reported in [Schäfer & Schneider, 2001].

Burton Cour-Palais has summarised his experience with liquid filled vessels protected by a bumper located at some distance in front of the vessel [Cour-Palais, 1979]. The concentrated damage area should not exceed 25 mm diameter and the wall thickness loss due to cratering and spallation should not exceed 25 percent of the wall thickness.

Pending the availability of more data, the curves on **Figure 3.2-6** and **Figure 3.2-7** provide a first order of magnitude for the limit between leakage and burst of gas-filled pressure vessels.

Shielded gas-filled vessels can be sized following the Cour-Palais recommendations for liquid filled vessels as evaluated in [Schäfer & Schneider, 2001].

3.2.4 Tethers

3.2.4.1 Tether Design

3.2.4.1.1 Functions

Tethers are flexible line, tape, net, or wire elements used to physically connect two or more spacecraft. Their longest dimension may be several orders of magnitude greater than their other dimensions, e.g., 20 km in length, but only 1 mm in diameter. Tethers are proposed for use in performing a variety of functions, such as: deployment and retrieval of experimental instruments and equipment; boost and deboost of spacecraft by momentum transfer; electrodynamic boost and deboost of spacecraft; boost and deboost of spacecraft by towing; and electrical power generation. In order to perform these functions, tethers must maintain their physical integrity, and, in cases involving data transmission and electrodynamic interactions, must maintain electrical continuity as well. Consequently, tether designs must consider their significant vulnerability to severance by collisions with meteoroids and orbital debris (M/OD).

3.2.4.1.2 Design Types

Simple strings or lines are typically braids or weaves of high-strength polymers such as Kevlar, Nomex, Dyneema or Spectra. However, unless these lines are relatively massive, their vulnerability to cuts by M/OD particles is high.

Multiline tether designs, such as the Hoytether [Hoyt, 1998] employ an open net of lines to provide redundancy against a single cut. The design is such that a spatial separation is maintained between lines even after individual lines are severed. This feature prevents a single small impactor from cutting the entire tether. Analysis indicates that Hoytethers can withstand

numerous cuts without failure, and this characteristic extends their useful on-orbit lifetimes with respect to M/OD severs by several orders of magnitude compared with simple string tethers of the same mass. Hoytethers can be flat tapes or nets, or hollow tubular shapes. However, Hoytethers have found limited interest for in-space application because of the complexity of their structure.

Tape tethers consist of flat stripes, that are wider and thinner than cylindrical strings. It has been argued that tape tethers are significantly more resistant than round wires [Khan, 2016; Francesconi, 2016]; tape tethers have been suggested for electrodynamic applications, thanks to their enhanced capability to collect electrons from the plasma environment as well as their survivability to debris environment [Khan, 2016].

For electrodynamic power generation or satellite reboost, and for towing of sub-satellites with real-time transfer of data, tether designs include conducting elements such as twisted copper or aluminium wires. Electrodynamic uses require good contact with the ambient plasma, which can be accomplished by using ion- or electron-emitting "plasma contactor" devices on the end masses, or by exposing a portion of the conductor to space to act as an electron collector and using an electron emitting device, or by a bare tether section to collect electrons and a coated section with a thin layer of a special material that emits electrons when illuminated by the Sun to close the circuit (low-work-function tether [Sánchez-Arriaga, 2020]).

Tethers are subjected to oscillations and libration modes; a full description of the complex dynamics of tethered systems is beyond the scope of this document. To mitigate these effects a section of the tether is usually manufactured with materials with high damping capabilities (e.g. polymers), in order to dissipate energy and stabilize the system.

3.2.4.2 Failure Modes

Despite their typically small cross sections, the great lengths of deployed tethers result in them presenting large areas for impacts by meteoroids and orbital debris [McBride, 1997]. For example, the SEDS tethers, while only 0.75 mm in width, were 20 km long, and so presented areas of about 15 m² to the M/OD environment. During the SEDS-2 flight, the tether was severed on the fifth day [Evans, 1995], presumably by the impact of an M/OD object.

Multi-strand tethers such as Hoytethers are designed to reduce the tether vulnerability to sever by including many redundant load-bearing elements [Hoyt, 1998]. Several physically nearby cuts must occur to cause such multi-element tethers to fail.

M/OD impacts on electrically conducting elements may result in sever of the tether, even if the impact does not cause an immediate cut. This is due to the possibility of arcing and burn-through by large electrical currents generated by the interaction with the Earth's magnetic field and ionospheric plasma. The TSS-1R mission suffered the loss of the end-mass satellite and a length of tether when current heating due to a defect in the tether's insulation burned / melted the tether in two.

Since most debris and meteoroids are too small with respect to tether size and can strike tethers off-centre, many hypervelocity impacts could be insufficient to cut tethers completely. In these

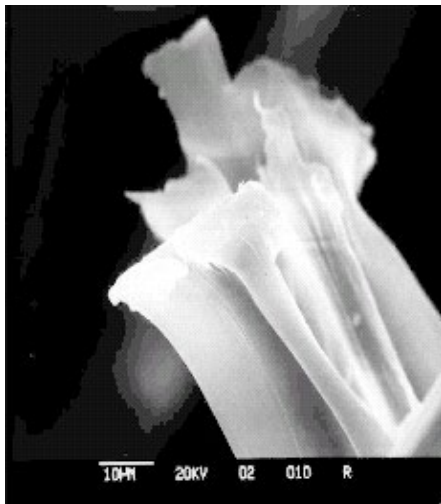
cases, it is important to establish the tether residual capability of completing its functional issues (structural, electrical, data transmission, etc.).

The choice and/or design of a tether for a particular mission should consider the possibility of tolerating many debris impacts without significant degradation of functional performance. Therefore, it must be thought that a tether can fail even if it has not been severed.

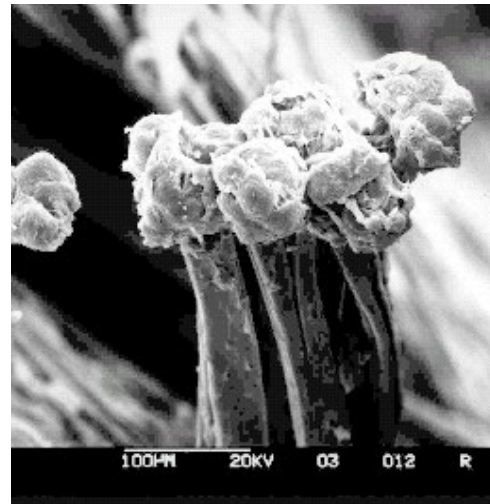
3.2.4.3 Damage Mechanisms

The damage to a tether, as a consequence of a HVI, depends on the tether design type (single strand, woven, flat type, etc.). Hence, it is not possible to identify a general mechanism to describe the damage evolution.

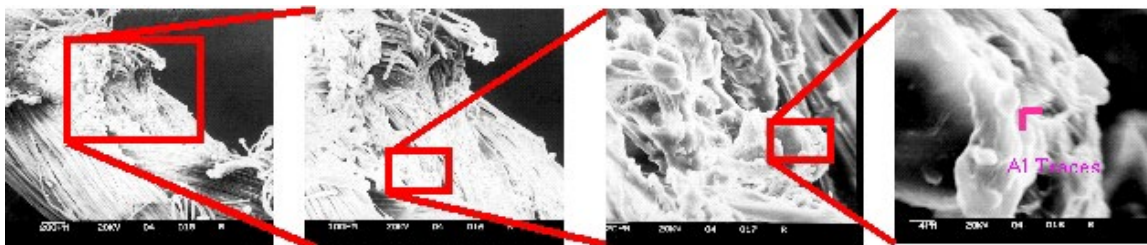
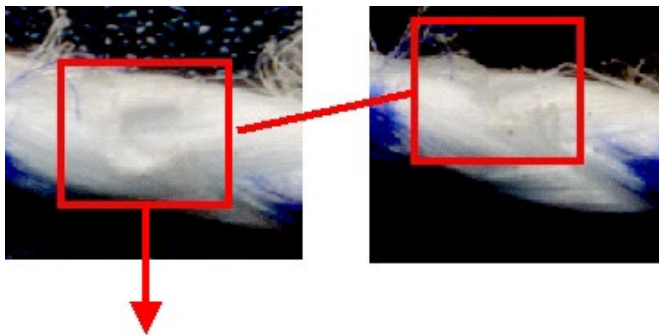
For example, if the tether is made of a bundle of individual fibres twisted together, HVI produces damage (mechanical, thermal) that propagates mainly along the direction of the fibres, as appears in **Figure 3.2-8**. SEM analysis shows that thermal effects propagate several diameters away from the edge along the fibre, while transversal propagation is limited. Filament structures due to fusion are present between different fibres groups.



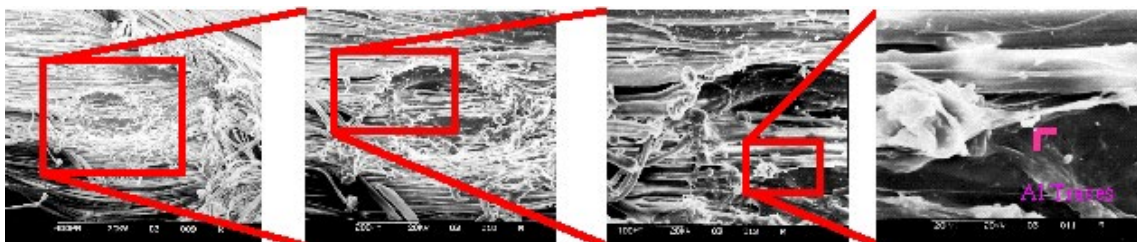
Mode 2. Penetration to Carbon



Curve 5



Mode 4.



Dyeema fibres

Figure 3.2-8: Tether impact damage morphology

Figure 3.2-9 refers to impact experiments performed on 1.36 mm-diameter Dyneema samples. Aluminium spheres of 1 mm diameter were launched at 3.5 km/s on tethers disposed in array configuration.

The experiments were performed at CISAS, using a support facility (**Figure 3.2-9**) that can hold at the same time 11 circular-section-tethers (up to 5 mm diameter and 200 mm length) or 2 flat-type tethers (up to 60 mm width and 200 mm length) in a double-array configuration, to strike at least one tether for each shot. The impact angle can be set in the range 0-35°.

Each tether can be loaded independently from the others by means of a spring-based mechanism. Force transducers measure tether tension before, during and after the impact. Tethers temperature can be controlled before the impact by a special thermostat configuration: the temperature cables can be set between 100-400K with a uniformity of about 10% over the array. To avoid uncertainties about axial force due to thermal effects, tether tensile stress is measured continuously during the thermal cycle.

After the HVI test, a morphologic analysis of the impact location is performed, and the residual tensile strength is derived using a machine developed to measure the deformation-stress profile of wires. Finally, the impacted area is analysed with SEM, to investigate the influence of a HVI on tethers microscopic characteristics and to identify the eventual presence of projectile traces on the impact location. These combined investigations aim to relate the microstructure of a tether with its residual tensile strength after a non-destructive impact.

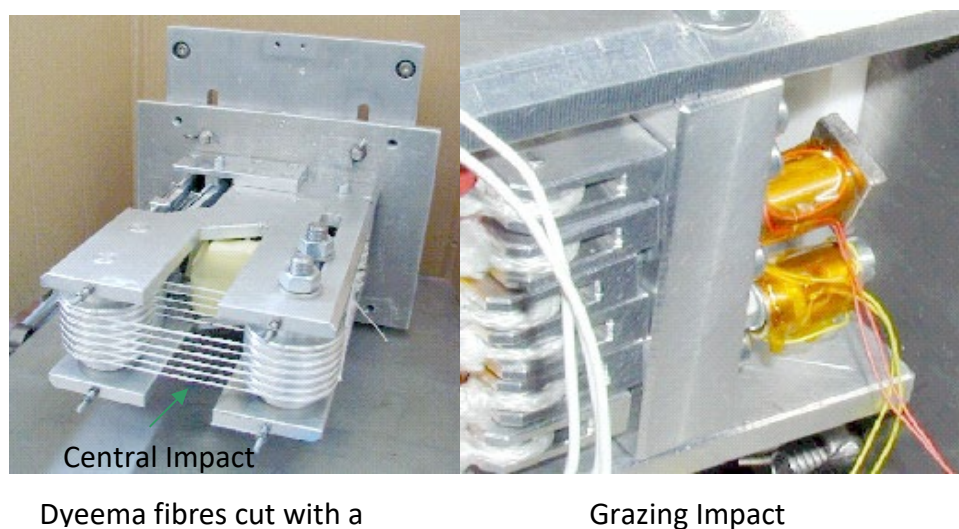


Figure 3.2-9: Tether test set-up

3.2.4.4 Protection Options

Due to their nature, it is impossible to "shield" tethers from the M/OD threat, in any ordinary sense of the word, and any protection design option is related to specific tethers design (structural geometry and choice of materials). Single tethers can be made large enough in diameter that the bulk of the M/OD threat will be incapable of severing them; however, this option will increase the tether mass considerably, and may pose problems for deployment.

Multi-element tethers like the Hoytether provide structural redundancy at minimal cost in terms of weight but significant cost in terms of complexity and deployment ease.

Round-wire electrodynamic tethers may need to have large diameters in order to provide sufficient conducting path for the expected current levels; tape tethers can be chosen thanks to their larger cross-section with respect to round wires. Data transmission tethers may be able to make use of redundant network designs such as nets or tapes; several independent conducting paths could be included in such designs.

3.2.4.5 Experimental Data, Models, and Equations

3.2.4.5.1 Damage Evaluation and Experimental Data

The most natural way of evaluating the damage to single line tethers is to determine if the tethers is cut or not, i.e., if the two end masses are still connected. Lesser degrees of damage are discernible with difficulty, even with careful close-up inspection.

Since damage mechanisms for tethers strongly depend on the tether design type, a possible approach is to assume that failure occurs when the impact crater exceeds a certain fraction of the undamaged cross section. The value of such fraction is defined each time according to the mission-related meaning of “failure” (severance, break-up of the electrical insulation, etc.).

That said, the definition of damage equations for tethers is difficult, because the extension of impact craters (i.e., the occurrence of failure conditions) depends not only on the usual parameters (projectile material, shape, size and velocity; impact angle; target size, material and temperature), but also on the location of the impact on the target. This latter variable is unknown a-priori and cannot be easily determined, even during post-impact analyses.

The Spectra tether of the SEDS-2 mission was the first manmade orbiting object to be seen from the Earth's surface not as a point of light but rather as a line of light. After it was cut its apparent length was reduced, and the freshly cut end appeared brighter than the rest of the tether.

Damage to Hoytethers, where the tether is not severed, may be discernible from nearby visual inspection; whether differences in the ground-based visual appearance of a degrading Hoytether will be seen remains an open question.

Damage to conducting tethers should be indicated by variations in measured current or resistance, or perhaps by the presence of visible discharges.

Experimental data

Hypervelocity impact experiments on 0.75 mm Spectra 1000 are reported in McBride & Taylor, 1997. The critical projectile diameter D_{crit} was between 0.2 and 0.3 mm at 5 km/s. Hence, the ratio R_{crit} between D_{crit} and D_{tether} was between 0.27 and 0.4.

Hypervelocity impact experiments on 1.36 mm Dyneema were carried out at CISAS (University of Padova) [Francesconi, 2003]. A projectile diameter of 0.585 mm just severed the tether at a

velocity between 4.9 and 5 km/s. The impact location on the tether was estimated by analysing SEM photographs. In this case, the ratio R_{crit} between D_{crit} and D_{tether} was 0.43.

Hypervelocity impact experiments on Aluminium Al-1100-H9 and PEEK tape tethers were carried out at CISAS [Francesconi, 2016]. 24 hypervelocity impact tests were performed at different impact angles spanning from 0 to 90 deg, with projectile diameters of 1.5 and 2.3 mm at velocities between 2 and 5 km/s. Tethers were 0.05 mm thick and 2.5 mm wide. A set of 94 numerical simulations was conducted using ANSYS AUTODYN 3D to expand the range of experimental data to different impact velocities (up to 20 km/s), projectile diameters (up to 15 mm), and tether thicknesses (up to 0.2 mm). Results showed that the impact damage is very close to the projectile size in case of normal impact, while it increases significantly at highly oblique impact angles for both target materials; in addition, it was observed that there is a minimum value of debris velocity v^* below which no critical damage is possible and, furthermore, there is a minimum velocity-dependent value d^* of debris diameter below which no critical damage is possible.

3.2.4.5.2 Models and Damage Equations

Round tethers

Several investigations on round-wire tethers show that, depending on single strand or woven configuration of the wire, the tether fails for impacting particles diameters between $1/3$ and $1/2$ of the tether diameter [Pardini, 2003; Pardini, 2009]. Similarly, Christiansen & Kerr found that for most tether materials, a debris object about 0.4 times the tether diameter will sever it if the strike is centre-to-centre. Most strikes will be off-centre, however, and Matney *et al.*, 2000, determined a penetration efficiency factor P that scales with the impact energy and obliquity of the impact as

$$P = m^{1/3} \rho^{1/2} (v \cos \theta)^{2/3} \quad [3.2-38]$$

where m is the mass of the fraction of the particle intercepting the tether, ρ is its density, v is its velocity, and θ is the angle from the centreline of the tether to the point on its surface where the centre of mass of the impacting particle fraction strikes, measured from a line parallel to v (see **Figure 3.2-10**).

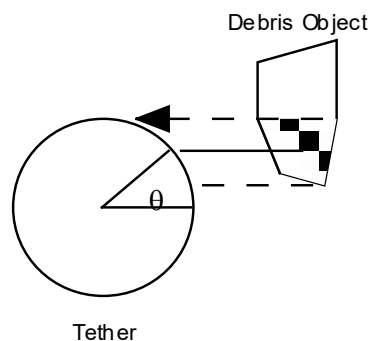


Figure 3.2-10: Tether penetration efficiency factor

Matney *et al.* then plot the ratio "computed sever cross section"/"tether diameter plus particle diameter" cross section (R_x) against the ratio "particle diameter"/"tether diameter" (R_D). The following values may be determined from their table:

Tether penetration efficiency factor														
R_D	0.4	0.5	0.6	0.7	0.8	0.9	1.0	2.0	3.0	4.0	5.0	6.0	7.0	10.0
R_x	0.00	0.50	0.60	0.65	0.70	0.72	0.75	0.88	0.92	0.94	0.96	0.97	0.98	0.99

Table 3-9: Tether penetration efficiency factor

The above results for round tethers are based on the assumption that any impact on the wire excavates a crater whose volume depends on the M/OD kinetic energy and provide a first estimation of the ballistic limit of a tether. However, modelling the impact damage as a crater may not be valid for tethers whose cross section is thin, e.g., tapes. Furthermore, the damage dependence from the impact velocity and impact angle may be significant for tethers with non-axis-symmetric cross sections, such as tapes.

Thin-Tape Tethers

Thin-tape tethers show a different response to space debris with respect to round wires. To consider the different geometry, Kahn (2016) assumed that a thin tape is severed by particles exceeding 1/3 of the orthogonal projection of the tape's section along the debris velocity vector. Francesconi (2016) showed that the shape of the BL equation varies in function of the impact angle (i.e. the angle between the normal to the tether plane and the debris velocity – see **Figure 3.2-11**): the minimum particle diameter which is just able to cut a tape at a given velocity decreases with increasing impact obliquity up to a certain angle above which the damage is reduced due to early debris fragmentation triggered by shock waves propagating into the material. As a result, the BLE of a thin paper is non-monotonic with respect to the impact angle.

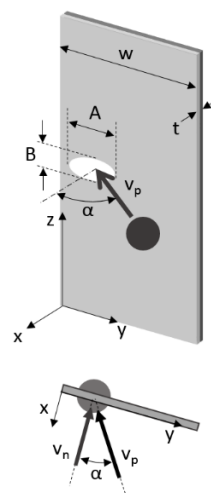


Figure 3.2-11: Tape tether reference geometry

Figure 3.2-12 shows the ballistic limit of an Al-1100 tape tether as function of the impact angle α for different values of the impact velocity v_p . In the same figure, the BLE is compared to the classic assumption stating that for a round wire with the same cross-section w (i.e., the wire diameter) a particle with size around 1/3 of the tether diameter is enough to cut it (black line).

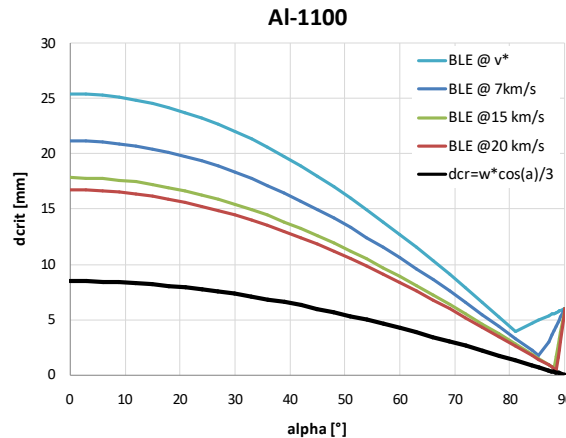


Figure 3.2-12: Piecewise BLE for Al-1100

The BLE in the figure indicates that there is a minimum value of debris velocity v^* (~3 km/s for Al-1100) below which no critical damage is possible and, furthermore, there is a minimum velocity-dependant value d^* of debris diameter below which no critical damage is possible. This feature of BLE sets a minimum particle diameter for risk assessment, e.g., for a 25 mm wide and 0.05 mm thick Al-1100 tape, d^* is between 0.3 and 0.6 mm for debris and between 0.2 and 0.4 mm for meteoroids, and this may exclude a large part of the flux from risk computations.

3.2.4.6 Tethers and Fragments as Hazards to other Spacecraft

Because of their large “effective collisional cross-section”, intact tethers and tether fragments represent an unusual impact hazard to other spacecraft. The effective collisional cross-section is determined by the length of the tether and the average size of the spacecraft. These combine to produce an “interaction area” greater than the tether area by 3 to 4 orders of magnitude. The impact hazard is also a function of altitude. Free tethers have a large area-to-mass ratio that accelerates the decay of their orbits if they experience atmospheric drag. Therefore, the orbital lifetimes will be lower thus reducing the collision risk. On the other hand, a tether attached to a payload will have a much smaller area-to-mass ratio. Consequently, the orbital life will be longer and the collision risk will be greater.

Because many tether materials are invisible to radar, tracking free tethers or tether fragments by ground-based radar networks will be almost impossible. When trackable end-masses are attached, or if the tether contains conducting elements, the deviation of the tether motion from that expected of a “point mass” in orbit may make predictions for collision avoidance a very difficult problem.

3.2.4.6.1 Area Presented and Volume of Space Threatened

The area of a tether may be simply computed as length times diameter. Assuming a zenith-nadir radial orientation of the tether, the portion of space swept by the tether on any given orbit is a ring in the altitude range r_1 to r_2 , where r_1 is the geocentric radius of the lower end of the tether, and r_2 is the radius of the upper end. Matney *et al.*, 2000, developed a method of computing collision rates between tethers and catalogued objects, utilising the radial probability distribution (due to Kessler) for a Kepler orbit:

$$P(r) dr = (r dr) / \{ \pi a [(r_A - r)(r - r_P)]^{1/2} \} \quad r_P \leq r \leq r_A \quad [3.2-39]$$

$$= 0 \quad r < r_P \text{ or } r_A < r \quad [3.2-40]$$

where r is the radius from the centre of the Earth to the catalogued object, r_A is its apogee radius, r_P is its perigee radius, and a is its semimajor axis. The fraction of time the object spends between r_P and r_A is given by:

$$F(r_1, r_2) = \int_{r_1}^{r_2} P(r) dr. \quad [3.2-41]$$

Assuming a randomly oriented argument of perigee of the satellite, and an angle between the satellite orbit plane and the tether orbit ring of γ , then the crossing angle of the satellite with respect to the tether, β , is given by:

$$\beta = \tan^{-1} \left[\frac{v_s \sin(\gamma)}{v_T - v_s \cos(\gamma)} \right] \quad [3.2-42]$$

where v_s is the satellite velocity and v_T is the tether velocity. In the frame of the tether, a satellite of diameter D can intersect the tether over a length δ at the ascending and descending points along the tether orbit, where δ is given by:

$$\delta = D / \sin(\beta). \quad [3.2-43]$$

The satellite – tether collision rate is given by:

$$R(\gamma) = F_s(r_1, r_2) [(\delta / 2\pi r_T) (2/\tau_s)] \quad [3.2-44]$$

where r_T is the tether orbit radius, and τ_s is the satellite orbit period. In other words, the probability of collision each time the satellite crosses the tether orbit is the ratio of δ to the tether orbit circumference, times the fraction of time the satellite is at the tether-crossing altitude, and this occurs twice per orbit. A further complication is introduced by the differential nodal regression of the satellite and tether orbits, which is a function of their inclinations, i_s and i_T , and the difference between their ascending nodes, $\Delta\Omega$:

$$\cos(\gamma) = \cos(i_s) \cos(i_T) + \sin(i_s) \sin(i_T) \cos(\Delta\Omega). \quad [3.2-45]$$

Because $\Delta\Omega$ is evenly distributed, the average collision rate can be found by integration:

$$R = \frac{1}{2\pi} \int_0^{2\pi} R[\gamma(\Delta\Omega)] d(\Delta\Omega). \quad [3.2-46]$$

Cooke *et al.*, 2000, applied Matney's method, convolved with publicly available orbit catalogue data for 8,398 objects on or near December 6, 2000. They defined an "encounter" as the passage of any portion of a 20 km tether within a radius of 500 m of a catalogued object, and computed

the following statistics, assuming a circular orbit for the tether centre of mass at the stated altitude and inclination:

Tether Orbit Altitude	Inclination / deg	Encounters / Year
400 km	28.5	9
	51.6	10
	88.0	16
800 km	28.5	166
	51.6	187
	88.0	296

Table 3-10: Statistical estimate of encounters/year between a 20 km tether and a catalogued object

Cooke *et al.* also applied a "brute force" method, numerically integrating two selected tether orbits (at 400 km and 800 km) and the orbits of that portion of the catalogued population that could intersect them. They compared computed positions over a specified range of times, and when a close approach was found, drastically cut the integration time step to examine the details of the encounter. The advantage of this process is that these are "real world" calculations against existing objects, and the approach circumstances are known to within the propagator precision. The disadvantage is the lengthy time required for the computations (~5 hours on a 733 MHz personal computer).

For the 400 km altitude tether at 28.5 deg inclination (other orbit parameters selected at random) they found two encounters with the same object – the Cosmos 1116 rocket body – which passed about 4 km away from the tether at the ascending node of the orbit, then to within 500 m of the tether at the subsequent descending node. While this is an unusual circumstance, it demonstrates that this type of encounter *can* happen.

The second example was a tether in an 800 km circular orbit at 51.6 deg inclination. Here the catalogued object population is much denser than at 400 km, due to the weakness of the drag deceleration and the usefulness of particular orbits at this altitude. There were twelve approaches to within 10 km during the *10-day simulation interval*, two of which were to within 500 m. Five of these events were close passes to active satellites (two DMSP's, two other DoD, and one science satellite).

Cooke *et al.* conclude as follows: (a) Both the Matney expressions and the brute force method indicate that a 20 km tether will have encounters to within 500 m on the order of once per month at 400 km altitude (see **Table 3-10** and every few days at 800 km: approximately 430 catalogue objects orbit near 400 km, while over 2100 (~25% of the catalogue) orbit near 800 km. (b) Some of the encounters will be with active satellites, which constitute about 6% of the catalogue. (c) The value of some of these assets, e.g., the ISS, will necessitate *collision avoidance manoeuvres*, either by the (propulsive) tether or the active satellite. Without collision avoidance, the odds of a tether striking an active satellite (assumed to have a 10 m² cross-section) are approximately 1% per year at 400 km, rising to 11% per year at 800 km. Tethers could require ISS to manoeuvre as often as once a month (see the next section).

This finding of the need for collision avoidance manoeuvres introduces a great deal of complication and uncertainty because, currently, ground-based surveillance and tracking assets

are unable to reliably determine the orbits of tethers, for a variety of reasons. So, collision avoidance by valuable assets, such as ISS, may not be reliably possible unless tether missions take steps to enhance their visibility / trackability.

3.2.4.6.2 Duration of Threat vs. Initial Altitude

One important consideration when examining the duration of the threat that (non-maneuvring) free tethers may pose to other satellites is the much shorter on-orbit lifetimes they may have when compared to other satellites when they are in low altitude orbits and subject to atmospheric drag.

The expression for drag deceleration on a satellite is usually given as

$$a_D = -\frac{1}{2} \rho(h) V^2 \left(\frac{A C_D}{m} \right) \quad [3.2-47]$$

where $\rho(h)$ is the atmospheric density as a function of altitude, V is the satellite velocity, A is its area, C_D its drag coefficient (typically assumed to be 2.2 in these hypersonic cases), and m its mass. This equation is used in calculations of drag on ordinary satellites, which can be considered to be point masses at a single altitude, h . However, tethers cover a range of altitudes, and so one must account for the variation in atmospheric density from the lower end to the upper end. If one does not have a detailed tether dynamics and atmospheric model, an approximation can be made by assuming the local atmospheric density to vary exponentially, and using this treatment to create an effective tether area, A_{eff} :

$$A_{eff} = \int_{-l_1}^{l_2} w_0 e^{-l/H} dl \quad [3.2-48]$$

where w_0 is the actual tether width, l_1 is the distance from the tether's lower end to its centre of mass at h , l_2 is the distance from the centre of mass to the upper end, and H is the atmospheric density scale height [Evans, 1995]. Then the tether can be assumed to occupy an area of A_{eff} at h , and the previous equation can be used to calculate the deceleration.

For low density synthetic tether materials the ballistic coefficient, $C_B = A_{eff} C_D / m$, will be large, leading to a high value of a_D , and a short on-orbit lifetime, if $\rho(h)$ is at all appreciable. Denser materials, such as braided copper wires, will have smaller C_B 's and will endure longer at a given altitude. Orbital lifetime will depend on orbital inclination, as well as altitude, since this parameter affects the atmospheric density profile through which the tether passes.

As an example, assume a tether is 10 km long and 2 mm in diameter, with a linear density of 3 g/m (total mass of 30 kg); if the atmospheric density scale height is 40 km, the tether's effective area will be 22.722 m², and the **Figure 3.2-13** shows its orbital lifetime as a function of initial centre of mass altitude and orbit inclination.

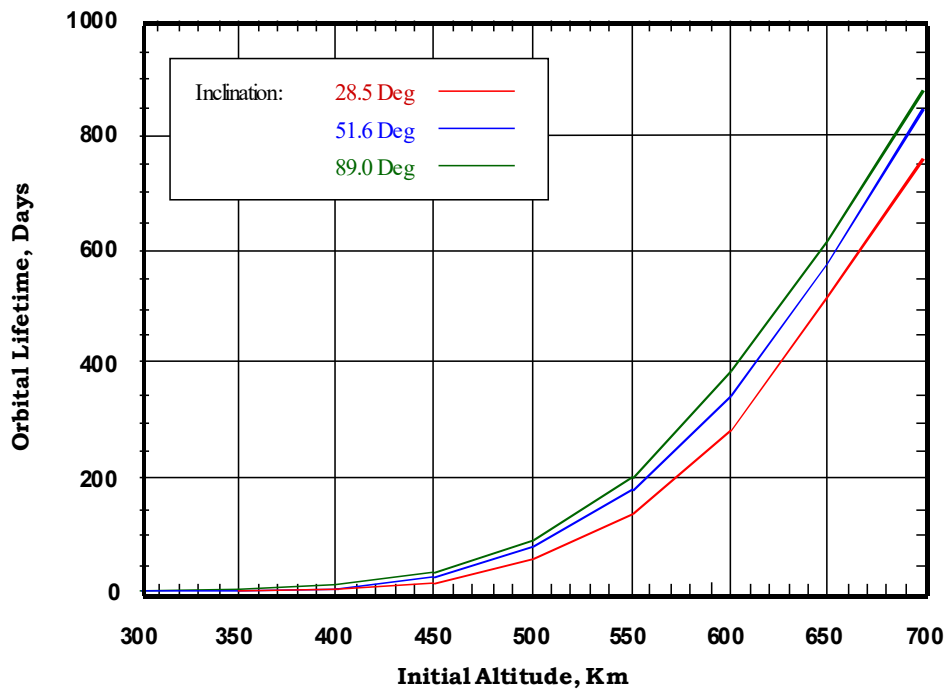


Figure 3.2-13: Tether orbital lifetime as a function of the altitude and orbit inclination

Lifetimes continue to increase rapidly above 700 km owing to the exponentially decreasing atmospheric density. The atmosphere model used to generate these curves is the Jacchia 1970 model [Jacchia, 1970], and the simulation was run for starting conditions of May 1996, i.e., near the minimum in the latest solar cycle, so the lifetimes given are near the maxima to be expected.

It should be noted that the preceding discussion is applicable only to tethers flying alone (i.e. severed tethers). Thus, the short orbital lifetimes presented in **Figure 3.2-13** were obtained for an object with a high area-to-mass ratio (i.e. $22.7 \text{ m}^2 / 30 \text{ kg} = 0.76 \text{ m}^2 / \text{kg}$). In the case where a tether is attached to a payload, the area-to-mass ratio of the system (and the decay rate due to air drag) would be smaller by about one order of magnitude, and so the lifetimes would be much longer.

3.2.4.6.3 Hazards to Deploying Spacecraft

Tethers are not only a collision hazard to other independent spacecraft, but since they may be severed during or after deployment, they may re-contact or entangle their parent spacecraft as well. Welzyn & Robinson, 1995, studied both the probability of sever by M/OD objects and the dynamics of the recoiling tether. Using a simple model of the recoiling tether acted on by gravity gradient forces, they developed several dynamic parameters. Take the example of a small end-mass deployed upward by a tether from a carrier vehicle, with the tether having linear density λ and stiffness AE . The tether will be under tension:

$$T = AE (l - l_0) / l_0 \quad [3.2-49]$$

where l is the current length of the tether and l_0 is its unstretched length. If the tether is cut at position $L < l$, a tension unloading wave will travel back along the tether toward the deploying vehicle at the acoustic speed:

$$c = \sqrt{AE / \lambda} \quad [3.2-50]$$

and the remnant recoil speed will be:

$$V = T / \sqrt{\lambda AE} \quad [3.2-51]$$

plus or minus any deploy / retrieval speed. The amount of tether fragment remaining above the attachment point to the carrier vehicle at time t after the cut is given by:

$$s(t) = L + \frac{3}{4}\Omega^2 L t^2 - Vt. \quad [3.2-52]$$

Here Ω is the angular rate of the carrier spacecraft in its orbit. The amount of slack accumulated at or below the attachment point is $L - s(t)$. For any given tether deployment configuration there will be some cut position below which all the attached tether will hit the carrier vehicle, and above which gravity gradient forces stop the recoil and pull the tether back out. This stabilisable length is given by:

$$L^* = \frac{\sqrt{3}}{3\Omega} V. \quad [3.2-53]$$

For breaks occurring above L^* the maximum amount of slack accumulated before pull-back will be:

$$S_{\max} = \frac{V^2}{3\Omega^2 L}. \quad [3.2-54]$$

Considering the case of "outbound" severed tether fragments, there is a possibility of re-contact of the tether fragment (and any attached end-mass) with its carrier vehicle on subsequent orbits or partial orbits. The probability of re-contact depends on the libration-, deployment / retrieval-, and recoil-velocity contributions to the orbit of the outbound remnant, and the relative C_B 's of the remnant and carrier vehicle. Especially in the case of a manned carrier vehicle, it would be prudent to plan a collision avoidance manoeuvre in case of a sever during deployed tether operations.

3.3 Subsystem Ballistic Limit Equations

3.3.1 Propulsion

3.3.1.1 Propulsion Subsystem Design

In the broadest sense, space propulsion systems provide four functions [Larson & Wertz, 1992]:

1. Lift the launch vehicle and its payload into low-Earth orbit or transfer orbit.
2. Transfer payloads into higher orbits or into trajectories for planetary exploration.
3. Provide thrust for attitude control and orbit corrections.
4. De-orbit or re-orbit at the end of mission.

The propulsion subsystem of launch vehicles has in general a very short operational life in orbit. Upper stages with high perigee orbits at the end of the launch present a risk for the environment only if their pressure vessels are not passivated. The function of launch vehicle will not be discussed further here.

The following types of propulsion subsystem are used on board spacecraft and space vehicles:

- Cold Gas. An inert gas is stored at high pressure and fed through a regulator to a number of small thrusters, primarily for attitude control purposes.
- Monopropellant hydrazine. Stored as a liquid under pressure, anhydrous hydrazine decomposes exothermically producing a hot gas that expands through a thruster nozzle. The subsystem is used for North-South station-keeping on geostationary spacecraft and for attitude and orbit control on low earth orbit spacecraft.
- Bi-propellant monomethyl hydrazine (MMH)/nitrogen tetroxide (N_2O_4). A technically complex, high-performance subsystem that combines orbit acquisition and AOCS functions.
- Solid propellant apogee motor. Circularises the orbit of a geostationary spacecraft using a high thrust, short duration burn from a solid propellant apogee boost motor.
- Electric Propulsion Systems. Externally provided electric power is used to accelerate a fluid to produce useful thrust.

The main propulsion subsystem elements are:

- Propellant tanks. Generally used to store propellant under pressure.
- Pressurant tanks.
- Thrusters. Mounted externally of the spacecraft to enable the full range of required attitude and orbit manoeuvres.
- Pipes. Used to distribute propellant from the tanks to the thrusters. They can be distributed both inside the spacecraft and externally, depending on the particular spacecraft design. Stainless steel and titanium are typical materials used in their construction. Pipework is often covered in MLI and has heater lines mounted on its surfaces to ensure that the propellant does not freeze.
- Pressure regulators.
- Valves.
- Sensors.

- Electronic units.

As an example, the ATV propulsion sub-system is sized to provide vehicle orbital and attitude control manoeuvres as well as ISS reboost and ISS attitude control assistance. It is a bi-propellant system using MON and MMH. The 8 identical titanium surface tension propellant tanks are pressurised with helium stored in two high-pressure tanks (310 bars) and regulated by pressure regulators down to 18 bar. The propellant tanks can accommodate up to 6960 kg of propellant, for main propulsion and reboost needs. The major part of the subsystem is housed in the equipped propulsion bay, which is part of the ATV Spacecraft (S/C). The various components are located in dedicated compartments.

The large velocity increments are performed using four Main Engines; the main characteristics are a thrust level of 490 N each and a specific impulse of more than 310 s.

The attitude control of the ATV, and all the manoeuvres for rendezvous with the ISS, are performed using 28 Attitude Control Thrusters with a thrust level of 220 N each and a minimum impulse bit (MIB) of less than 5 Ns (Newton second). Each thruster is hydraulically linked to the opposite unit. If a thruster fails either to open or to close, it is isolated by the latching valve together with the opposite unit, but the thrust function can still be accomplished.

The subsystem contains also the propulsive drive electronics, which is based on 4 non-redundant channels, each of them controlling one quarter of the propulsion and reboost subsystem valves and sensors.

3.3.1.2 Damage Modes

Tanks and pipes located externally of the main body structure may be especially vulnerable to primary impact damage from the debris flux.

The cloud of high and low velocity ejecta particles produced when there is perforation of the structure presents the highest risk of mechanical damage to propulsion system equipment located inside the spacecraft body. In this case, internally located tanks and pipes are at risk, particularly if they are near to vulnerable body faces.

An impact on a pressurised structure such as a propellant tank can weaken the structural material, thus making it more susceptible to failure if subjected to further impacts. An impactor can also generate a shock wave in the propellant and raise the internal tank pressure. This can lead to a range of failure modes from leakage to a burst tank (Section 3.2.3 on Pressure Vessels).

A non-perforating impact on a tank or pipe may release spall ejecta that could contaminate the propellant and any associated pumping systems. If the level of contamination is severe, there may be complete and permanent loss of AOCS.

A puncture falling below the burst threshold of a tank can cause propulsive thrusts that exceed the structural constraints of the tank and lead to loss of attitude control, and therefore a shortened mission life. Tests have shown that a relatively narrow margin exists between the simple perforation and catastrophic rupture of a pressurised wall under hypervelocity impact.

Clearly, the most damaging scenario involves a catastrophic burst of a tank resulting in immediate loss of mission and possibly an explosive break-up of the spacecraft.

3.3.1.3 Technological Work on Propulsion Subsystems

Technological work on pressure vessels is reported in Section 3.2.3.

Kinslow, 1970, reports impact testing on tubular targets. The results show that the penetration depth in aluminium is substantially decreased for a constant material thickness (11.3 mm) as the inside diameter is decreased from infinity (flat target) to 12.7 mm. Below this value little change in penetration is observed. The ability of the circular target shape to sustain impact damage stems from the fact that shock propagation through the circular section is affected by more free surface. Consequently, the rarefaction waves which act to diminish the intensity of the transient pulse react more quickly, thus weakening the shock and diminishing its ability to perforate the target or to cause spall. The beneficial effects of having an inner liner (steel liner in an aluminium tube) in preventing spallation is also experimentally shown.

3.3.1.4 Shielding Options

Options for protecting tanks and pipes include:

- Varying the properties of any structure protecting the tanks / pipes. If the tanks / pipes are surrounded by spacecraft structure, then structural enhancements can if necessary provide improved protection.
- Varying the properties of any blankets protecting the tanks / pipes. MLI blankets are commonly wrapped around tanks and pipes to provide the required insulation. If extra protection is identified as a requirement late in the design, then the MLI can be enhanced with layers of Beta cloth or Kevlar. Care must be taken to ensure that temperatures stay within acceptable ranges since propellants such as Hydrazine can degenerate if overheated.
- Varying the structure thickness of the tanks / pipes.
- Varying the internal pressure of the tanks / pipes.
- Placing external tanks close together to maximise the benefits of shadowing.
- Improved operations, such as depleting and depressurising exposed vulnerable tanks prior to tanks in less vulnerable positions.

3.3.2 Thermal Control System

3.3.2.1 Thermal Control Subsystem Design

The thermal control subsystem maintains the thermal balance of a spacecraft by ensuring that all equipment operates within acceptable temperature ranges. On unmanned spacecraft the structure itself can act as a radiator and provide one of the main means of radiating excess heat generated by high power equipment inside the spacecraft. To aid the radiation coupling with space, the structure can be coated or covered with materials such as paint, which are chosen because of their thermo-optical properties. Where low-temperature insulation is required (maximum temperature of 120°C to 290°C), the structure is usually covered in thermal blankets such as multi-layer insulation (MLI).

3.3.2.1.1 Radiators

Radiators can absorb or emit heat in order to maintain a satisfactory thermal balance for the spacecraft. High power units requiring heat dissipation can be mounted on or near to the radiator surface, thus ensuring a good conductive coupling. To be effective as radiators of heat, panels of the body structure should face towards space. By choosing suitable values of absorptivity and emissivity, a thermal coating such as paint can optimise the radiator structure's required thermal coupling with space. Other materials include glass secondary surface mirrors, optical surface reflectors, or aluminised / silvered Teflon tape.

Active radiators contain coolant loops to maximise heat rejection capability. The coolant can be single-phase or two-phase (liquid & vapour), either pumped at high-pressure or operating at low-pressure. Active radiators are susceptible to meteoroid/debris impact damage and puncture of the coolant lines contained within the panels, leading to degradation or failure of the heat rejection system. Hypervelocity impact tests have been performed on various radiator panel configurations to assess vulnerability to meteoroid/debris impact and develop ballistic limits [Rhatigan *et al.*, 1990, 1992; Melin, 1990].

Methods to improve radiator survivability include:

1. thickening or toughening the flow tubes in the radiator panel as well as interconnect lines/jumpers,
2. adding one or more redundant flow loops within each panel,
3. including automatic shutoff valves to limit coolant loss given a puncture of the flow path.

Shuttle radiators were modified to add 0.5mm thick aluminium “doublers” over the flow tubes [National Research Council, 1997] (see **Figure 3.3-1**). The doublers increased particle size causing tube puncture from ~0.4mm to 0.6mm diameter (for aluminium sphere at 7km/s, 0°) which has a significant effect on failure probabilities. In addition, automatic flow control valves were added in the Shuttle thermal control system to minimise loss of coolant if a puncture occurs.

NASA active thermal control radiators on the ISS are constructed with enhanced meteoroid/debris protection. The flow tubes are thicker wall, compared to Shuttle design, and are “buried” within the panel as illustrated in **Figure 3.3-2**. This combines to increase the particle

size causing tube puncture to 2mm (for aluminium sphere at 7km/s, 0°). In addition, a primary- and an independent secondary-flow loop alternate throughout the panel, so that radiator function is not completely lost if one loop is punctured.

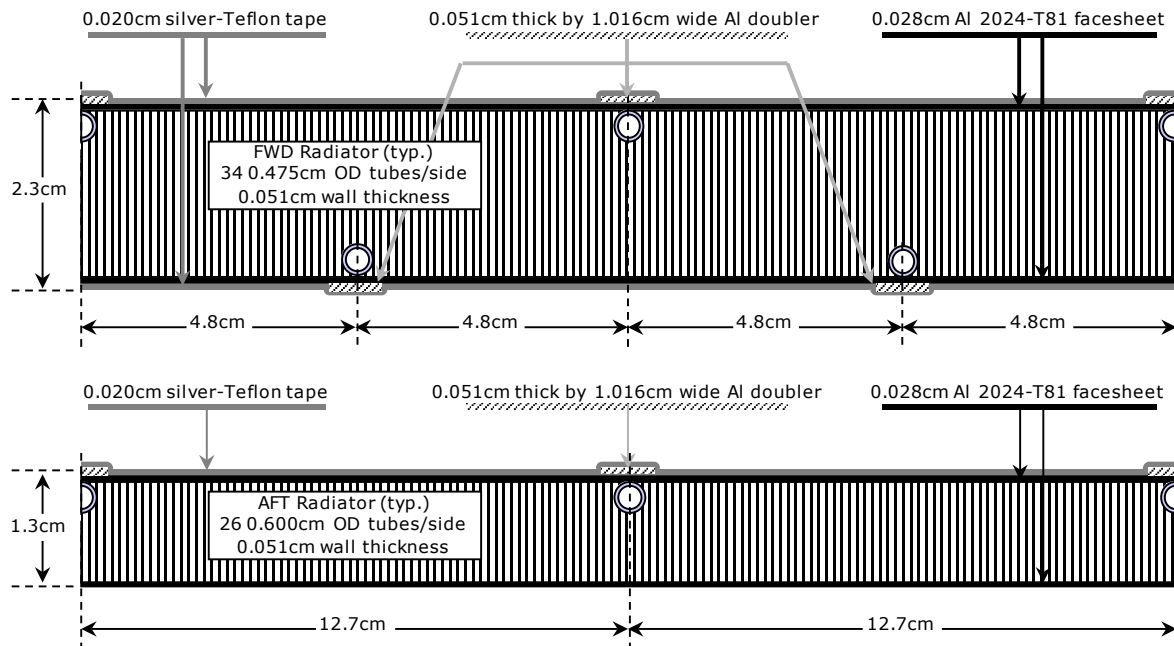


Figure 3.3-1: Shuttle radiator panels after “doubler” modification

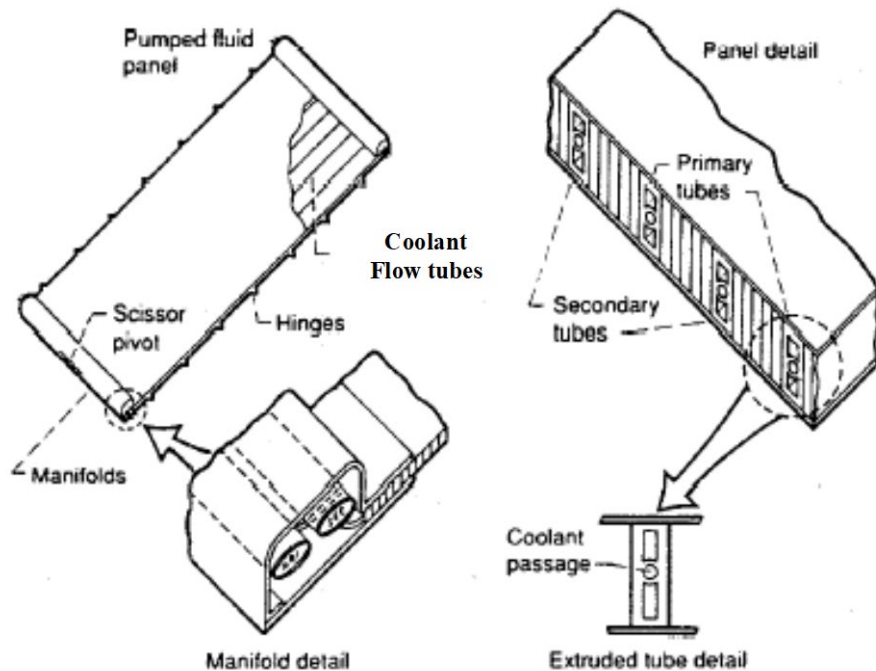


Figure 3.3-2: ISS radiator panel schematic

3.3.2.1.2 Insulators

Insulators ensure that the temperature of a sensitive unit does not fall below an acceptable minimum. Transient temperature changes are minimised because the insulator is a poor conductor and radiator of heat. MLI is the most common form of spacecraft insulator. Typically, it comprises 10 to 20 layers of Mylar interleaved with Dacron net. Either a layer of Kapton or Teflon-impregnated Betacloth covers the outer layers of the blanket. MLI is especially effective since gaps between the blanket layers prevent conduction and trap radiation. It is generally attached to the outer face-sheet of a structure panel, although it can also be fixed to individual units, particularly those that are exposed to space.

3.3.2.1.3 Thermal Coatings

Thermal coatings include paint, silver- and aluminium-teflon tape, and anodisation. Painted surfaces are subjected to spall (detachment) around the impact site, although this may not be very significant for properly prepared and painted surfaces. For instance, Z-93 painted radiator surfaces spalled approximately 2-3 hole diameters around the impact point in one series of hypervelocity impact tests at NASA Johnson Space Center [Rhatigan *et al.*, 1990, 1992]. Silver-teflon tape on honeycomb panels will debond to a similar extent around hypervelocity impact sites [Christiansen *et al.*, 1993, 1998]. Silver-teflon has also exhibited dark rings around impact sites on-orbit, possibly due to long-duration interaction with atomic oxygen on exposed silver surfaces in the delamination zone. This has occurred with certain Hubble Space Telescope (HST) aft-shroud impact sites [Byrne *et al.*, 1998], as well as the silver-teflon blankets on the Long-Duration Exposure Facility (LDEF) [See *et al.*, 1990]. Some anodised aluminium surfaces are also brittle and subject to spallation as exhibited by actual impact spall features found on anodised Shuttle surfaces [Christiansen *et al.*, 1998].

3.3.2.1.4 Fluid Lines

Fluid lines containing fluids, which are hazardous to the crew, like Ammonia cooling lines or propulsion system fuel lines, are almost without exception run outside the pressure shell of manned vehicles, beneath the M/OD shielding. This is done to eliminate the hazard of having leakages of hazardous fluids into the crew compartments.

Lines containing non-hazardous fluids (e.g., O₂, N₂ and water) are also routed inside the pressurised compartments and therefore have the added protection of the external shell against space debris.

External fluid lines will nominally be located under the M/OD protection and also be covered with necessary thermal protection (MLI).

From a reliability point of view fluid lines are considered as primary structure, i.e., the risk of pipe failure is judged to be negligible. However, all fluid systems will contain other equipment (e.g., valves, heat exchangers, controllers, etc) that may fail. For these reasons, it is necessary to design adequate redundancy into the system to ensure proper operation after a failure, be it from equipment failure or line leakage. Fluid systems will have shut off valves and redundant paths so that isolation and redirection of the flow is possible after a failure. This is very important as

repairing or replacing fluid lines located externally under the M/OD and MLI by EVA will prove very difficult if not impossible.

Survivability against debris impacts can be ensured by putting adequate shielding in critical locations for extra piping protection and by putting in redundant piping with remote valve control to ensure functionality after failure. Capability to perform fluid refilling on orbit may be mandatory for certain systems in order to restore the system after repair.

3.3.2.2 Damage Modes

The shock from an impact on a surface coating such as paint can remove material well beyond the crater diameter. This damage may combine with other environmental effects such as atomic oxygen and ultra-violet radiation to create more damage than the individual effect could cause.

Multiple small impacts on coatings such as paint can affect the total available surface area, thereby altering radiative and conductive properties, and compromising the thermal balance of underlying components. For example, analysis of the LDEF spacecraft revealed that the ejecta associated with impacts removed approximately 5% of the paint on space exposed surfaces.

The damage from a penetrating particle can potentially affect the thermal control performance of honeycomb structure panels, which are often used as radiators on unmanned spacecraft. Impact burst or blast damage to the honeycomb core will reduce the localised thermal control in all three directions through the structure. If alternative heat flow paths do not exist, then hot or cold spots will result.

An accumulation of impacts on a radiator structure may result in equipment items (mounted on or near the radiator) operating outside acceptable temperature ranges, ultimately leading to their failure. Depending on the importance of the equipment, and its level of redundancy, the consequences for the mission may range from minor to catastrophic. Furthermore, an accumulation of impacts causes a change in the local heat distribution thereby giving rise to additional thermal stresses in the structure.

MLI blankets can also be badly damaged by repeated impacts from small size particles, thereby reducing the thermal insulation properties and causing cold spots that may ultimately lead to equipment failure.

3.3.2.3 Shielding Options

For MLI blankets covering the structure of an unmanned spacecraft, the following shield enhancements might be considered [Turner *et al.*, 2000], as shown in **Table 3-11**.

Shield type		Predicted influence on shield performance
1	Use MLI + front layer (Nextel, Kevlar, Betacloth, Al mesh)	MLI acts as a multi-shock shield. Additional front layer disrupts projectile
2	Use MLI + rear layer (Nextel, Kevlar, Betacloth, Al mesh)	MLI acts as a multi-shock shield. Additional rear layer contains / disrupts debris cloud
3	Use MLI + intermediate layer (Nextel, Kevlar, Betacloth, Al mesh)	MLI acts as a multi-shock shield. Additional intermediate layer disrupts debris cloud
4	Use MLI + spacer rods	MLI offset equivalent to a multi-shock bumper shield

Table 3-11: MLI shielding options.

A number of factors affect the options listed in **Table 3-11**. When enhancing MLI, a layer of strong fabric can be placed between the MLI and structure but not in front of the MLI. This is primarily for thermal reasons, although other effects such as degradation due to atomic oxygen and ultra-violet are also important to consider. The fabric can also be interleaved with the inner Mylar layers and manufactured as part of the blanket. The areal density of a typical 20 layer blanket is 0.6 kg/m² and AF62 Nextel is 1 kg/m², so the total mass of the enhanced MLI may require different attachment studs.

The MLI blanket could also be placed on spacer rods and effectively be used a bumper, although this may require the use of additional inserts to attach the rods. Tests have shown that MLI acts as a multi-shock shield, and so the spaced MLI configuration may be quite effective at disrupting a projectile (**Figure 3.3-3**). Splitting the Mylar layers into multiple blankets can further enhance the impact protection without any loss of thermal performance. Kapton thickness can also be increased at no cost to thermal performance.

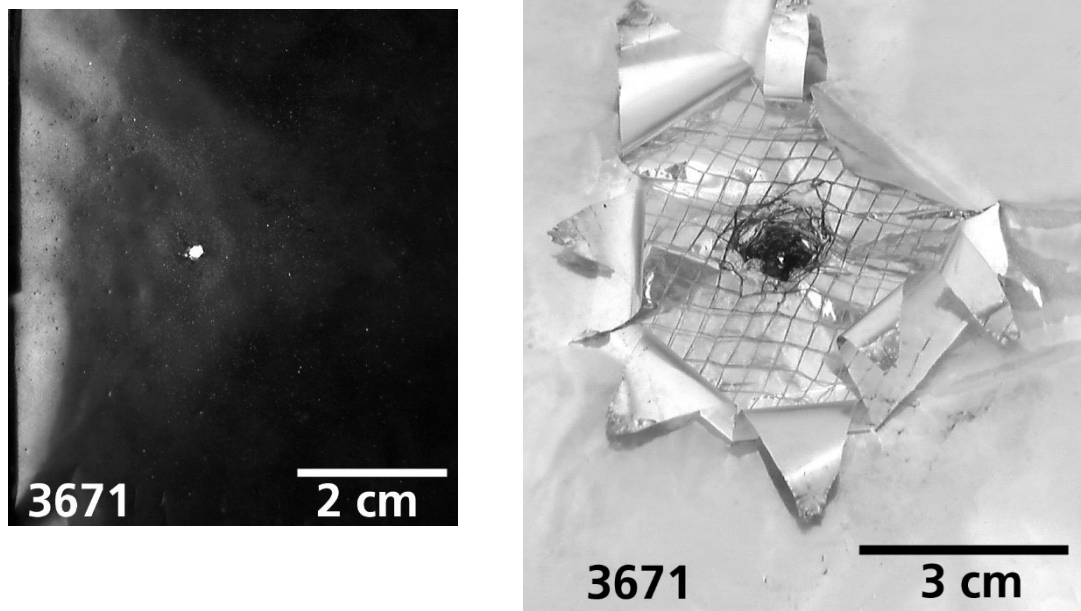


Figure 3.3-3: Impact damage on MLI-top and rear side [Lambert et al., 2001]

For an unmanned spacecraft late in the design phase (when hardware exists), consideration should be given to implementing one of the following on any MLI-covered vulnerable (e.g. RAM-facing) surfaces [Turner et al., 2000]:

- Make the MLI blankets on the vulnerable faces at least 20 layers thick.
- Use two 10-layer blankets and separate them, e.g. by 5 to 10 mm.
- Add Betacloth or aluminium mesh to a 20-layer blanket, just underneath the external thermal control layer. Add Kevlar in the middle of the blanket (between the 10th and 11th layers) to further enhance the MLI.
- Use two 10-layer blankets separated by 5 to 10 mm. Add Betacloth or aluminium just underneath the external thermal control layer of the outer blanket. Kevlar can be added to the outer layer of the inner blanket.

The chosen option will depend primarily on the mass budget and/or survivability requirement. A secondary factor is cost, which depends on the number of MLI layers.

3.3.2.4 Summary of Experimental Data

Impact tests onto MLI + component systems are summarised in **Table 3-12** (taken from a literature review conducted in Turner *et al.*, 2000). Projectiles are aluminium spheres. The results show that MLI can play a significant role in increasing the tolerance to hypervelocity impact.

System	Materials	t mm	# tests	θ (°)	d _p mm	V km/s	Comments
Mariner 1971	25 layers Mylar (1/4 mil) + 1 mil Teflon	-	4	0	0.79	4-7	Back-wall not damaged at 13 mm spacing
Hubble MLI	3 sub-blankets	3 x 3.3	7	0	0.41, 0.82	4-7	At higher velocities, performs better than equivalent Al plate
MLI	Radarsat	-	1	30	1	7.6	Depth of penetration 0.5mm
MLI + Nextel	Radarsat MLI + 1 Nextel AF10	-	1	30	1	7.3	Depth of penetration 0.2 mm
MLI + Mesh	Radarsat MLI + 2 or 3 mesh layers	-	2	30	1	7.6 – 7.7	Depth of penetration 0.2 and 0.4 mm
MLI (1 layer)	MLI + 2mm Al 2219 plate	>2	2	0	1.0 – 1.2	6	BL between impactor parameters
MLI (1 layer + spacing)	MLI + 2mm Al 2219 plate with 10mm space	>12	2	0	1.2	5.5 – 5.9	BL between impactor parameters
MLI (1 layer + spacing)	MLI + 1mm Al 2219 back-wall with 25mm space	>27	2	0	1.1 – 2.0	7	BL between impactor parameters
MLI (2 layers)	MLI + 2mm Al 2219 plate	>2	2	0	1.5 – 1.7	6	BL between impactor parameters
MLI (3 layers)	MLI + 2mm Al 2219 plate	>2	4	0	1.5 – 2.0	6	BL between 1.7 and 1.8 mm
MLI	MLI + 1mm Ti6Al4V back-wall with 25mm space	>26	6	0	1.0 – 2.0	6.5 – 7.0	BL between 1.2 and 1.3 mm
Basic space suit	Nomex, Mylar, Dacron, Nylon	-	36	0-60	0.3 – 1.4	5 – 7	BL > 0.5 – 0.6 mm, not strongly angle dependent
Space suit glove finger	Teflon fabric, Mylar, Dacron, Rucothane	-	6	0	0.2 – 0.5	5 – 7	BL > 0.3 – 0.4 mm
Space suit glove gauntlet	Teflon fabric, Mylar, Dacron, Nomex, Nylon	-	3	0, 60	0.8 – 1.0	6 – 7	BL > 1.0 mm

Table 3-12: Summary of MLI and enhanced MLI hypervelocity impact data

The MLI + Teflon-impregnated Betacloth configuration was used to shield the fuel tanks on the Mariner Mars mission. 25 layers of Mylar + outer layers was offset from the tanks by a variable

spacing. The MLI on the Hubble Space Telescope comprised three layers of sub-blankets with a total equivalent thickness of 0.36mm aluminium. The multiple layers were observed to provide better penetration performance than the equivalent thickness of aluminium for impacts at ~7 km/s (projectile diameter < 0.8mm, and the whole blanket was not perforated). This may be because the MLI acts as a multi-shock shield, progressively disrupting and shocking the projectile as it passes through the layers. One advantage of MLI is that it does not produce a large number of fragments, thereby reducing contamination.

MLI configurations, which have been enhanced with additional material layers, have been tested for the Radarsat [Warren & Yelle, 1994] and Iridium satellites [Hyde, 2001]. The Radarsat tests investigated the response of MLI enhanced with one layer of Nextel AF10, and 2 or 3 layers of aluminium mesh. The Nextel AF10 and 3-layer mesh configurations provided equivalent shielding performance. The ballistic limit of the Iridium MLI is enhanced by 60%, by projectile diameter, with the addition of two layers of Nextel AF10 just behind the Betacloth. NASA has, in some cases with its ISS partners, investigated and implemented a number of toughened MLI configurations for protecting wire and cable bundles, fluid lines, and modules on Space Station [Friesen, 1996; Christiansen, 1999; Lyons, 2001a, 2001b, 2001c].

Interleaved layers of Mylar, Dacron, and Teflon, with nylon as the internal layer and Nomex or Teflon fabric as the outer layer, provide the hypervelocity impact resistance of space suits [Friesen & Christiansen, 1997; Christiansen *et al.*, 1999; Burt & Christiansen, 2001]. The materials provide better resistance than the equivalent areal density of aluminium, again due to the multi-shock effect.

3.3.3 Power

3.3.3.1 Power Subsystem Design

The power subsystem on a typical unmanned spacecraft comprises primary and secondary energy sources and a power control / distribution network [Larson & Wertz, 1992].

3.3.3.1.1 Solar Panels

Solar panels are the primary source of power generation on most unmanned spacecraft. They provide electrical power to the entire spacecraft when it is not in the eclipse phase of its orbit. A solar panel comprises an assembly of many thousands of solar cells connected to provide direct current power. Each cell typically comprises a semiconductor p-n junction, a cover glass for environmental protection, and a backing substrate such as Kapton, all of which is mounted onto a (honeycomb) panel structure. The panels can be either mounted to the body of the satellite or deployed as arrays. Body mounted panels are usually employed on spin stabilised spacecraft, whereas deployable arrays are used on 3-axis stabilised spacecraft.

3.3.3.1.2 Batteries

Batteries are the secondary source of power generation on unmanned spacecraft. They provide electrical power to the entire spacecraft when it is in the eclipse phase of its orbit. Additionally,

batteries can help to recover a spacecraft experiencing a pointing anomaly, by providing power if the solar panels are not pointing towards the sun.

All spacecraft in an Earth orbit, regularly immersed in the Earth's shadow, need batteries. Batteries are pressure vessels (except for the tiny button-type sort), which typically are kept outside pressurised, manned modules because of the necessary safety precautions. Rupturing batteries constitute a safety hazard because of release of shrapnel and the toxic chemicals they contain. Pressure vessels, even those designed for leak before rupture from a fracture-control point-of-view, can potentially burst violently if the pressure shell is penetrated by meteoroid/debris impact. One sure method of protection is to never let a particle even scratch the surface, within the limits asked for by the PNP requirement. This method is neither elegant nor mass efficient, though. On unmanned spacecraft, batteries are normally located inside the main body, which provides a measure of protection from meteoroid/debris impact, or they are positioned on a space facing part of the structure in order to enable heat dissipation.

3.3.3.1.3 Power Control / Distribution Network

The main units in a power control / distribution network are:

- **Harness.** Provides electrical connectivity between all subsystem units and payload equipment. Additionally, it provides subsystems with electrical bonding and electromagnetic screening. The majority of the harness is distributed throughout the interior of the spacecraft. Large groups of wires are usually bunched together during the assembly and integration phase.
- **Array regulator.** Controls the variable amounts of power required by a spacecraft during its mission by switching in or out segments of the solar array.
- **Battery management unit (BMU).** Monitors the battery's temperature, voltage and pressure. It also acts as the interface between the power subsystem and the data handling subsystem, and provides control inputs to the charge regulation of the batteries.
- **Battery charge regulator (BCR).** Provides a constant current charge of the battery during sunlight operation.
- **Battery discharge regulator (BDR).** Supplies a constant current to the spacecraft bus.
- **Power control and distribution unit (PCDU).** Provides monitoring and protection for the bus current.
- **Power conversion unit (PCU).** Supplies the individual voltage / current characteristics required for loads.

3.3.3.2 Damage Modes and Hypervelocity Impact Test Results

3.3.3.2.1 Solar Panels

Solar panels are exposed to meteoroid/debris impact damage. The damage can be minor and localised, e.g. to individual cells, or it can be more serious such as failure of a string of cells. Impacts may result in cut conductors within panels or between cells, leading to open-circuits. Damage to cells and conductors can also cause short-circuits if damage to insulating layers (or projectile residue) creates a contact between a panel conductor and ground or conducting-substrate. With bypass-diodes and redundant wiring, open-circuits will often lead to either no

appreciable or a small loss of electrical generation. An impact on a brittle material such as a solar cell coverglass can lead to concentric and radial cracks that extend much further than the crater, that can locally increase sunlight reflection from the affected cell(s) surface with an attendant decrease in power generation. Results and damage equations resulting from hypervelocity impact (HVI) tests on HST solar panels are described in Section 3.2.2.3, and Mir solar panels in [Burt & Christiansen, 2001].

Careful design of the solar cells and panels is needed to ensure that primary damage from individual impacts does not cause failure of one or more strings of cells. Multiple impacts on panels over the mission life may contribute to the gradual degradation in power generation that is normally experienced from environmental factors. Typically, solar arrays are over-sized by a few percent to compensate for power loss due to meteoroid/debris impacts over their lifetime.

A particle impacting a solar array pointing / steering mechanism could release spall from the housing wall into the motor casing thereby causing it to jam. Such a failure will result in the array pointing away from the sun, thereby severely reducing the power generation capacity required by the spacecraft, and ultimately limiting the effectiveness and life of the mission.

3.3.3.2.2 Batteries

The cloud of high and low velocity ejecta particles produced when there is perforation of the spacecraft structure presents the highest risk of mechanical damage to power system equipment located inside the spacecraft. Specifically, the batteries, harness, etc... are at risk, particularly if they are mounted directly on or near to vulnerable body faces.

Impact testing of a nickel-hydrogen (Ni-H₂) battery cell design for Space Station showed the cells leak from certain hypervelocity impacts, rather than explode [NASA, 1992]. The impacted cells were development models of Ni-H₂ cells used in energy storage systems of NASA electrical power system on the International Space Station. The cells were Inconel 718 pressure vessels, nominally 0.64mm thick, cylindrical ~30cm long by 9cm diameter with hemi-spherical end-domes. The cylindrical portion of the vessel is wrapped with a thermal sleeve consisting of an outer 3.8mm thick aluminium (Al 6063-T6) layer, backed with a 0.2mm thick glass-silicon rubber layer. The cells are pressurised with hydrogen gas at 900 psi (6.2MPa) under nominal full-charge operating conditions, as well as during the HVI tests. The Ni-H₂ cells are contained within an ORU box consisting of 12.7mm thick aluminium 5056-H39 honeycomb and 0.4mm thick facesheets of aluminium (Al 7075-T73). The gap between the inside of the box cover and battery cell varies, but is not less than 2cm. Ten HVI tests were performed, 5 on simulated unpressurised targets, and 5 on pressurised and operating Ni-H₂ cells. Tests on the cylinder portion of the cell, with thermal sleeve, included a test with a 4.8mm diameter Al2017-T4 spherical projectile (at 5.85 km/s and 0°) which penetrated the honeycomb and thermal sleeve, denting the pressure shell but not perforating it, and causing internal damage which shorted the cell (cell lost charge over ~45minutes). Another test on the cylinder portion of the cell with a 6.4mm diameter Al2017-T4 spherical projectile (at 5.88 km/s and 0°) created a 10mm hole in the pressure vessel with wing cracks from 10mm-18mm long, depressurising the cell and the cell stopped functioning immediately. On the end dome, a 4.8mm diameter Al 2017-T4 spherical projectile (at 6.72 km/s and 0°) created a 3.0cm long tear in the pressure vessel, which depressurising the cell and caused cell function to cease. The tests did not result in catastrophic rupture of the vessel, and impact

damage would not propagate to near-by cells as evidenced by limited damage to witness plates, although in all cases the tests caused the impacted cell to stop functioning. Venting of cell gases in these tests caused bulging damage to the outer honeycomb panels and attach frame (representing the ORU box cover), and the velocity of fragments released from the honeycomb targets were measured in high-speed cameras from 10m/s to 30m/s.

Typically, multiple battery cells are wired in series and parallel, so that loss of one cell will not result in significant loss of overall spacecraft battery power. Even complete loss of battery power will not necessarily result in loss of a spacecraft, although it would at the very least render the spacecraft inoperative during periods of eclipse.

3.3.3.2.3 Power Control and Distribution

High velocity cloud ejecta impacting the harness could penetrate or even sever one or more wires. This in turn can lead to short-circuiting or isolation of the current. Depending on the equipment affected and the level of redundancy, the consequences to the mission could range from minor to catastrophic.

Hypervelocity impact test results are given in the literature on various types of power cables and wire bundles for Space Station [Lazaroff & Fukushima, 1995; Westberry, 1995; Lyons *et al.*, 1997a, 1997b; Kerr *et al.*, 2000] and RADARSAT [Terrillon *et al.*, 1991]. Many of the power cable HVI tests have been performed in the laboratory with electrical conditions (current & voltage) similar to those experienced on-orbit. Sustained arcing of damaged cables through impact plasma to grounded structures has been observed in these tests (**Figure 3.3-4** and **Figure 3.3-5**). Usually, spacecraft electrical systems will contain ground-fault interrupts (GFI), which will activate in the case of conditions with short-to-ground to power-down the damaged system. A shutdown system would need to be re-activated, and in some cases, the damaged cables may still be operable, depending on the extent of damage from the impact and from arcing after impact. In some test cases, cables have been melted through due to arcing. Generally the GFI systems prevent long-lived arcing so that secondary damage from arcing is minimal (**Figure 3.3-4**).

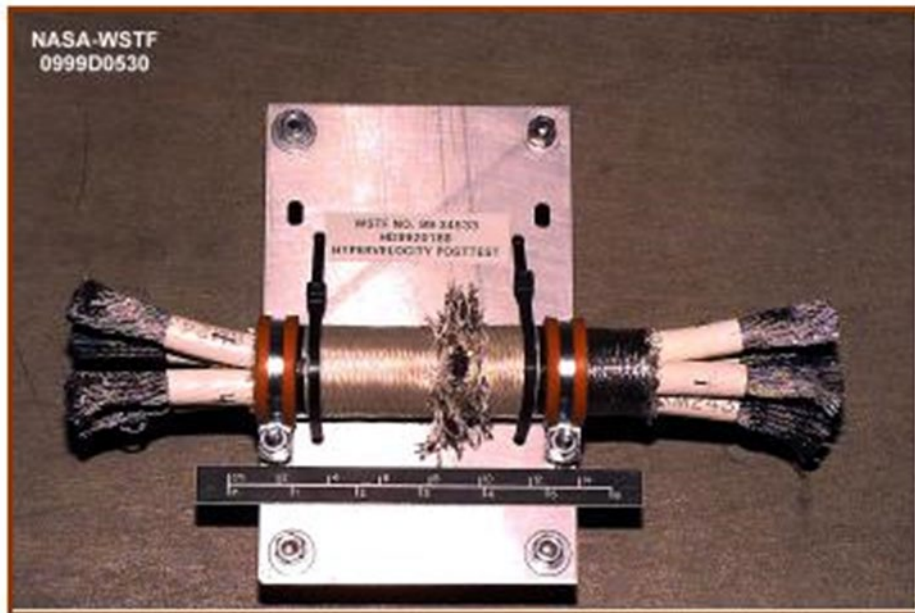


Figure 3.3-4: Post-test photo of a single primary-power cable impacted by a 3.57 mm diameter aluminium sphere at 6.6 km/s and a 45 degree impact angle



Figure 3.3-5: High speed cinema image of primary-power cable arcing during test shown in Figure 3.3-4. The arcing lasted a total of 179 ms.

3.3.3.3 Protection Options

3.3.3.3.1 Solar Arrays

For deployable solar arrays, several options may be possible [Turner *et al.*, 2000]:

- Use thin, flexible arrays so that a penetrating particle may pass through causing relatively little damage.
- Incorporate robust wiring architecture, with redundant electrical connections between cells, strings, modules, and arrays, and with suitable numbers of by-pass diodes to minimise power loss if a string of cells drops out of power-generation circuit.
- Use toughened panels to absorb the kinetic energy of the particle. The following options can be considered:
 - Toughen and / or laminate solar cell cover glasses.
 - Cover the working surfaces in some sort of foam or gel such as Aerogel. However, research is needed to identify how thick the gel should be, and its method of adhesion to be able to withstand launch loads. Any foam or gel should also have a very low dielectric constant and density.
 - Add MLI or enhanced MLI to the rear of the panel structure (refer to Section 3.3.2 for information on enhancements).

3.3.3.3.2 Power Control and Distribution

Consideration should be given to protecting vulnerable wire harnesses with thicker insulation, or added protective layers of Nextel, Kevlar or Beta cloth, whilst not compromising the thermal radiation requirements of the harness. Vulnerable external harnesses and coaxial cables should be protected with MLI and Nextel (the Nextel may have to be sealed below an outer beta-cloth layer, or inside a protective “bag” of Mylar). Redundant power cables should be separated so that one impact cannot fail all redundant paths.

3.3.4 Communications and Data Management

3.3.4.1 Antennae

The high-gain antenna on a spacecraft in most missions is mission critical, as it downlinks the data collected during the mission. In most cases the high-gain antenna is not redundant due to restrictions with respect to its location on the spacecraft and its orientation towards the ground station or the data relay satellite. The dish cannot be protected on its front side, and no flux can be expected from the rear side. The dish must be sturdy enough to guarantee its geometrical stability, and thin enough to let a particle pass through without the particle knocking a hole in the dish much larger than the diameter of the particle. The antenna feed needs shielding. It can be made redundant at the expense of some power attenuation due to switching elements. The antenna feed driver sitting beneath the dish needs significant shielding, as does the gimbal system for orientating the dish.

Telemetry, Command & Data Handling

The Telemetry, command and data handling subsystem enables a two-way flow of information between a spacecraft and the ground control station. It comprises:

- A telemetry downlink encoder, which provides the ground control operators with data on housekeeping, attitude, and payload.
- A command uplink decoder, which enables ground controllers to change some aspect of the spacecraft functionality, such as fault correction, reorientation, or mechanism deployment.
- A ranging transponder, which is integrated into the telemetry/command subsystem, to enable the ground controllers to track the spacecraft and determine its orbit.
- On board data handling for command and data management. Typically, a central processor is connected via a video or digital path to the RF communications subsystems. The processor communicates with other subsystems and payload units via a serial bus.

3.3.5 Attitude Control Subsystem (ACS)

3.3.5.1 ACS Design

The principle aim of the attitude control subsystem (ACS) is to maintain the correct orientation of the spacecraft to the required level of accuracy [Larson & Wertz, 1992]. The ACS must be capable of controlling various disturbance torques. Torques internal to the spacecraft include: mechanisms, fuel movement, astronaut movement, flexible appendages, and general mass movement. External torques comprise: aerodynamic, magnetic, gravity gradient, solar radiation, and thrust misalignment. Methods for controlling torques, i.e. torquers, are listed below:

- Thrusters. When used for orbit changing manoeuvres thrusters can provide large source of force and torque on a spacecraft. Thrusters are discussed in Section 3.3.1.1.
- Magnetorquer. Rod-like electromagnets are normally used to interact with the Earth's magnetic field thereby providing a controllable external torque.
- Momentum storage torquers. Used for attitude control, these momentum storage devices are usually purpose-built precision-engineered wheels that rotate about a fixed point, with a built in torque motor. Two types of wheel are common:
 - Reaction wheel, which has zero nominal speed but can be rotated in either direction to achieve the required torques.
 - Momentum wheel, which has a high mean speed in order to provide momentum bias. The control torques then slow down or increase the wheel speed.

For three-axis control, three orthogonal wheels are required, although a fourth is usually added for redundancy. A more advanced form of the momentum wheel, the control moment gyroscope (CMG), can also be used for three-axis control. Here, the wheel is mounted in gimbals fitted with torque motors to achieve the three torque components.

Two categories of sensor are used to measure the spacecraft attitude:

1. A reference sensor, which gives a position fix by measuring the direction of an object such as the Sun, Earth, or a star. Basic components of a Sun sensor are a detector element (such

as photocells) and an optical system. An Earth sensor typically comprises an infra-red detector that scans the horizon by means of an internal mechanism. Star sensors utilise CCD detectors, and can be used either as scanners (for mounting on a rotating base), trackers or mappers (both of which are mounted on three-axis stabilised bases). Other types of reference sensor include: radio frequency beacons and magnetometers.

2. Inertial sensors continuously measure changes in attitude, effectively relative to a gyroscope rotor, which is mounted in a single gimbal. More recently, ring laser gyroscopes have been developed as an alternative.

3.3.6 Inflatable structures

3.3.6.1 Inflatable Transformable Modules

Work on development of spacecraft using transformable design structures is undergoing in Russia. The module wall of such OS is made of a flexible material. The station module is folded on the ground but unfolds for the operation in space. The volume of such module does not depend on the diameter of the LV payload bay. It is obvious that the existing protection conception cannot be applied to inflatable transformable modules and requires use of new safety assurance principles.

A 3D model of inflatable module embedded protection design is presented in Figure 3.3-6.

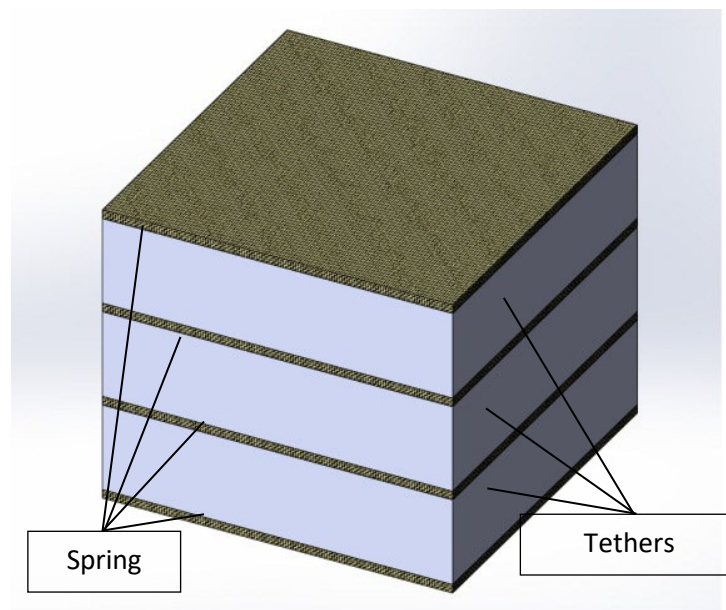


Figure 3.3-6: Embedded protection design

Protection mock-up configuration is specified in **Table 3-13**.

Table 3-13: Protection mock-up configuration

No	Element
1.	The first protection shield
2.	Interlayer
3.	The second protection shield
4.	Interlayer
5.	The third protection shield
6.	Interlayer
7.	The fourth protection shield
8.	Pressure shell
9.	Flexible pressure-tight protection of the transformable module

The protection mock-up used for the development tests of high-velocity impacts is presented in **Figure 3.3-7**.

**Figure 3.3-7:** Protection mock-up for impact tests

Results of inflatable module protection tests against high-velocity impacts are presented in **Figure 3.3-8**.

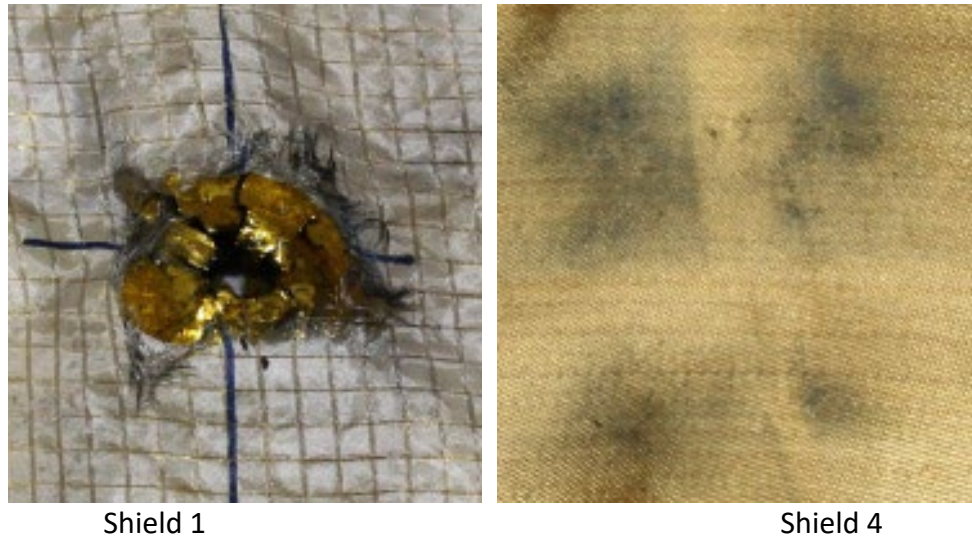


Figure 3.3-8: Results of the inflatable protection development tests

The finite-element design computation methods ensure modelling of penetration process with sufficiently high accuracy. The design BLE for inflatable module protection is specified in **Figure 3.3-9**.

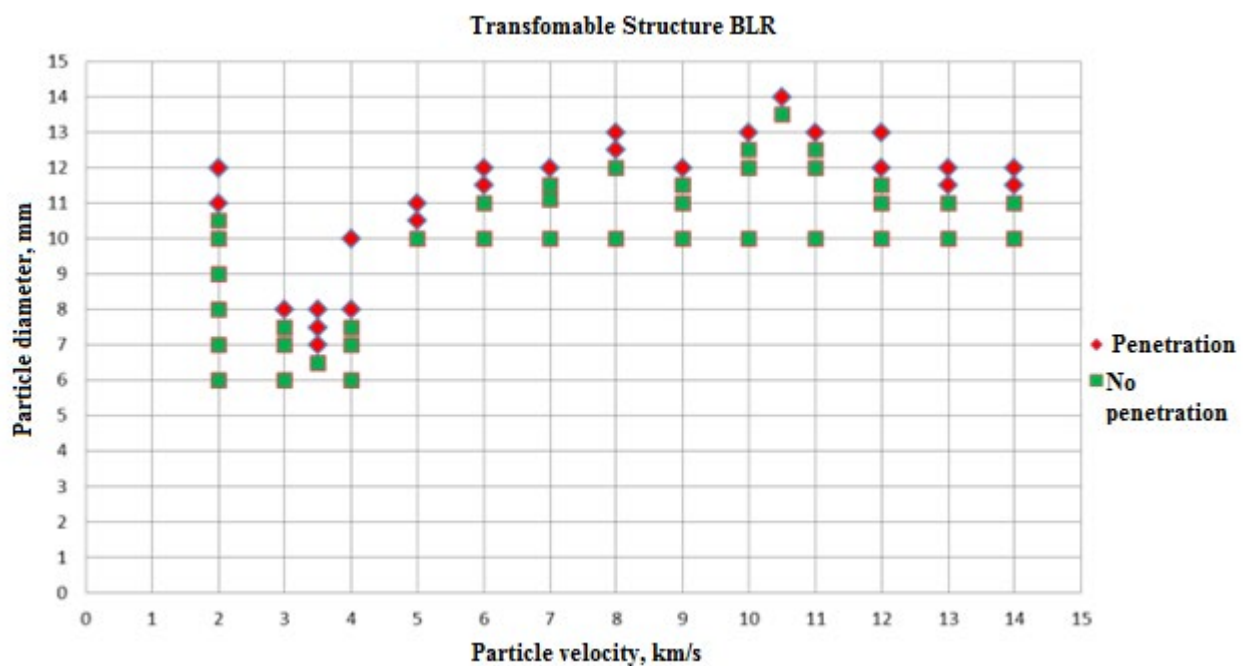


Figure 3.3-9: Ballistic limit equation of inflatable module protection

Thus, the principle feasibility of development of inflatable modules on the basis of flexible structures, that are highly competitive with conventional ISS Russian segment shield protection structures in resistance to high-velocity impacts, has been confirmed.

3.4 References

Alwes D., *Life Prediction of Viewports*, ESA Contract 6369/85, Bremen, November 1988.

Beruto E., R. Destefanis, and M. Faraud, *Debris Shielding Development for the Columbus Orbital Facility*, Proceedings of the 2nd European Conference on Space debris, ESOC, Darmstadt, Germany, March 1997.

Burt R., E.L. Christiansen, and J.H. Kerr, *Calibration of proposed RSC "Energia" SM Ballistic Limit Equation Including Semi-Transparent Shadowing Barriers*, JSC 28509, HITF report, JSC, NASA, May 2001.

Burt, R., and E. Christiansen, *Hypervelocity Impact Testing of ISS Orlan Suit*, NASA Report JSC-29105, 2001.

Burt, R., and E. Christiansen, NASA Report JSC-28307, *Hypervelocity Impact Tests on Hubble Space Telescope (HST) Solar Array Cells*, 2001d.

Burt, R., and E. Christiansen, NASA Report JSC-29151, *ISS Cupola Shutter Development Hypervelocity Impact Testing*, Phase I, 2001a.

Burt, R., and E. Christiansen, NASA Report JSC-29330, *ISS Cupola Shutter Development Hypervelocity Impact Testing*, Phase II, 2001b.

Burt, R., and E. Christiansen, NASA Report JSC-29411, *Pre-Declared HVI Testing of ISS Hatch Window Cover*, 2001c.

Burt, R.R., and E.L. Christiansen, *SM Solar Array and SM Cylinder Shield (Zone 10) HVI Tests*, NASA Johnson Space Center Report No. JSC-29485, 2001.

Byrne, G., et al., *Survey of the Hubble Space Telescope Micrometeoroid and Orbital Debris Impacts from Service Mission 2 Imagery*, NASA Report JSC-28472, 1998.

Celestian, J, and W. Schonberg, *Dynamic Response of the Space Station Freedom due to a Module Perforation by a Hypervelocity Impact*, International Journal of Impact Engineering, Vol. 13 No 2, pp 353-365, 1993.

Christiansen E., A.V. Gorbenko, V.A. Feldstein, V.P. Romanchenkov, N.G. Panichkin, V.G. Sokolov, Yu.V. Yachlakov, and L.V. Zinchenko, *The Effect of Thin Deployable Construction Elements of the International Space Station on the Probability of its Hull Penetration by Meteoroids and Space Debris*, Hypervelocity Impact Symposium, Galveston, Texas, November 2000.

Christiansen E., and J. Kerr, *Mesh Double-Bumper Shield: A Low-Weight Alternative for Spacecraft Meteoroid and Orbital Debris Protection*, Journal of Impact Engineering, Vol. 14, 1993.

Christiansen E., D. Curry, J. Kerr, E. Cykowski, and J. Crews, *Evaluation of the Impact resistance of Reinforced Carbon-Carbon*, Ninth International Conference on Composite Materials (ICCM-9), Madrid, Spain, July 12-16, 1993.

Christiansen E., *Design and Performance Equations for Advanced Meteoroid and Debris Shields*, Journal of Impact Engineering, Vol. 14, pp. 145-156, 1993.

Christiansen E., J. Crews, J. Williamsen, J. Robinson, and A. Nolen, *Enhanced Meteoroid and Orbital Debris Shielding*, Journal of Impact Engineering, Vol. 17, 1995.

Christiansen E., L. Friesen, *Penetration Equations for Thermal Protection Materials*, International Journal of Impact Engineering, Vol. 20, 153-164, 1997.

Christiansen E.L., *Design Practices for Spacecraft Meteoroid/Debris (M/D) Protection*, Proceedings of the 1998 Hypervelocity Shielding Workshop, IAT Catalog number IAT.MG 0004, Institute for Advanced technology, The University of Texas at Austin, 1999.

Christiansen, E., B. Cour-Palais, and L. Friesen, *Extravehicular Activity Suit Penetration Resistance*, International Journal of Impact Engineering, 23, 113-124, 1999.

Christiansen, E.L., et al., *Assessment of high velocity impacts on exposed Space Shuttle surfaces*, ESA SD-01, Proceedings of the First European Conference on Space Debris, 447-452, 1993.

Christiansen, E.L., et al., NASA Report JSC-28033, *Orbiter Meteoroid/Orbital Debris Impacts: STS-50 (6/92) through STS-86 (10/97)*, p.60.

Cooke, W.J., B.J. Anderson, and H. Lewis, *LEO Population Considerations for Tether Missions*, working paper, December 2000.

Cour-Palais, B., *Hypervelocity Impact in Metals, Glass and Composites*, International Journal of Impact Engineering, Volume 5 pp 221-237, 1987.

Cour-Palais, B., *Space Vehicle Meteoroid Shielding Design*, ESA SP-153, Proceedings of a Workshop on "The Comet Halley Micrometeoroid Hazard", ESTEC, 18-19 April 1979.

Cour-Palais, B.G., *Hypervelocity Impact Investigation and Meteoroid Shielding Experiments Related to Apollo and Skylab*, Orbital Debris, CP-2360, 247-275, 1982.

Destefanis R., M. Faraud, and M. Trucchi, *Columbus Debris Shielding Experiments and Ballistic Limit Curves*, HVIS 1998, November, Huntsville, Alabama, 1998.

Evans, S.W., *Comparison of Predicted and Actual Orbital Lifetimes for the SEDS-2 Mission*, Fourth International Conference on Tethers in Space, Washington, D.C., 10 – 14 April 1995.

Fechtig, H., J.B. Hartung, K. Nagel, and G. Neukum, Proc. 5th Lun. Sci. Conf., Geochimica and cosmochemica, 3, suppl. 5, 2463-2474, 1974.

Francesconi A., Pavarin D., Rondini D., Bettanini C., Colombatti G., Angrilli F. (2003), Hypervelocity Impacts test campaign on space tethers. *XVII Congresso Nazionale AIDAA. Roma, Italy, September 2003, vol. 1, p. 429-434*

Francesconi A., Pavarin D., Rondini D., *Impact experiments at low temperature*, CISAS - University of Padova, 22nd IADC meeting Abano Terme, April 19-22, 2004.

Francesconi A., Giacomuzzo C., Bettiol L., Lorenzini E. C., A new Ballistic Limit Equation for thin tape tethers, *Acta Astronautica*, 129, 325-334, 2016.

Frate, D.T., H.K. Nahra, *Hypervelocity Impact testing of Nickel Hydrogen Battery Cells*, AIAA Space Programs and Technologies Conference, Huntsville, Alabama, AIAA 96-4292, September 1996.

Friesen, L., and E. Christiansen, *Hypervelocity Impact Tests of Extravehicular Mobility Unit (EMU) Material Samples*, Part 1, NASA Report JSC-27856, 1997.

Friesen, L., *Initial Hypervelocity Impact Tests of Canadian Space Agency Space Station Remote Manipulator Systems Components*, NASA Report JSC-27576, 1996.

Friesen, L., J. Whitney and E. Christiansen, *Hypervelocity Impact Tests of Shuttle Material Targets*, NASA JSC-27315, 1996.

Frost, C.L., P.I. Rodriguez, *AXAF Hypervelocity Impact Tests Results*, Proceedings of the Second European Conference on Space Debris, ESA SP-393, pp. 423-428, 1997.

Gault, D.E., *displaced mass, depth, diameter and effects of oblique trajectories for impact craters formed in dense crystalline rocks*, Moon, 6, 32-44, 1973.

Gehring, J.W., *High Velocity Impact Phenomena (Chapter IX: Engineering Considerations)*, Academic Press, New York, ed. R. Kinslow, 1970.

Graham, G.A., N. McBride, A.T. Kearsley, G. Drolshagen, S.F. Green, J.A.M. McDonnell, M.M. Grady, and I.P. Wright, *The chemistry of micrometeoroid and space debris remnants captured on Hubble Space Telescope solar cells*, Int. J. Impact Engin, 26, 263-274, 2001.

Hayhurst C., I. Livingstone, R. Clegg, G. Fairlie, S. Hiermaier, and M. Lambert, *Numerical Simulation of Hypervelocity Impacts on Aluminium and Nextel/Kevlar Whipple Shields*, Hypervelocity Shielding Workshop, Galveston, Texas, 8-11 March 1998.

Hayhurst C., S. Hiermaier, R. Clegg, W. Riedel, and M. Lambert, *Development of material models for Nextel and Kevlar-epoxy for high pressures and strain rates*, International Journal of Impact Engineering, Vol. 23, pp 365-376, 1999.

Herbert, M.K., and J.A.M. McDonnell, *Morphological classification of impacts on the Eureka & Hubble Space Telescope solar arrays*, Proc. 2nd Euro. Conf. on Space Debris, ESA SP-393, pp. 169-175, 1997.

Hiermaier S.J., W. Riedel, C.J. Hayhurst, R.A. Clegg, and C.M. Wentzel, *“Advanced Material Models for Hypervelocity Impact Simulations (AMMHIS)”*, ESA contract 12400/97/NL/PA(SC), EMI Report No. E 43/99,

Hoyt, R.P., and R.L. Forward, *The Hoytether: A Failsafe Multiline Space Tether Structure*, Tether Technology Interchange Meeting, Huntsville, AL, Sept. 9 – 10, 1998.

Hyde, J.L., et al., *Meteoroid and Orbital Debris Risk Mitigation in a Low Earth Orbit Satellite Constellation*, International Journal of Impact Engineering, 26, 345-356, 2001.

Jacchia, L.G., *Revised Static Models of the Thermosphere and Exosphere with Empirical Temperature Profiles*, SAO Special Report No. 313, 1970.

Jex, D.W., A.M. Miller, C.A. Mackay, *The Characteristics of Penetration for a Double-Sheet Structure with Honeycomb*, NASA TM X-5397, 1970.

Kamoulakos, A., E. Schneider, M. Lambert, P. Greff, and C. Bonnal, *Ariane 5 Attitude Control System Passivation: Theoretical and Experimental Determination of the Explosion Threshold Pressure*, International Journal of Impact Engineering, Vol. 20, 1997.

Kerr, J., E. Christiansen, and F. Lyons, *Hypervelocity Impact Testing of International Space Station Primary Power Lines*, Paper No.178, Presented at HVIS-2000, Galveston 2000.

Khan, S. B., Francesconi, A., Giacomuzzo, C., & Lorenzini, E. C. (2016). Survivability to orbital debris of tape tethers for end-of-life spacecraft de-orbiting. *Aerospace Science and Technology*, 52, 167-172.

Kinslow R., *High-Velocity Impact Phenomena*, Academic Press, 1970.

Lambert M., E. Schneider, *Shielding against space debris. A comparison between different shields: The effect of materials on their performances*, International Journal of Impact Engineering, Vol. 17, pp. 477-485, 1995

Lambert M., F. Schaefer, and T. Geyer, *Impact Damage on Sandwich Panels and Multi-Layer Insulation*, International Journal of Impact Engineering, Vol. 26, pp 369-380, 2001.

Lambert M., F. Schäfer, *Hypervelocity impacts on thermal protections, a review of the ESA work*, 3rd European Workshop on Thermal Protection, 25-27 March 1998, ESTEC, ESA-WPP-141, 1998.

Lambert, M., F. Schaefer, and T. Geyer, *Impact damage on sandwich panels and multi-layer insulation*, International Journal of Impact Engineering, Vol 26, pp 369-380, 2001

Lambert, M., *Hypervelocity impacts and damage laws*, Ad. Space Res., 19(2), pp. 369-378, 1997.

Lamontagne, C.G., G.N. Manuelpillai,, E.A. Taylor, and R.C. Tennyson, *Normal and Oblique Hypervelocity Impacts on Carbon Fibre/PEEK Composites*, International Journal of. Impact Engineering., vol 23, 1999.

Larson W., and J. Wertz, *Space Mission Analysis and Design*, Kluwer Academic Publishers, 1992.

Lazaroff, S.M., and J. Fukushima, *Hypervelocity impact testing of the utility distribution system for the Space Station Freedom*, International Journal of Impact Engineering, 17, 497-508, 1995.

Lemcke, C., et al., *Enhanced Debris / Micrometeoroid Environment Models and 3D Software Tools*, ESABASE/DEBRIS Release 2, Final Report, ESA-CR-P-4214, August 1998a.

Lemcke, C., G. Scheifele, M. C. Maag, *Enhanced Debris / Micrometeoroid Environment Models and 3D Software Tools*, ESABASE/DEBRIS Release 2 Final Presentation, June 1998b.

Lyons, F., and E. Christiansen, *Soyuz/Progress Transport Vehicles Hypervelocity Impact Tests*, Part 2, NASA Report JSC-29460, 2001c.

Lyons, F., *Hypervelocity impact testing of reinforced carbon-carbon*, NASA JSC-29398, 1998.

Lyons, F., R. Westberry, and J. Kerr, *Phase-II Hypervelocity Impact Testing of International Space Station Wire Harness*, NASA JSC-27808, 1997a.

Lyons, F., R. Westberry, and J. Kerr, *Phase-III Sure-Kill Hypervelocity Impact Testing of International Space Station Wire Harness*, NASA JSC-27809, 1997b.

Lyons, F., *Soyuz Transport Vehicle Hypervelocity Impact Tests*, NASA Report JSC-28968, 2001b.

Lyons, F., *Toughened Thermal Blanket Hypervelocity Impact Assessment*, NASA Report JSC-28836, 2001a.

Matney, M., D. Kessler, and N. Johnson, *Calculation of Collision Probabilities for Space Tethers*, IAA-00-IAA-6.5.02, 51st International Astronautical Congress, Rio de Janeiro, Brazil, 2 – 6 Oct. 2000.

McBride N., and E. Taylor, *The risk to satellite tethers from meteoroid and debris impacts*, Proceedings of the Second European Conference on Space Debris, ESOC, 17-19 March 1997, ESA SP 393, 1997.

McHugh, A.H., and A.J. Richardson, *Hypervelocity particle impact damage to glass*, North American Aviation, STR-241, 1974.

Melin, R.W., *Hypervelocity impact testing of heat pipe samples*, International Journal of Impact Engineering, 10, 389-401, 1990.

Myers, B. A., Schonberg W. P., and Williamsen J. E., *Temperature Effects on Bumper Hole Diameter for Impact Velocities from 2 to 7 km/s*, HVIS 2003, Noordwijk, The Netherlands.

Military Standards, *MIL-STD-1522A*, 20 November 1986.

NASA CP 2360, 1985.

NASA Johnson Space Center, *Hypervelocity Impact Technology group web site*:
<https://hvit.jsc.nasa.gov>

NASA, Johnson Space Center – *White Sands Test Facility report*, LeRC Ni-H2 Cell Hypervelocity Test Report, 1992.

National Research Council, *Protecting the Space Shuttle from Meteoroids and Orbital Debris*, National Academy Press, Washington D.C., 1997.

Pardini, C., Hanada, T., & Krisko, P. H. (2009). Benefits and risks of using electrodynamic tethers to de-orbit spacecraft. *Acta Astronautica*, 64(5-6), 571-588.

Piekutowski A., *A Method of Estimating the State of the Material in an All-Aluminum Debris Cloud*, AIAA Space Program and Technologies Conference, Huntsville, Alabama, September 27-29, 1994.

Piekutowski A., *Effect of Scale on Debris Cloud Properties*, International Journal of Impact Engineering, Vol.20, pp.639-650, 1997.

Poe, R., and M. Rucker, *Evaluation of pressurized vessels following hypervelocity particle impact*, Proceedings of the First European Conference on Space Debris, ESA SD-01, Darmstadt, Germany, 5-7 April 1993.

Putzar, R., F. Schäfer, O. Romberg, and M. Lambert, Vulnerability of shielded fuel pipes and heat pipes to hypervelocity impacts, *Proceedings of the 4th European Conference on Space Debris*, ESA SP-587, ESA/ESOC, Darmstadt, Germany, 2005.

Putzar, R., F. Schäfer, H. Stokes, R. Chant, and M. Lambert, Vulnerability of spacecraft electronics boxes to hypervelocity impacts, in: Bendisch, J. (Ed.), *Space debris and space traffic management symposium 2005*, Vol. 112 Science and Technology Series, San Diego, California, Univelt, ISBN 0-87703-533-4, pp 307-321, IAC-05-B6.4.02, 2006.

Putzar, R., F. Schäfer, and M. Lambert, Vulnerability of spacecraft harnesses to hypervelocity impacts, *International Journal of Impact Engineering*, 35, pp 1728-1734, 2008.

Reimerdes H.-G., *MDPS Technical Note 4, Shielding-Performance Characterization*, European Space Agency Contract No. 8732/90/NL/PP, Dec. 1992.

Reimerdes, H.-G., K.-H. Stecher, and M. Lambert, *Ballistic Limit Equations for the Columbus Double Bumper Shield Concept*, Proceedings of the First European Conference on Space Debris, ESA SD-01, Darmstadt, Germany, 1993.

Rhatigan, J.L., E.L. Christiansen, and M.L. Fleming, *"On Protection of Freedom Solar Dynamic Radiator from the Orbital Debris Environment: Part 2 – Further Testing and Analyses,"* NASA TM-104514, April 1992.

Rhatigan, J.L., E.L. Christiansen, and M.L. Fleming, *"On Protection of Freedom Solar Dynamic Radiator from the Orbital Debris Environment: Part 1 - Preliminary Analysis and Testing,"* NASA TM-102458, April 1990.

Rosenberg, Z., S. Bless and J.P. Gallagher, *A Model for Hydrodynamic Ram Failure Based on Fracture Mechanics Analysis*, International Journal of Impact Engineering, Vol. 6, 1987.

Salomé, R., V. Albouys, Ch. Le Floc'H, D. Sornette, and J.P. Vila, *High Pressure Composite Tanks Behaviour under an Hypervelocity Impact*, Proceedings of the Third European Conference on Space Debris, ESA SP-473, ESOC, Darmstadt, Germany, 19-21 March 2001.

Sanchez, G., R. Westberry, and E. Christiansen, NASA Report JSC-27509, *ISS Common Module, Node and Cupola Windows Meteoroid and Orbital Debris Development Tests*, Phase 1, 1998.

Sánchez-Arriaga, Gonzalo, et al. "The ET PACK project: towards a fully passive and consumable-less deorbit kit based on low-work-function tether technology." *Acta Astronautica* 177 (2020): 821-827.

Schäfer, F. K., R. Putzar, and M. Lambert, Vulnerability of satellite equipment to hypervelocity impacts, *Proceedings of the 59th International Astronautical Congress*, Glasgow, Scotland, UK, IAC-08-A6.3.2, 2008.

Schäfer, F. K., S. Ryan, M. Lambert, R. Putzar, Ballistic limit equation for equipment placed behind satellite structure walls, *International Journal of Impact Engineering*, 35, No. 12, pp 1784-1791, 2008.

Schäfer F., Jadhav G., *Influence of temperature on the performance of Whipple Shields*, IADC 22, Abano Terme, April 21, 2004.

Schäfer F., and L. Günther, *Impact Testing on ATV-ICC Meteoroid and Debris Shield*, EMI E28/2000, 14 February 2001.

Schäfer, F., and E. Schneider, *Hypervelocity Impact Testing on Pressure Vessels*, EMI report I-27/01, ESA Contract 10556/93, Freiburg, Germany, April 30, 2001.

Schäfer, F., E. Schneider, and M. Lambert, *Hypervelocity Impacts on Cylindrical Pressure Vessels- Experimental Results and Damage Classification*, ASME Pressure Vessels and Piping Conference, Orlando, Florida, July 27-31, 1997.

Schneider, E., et al., *Micrometeorite and Space Debris Simulation for Columbus Hull Components*, Int. J. Impact Engng., vol 10, 499-508, 1990.

See, T., et al., *Meteoroid and Debris Impact Features Documented on the Long Duration Exposure Facility*, NASA Report JSC-24608, 1990.

Sennett, R.E. , B.L. Lathrop, *Effects of Hypervelocity Impact on Honeycomb Structures*, Journal of Spacecraft and Rockets, Vol 5, pp 1496-1497, 1968.

Shiraki K., A. Takano, *Space Debris Protection Shield Design Status for the Space Station JEM*, 13th IADC WG3, February 1996

Shiraki K., and M. Harada, *JEM Space Debris Protection Design Capability and Performance Verification*, 22nd International Symposium on Space Technology and Science, Morioka, Japan, May 28-June 4, 2000.

Shiraki K., and N. Noda, *Evaluation of Space Station JEM MM-OD Shield and Structural Design*, IAF-98-I.5.07, 49th International Astronautical Congress, Melbourne, Australia, September 28-October 2, 1998.

Shiraki K., F. Terada, and M. Harada, *Space Station JEM Design Implementation and Testing for Orbital Debris Protection*, International Journal of Impact Engineering, Vol. 20, pp 723-732, 1997.

Sokolov V., *Problems and Features of ISS Russian Segment Meteoroid/Orbital Debris (M/OD) Shielding*, 16th IADC, WG3, November 3, 1998.

Tanaka K., Nishida M. and Takahashi M., *Penetration of a High-Speed Projectile into Carbon Steels at Low Temperatures*, Volume 109, Science and Technology Series, Space Debris and Space Traffic Management Symposium 2003, (IAA 03-5.3.08).

Taylor, E., C. Hayhurst, and K. Tsembelis, *Hydrocode modelling of space debris hypervelocity impact on soda-lime glass using the Johnson-Holmquist brittle material model*.

Taylor, E., K. Tsembelis, C. Hayhurst, L. Kay, and M. Burchell, *Hydrocode modelling of hypervelocity impact on brittle materials: depth of penetration and conchoidal diameter*, International Journal of Impact Engineering, Vol. 23, 1999a.

Taylor, E., L. Kay, and N. Shrine, *Hypervelocity impact on brittle materials of semi-infinite thickness: fracture morphology related to projectile diameter*.

Taylor, E.A., M.K. Herbert, and L. Kay, *Space Debris Hypervelocity Impact On Carbon Fibre Reinforced Plastic (CFRP)/Al Honeycomb At Normal And Oblique Angles*, Proceedings of the Second European Conference on Space Debris, ESA SP-393, pp. 429-434, 1997b.

Taylor, E.A., M.K. Herbert, B.A.M. Vaughan, J.A.M. McDonnell, *Hypervelocity Impact on Carbon Fibre Reinforced Plastic / Aluminium Honeycomb: Comparison with Whipple Bumper Shields*, International Journal of Impact Engineering, Vol 23, pp. 883-894, 1999.

Taylor, E.A., M.K. Herbert, D.J. Gardner, L. Kay, *Hypervelocity Impact on Carbon Fibre Reinforced Plastic (CFRP)/Aluminium Honeycomb*, Proceedings of the Institute of Mechanical Engineers, 211 (Part G), pp. 355-363, 1997a.

Taylor, E.A., M.K. Herbert, L. Kay, *Hypervelocity Impact on Carbon Fibre Reinforced Plastic (CFRP)/Aluminium Honeycomb at Normal and Oblique Angles*, Proceedings of the Second European Conference on Space Debris, ESA SP-393, pp. 429-434, 1997b.

Taylor, E.A., N.R.G. Shrine, N. McBride, S.F. Green, J.A.M. McDonnell, and G. Drolshagen, *Space Debris Impacts on HST and EURECA Solar Arrays Compared With LDEF Using a New Glass-to Aluminium Conversion*, Adv. Space Res, 1999b.

Taylor, E.A., R. Marston, P. Irving, A.J. Russell, and C.J. Hayhurst, *Cost Effective Debris Resistant Composite Structures*, presented at the Protection Working Group meeting of the 19th IADC, DLR, Cologne, Germany, March 2001.

Telitchev, I., F. Schäfer, E. Schneider, and M. Lambert, *Analysis of the Fracture of Gas-Filled Pressure Vessels under Hypervelocity Impact*, International Journal of Impact Engineering, Vol. 23 No 1, pp 905- 919, 1999.

Terrillion, F., H.R. Warren, and M.J. Yelle, *Orbital Debris Shielding Design Of The Radarsat Satellite*, IAF-91-283, 42nd Congress of the International Astronautical Federation, 5-11 October, Montreal, Canada, 1991.

Turner, R., L. Berthoud, A.D. Griffiths, J.A.M. McDonnell, P. Marriott, P.H. Stokes, E.A. Taylor, and J.E. Wilkinson, *Cost-Effective Debris Shields for Unmanned Spacecraft: Final Report, Issue 2*, Submitted to ESA under Contract No. 12378/97/NL, 2000.

Turner, R.J., E.A. Taylor, J.A.M. McDonnell, H. Stokes, P. Marriott, J. Wilkinson, D. Catling, R. Vignjevic, L. Berthoud, M. Lambert, *Cost Effective Honeycomb and MLI Debris Shields for Unmanned Spacecraft*, International Journal of Impact Engineering, Vol 26, 2001.

Unispace Kent, U.K., *Meteoroids & Debris Flux Ejecta Modelling - Final Report*, ESA CR(P)-4252, McDonnell, J.A.M. (Ed.), 1998.

Warren, H.R., and M.J. Yelle, *Effects of Space Debris on Commercial Spacecraft – The RADARSAT Example*, pp.77-83, in Preservation of Near-Earth Space for Future Generations, John A. Simpson (Ed.), Cambridge University Press, 1994.

Welzyn, K.J., and J.H. Robinson, *Severed Tether Dynamics and Probability*, Fourth International Conference on Tethers in Space, Washington, D.C., 10 – 14 April 1995.

Westberry, R., *Hypervelocity Impact Test for International Space Station Wire Harness*, Phase I, NASA JSC-27285, 1995.

Whipple, F.L., *Meteorites and Space Travel*, Astronomical Journal, No. 1161, p.131, 1947.

Whitney, J., Hypervelocity Impact Tests of Shielded and Unshielded Pressure Vessels, NASA JSC 32294, March 1993.

4 Test Methods and Facilities Calibration

This chapter provides the PWG calibration procedures for hypervelocity impact launcher facilities, the status of cross-calibration among PWG launchers, and a description of test facilities and numerical simulation computer codes.

4.1 Impact Testing

The most straightforward method of deriving Ballistic Limit Equations (BLE) is to run a series of hypervelocity impact experiments and to analyse and relate the damage data collected. Ballistic Limit Equations must span the impact velocity ranges of on-orbit impacts, which is 1-16 km/s for debris and 11-72 km/s for meteoroids. Since these velocities are far away from the capabilities of laboratory hypervelocity launchers, BLEs must be obtained both from laboratory experiments and numerical simulations (**Figure 4.1-1**).

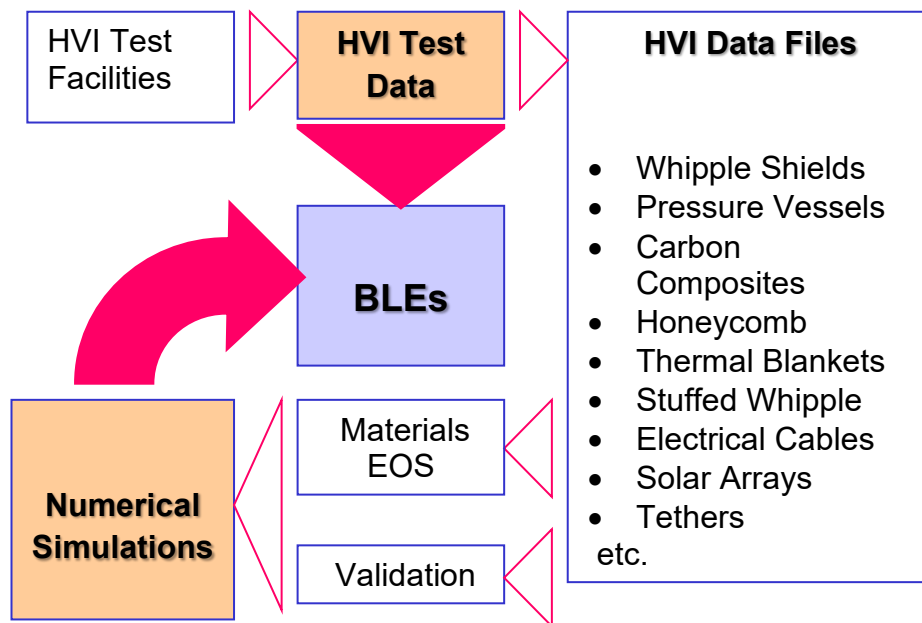


Figure 4.1-1: The role of HVI experiments

Databases of HVI data collected from laboratory experiments are extremely useful not only to derive BLEs in the testable velocity range, but also to validate numerical simulations and to establish the behaviour of tested materials in the HVI conditions.

In fact, numerical simulations represent the only mean to analysing impact phenomena in the velocity ranges not easily accessible to launch facilities, and their reliability and accuracy strongly depend on the knowledge about materials behaviour in the hypervelocity regime, which is itself an objective of the research. This aspect is particularly important when considering shielding strategies or S/C subsystems involving new lightweight materials (such as plastics and/or composites), or structures (such as honeycomb, stuffed Whipple, etc).

As a consequence, complete understanding of the impact phenomena at reduced velocity becomes essential to extend experimental results and computation philosophy to impacts occurring at higher velocity and laboratory tests must be used to establish the Equations of State (EOS) of shielding materials at testable velocity.

Therefore, HVI tests are necessary to:

- obtain the reference points of BLEs within the testable range and their verification;
- provide data for testing (verification, calibration) of the numerical codes (including models of materials behaviour under HVI conditions).

The set-up of a test (both launching facility and registration methodology) depends on its aim. It could be either a simple low-cost series of tests, or a detailed set of tests to thoroughly assess the impact process.

The facilities normally used for Hypervelocity impact are:

- one-stage powder guns;
- two-stage light-gas guns (LGG);
- electromagnetic launchers;
- electrostatic launchers;
- blast (explosive) launchers.

The following types of measurement technique could be involved:

- process' optical registration (high frame-rate photography);
- process' X-ray registration (if possible, multi-flash and multi-aspect X-ray);
- registration of dynamic pressures, stresses and impulse by gages placed into target;
- registration of time of arrival by contact gages;
- post-test study of damage (craters, holes, etc.).

The following section presents a brief description of hypervelocity launchers techniques suitable for impact tests.

4.1.1 Hypervelocity Launchers

The most common hypervelocity propulsion systems consist of pneumatic launchers and blast launchers. The leading facilities for impact testing generally employ two-stage light-gas guns (LGGs) that are a type of pneumatic launcher. They are particularly suitable for their ability to accelerate projectiles of arbitrary shape at velocities ranging from 2 km/s to 10 km/s, using hydrogen as a propellant for the projectile.

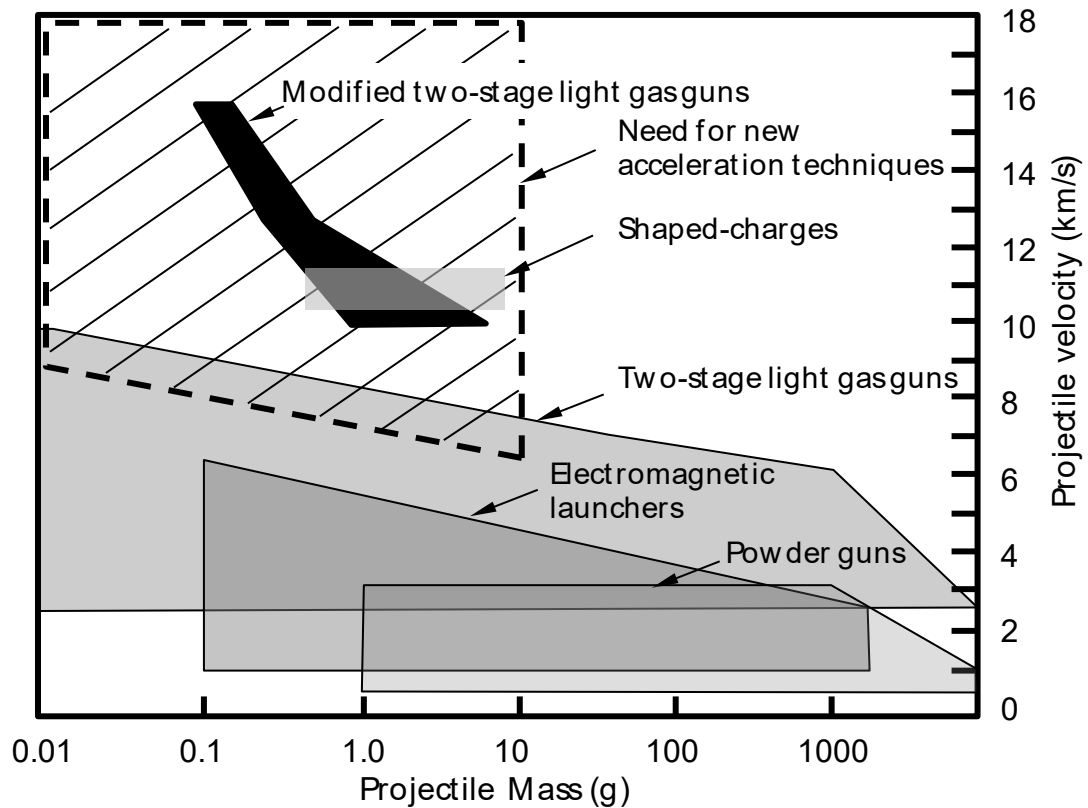


Figure 4.1-2: Performance ranges of hypervelocity launchers.

Other facilities (based on electrostatic, electromagnetic or hybrid launchers) are less common. Electrostatic machines are of little use, because of their capability of accelerating very small projectiles only [Keaton; Septier, 1967; Persico, 1968]. Electromagnetic launchers seem to represent the most promising approach to accelerate projectiles of a few grams above 10 km/s, but only few prototypes are in use. Hybrid launchers are machines based on explosive techniques and 3-stage methods. Their future development represents a means of reaching velocities (around 16 km/s) that cannot be achieved by traditional light-gas guns but are necessary to verify BLEs under conditions which are possible on-orbit from M/OD impacts.

4.1.1.1 Pneumatic Launchers

One-stage guns and two-stage light-gas guns (LGGs) fall into the category of pneumatic launchers, which represents the most studied launching technique. This class of facilities exploits the thrust of a pressurised expanding propellant to accelerate the projectile.

Since the best way of pneumatically accelerating an object is to provide a constant pressure behind it, the operating conditions for a pneumatic launcher must be chosen to reduce at a minimum the pressure drop that occurs behind the projectile as a consequence of the gas expansion. This can be done by (1) appropriate choice of the propellant and/or (2) adding energy to the gas to compensate for its pressure decrease.

1. Propellant requirements:

Conservation of momentum applied to a gas layer shows that the pressure decrease needed to effect a given velocity increase is proportional to the acoustic inertia “ ρa ” of the propellant (“ ρ ” is the density, “ a ” is the sound speed).

$$dP = -\rho a dU \quad [4.1-1]$$

Integration of this equation for perfect gases that expand at constant entropy [Canning; Seigel, 1965] reveals that the higher is the initial sound speed “ a_0 ” in the propellant, the lower is the pressure decrease behind a projectile. A high value of “ a_0 ” requires a low molecular mass and a high initial temperature for the gas. Hence, the best propellant is a hot and “light” gas, such as helium, hydrogen or helium-hydrogen mixtures heated by means of adequate procedures.

As a first rough estimation, the maximum velocity that can be reached by a pneumatic-accelerated projectile finds its limit in the “propellant escape velocity” that is attained when the pressure has dropped to zero and the gas can push no more the projectile [Seigel, 1965]. Since the escape velocity is proportional to the initial propellant sound speed, the performance limit of any pneumatic launcher is given only by the technical possibility of heating and managing gas at extremely high temperature (standard two-stage light-gas guns bring hydrogen up to 5000 K).

2. Energy addition to the gas during the expansion phase:

The effects of propellant expansion could be somewhat compensated by injecting energy in some ways in the gas [Seigel, 1965]. Although one-stage and two-stage guns can provide different means of increasing the gas *initial* temperature, only a particular arrangement (see tapered section in **Figure 4.1-3**) belonging to two-stage guns is commonly used to add energy to the gas *during the projectile travel* along the barrel.

Mass limitations for the accelerated projectiles are given only by technical constraints related to the capacity of mechanically scaling the machine dimensions.

One-Stage Guns

In one-stage guns, high pressure gas is discharged directly on the back of the projectile through a rupture valve or a fast valve. If the propellant is used at ambient temperature, the low speed of sound limits the attainable velocity to 1.5-2 km/s. On the contrary, the propellant can be heated by means of the energy produced by powder ignition or by chemical reactions, such as the combustion of hydrogen [Charters, 1987]. Anyway, the propellant mixture can reach a sound speed that is considerably lower than that for pure hydrogen or helium [Canning; Seigel, 1965]. This is why one-stage guns are not of common use and are adequate only to accelerate projectiles at velocity lower than 3-3.5 km/s.

Two-Stage Guns

Two-stage light-gas guns provide a more effective mean of heating and adding energy to the propellant during the projectile motion along the barrel [Crozier, 1957; Charters, 1987; Grosch, 1993; Stilp, 1995]. These machines have two gas chambers: energised gas in a first stage drives a piston in a pump tube, to compress the second stage propellant, which in turn accelerates the projectile.

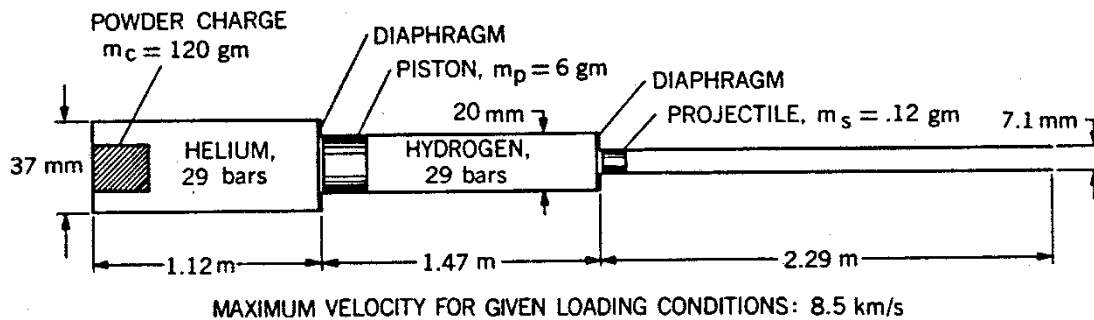


Figure 4.1-3: Schematic of a simple two-stage light-gas gun [Canning]

Commonly, the first stage driver gas is a gunpowder, and the gun operations begin with the ignition of this propellant. The first stage chamber is separated from the pump tube by means of a rupture valve which breaks at a pre-set pressure. The pump tube is initially filled with the light propellant and separated from the barrel by means of a second rupture diaphragm. The gas energised by the combustion in the first stage drives the piston, which compresses the gas in the second stage to high pressure and temperature. When the pressure in the second stage reaches a sufficiently high value, the second diaphragm ruptures and the projectile is accelerated along the barrel. The working principle of two-stage light-gas guns is summarised in **Figure 4.1-4**.

The best results are obtained when the compression continues during a substantial part of projectile travel in the launch tube, providing energy to maintain the projectile base pressure at a reasonable high value. This effect can be achieved using a tapered transition section between the pump tube and the launch tube, in which a deformable and heavy piston extrudes (**Figure 4.1-3**), sustaining the compression during the whole projectile travel into the barrel. A high piston mass is needed to drive the piston at a low speed with respect to the gas sound speed, so that strong shock waves are not formed and the resulting compression is nearly isentropic [Canning].

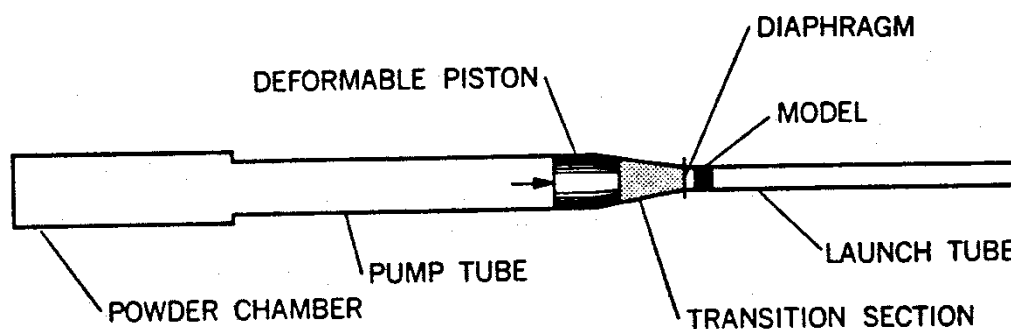


Figure 4.1-4: Deformable piston two-stage light gas gun [Canning]

Actually, this arrangement is the most widely used for LGGs for impact testing and for impact facilities in general, and it is known to be the best way of obtaining a nearly constant base pressure behind the projectile.

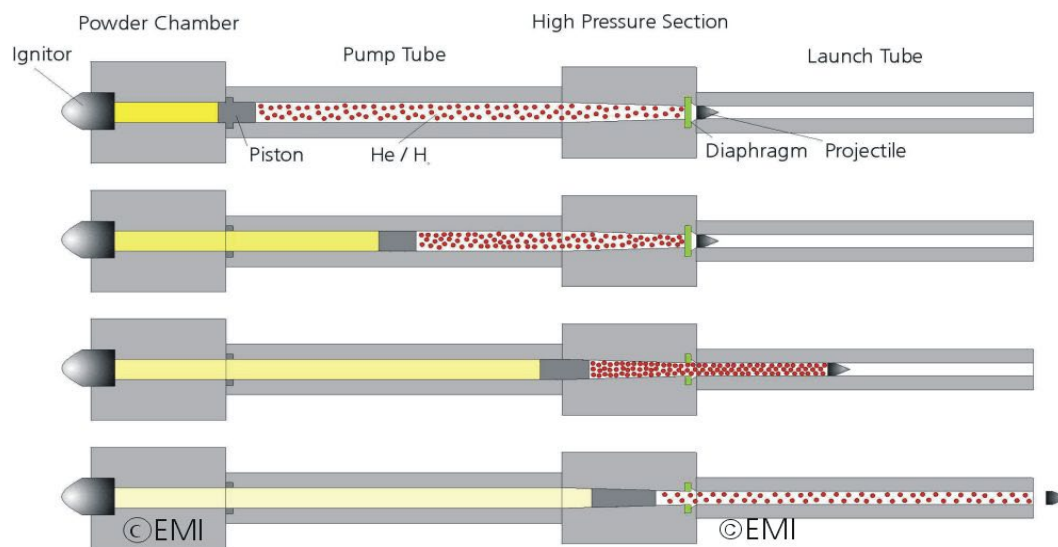


Figure 4.1-5: Working principle of a two-stage light gas gun.

Pellet Injectors for Plasma Fuelling

Since the penetration of fresh fuel was revealed to be a powerful tool to influence plasma parameters [Combs, 1985, 1990, 1993; Frattolillo, 1999], the injection of frozen hydrogen isotope pellets at high velocities has become the lead technology for fuelling plasma fusion devices. Because the efficiency of pellets penetration in the confining magnetic field increases with the velocity and the mass of the injected projectile and with the capability of the injector to operate repetitively for long pulse lengths (hundreds of seconds to steady state), pellet injectors that operate at quasi-steady state (1-40 Hz) have been developed. To achieve higher velocity, pellet injectors based on two-stage light-gas guns have become predominant with respect to one-stage guns, and specific technologies have been introduced to obtain fast preparation of shot operations. Fast valves have replaced rupture disks, high-pressure gas is used instead of powder in the first stage, valve systems return the piston in its initial position and refill the first and second stage volumes to appropriate pressure, dedicated mechanisms reload the breech with a new projectile after each. These guns are normally less powerful than explosive driven two stage guns but are also quicker to operate and allow fast, low-cost hypervelocity campaigns.

4.1.1.2 Blast Launchers

Shaped Charge Launchers (SCL) use a cylindrical block of explosive with a coaxial shaped (usually conical) cavity at one end, lined with a metal. The detonation of the explosive produces the collapse of the conical liner onto its axis, the forming of a metallic jet and its ejection [Walker, 1993; Bol, 1997; Kibe, 1999].

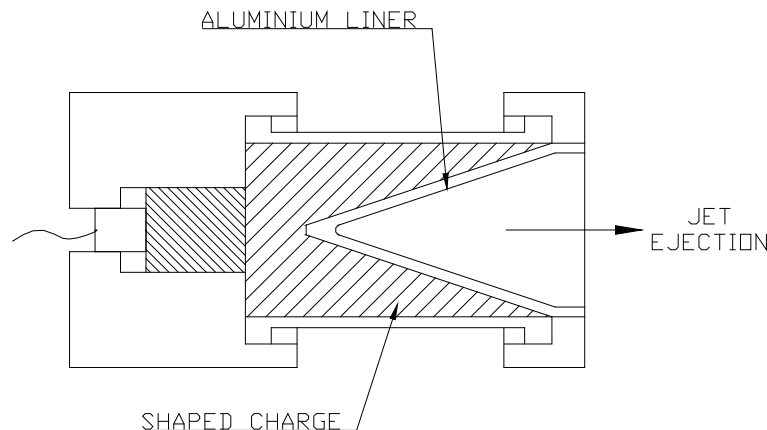


Figure 4.1-6: Schematic of a Conical Shaped Charge launcher

Although this technique allows projectiles of a few grams to be accelerated up to 12 km/s, shaped charges are not completely adequate to derive Ballistic Limit Equations, since the jet tends to stretch and becomes unstable during its travel, finally separating into individual droplets of complex shape. This drawback complicates data analyses, in fact experiments confirm that BLEs depend on the shape of the impactor [Riedler, 2000] but analytical models for the damage produced by objects of complex shape have not yet been developed. As a consequence, it is difficult to obtain reproducible results, which are fundamental for reliable statistical analyses. Although many attempts to modify the technique have been implemented in order to obtain single projectiles of stable shape, SCL still lead to extremely “dirty” tests and the international community still consider shaped charges not reliable enough to derive BLEs.

Some work has been done on another class of blast launchers which use an explosive lensing principle. These launchers accelerate projectiles in two stages: the first stage is a linear explosive driver consisting of a reservoir of helium contained in a metal tube surrounded by a high explosive. The tube is collapsed inward by detonation, and produces a virtual piston travelling towards the projectile at the detonation velocity. The projectile and driver gas are accelerated into the second stage, igniting an explosive lens which also produces a virtual conical piston that accelerates the projectile to the final velocity. By proper selection of detonation rates and lens geometry, the virtual piston can travel at speeds well above the highest detonation speed.

With this method, velocities greater than 12 km/s have been obtained with projectiles of 0.2 grams [Canning].

ESA Shaped Charge

Battelle (Germany) developed for ESA a shaped charge technique that permits the generation of a single aluminium projectile having an impact velocity of 11.2 km/s, a cylindrical shape and adjustable aspect ratio of 3 to 6, and a mass between 0.8 and 1.5 g. The geometry of the device has been adapted to produce a non-stretching massive particle at the tip of the aluminium jet (**Figure 4.1-7**). The assembly includes a particle catcher and a slug catcher (**Figure 4.1-8**). The length of the isolated projectile is adjusted to the desired aspect ratio by consuming its leading portion by perforating a PVC-plate of proper thickness. Porous PVC foam catches small fragments ejected out of the shortening plate.

Experiments have highlighted the need to use a highly homogeneous charge of high explosive and an aluminium liner made of high purity material with fine grain size. Impact velocity is very reproducible [Bol, 1993, 1997].

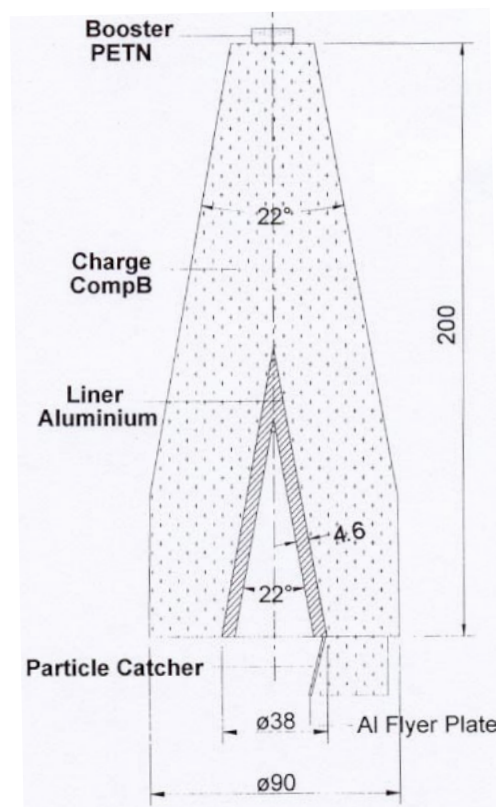


Figure 4.1-7: Battelle Shaped Charge

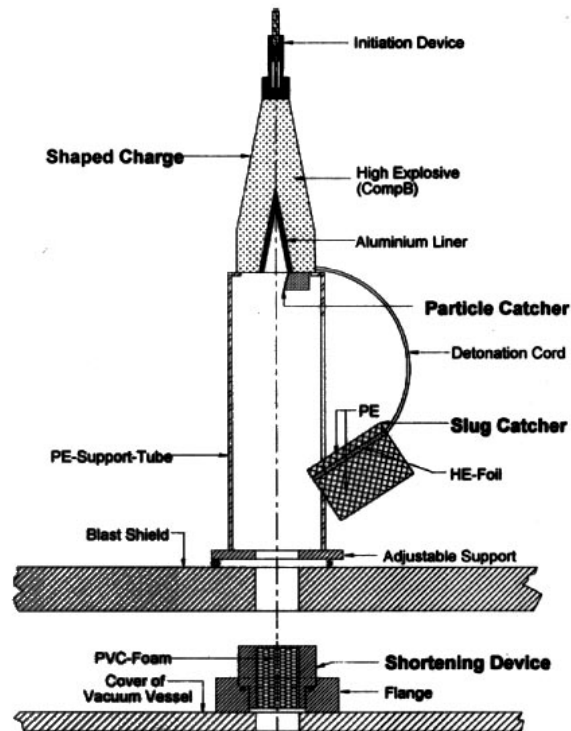


Figure 4.1-8: Battelle shaped charge assembly

NAL Shaped Charge

A description of the NAL shaped charge launcher is given in Kibe, 1999.

NASA Shaped Charge

NASA JSC has sponsored the development of an inhibited shaped charge launcher (ISCL) at Southwest Research Institute (SwRI), San Antonio Texas. The ISCL comes in four basic sizes. It is capable of launching nominally 0.25g, 0.5g, 1g, and 2g aluminum projectiles at 11.5 km/s. The projectiles are in the shape of hollow “cylinders”; i.e., pipe shape.

4.1.1.3 Hybrid Launchers

Since LGGs cannot accelerate impactors up to velocities typical of M/OD orbiting in LEO, many attempts have been made of developing new ultra high-speed launchers, to cover the velocity range of 10-15 km/s. These techniques, which fall in the category of Hyper Velocity Launchers (HVL), mainly implement a modification of standard LGGs, adding a third stage of acceleration. At the end of the launch tube, the second stage projectile impacts a sandwich of graded-density materials expressly designed to focus the shock waves on a flyer plate, which is accelerated up to 15 km/s [Chhabildas, 1995]. At the moment, the most important drawback of these machines is the possibility of launching disk-shaped projectiles only. Even the physical state of the impactor matter is difficult to control.

4.1.1.4 Electromagnetic Launchers

Electromagnetic Launchers are usually referred to as Rail Guns. Rail guns use Lorenz force to accelerate a metallic or plasma armature, which is the mobile part of an electric circuit immersed in a magnetic field. The travelling armature is designed to propel the projectile, which is thus accelerated (**Figure 4.1-9**).

One of the most interesting features of a rail gun launcher is its capability to serve as a booster accelerator. Since plasma-arc armature velocities higher than 14 km/s are routinely possible, rail guns could be used as the third stage of a LGG, to further increase the final output velocity of the projectile [Kim; Weldon, 1987; Toewer, 1987]. In this case, an adequate portion of the second stage propellant that follows the projectile from the LGG would be arc-energised to form the conducting plasma travelling armature of the rail gun. This arc formation event coincides with the triggering of the main rail gun current and allows the plasma arc armature to propel the projectile to very high velocity.

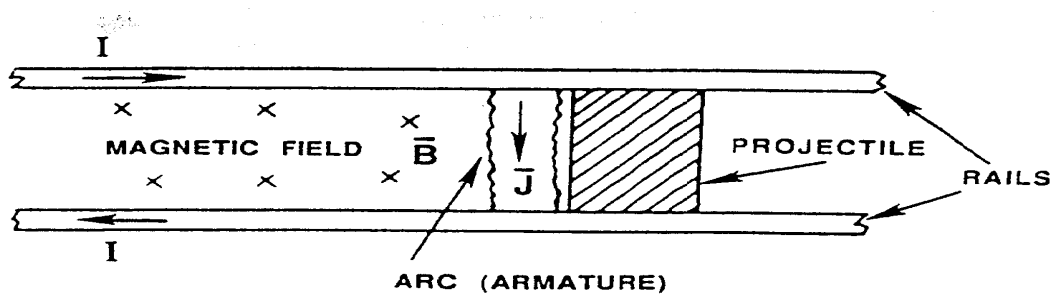


Figure 4.1-9: Rail Gun working principle.

The most crucial element of such an accelerator is that the gas breakdown that produces the plasma armature tends to occur in front of the projectile and not behind it. Moreover, the arc formation must be synchronised to the propellant exhaustion from the gas gun, and reliable triggering systems are still in the development phase.

4.2 Calibration Procedures

The purpose of the calibration is to ensure test results are reliable. A good shot can be defined as: a test with a complete record of the test conditions (mass and size of the projectile, dimension and mass of the target, impact incidence), good diagnostics (impact velocity, projectile integrity prior to impact, pressure in the test chamber), impact velocity within 0.1 km/s of the desired velocity and no degradation of the target by objects which are not the projectile (i.e., a clean test).

The PWG agreed that calibration of the test facilities is important to ensure that the tests at various facilities provide comparable results. The procedure to be used is:

- Hypervelocity impact test series is conducted by one agency (A) on multi-layer shields (usually 4 to 5 tests). All tests are to be near perforation/detached spall ballistic limit of the shields.
- Exact same test articles are prepared by the first agency (A) and shipped to the second agency (B) with projectiles and test instructions.
- Agency B completes the tests and sends targets back to Agency A.
- Agency A may have to repeat some tests to obtain close agreement in impact conditions such as impact velocity obtained at Agency B.
- Comparisons of results are made by both Agencies. Results are presented at IADC PWG meetings and documented in the PM.

4.3 Hypervelocity Launchers and Calibration

4.3.1 NASA

NASA hypervelocity impact launchers are located at Johnson Space Center's (JSC) White Sands Test Facility (WSTF). WSTF has 4 two-stage light-gas gun (LGG) ranges with launcher bore diameters of 1 inch (2.5cm), 0.5 inch (1.3cm), 0.17 inch (0.43cm), and 0.07 inch (0.17cm). The LGG guns at WSTF were calibrated with JSC-Houston hypervelocity impact launchers in 1998-1999 (prior to the JSC-Houston guns being consolidated at WSTF). Test reports are available demonstrating the good comparison between WSTF and JSC launchers. **Figure 4.3-1** provides some of the tests conducted in the calibration test series.

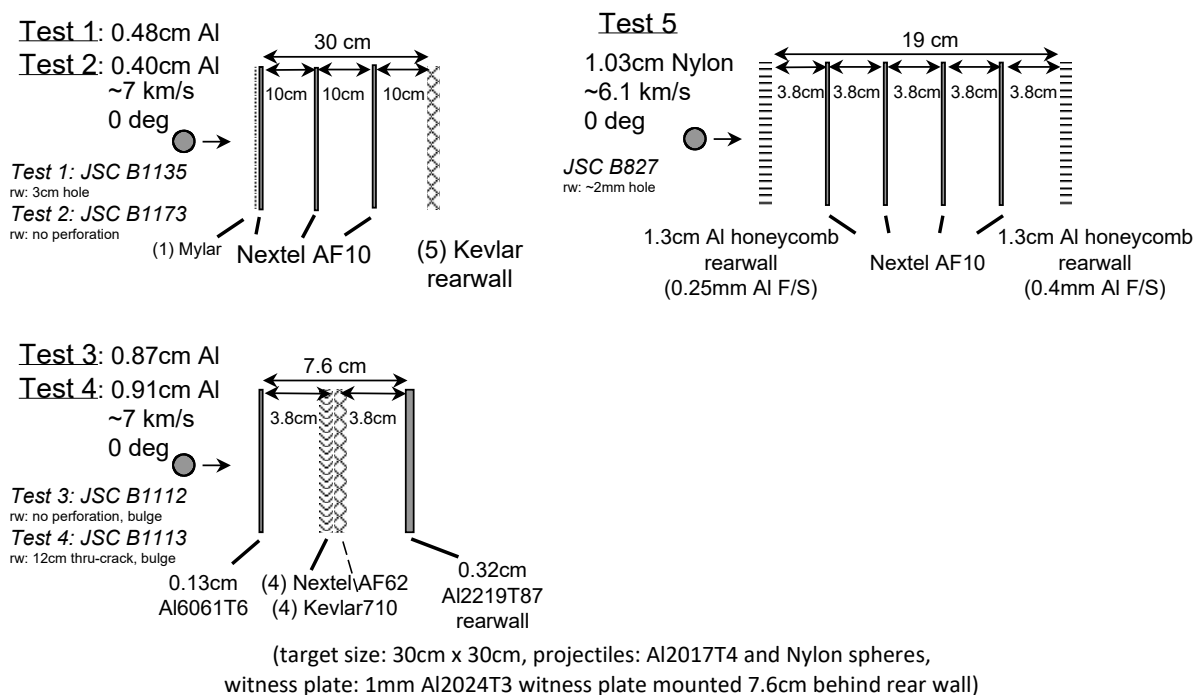


Figure 4.3-1: JSC HITF and WSTF test articles for WSTF 1" calibration with JSC 0.5" launcher

4.3.2 ESA – NASA Calibration

ESA/Ernst Mach Institute (EMI) and NASA JSC-Houston test facilities exchanged test articles in 1992. ESA has performed calibration shots on NASA Multi-Shock Shields and Mesh Double Bumper Shields at Ernst Mach Institute [Lambert, 1993].

All tests (at NASA & ESA) resulted in bulge but no perforation of the rear wall for the four different configurations (**Figure 4.3-2**). Results for two of the tests are summarised in **Table 4-1**. Based on all the tests performed, good agreement was observed between the ESA and NASA facilities.

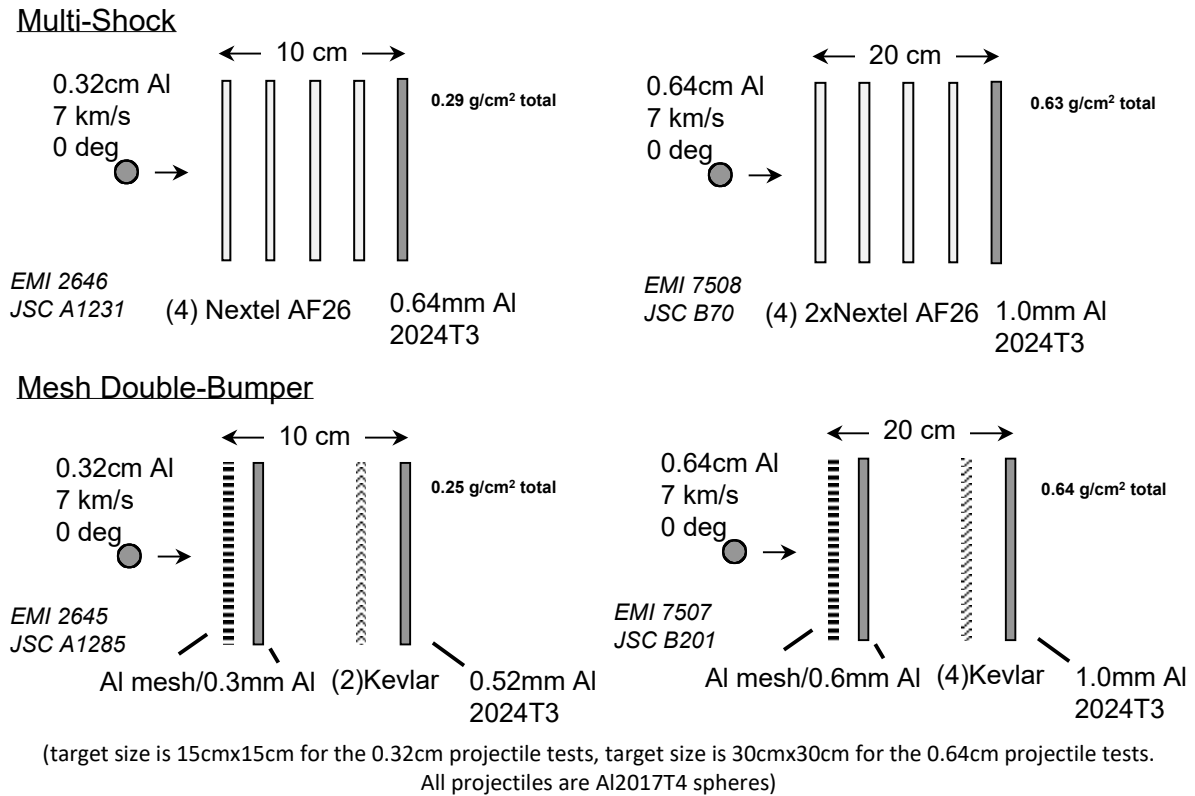


Figure 4.3-2: 1992 ESA-NASA calibration tests

Target	Backwall damage	Diameter total damaged area (mm)	Central crater diameter (mm)	Central crate depth (mm)	Diameter of the residual plastic deformation area (mm)	Height of the residual plastic deformation (mm)
Multi-Shock Shield (EMI test 7508)	Plastic deformation, no hole	59	not measurable	not measurable	115	12
Mesh Double Bumper Shield (EMI test 7507)	Plastic deformation, craters, no hole	64	0.7	0.4	70	7

Table 4-1: Summary of EMI test results for shields with 1mm Al 2024 T3 back-walls

4.3.3 NASA JSC-Houston and Khrunichev Space Center GOSINAS Calibration

Tests conducted in the NASA-KSC test calibration are described in **Figure 4.3-3**.

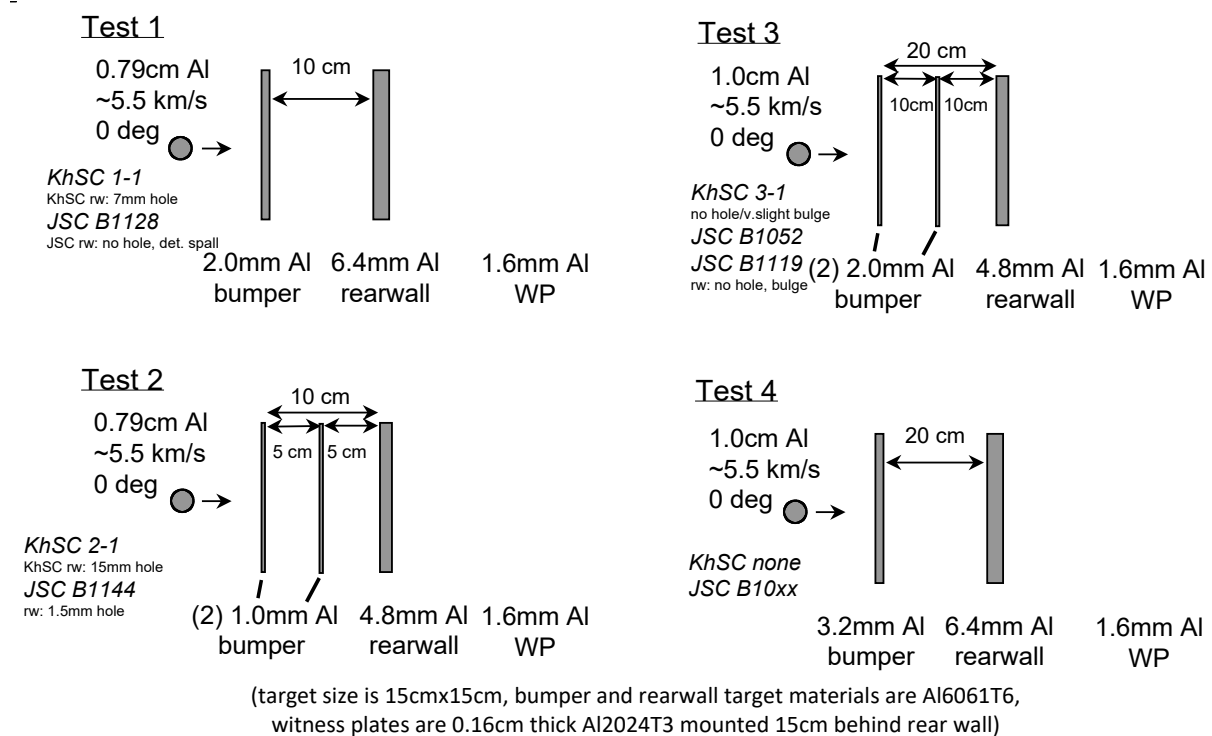


Figure 4.3-3: NASA JSC and KhSC calibration tests

Test Condition	NASA JSC		KhSC-GOSNIAS	
	Test #, Vel(km/s)	RW Damage	Test #, Vel(km/s)	Result
Test 1: 0.79 cm Al	B1128, 5.5	33 mm Det.Spall	KhSC-1, 5.37	Perf, 0.3 x 0.9 cm hole
Test 2: 0.79cm Al	B1144, 5.75	(2)Perfs, 1.5 mm	KhSC-2, 5.67	Perf, 1.5 cm hole
Test 3: 1.0 cm Al	B1119, 5.87	No perf, craters/bumps	KhSC-3, 5.97	No perf, craters
Test 4: 1.0 cm Al	B1050, 5.84	No perf, craters/bumps	Not Performed	None

Table 4-2: Summary of NASA - KhSC test results

4.3.4 NASA JSC and CNES

CNES and NASA JSC-Houston test facilities exchanged test articles in July 2000. CNES has performed calibration shots on NASA Multi-Shock Shields and Mesh Double Bumper Shields at CEG, France.

4.3.4.1 Test Description

Tests conducted in the CEG test calibration are described in **Figure 4.3-4**.

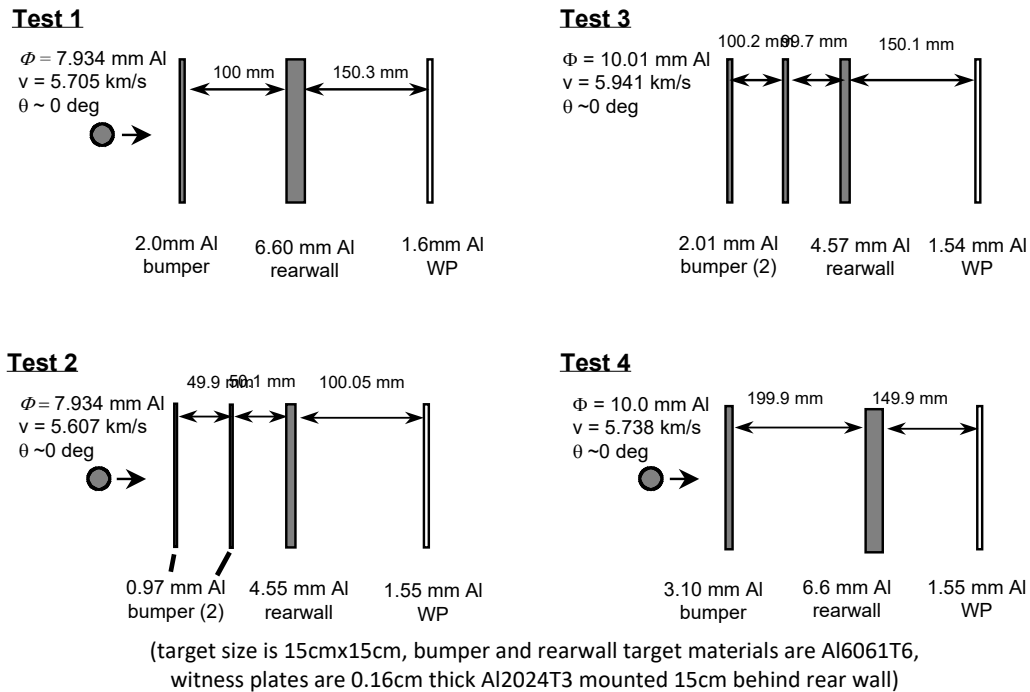


Figure 4.3-4: CNES and NASA JSC calibration tests

4.3.4.2 Test Results

Tests results are given in **Table 4-3**.

	Speed (km/s)	Plate 1	Plate 2	Plate 3	Witness Plate
Test #1	5.705	16.4 mm Hole	- 25*20 mm spall - multiple craters <3mm	NA	No damage
Test #2	5.607	12.6 mm Hole	- 37*40 mm hole - multiple craters <2mm	- no perforation - multiple craters <4mm	No damage
Test #3	5.941	18.9 mm Hole	- 85*75 mm hole - multiple holes <3mm - multiple craters <3mm	- no perforation - multiple craters <11mm	No damage
Test #4	5.738	22 mm Hole	- multiple craters <5mm	NA	No damage

Table 4-3: CNES and NASA JSC calibration tests

4.3.4.3 Test Simulations

All of the tests have also been simulated using the OURANOS Eulerian software; the aim being to determine the capabilities of OURANOS to simulate high velocity impacts on space structures.

Numerical Model

All calculations were made with OURANOS software V2R1 available at CEG.

The Eulerian calculation consists of a static mesh in which the physical phenomena occur. Material movements are followed through this fixed mesh.

All the space, which is supposed to receive materials after the projectile impact, is meshed.

The model is axisymmetric: the simulated plates are not squares but cylinders. Their radius was arbitrary fixed at 90 mm (intermediate value between the real half - side: 75mm and the diagonal of the square: 106mm)

The spatial mesh resolution is 2 elements / mm. This resolution allows results to be produced within reasonable CPU time.

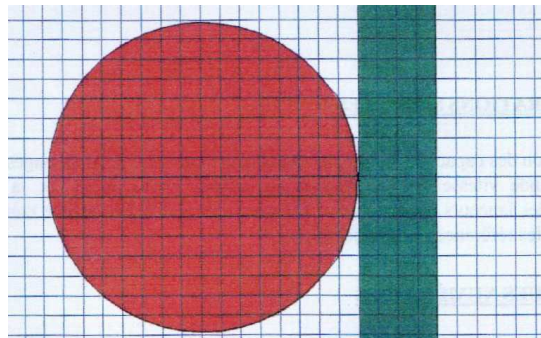


Figure 4.3-5: Numerical model using spatial mesh resolution of 2 elements / mm.

Projectile materials are simulated with a Mie - Gruneisen Equation of State; the Johnson - Cook EOS is used for the bumpers.

Damage of the bumpers is obtained for a stress higher than -1200 MPa.

Damage of the projectile is taken into account; a Tuler - Butcher model is used.

Calculation Results

Calculation results are presented hereafter. Time is chosen to be as representative as possible for the interference phenomena.

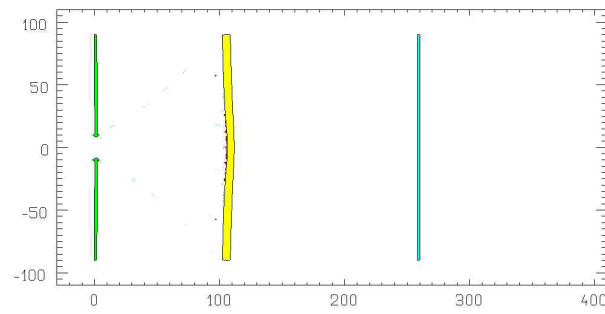


Figure 4.3-6: Test 1 @ 200 μ s

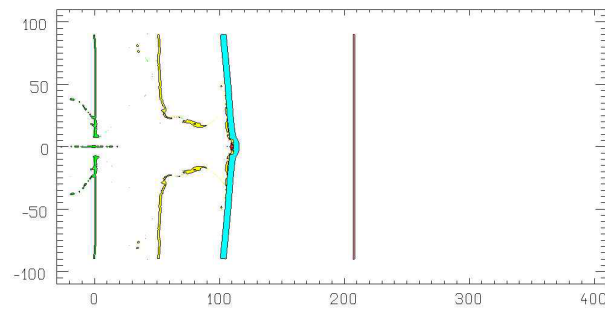


Figure 4.3-7: Test 2 @ 250 μ s

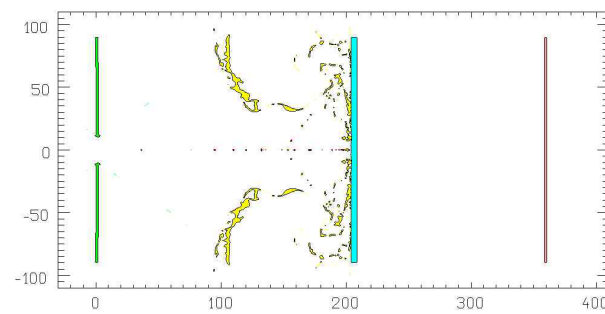


Figure 4.3-8: Test 3 @ 400 μ s

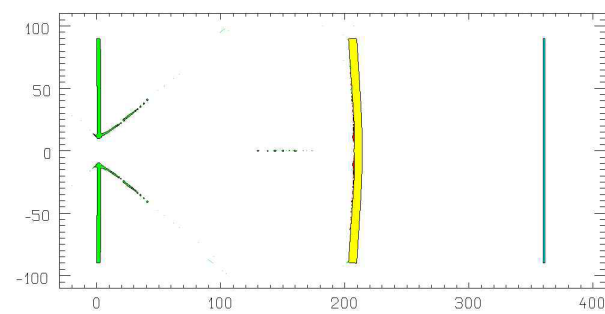


Figure 4.3-9: Test 4 @ 400 μ s

- Bumpers damage:

All the experimental and calculation results are summarised in Table 4-4. The targets are composed of one or two bumpers BP1 / BP2, a rear wall RW and a witness plate WP. Experience is correctly simulated with OURANOS.

	Test	BP1	BP2	RW	WP
Test 1	Ouranos calculation	φ 17 mm Hole	NA	Deformed (deflect. 3mm)	No damage
	Experiment	φ 16,4 mm Hole	NA	Detached spall	No damage
Test 2	Ouranos calculation	φ 14,1 mm Hole	φ 50 mm Hole	Deformed (deflect. 10mm)	No damage
	Experiment	φ 12,6 mm Hole	φ 37 mm Hole	Deformed	No damage
Test 3	Ouranos calculation	φ 19,6 mm Hole	φ 60 mm Hole Deformed φ 120	~Deformed	No damage
	Experiment	φ 18,9 mm Hole	φ 78 mm Hole Craters φ 105	Deformed	No damage
Test 4	Ouranos calculation	φ 21,4 mm Hole	NA	Deformed (deflect. 5mm)	No damage
	Experiment	φ 21,7 mm Hole	NA	Deformed	No damage

Table 4-4: Experimental and calculation results

- Fragments cloud:

All the physical characteristics of the fragment clouds after first plate perforation are given in Table 4-5.

	Test	Axial Speed (m/s)	Radial Speed (m/s)	BP1 hole diam (mm)	Cloud length (mm)	Cloud diam. (mm)	Length /diam.
Test 1	Experiment @ ---μs (*)	---	---	16.4	---	---	---
	Simulation @ 16μs	4735	1495	17.0	55.2	72.5	1.31
	Deviation			+3.6%			
Test 2	Experiment @ 7,4μs	5701	---	12.6	37	41.1	1.11
	Simulation @ 8μs	5080	1420	14.1	30	38.4	1.28
	Deviation	-10.8%		+11.9%	-18.9%	-6.6%	+3.5%
Test 3	Experiment @ 15.9μs	5296	---	18.9	65.6	81.1	1.24
	Simulation @ 16.0μs	5138	1645	19.8	61.2	78	1.27
	Deviation	-3%	-3.8%	+4.7%	-6.7%	-3.8%	+2.4%
Test 4	Experiment @ 11.7μs	4704	1440	21.7	43.1	49.3	1.14
	Simulation @ 11.0μs	4577	1460	21.4	41.2	45.6	1.10
	Deviation	-2.7%	+1.4%	+1.4%	-4.2%	-7.5%	+3.5%
	Experiment @ 21.8μs				91.7	71.2	1.28
	Simulation @ 21μs				91.5	72.1	1.35
	Deviation				-0.2%	+1.2%	-5.1%

Table 4-5: Physical characteristics of cloud fragments

The BP1 hole diameter is simulated relatively well, but always with a positive deviation. The deviation does not exceed 4 %, except for the case 2 where it was 12%. This high deviation can be explained by the very light thickness of the BP1 (1mm) for which the accuracy of the meshing (0.5 mm) is limited.

The dynamic expansion speed of the cloud is underestimated (between 2 and 10 %) which is correlated with the underestimation of the cloud length.

The deviations of length and diameter of the cloud are given for information only, since the time-steps for the test results and simulation results are not exactly the same. A better indicator is the ratio of length to diameter. **Figure 4.3-10** and **Figure 4.3-11** propose a visualisation of the test result / simulation comparison (test 2, first impact).

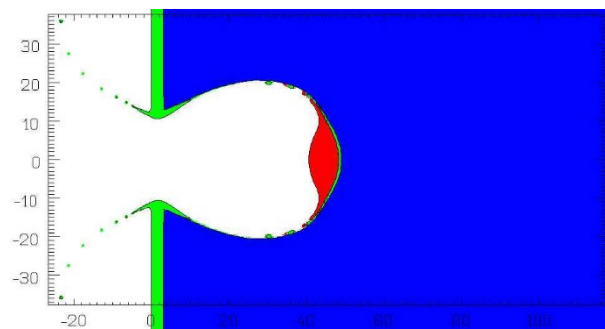


Figure 4.3-10: Test 2 @ $8\mu s$

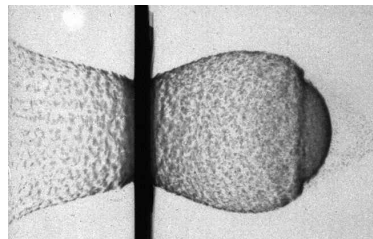


Figure 4.3-11: Test 2 @ $7.4\mu s$

Although the detailed composition of the cloud is not very well simulated, the physical mechanisms involved in the particle's motion are reproduced well.

Figure 4.3-12 and **Figure 4.3-13** propose a visualisation of the test result / simulation comparison (test 2, second impact).

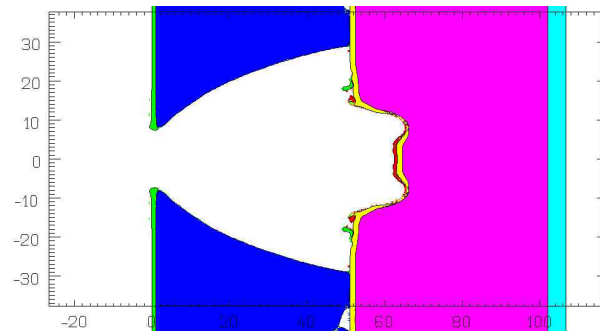


Figure 4.3-12: Test 2 @ 18 μ s

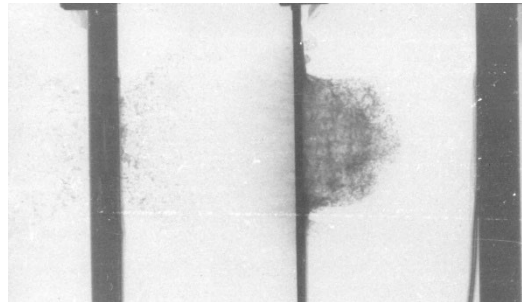


Figure 4.3-13: Test 2 @ 17.4 μ s

The results presented confirm the capabilities of the OURANOS Software to compute high velocity calculations. The Eulerian component of the software, which was used for these computations, allows the primary impact to be simulated and the flight of the debris cloud to be followed. The calculation duration is compatible to give responses in a relatively short delay. The actual limitation is the need for fine meshing to simulate more accurately the interaction process between projectile and bumpers.

4.3.5 NASA JSC and CNSA Test Calibration

NASA and China (CNSA) conducted a hypervelocity impact test series in 2011 and 2012. The target tested was a Whipple shield illustrated in **Figure 4.3-14**, using materials provided by CNSA. Projectiles were 3.2mm diameter aluminum 2017 spherical projectiles provided by CNSA. Three different test conditions were defined for these tests, specifically: (1) 5.8 km/s, 0 deg impact angle, (2) 5.5 km/s, 30 deg impact angle, and (3) 5.0 km/s, 30 deg impact angle. The results from the tests are given in Table 4-6 and Table 4-7. Photos of the impact damage are provided in **Figure 4.3-15**.

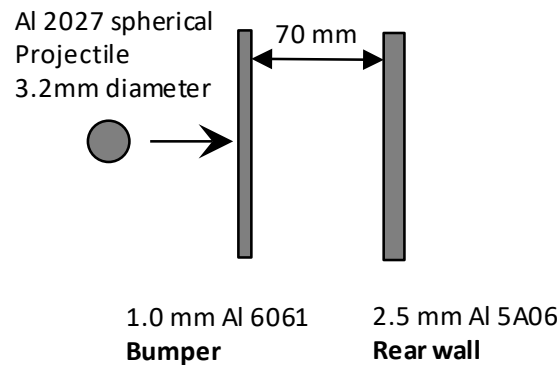


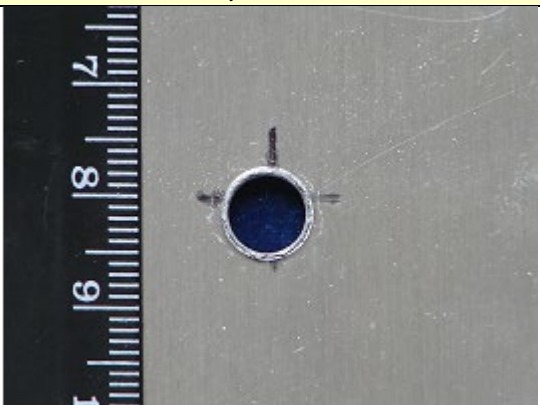
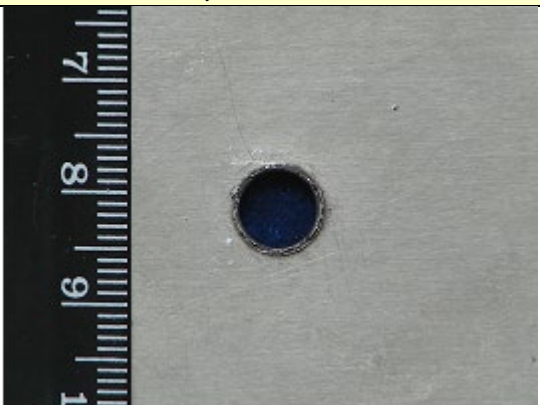
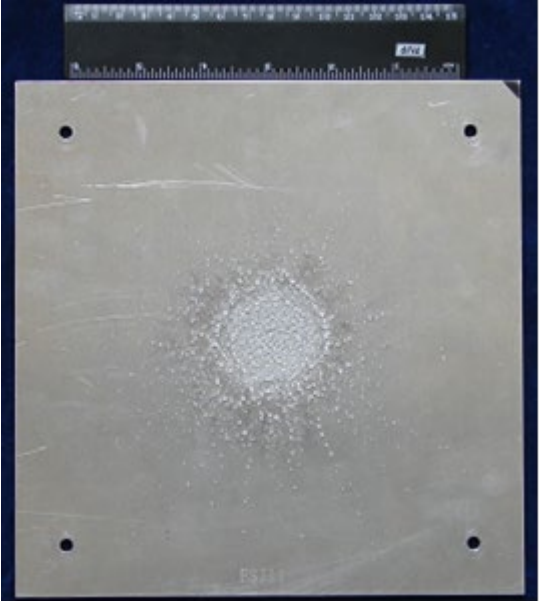
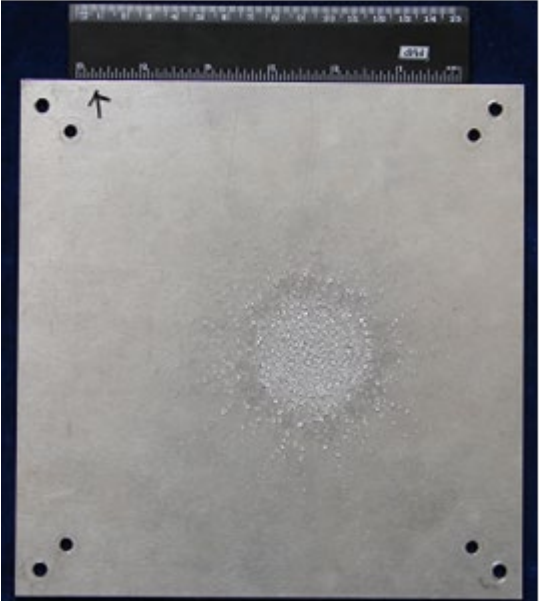

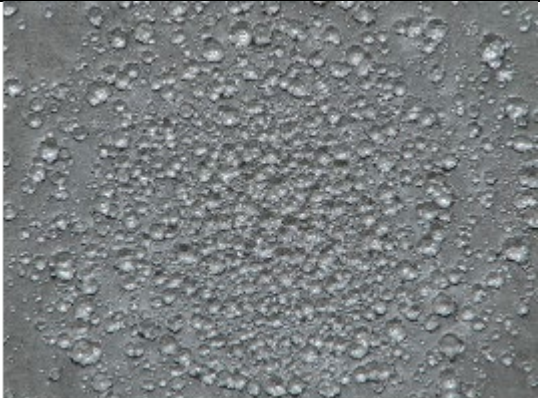
Figure 4.3-14: CNSA and NASA calibration test article


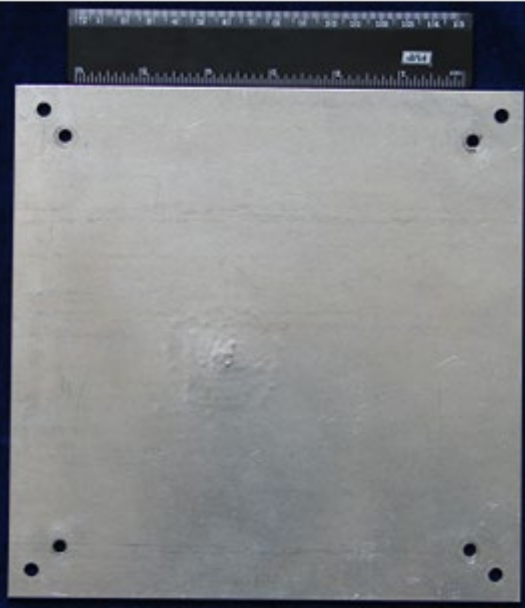


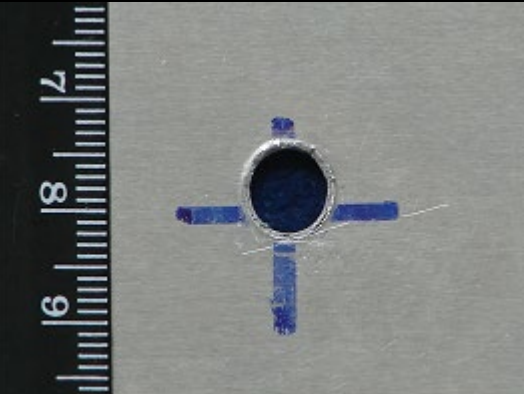
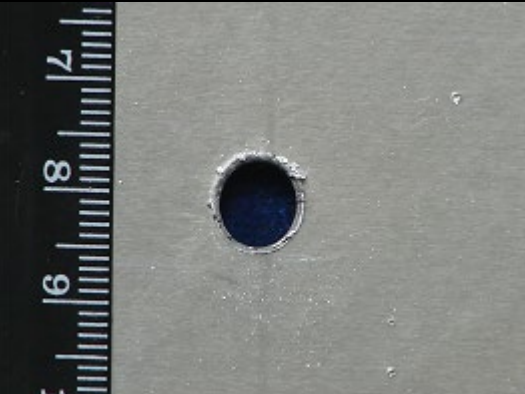
Test No.	Projectile diameter (mm)	Projectile mass (g)	Velocity (km/s)	Impact angle (deg.)	Rear wall (pen. / no pen.)	Bumper and Rear wall damage
1 HITF-11146	3.2	0.04779	5.77	0	No pen.	Bumper: One hole, inside diameter 6.8 mm, outside diameter 8.0 mm Rear wall: Multiple craters on front and bumps on back, largest crater on front 1.6 mm diameter by 1.7 mm deep, largest bump on back 0.8mm height.
2 HITF-11147	3.2	0.04788	5.30	30	No pen.	Bumper: One hole, inside diameter 7.5 x 6.9 mm, outside diameter 9.2 x 8.4 mm Rear wall: Multiple craters on front and bumps on back, largest crater on front 3.5 mm x 3.2 mm diameter and 1.8 mm deep, largest bump on back 0.8mm height.
3 HITF-12092	3.2	0.4767	5.01	30	Complete penetration	Bumper: One hole, inside diameter 7.4 x 6.8 mm, outside diameter 9.3 x 8.2 mm Rear wall: One perforation and multiple craters on front and bumps on back, perforation 1.4 x 0.8 mm diameter, largest crater on front 3.4 x 2.6 mm diameter, largest bump on back 2.1mm height.







Table 4-6: Summary of NASA JSC test results



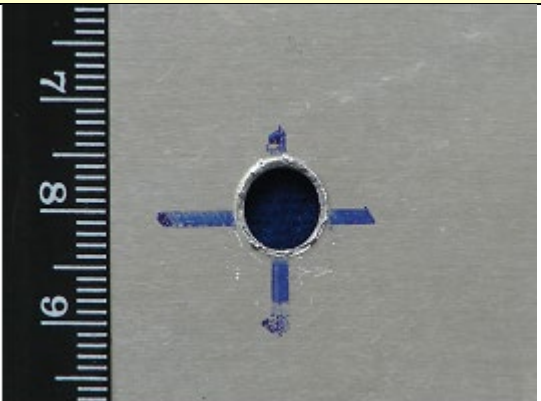
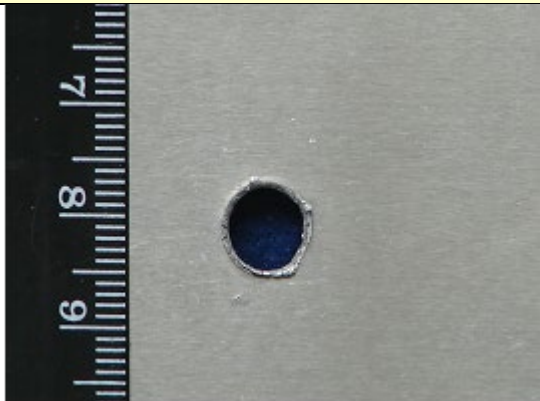


Test No.	Projectile diameter (mm)	Projectile mass (g)	Velocity (km/s)	Impact angle (deg.)	Rear wall (pen. / no pen.)	Bumper and Rear wall damage
1	3.2	0.04778	5.78	0	No pen.	Bumper: One hole, inside diameter 6.89 mm, outside diameter 8.1 mm Rear wall: Multiple craters on front and bumps on back, largest crater on front 1.68 mm diameter by 1.78 mm deep, largest bump on back 1mm height, a 0.7mm length small crack present.
2	3.2	0.04782	5.58	30	No pen.	Bumper: One hole, inside diameter 7.59 x 6.93 mm, outside diameter 8.99 x 8.15 mm Rear wall: Multiple craters on front and bumps on back, largest crater on front 2.39 mm diameter and 2.95 mm deep, largest bump on back 1.68mm height.
3	3.2	0.04785	5.00	30	No pen.	Bumper: One hole, inside diameter 7.38 x 6.72 mm, outside diameter 8.58 x 7.83 mm Rear wall: Multiple craters on front and bumps on back, largest crater on front 2.2 mm diameter and 2.28 mm deep, detached spall area 3.96mm × 3.99mm.

Table 4-7: Summary of CNSA test results

	NASA Test 1, HITF-11146	CNSA Test 1, HITRC-2011105
Bumper (close-up)		
Rear wall (front)		
Rear wall (front, close-up)		

	NASA Test 1, HITF-11146	CNSA Test 1, HITRC-2011105
Rear wall (back)		
Rear wall (back, close-up)		
	NASA Test 2, HITF-11147	CNSA Test 2, HITRC-2012011
Bumper (close-up)		

	NASA Test 2, HITF-11147	CNSA Test 2, HITRC-2012011
Rear wall (front)		
Rear wall (front, close-up)		
Rear wall (back)		

	NASA Test 2, HITF-11147	CNSA Test 2, HITRC-2012011
Rear wall (back, close-up)		
	NASA Test 3, HITF-12092	CNSA Test 3, HITRC-2012015
Bumper (close-up)		
Rear wall (front)		







	NASA Test 3, HITF-12092	CNSA Test 3, HITRC-2012015
Rear wall (front, close-up)		
Rear wall (back)		
Rear wall (back, close-up)		

Figure 4.3-15: Photographs of NASA and CNSA test articles

4.3.6 NASA JSC and CSA Test Calibration

NASA and Canada (CSA) completed a hypervelocity impact test series in 2012. The NASA tests were performed at White Sands Test Facility (WSTF) and CSA tests were performed at HIT Dynamics (HITD) in Fredericton. The targets tested were two sizes of multishock shields and two sizes of mesh double-bumper shields illustrated in **Figure 4.3-16**, using materials provided by CSA. The mass per unit area of the targets is 0.359 g/cm² and 0.647 g/cm² for the small and large multishock shields, respectively, and 0.330 g/cm² and 0.651 g/cm² for the small and large mesh double-bumper shields. Projectiles were 3.2 mm and 6.4 mm diameter aluminum 2017-T4 spherical projectiles provided by CSA. All tests were performed at a nominal velocity of 7 km/s and impact angle of 0 deg. The results from the tests are given in Table 4-8 and Table 4-9. Photos of the impact damage are provided in **Figure 4.3-17**.

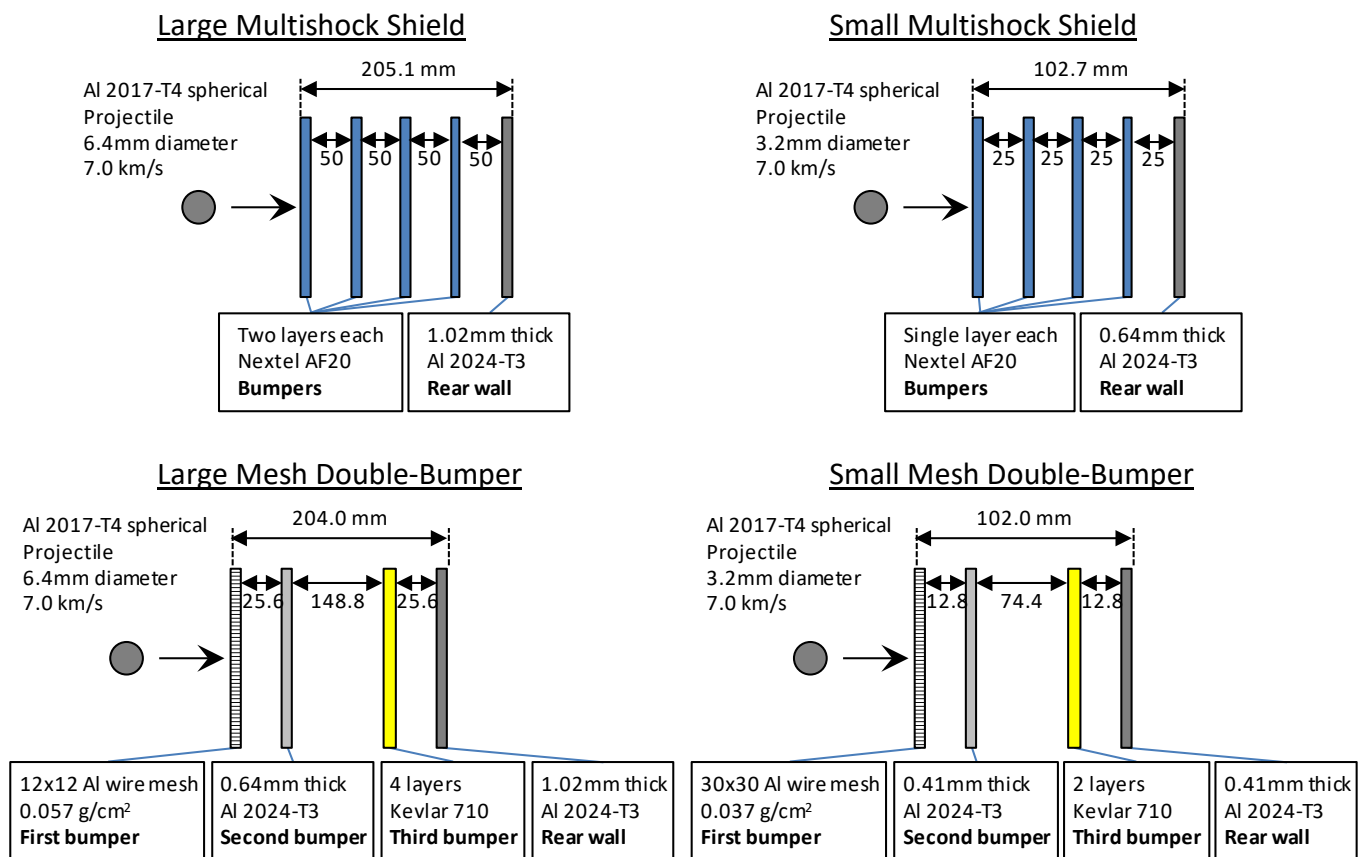


Figure 4.3-16: CSA and NASA test articles

Test No.	Projectile impact conditions	Target configuration and overall mass per unit area	Damage to bumper layers	Damage to Rear Wall
1 HITF-12001	3.2mm diameter Al, 0.04725g, 6.93 km/s, 0 deg impact angle	Small Multishock shield, 0.36 g/cm ²	Layer 1: 5.5 x 4.6 mm hole Layer 2: 17 x 17 mm hole Layer 3: 43 x 28 mm hole Layer 4: 45 x 33 mm hole	Bulge, dish (no failure) Impacted area 48mm diameter, bulge is 60mm diameter by 3.5mm high
2 HITF-12002	6.4mm diameter Al, 0.37406g, 6.86 km/s, 0 deg impact angle	Large Multishock shield, 0.65 g/cm ²	Layer 1: 10 x 10 mm hole Layer 2: 30 x 27 mm hole Layer 3: 47 x 44 mm hole Layer 4: 66 x 51 mm hole	Bulge, dish (no failure) Impacted area 86mm diameter, bulge is 116mm diameter by 9.4mm high
3 HITF-12003	3.2mm diameter Al, 0.04725g, 6.85 km/s, 0 deg impact angle	Small Mesh Double Bumper shield, 0.33 g/cm ²	Layer 1: 6.3 x 5.9 mm hole Layer 2: 8.9 x 8.7 mm hole Layer 3 (last layer of Kevlar): multiple perforations in 54 x 42 mm area with largest hole 3.9 x 3.8mm	Bulge, dish (no failure) Impacted area 48 x 42mm diameter, bulge is 43 x 37mm diameter by 1.3mm high
4 HITF-12004	6.4mm diameter Al, 0.37407g, 6.91 km/s, 0 deg impact angle	Large Mesh Double Bumper shield, 0.65 g/cm ²	Layer 1: 15 x 13 mm hole Layer 2: 26 x 15 mm hole Layer 3 (last layer of Kevlar): two perforations in 65 x 41 mm area, with largest hole 53 x 44mm	Bulge, dish with two small perforations Impacted area 87 x 70mm diameter, bulge is 98 x 95mm diameter by 4.9mm high, largest perforation is 1.7mm x 1.6mm diameter

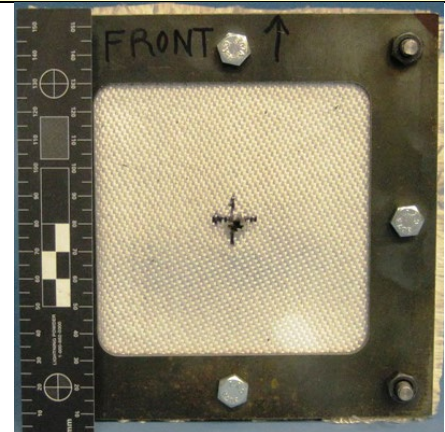

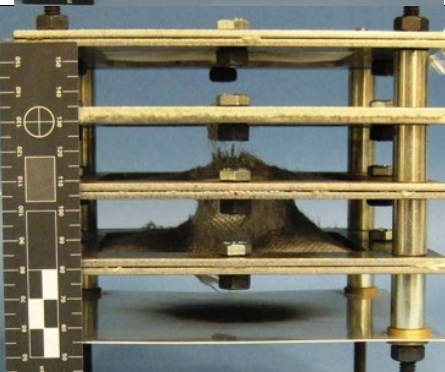


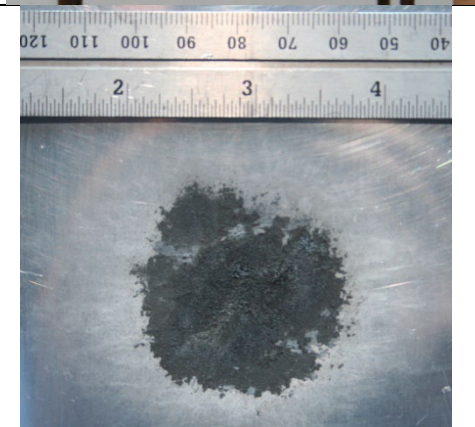


Table 4-8: Summary of NASA JSC test results

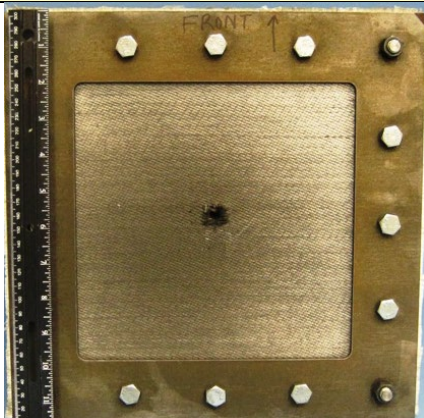
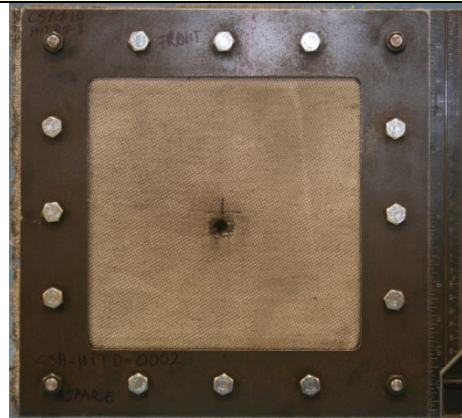



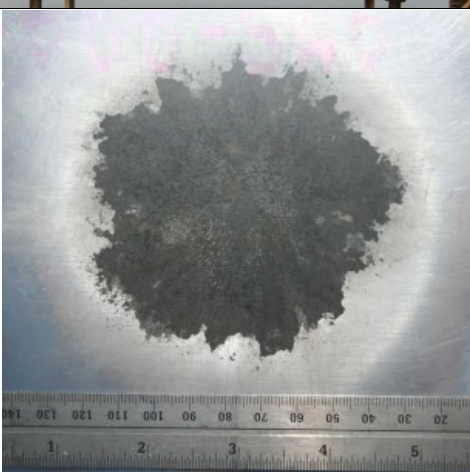

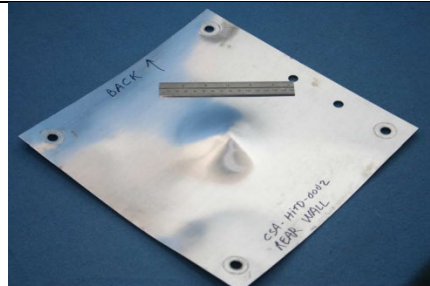
Test No.	Projectile impact conditions	Target configuration and overall mass per unit area	Damage to bumper layers	Damage to Rear Wall
1 CSA-HITD-0001	3.2mm diameter Al, 7.04 km/s, 0 deg impact angle	Small Multishock shield, 0.36 g/cm ²	Layer 1: 4.5 x 4.5 mm hole Layer 2: 17 x 17 mm hole Layer 3: 31 x 30 mm hole Layer 4: 41 x 39 mm hole	Bulge, dish (no failure) Impacted area 45mm diameter, bulge is 58 x 55 mm diameter by 2.6mm high
2 CSA-HITD-0002	6.4mm diameter Al, 7.00 km/s, 0 deg impact angle	Large Multishock shield, 0.65 g/cm ²	Layer 1: 10 x 10 mm hole Layer 2: 29 x 30 mm hole Layer 3: 52 x 56 mm hole Layer 4: 71 x 68 mm hole	Bulge, dish (no failure) Impacted area 87 x 82 mm diameter, bulge is 107 x 105mm diameter by 10 mm high
3 CSA-HITD-0003	3.2mm diameter Al, 7.07 km/s, 0 deg impact angle	Small Mesh Double Bumper shield, 0.33 g/cm ²	Layer 1: 5.3 x 6.3 mm hole Layer 2: 10 x 9.3 mm hole Layer 3: multiple perforations in 40 x 46 mm area, with largest hole 4.5 mm diameter (see Note 1)	Bulge, dish (no failure) Impacted area 42 x 37 mm diameter, Bulge is 51 x 47mm diameter by 1.2mm high
4 CSA-HITD-0004	6.4mm diameter Al, 7.01 km/s, 0 deg impact angle	Large Mesh Double Bumper shield, 0.65 g/cm ²	Layer 1: 11 x 10 mm hole Layer 2: 18 x 17 mm hole Layer 3: 55 x 53 mm hole (see Note 2)	Bulge, dish (no failure) Impacted area 73 x 62 mm diameter, Bulge is 90 x 85mm diameter by 4.4mm high

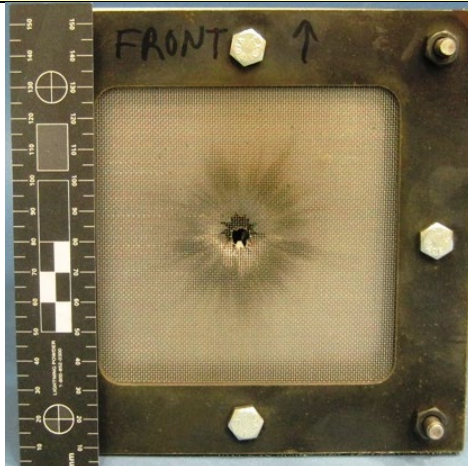
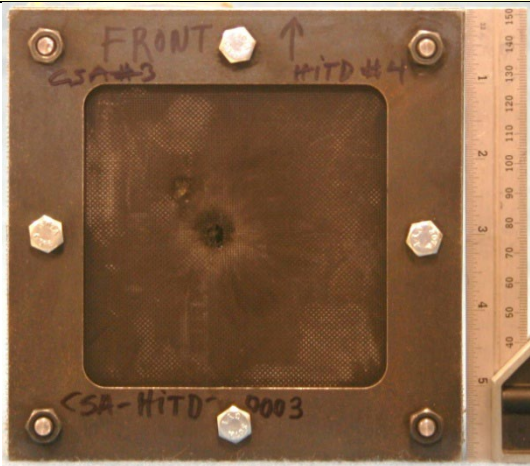
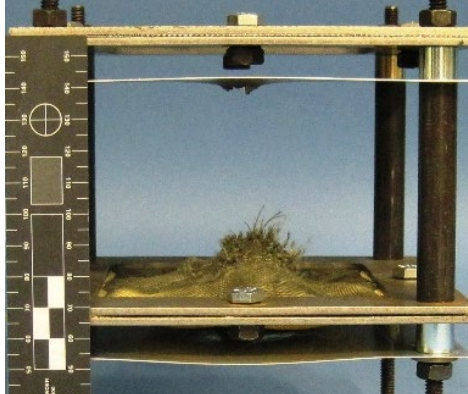
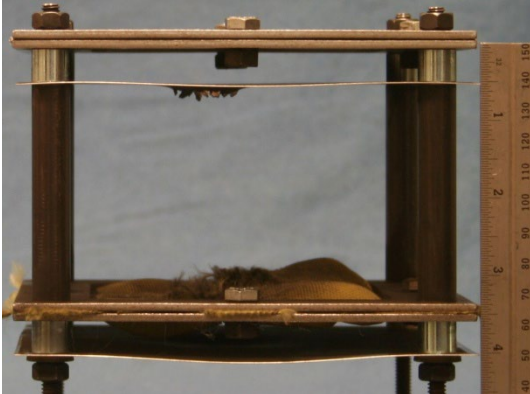
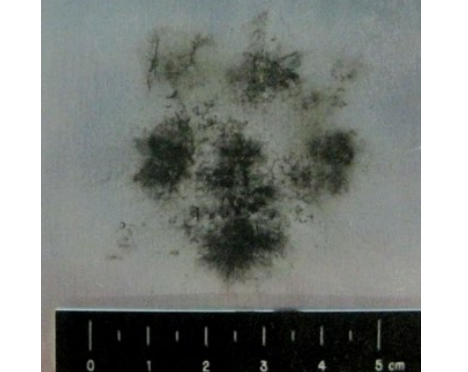

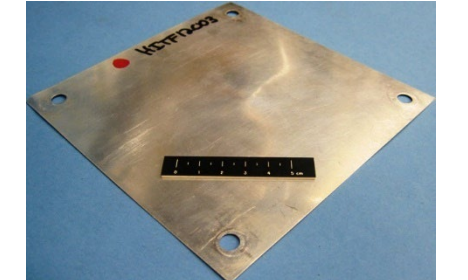

Note 1: 1 secondary impact from sabot debris caused full perforation of 1st layer (3mm dia.) and on the 2nd layer (12 x 6 mm).

Note 2: 3 secondary impacts from sabot debris caused full perforation of the 1st layer (2 to 5 mm dia.) and small indents on 2nd layer.

Table 4-9: Summary of CSA test results

	NASA Small Multishock, HITF-12001	CSA Small Multishock, CSA-HITD-0001
Target (front)		
Target (side)		
Rear wall (front, close-up)		
Rear wall (back, oblique)		

	NASA Large Multishock, HITF-12002	CSA Large Multishock, CSA-HITD-0002
Target (front)		
Target (side)		
Rear wall (front, close-up)		
Rear wall (back, oblique)		

	NASA Small Mesh Double, HITF-12003	CSA Small Mesh Double, CSA-HITD-0003
Target (front)		
Target (side)		
Rear wall (front, close-up)		
Rear wall (back, oblique)		

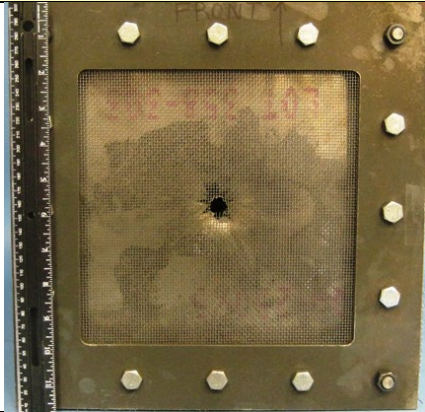
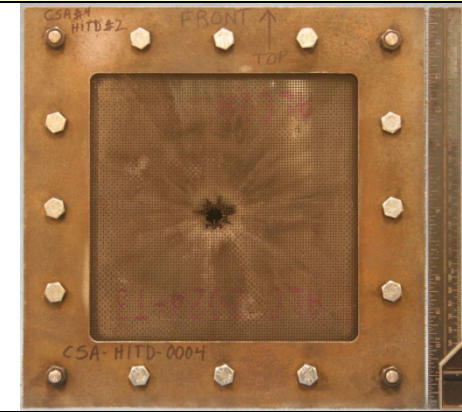
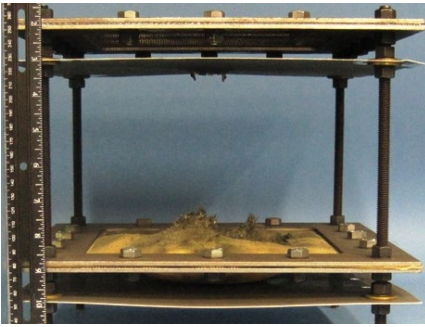
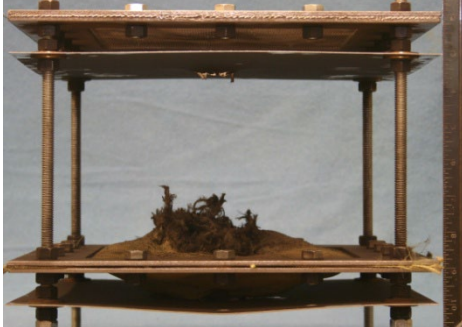
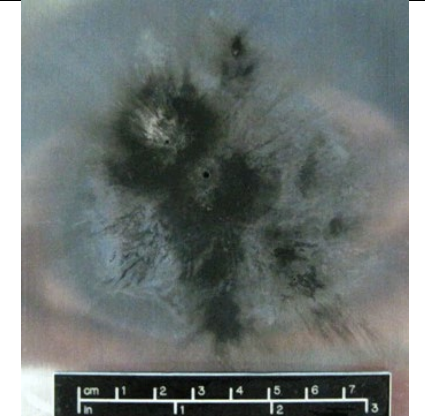
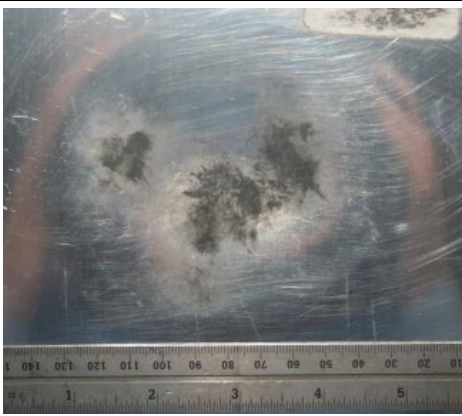


	NASA Large Mesh Double, HITF-12004	CSA Large Mesh Double, CSA-HITD-0004
Target (front)		
Target (side)		
Rear wall (front, close-up)		
Rear wall (back, oblique)		

Figure 4.3-17: Photographs of NASA and CSA test articles

4.4 Test Facilities

4.4.1 JAXA Two-Stage Light Gas Guns

The hypervelocity Impact facility, the Institute of Space and Astronautical Science (ISAS), Japan Aerospace Exploration Agency (JAXA) has 2 accelerators for space engineering and planetary sciences.

One is a horizontal one- and/or two-stage light gas gun with a 7.0 mm bore launch tube. Achievement range of velocity of the horizontal accelerator is 0.03-0.7 km/s using one stage mode and 0.6-8 km/s using two-stage mode. These include unsteady operation, and the actual performance of velocity range is 0.3-0.7 km/s using one stage mode and 0.6-7 km/s using two-stage mode. Acceleration of a projectile with diameter 0.08-3.2 mm and powder with diameter 0.003-0.5 mm is possible using a sabot. The accelerator has a 1 m diameter chamber with 2 m length.

Another is a vertical one- and two-stage light gas gun with a 4.65 mm bore launch tube. Achievement range of velocity of the horizontal accelerator is 0.09-0.8 km/s using one stage mode and 0.9-7 km/s using two-stage mode. These include unsteady operation, and the actual performance of velocity range is 0.3-0.7 km/s using one stage mode and 0.6-6 km/s using two-stage mode. Acceleration of a projectile with diameter 1-2 mm is possible using a sabot. The accelerator has a 1.5 m diameter chamber with 2 m length.

The vacuum degree of the test chamber of both accelerators is several Pa. The facility has high speed cameras as *In-situ* instruments. The facility also has electric scales, an optical microscope, an electron microscope, a laser displacement meter, and a compression testing machine for analysis of pre- and/or post-impact.



Figure 4.4-1: JAXA two-stage light gas guns: (left) the horizontal accelerator, (right) the vertical accelerator.

4.4.2 ROSAVIAKOSMOS

The usual means are LGG [Jakhlakov, 1997]. The velocity of an impactor along the range and just before the sample can easily be measured by registration of the times of impactor passage through several points. Registration is made with the help of piezoelectric, photoelectric and inductive sensors. Signals from sensors are registered in one reference time system by oscilloscopes. The velocity measurement system is certified. Accuracy of velocity measurement is within 1.5%.

The State Research Institute of Aviation Systems (SRIAS - ROSAVIAKOSMOS) also have standard LGG installations. They are also developing a new small-size two-stage acceleration device; the second step is a running explosive barrel squeeze [Petrinin; Smirnov; Gadassine, 1998, 1999]. At the present time, 2-10 mm diameter steel, titanium and aluminium projectiles have been accelerated. Yielded velocities are in the 5-11 km/s interval.

Multistage explosive advanced launching technology (at the Institute of Experimental Physics of Russian Federal Nuclear Center) can propel projectiles up to 15 km/s [Lebedev]. Using a special buffer they manage to moderate the shock wave's intensity. For this method it is important that there are advanced diagnostic apparatuses available; i.e. both optical and X-ray.

4.4.3 Russian Federal Nuclear Center VNIIEF (RFNC-VNIIEF, Sarov)

Two-stage LGG facilities of 12.7, 23, 34, 50, 85 and 100 mm calibre are available at VNIIEF for HVI testing of S/C elements. All of the LGGs have a powder-driven first stage, and hydrogen or helium is used in the second stage. Projectiles of various forms (sphere, cylinder, disk) made of aluminium, titanium alloys, or steel can be used. Work range: velocity up to 4 km/s for projectiles of mass 1-1.5 kg, and up to 7 km/s for 1-10 g projectiles [Bokhan *et al.*, 1992; Belov *et al.*, 1993, 1997; Schlyapnikov *et al.*, 1998; Kulikov *et al.*, 1998; Kostin *et al.*, 1998].

Because of barrel wear and projectile distortion during operation at extreme velocities (>6 km/s), projectile velocities 1-2 km/s higher are obtained by coupling of LGGs and blast accelerating systems (BAS) for additional acceleration of projectiles [Mogilev *et al.*, 1998].

Blast accelerating systems (BAS) use high power high-order explosives (HE), where energy is effectively transformed by specially shaped systems into projectile kinetic energy. BAS-launched projectiles can be of a constant shape, or vary their shape during acceleration. Projectiles may be spherical (ellipsoidal), disks or thin-walled shells. Some types of BASs produce a directed stream comprising a large number of separated hypervelocity small-sized projectiles. Parameters of projectiles produced by some types of BASs are presented in Table 4-10 (for ellipsoidal projectiles: d - diameter, L - length, $l=L/d$; for disk projectiles: d - diameter, h - thickness) [Belov *et al.*, 1993, 1993, 1993, 1995, 1997; Yu.V. Bat'kov *et al.*, 1997].

Projectile mass (g)	Projectile velocity (km/s)	Type of projectile
300-350	3	Ellipsoid, l=2
170	4-5	Ellipsoid, l=1
20	6	Ellipsoid, l=1
0.7-2.1	7-8	Ellipsoid, l=1.5
0.1-0.7	7-8	Ellipsoid, l=1
3.5 10 ³	4.2	Disk d=240mm, h=10mm
180	7.5	Disk d=120mm, h=2mm
9	9.3	Disk d=60mm, h=0.5mm
2.8	12.5	Disk d=40mm, h=0.5mm (Ti)
0.5	5.5	Directed stream of projectiles
0.01-0.2	>12	Directed stream of projectiles

Table 4-10: Achieved range of BAS acceleration parameters.

Hypervelocity impact studies can be performed using vacuum chambers coupled with cut-off devices. Thus, only the projectile passes into the chamber, the target is protected from explosion products, and debris is caught after target fracture.

Numerical codes RXL, B71, DMK and EGAK are used for numerical simulation of the acceleration process [Derjugin *et al.*, 1988; Meltsas *et al.*, 1993, 1997].

Flash X-ray units; high-speed cameras; various types of sensors, stress, impulse and acceleration gauges are used for registration of projectiles acceleration, forming and interaction with target processes [Belov *et al.*, 1993, 1997].

The main parameters of some stationary X-ray units implemented at RFNC-VNIIEF are presented in Table 4-11. Available movable soft X-ray units with gamma-quantum energy of <1 MeV can be used also. Two- and three-aspect X-ray registration can be provided. NORA, MIRA, PIR soft X-ray units are used also.

Unit	Quantum energy (MeV)	Flash duration (mks)	Number of flashes	Capacity (mm of lead)
BIM 234	70	0.25	1-10	180
BIM 234	70	0.25	1	220
GONG	1	0.01	1	50
Eridan-3	1	0.3	1 и 2	60

Table 4-11: Main parameters of stationary X-ray units

The main parameters of some high frame-rate cameras implemented at RFNC-VNIIEF are presented in Table 4-12. Multi-aspect optical registration can be provided (it is possible to synchronise control of up to seven cameras SFR-2M (VFU-1)). Flash stationary and explosive illumination devices of up to 100 MW can be used.

Camera type	SFR-2M	VKF-13
Film speed, km/s	0.25-3.75	0.5-16
Maximal framing rate, 10 ⁶ frames/s	2.5	8
Maximal frame size, mm	10	16×22
Size of photogram, mm	22×375	70×550
Resolution, lines/mm	16-24	30
Time intervals resolution in streak-camera regime, ns	20	5

Table 4-12: Main parameters of high frame-rate cameras

The main parameters of apparatus applied at RFNC-VNIIEF for measuring of plasma parameters while hypervelocity projectile-target interaction are presented in Table 4-13.

Calorimeter TPI-2-5	Spectral range	0.2-10 μm
	Sensitivity	0.02 J
	Radiation receiver area	12 cm^2
Coaxial photometer FEK-22	Spectral range	0.25-0.7 μm
	Sensitivity at radiation wavelength 350 nm	1 W
	Photo-cathode area	12 cm^2
Spectrograph STE-1	Spectral range	0.25-0.7 μm
	Resolution at radiation wavelength 250 nm	0.04 nm
Streak camera SFR-2M with spectroscopic unit SP-77	Spectral range	0.3-0.65 μm
	Resolution at radiation wavelength 400 nm	2 nm
	Time intervals resolution	0.2 μs

Table 4-13: Main parameters of apparatus for plasma parameters measuring.

Among the test facilities in Russia, there is the Model Ballistic Range (MBR) located at: Laboratory of Aeroballistic Research, Scientific Technological Center #1, TSNIIMASH, Pionerskaya Str. 4, Korolev, Moscow Region, 141070, Russia.

MBR includes:

- two stage light gas gun,
- vacuum chamber,
- gas distribution system,
- vacuum system,
- power system,
- remote control system,
- diagnostic and measurement system.

There are two regimes of the first stage:

- powder regime (in velocity range 4-6 km/s),
- nitrogen regime (in velocity range 2.5-4 km/s).

The impactor is enclosed in a sabot. It is accelerated in the barrel with the help of hydrogen compressed by a piston in the first stage. The vacuum chambers have an overall volume of 15

cubic meters, and are connected to each other with a total length of 19 m. The chamber diameter is 1.8m within the first 14 m, and 1.5 m along the remaining length.

Shield samples are installed in the 1.5 m diameter vacuum chamber at a distance of 14.5m from the barrel's end. Vacuum pressure is in the range of 10-50 mm of mercury necessary for sabot aerodynamic separation.

The velocity of an impactor along the range and just before the sample is measured by registration of the times of impactor passage through several points. Registration is made with the help of piezoelectric, photoelectric and inductive sensors. Signals from sensors are registered in one reference time system by oscilloscopes. The velocity measurement system is certified. Accuracy of velocity measurement is within 1.5%.

4.4.4 ASI-CISAS

CISAS hypervelocity impact facility is based upon a two-stage light-gas gun (see Table 4-14), that has been designed to achieve a very high shot repetition rate (shot frequency in the following) together with low operational costs, thus overcoming one of the limitations in the field of hypervelocity impact testing, i.e. the lack of experiments. The opportunity of reaching a high shot frequency is due to the particular LGG set-up, that uses (i) a light gas to push the piston along the pump tube, (ii) pneumatic and electric valves instead in the high pressure section, and (iii) a pneumatic damping system to avoid piston strike in the transition section between the pump tube and the barrel. As a consequence, CISAS LGG [Angrilli, 1999] is able to accelerate a mass (sabot + projectile) of 100 mg up to 5.5 km/s, with a shot frequency of 1-2 shots per hour, including the time required to replace the target in the test chamber and the projectile in the barrel.

In a typical shot operation, high pressure gas is stored in the first stage reservoir, until discharged on the back of the piston through the opening of a custom fast valve. The driver gas coming from the first stage pushes the piston along the pump tube, thus compressing the propellant in the second stage up to very high pressure (max. 7000 bar) and temperature. The operating conditions are chosen to allow the piston to stop within a few mm of the cylinder head and reverse direction before striking onto the gun head. At the same time, the compressed gas is channelled into the launch tube through a dedicated group of valves, that have been developed to achieve the optimal energy transfer from the second stage gas to the projectile. The piston bounces on the gas cushions of the first and second stage, beginning a sequence of free oscillations. Each functional component of the gun (i.e., the first stage valve, the piston and the head valves) has been designed to survive many shots (at least 50 for the weakest component) without maintenance operations. This is possible through the exploitation of a particular management system, that checks continuously a set of diagnostic parameters [Angrilli, 1998; De Cecco, 1998], to establish the level of deterioration of each subsystem and the overall LGG performance. Moreover, the management system is dedicated to controlling the gas flow towards the barrel and the pump tube re-filling with fresh gas, to damp piston oscillations and avoids piston impacts on the gun head with consequent seize-up.

CISAS LGG can launch both solid cylinders and sabots. The latter are separated by means of aerodynamic drag in the flight chamber and can carry projectiles in the diameter range 0.4 – 3 mm.

The sabot and projectiles velocity is measured by two laser barriers [De Cecco, 1998], that are able to sense 0.4 mm particles flying at 6 km/s. The target vacuum chamber has been designed to allow fast and easy target substitution operations. The maximum target size is 400 mm x 400 mm (200 mm x 200 mm is the standard condition); target temperature control is possible in the range 160 – 380 K, to test components in an environment that better represents space conditions. At present, the available instrumentation includes (i) an optical impact detector that senses the visible flash emitted by the hypervelocity impact, (i) three shock accelerometers attachable to the target and/or to the target support system, (iii) a photographic equipment to catch 4 shadowgraphs with a maximum frame rate of 1 MHz (see Table 4-15), (iv) a contact-less Co-ordinate Measuring Machine for target mapping.

First stage reservoir	Working gas	He
	Volume [dm ³]	3
	Filling pressure [bar]	1 - 200
Pump tube	Working gas	H ₂ /He
	Inner diameter [mm]	35
	Length [m]	3
Barrel	Volume [dm ³]	3
	Filling pressure [bar]	1 - 5
	Inner diameter [mm]	4.76, 6
Shot frequency	Length [m]	1.5 – 2.5
	[shots/day]	10 - 15
	Sabot	
Projectile	Aerodynamic separation	
	Mass [mg]	Up to 100
	Diameter [mm]	0.4 – 3
	Velocity [km/s]	Up to 5.5

Table 4-14: CISAS LGG – main functional parameters

Number	Description
2	High-sensitivity laser barriers to measure the projectile speed
1	Optical impact detector to sense the flash emitted by the hypervelocity impact
2	Vacuum gauges to measure the pressure in the flight chamber and in the vacuum chamber
10	RTD gauges to measure the target temperature at different locations
2	Shock accelerometers to be paced on the target and/or support system
1	Shadowgraph equipment to catch 4 images with a frame rate up to 1 MHz
1	Contact-less co-ordinate measuring machine for target mapping (max target size 400 mm x 400 mm)

Table 4-15: Instrumentation available

Moreover, the CISAS hypervelocity impact facility has the following unique characteristics:

- No part of the LGG needs to be disassembled, checked or substituted after a shot;
- The high shot frequency (up to 15 shots per day) allows hypervelocity impact tests to be performed in a short time, easily changing the experimental configuration.
- The high shot frequency allows a lot of test data to be collected, to employ a statistical approach in analysing the results.
- The target chamber allows HVI tests to be performed with target temperature control.

Finally, CISAS is also designing a new unit to accelerate 1g sabot projectile at 6 km/s with the same shot frequency of the unit already developed [Francesconi, 2001].

4.4.5 Ernst-Mach-Institute

At the Ernst-Mach-Institute (EMI), three high-velocity impact facilities are used for the simulation of space debris and micrometeoroid impacts on spacecraft components. The impact facilities are closed indoor two-stage light-gas guns. All guns are operated with Hydrogen or Helium gas. All two-stage light gas guns can also be operated in powder gun mode. A detailed description of the guns can be found in Stilp [Stilp, 1987].

The small light gas gun (SLGG, babygun) has a 4 mm or 5 mm diameter launch tube and a 15 mm diameter pump tube. It is used for projectile sizes between 100 μm and 2 mm. Particles with a diameter below 500 μm (down to 100 μm) can only be accelerated in shotgun mode (**Figure 4.4-2**). The maximum velocity at this gun is approximately 8.5 km/s.

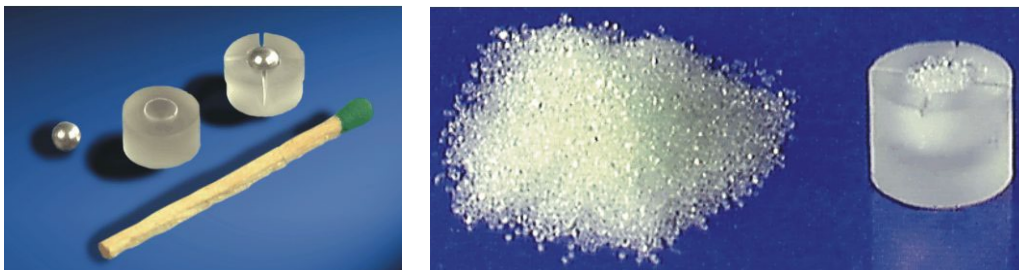


Figure 4.4-2: Sabot for the acceleration of individual projectiles (left) and projectiles having a diameter of a fraction of a millimeter (right)

The medium-size light gas gun (MLGG, **Figure 4.4-3**) is operated with launch tube diameters ranging from 6.5 mm to 15 mm. The pump tube diameter is 40 mm. The maximum velocity it reaches is about 10 km/s for projectile masses of about 5 mg.

The large light gas gun (LLGG) has launch tube diameters between 20 and 50 mm. The pump tube diameter is 65 mm. Its maximum velocity is 8 km/s for projectile masses up to 1 gram. This gun is usually operating at velocities below 3 km/s involving the acceleration of large masses.

Figure 4.4-4 shows a performance diagram of the EMI light gas guns. Mass refers to the total mass that is accelerated i.e., projectile mass and the mass of the sabot. The figures of the

individual performance curves refer to the pump tube diameter and launch diameter. **Figure 4.4-5** shows a performance diagram of all acceleration facilities available at EMI. The masses plotted in this diagram refer to the projectile masses that are accelerated.

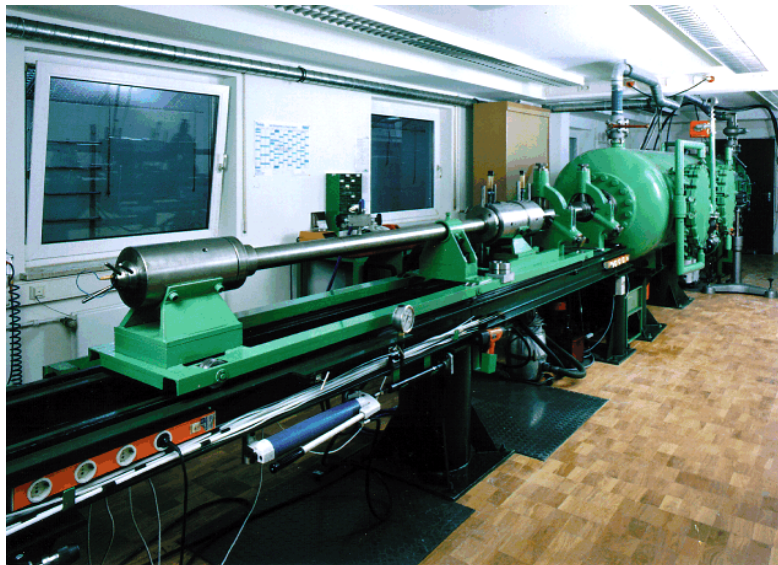


Figure 4.4-3: Medium two-stage light-gas gun (6.5-15 mm launch tube and 40 mm pump tube diameter) at EMI

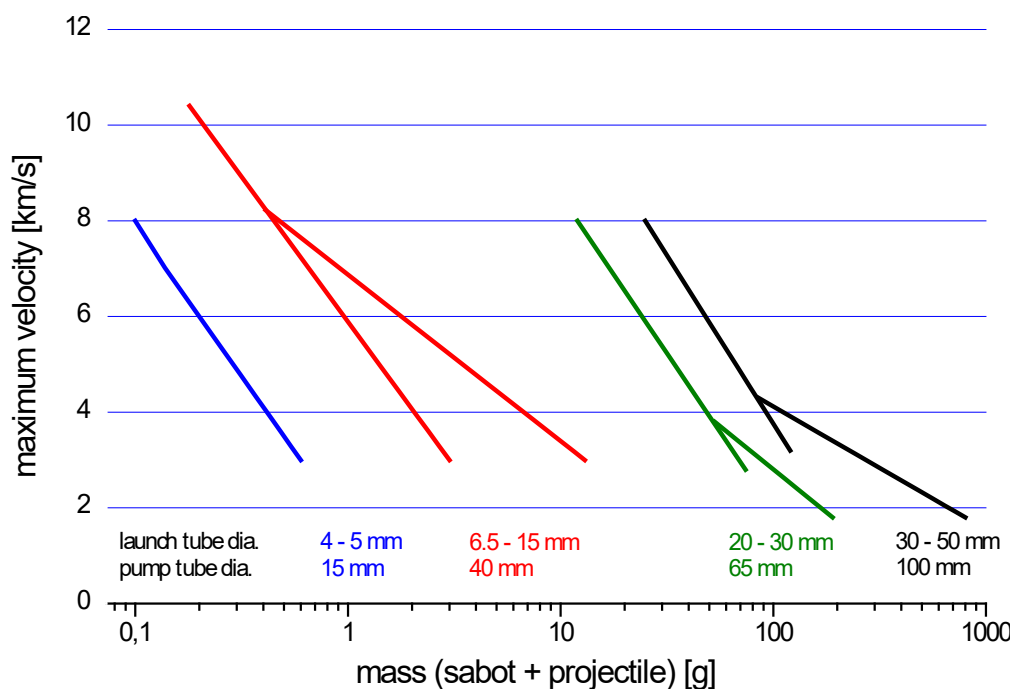


Figure 4.4-4: Performance diagram of EMI's light-gas guns (total mass versus velocity)

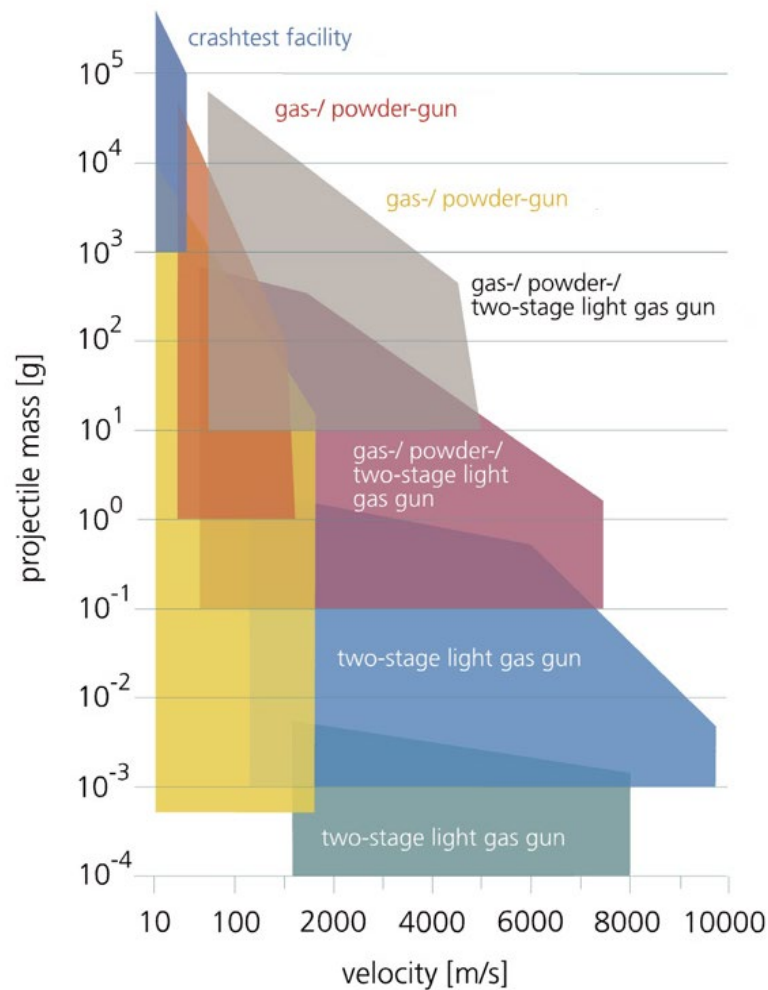


Figure 4.4-5: Performance diagram of all EMI facilities

4.4.6 CSA-Canada

The CSA-Canada HVI launcher used for this calibration exercise (refer to Section 4.3.6) is a two-stage light gas gun (LGG) developed by HIT Dynamics (HITD), located in Fredericton, New Brunswick, Canada. The LGG has a gas driven first stage. The gun has a 10 cm-diameter bore, 8.5 m long first stage (pump tube) and a 2.5 cm-diameter bore, 6 m long second stage (launch tube).

The shots performed at HITD were characterized via laser trap, high-speed video and framing cameras. All instruments were set to capture the projectile in flight for different sections of the LGG (**Figure 4.4-6**) and to capture the contact between the projectile and the target bumpers in the target chamber (**Figure 4.4-7**). Velocity capture involved high-speed video (drift tube viewing), framing camera (target tank location) and laser line sensor kit (drift tube location).

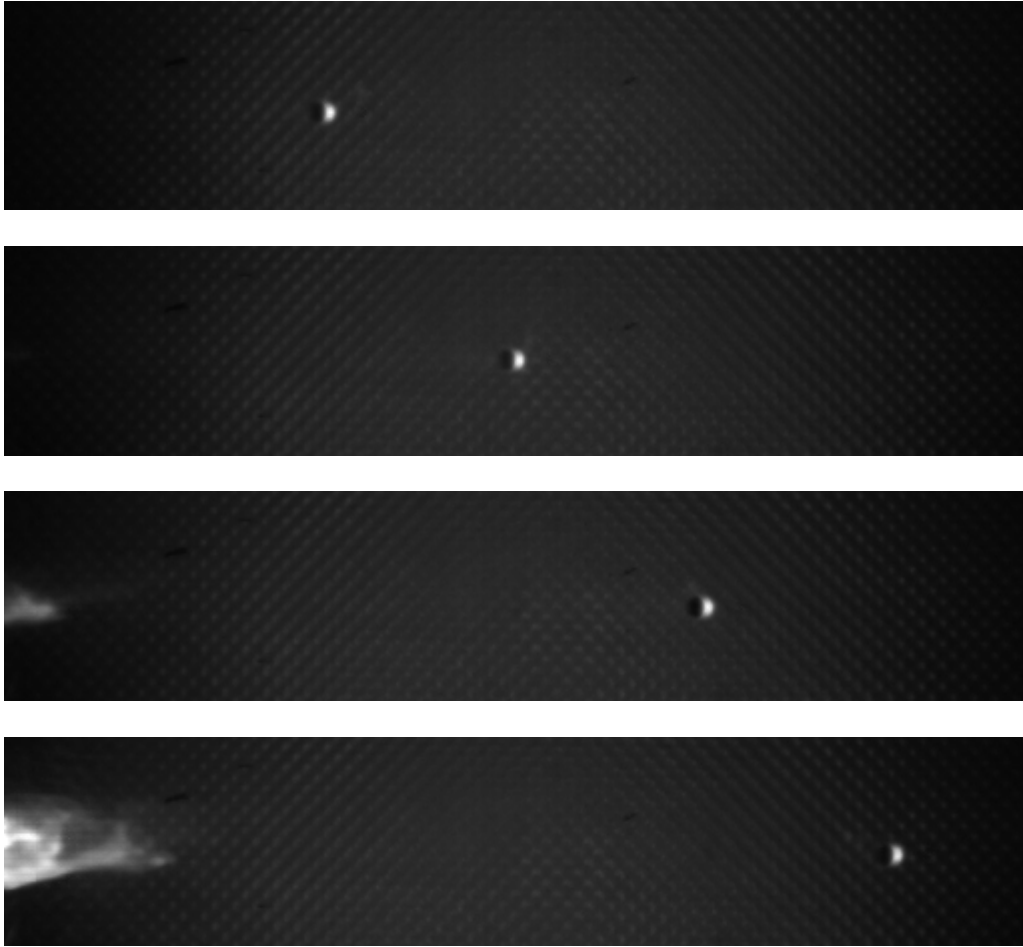


Figure 4.4-6: Video capture of the projectile in flight, showing the integrity of projectile prior to target impact.

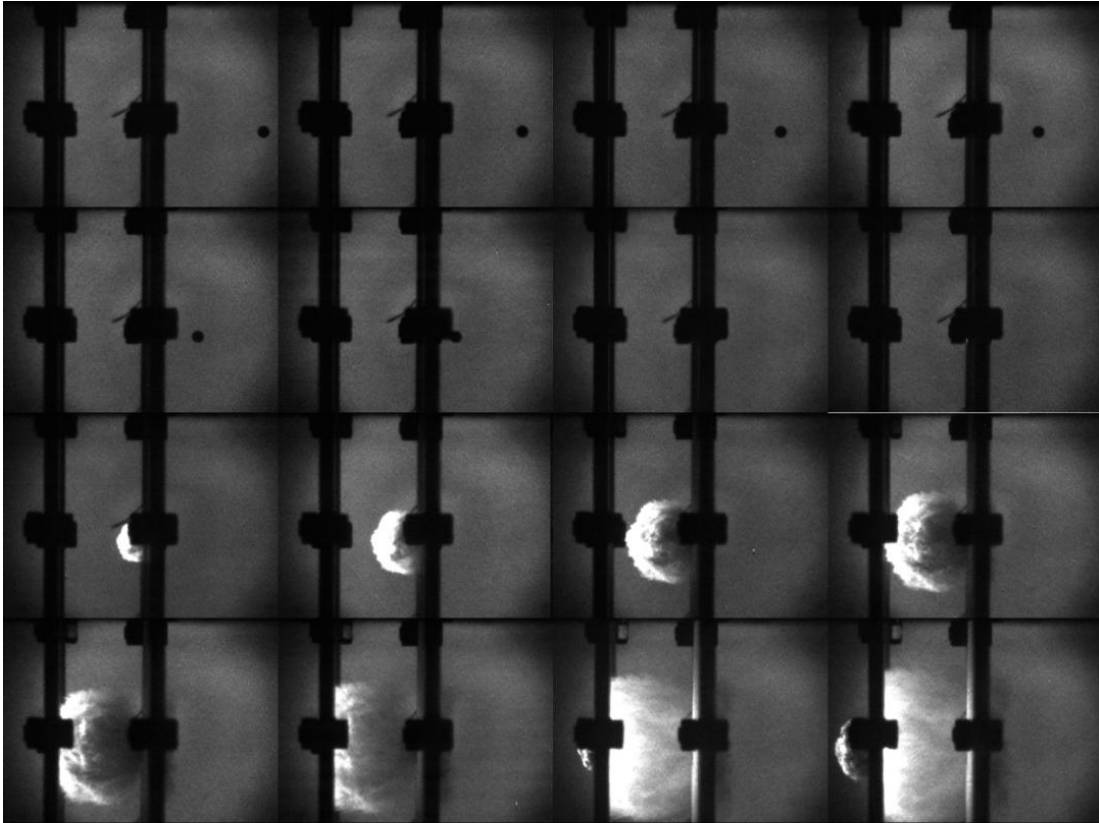


Figure 4.4-7: Syn-shot framing camera sequence (16 frames). Start top left image and step down to next row and move left to right for sequence. Last image is bottom-right, two outer plates shown only.

A summary of the tests characteristics, the result of hypervelocity impact tests and the diagnostics data acquired are presented in the following table (Table 4-16)

CSA-HITD Shot #	Velocity (km/s)	Uncertainty (km/s)	Projectile Diameter (in)	Target Type	Number of Shields	Number of Shields Perforated	Diagnostics Data (Laser/Video/Framing) Acquired
0001	7.040	0.068	0.125	Small (Multi-Shock)	5	4	L/V/F
0002	7.004	0.138	0.250	Large (Multi-Shock)	5	4	L/F
0003	7.071	0.084	0.125	Small (MDB: K710)	4	3	L/V/F
0004	7.010	0.079	0.250	Large (MDB: K710)	4	3	V

Table 4-16: Summary of HVI tests including diagnostics (MDB = Mesh Double Bumper).

4.4.7 CNSA

At Harbin Institute of Technology (HIT), the non-powder two-stage LGG facility (**Figure 4.4-8**) is mainly used for the simulation of space debris and micrometeoroid impact on spacecraft components. The projectile is enclosed in a sabot. It is accelerated in the barrel with the help of hydrogen or helium compressed by a piston in the pump tube. A detailed description of the gun can be found in Table 4-17. The two-stage gun can be transformed to one-stage LGG which can accelerate cylinder projectile up to 1.4km/s by improving the barrel of two-stage LGG.



Figure 4.4-8: Two-stage light-gas gun at HIT

First stage reservoir	Working gas	N ₂
	Volume [dm ³]	50
	Filling pressure [bar]	1-280
Pump tube	Working gas	H ₂ /He
	Inner diameter [mm]	57
	Length [m]	12
	Volume [dm ³]	30.6
	Filling pressure [bar]	5-10
Barrel	Inner diameter [mm]	5.8, 7.6, 12.7, 14.5
Shot frequency	[shots/day]	5-10
Sabot	Aerodynamic separation and inhibited separation	
	Mass [mg]	Up to 5
Projectile	Diameter [mm]	1-10
	Velocity [km/s]	Up to 7

Table 4-17: Two-stage LGG-main functional parameters

For one-stage and two-stage LGG, projectile velocity is measured by laser system and magnetism induction system. Scandiflash 150kV soft X-ray system is used to take shadow graph of material interior and determine the mass and velocity distribution of debris cloud in the target chamber. This X-ray system consists of 8 single-anode tubes and 2 multi-anode tubes. In each multi-anode tube, there are 4 anodes. Both single-anode and multi-anode tube can take 4 pairs of orthogonal radiographs. The main parameters of the X-ray system implemented at HIRC are presented in Table 4-18.

Unit	Source Voltage (kV)	Flash duration (ns)	Number of flashes
Single-anode	150	30	8
Multi-anode	150	30	8

Table 4-18: Main parameters of X-ray system

HSFC-PRO ultra-high speed framing camera, with a frame rate of 333 million per second, is equipped to capture the evolution of secondary debris clouds formed by the projectile's hypervelocity impact on thin target.

4.4.8 TSNIIMASH Structural Test Center

Double-stage ballistic light-gas gun facility for particles bombardment at velocity up to 8.0 km/s has been constructed in FGUP TSNIIMASH. The first facility stage uses powder, the second stage uses hydrogen or helium. The facility design ensures operation mode without diaphragm and free projectile launching without a flat pallet.

4.4.9 CNES

In France, hypervelocity impacts tests can be performed in THIOT INGENIERIE shock physics lab.

THIOT INGENIERIE is a non-governmental 100% private SME located in Puybrun, Lot. Its laboratory's four launchers cover a speed range from a few meters per second to ten kilometers per second. The two double-stage launchers cover a range from 0.6 km/s to 10 km/s. Medium velocity (up to 3 km/s) and higher mass tests are carried out on **Vulcain**'s 35mm two stage light gas gun. Higher velocity tests with lower masses are carried out on **Hermes**'s gas gun (**Figure 4.4-9**). Hermes launcher setup is equipped with a vacuum impact chamber diameter 1.6 m and 3 m long (**Figure 4.4-10**). This chamber has been designed with several windows to observe impacts from different point of view with a fast camera or X-ray flashes. Launching any projectile's shape is made possible by the use of simulation during the development phase of the test campaign and by the experience acquired. Examples of hypervelocity impacts are shown in **Figure 4.4-11**.

THIOT INGENIERIE's activities also include global expertise in dynamic behavior of materials, training courses, and development, manufacturing and worldwide distribution of gas gun laboratory launchers and other facilities to study the behavior of materials and structures when subjected to shock stress.

Web site: www.thiot-ingenierie.com (French and English).



Figure 4.4-9: HERMES launcher

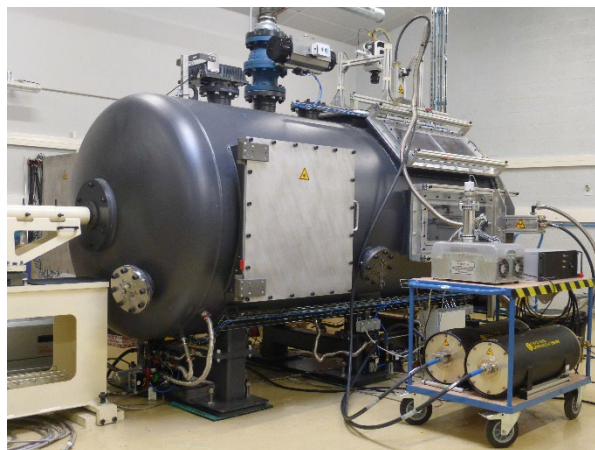
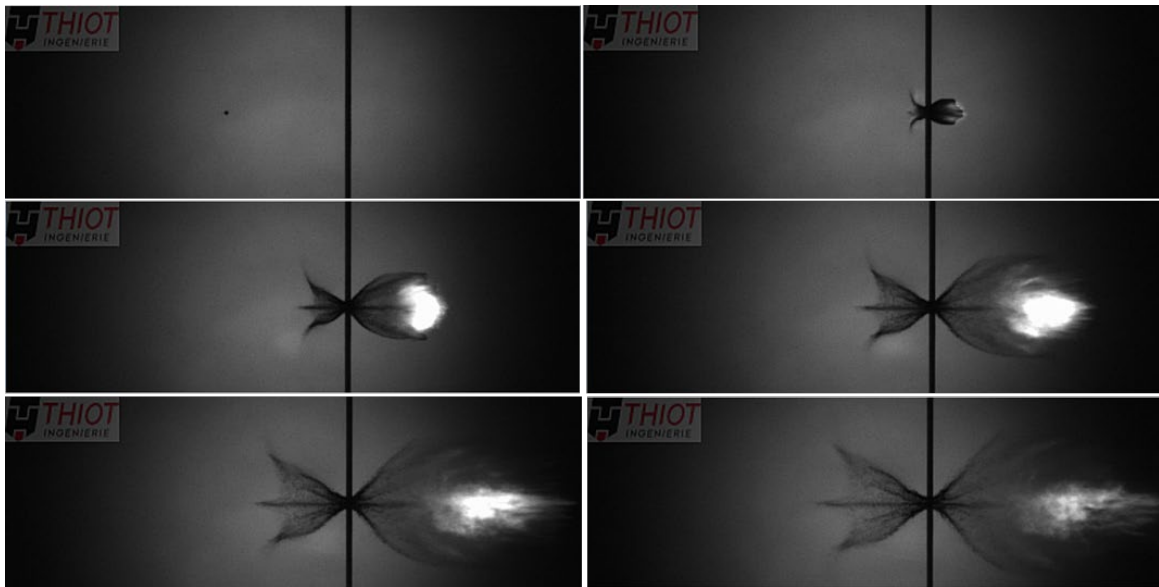


Figure 4.4-10: HERMES 's impact chamber

Table 4-19: Instrumentation

Quantity	Description
1	High sensitivity laser barriers to measure the projectile velocity
2	Vacuum gauges to measure the pressure in impact chamber
2	X-ray flashes
1	Very high speed camera
1	Data acquisition system a frequency of 1MHz

**Figure 4.4-11: example of hypervelocity impact**

4.5 References

Angrilli, F., M. De Cecco, and D. Pavarin, Diagnostic Procedure for two stage light gas gun pellet injector, *Fusion Technology*, v. 34, pp 430-434, 1998.

Angrilli, F., D. Pavarin, M. De Cecco, and A. Francesconi, Impact facility based upon high frequency two stage light-gas gun, *50th IAF Congress, 4-8 October 1999, Amsterdam, The Netherlands, on Press in ACTA Astronautica*.

Bol, J., and W. Fucke, Shaped Charges for Hypervelocity Impact Testing, *ESA CR(P) 4104*, January 1997.

Bol, J., and V. Friehmelt, Hypervelocity Impact Test Facility to Simulate Orbital Debris by Shaped Charge Single Projectile, *ESA SD-01, First European Conference on Space Debris*, Darmstadt, April 1993.

Bol, J., and W. Fucke, Shaped Charges for Hypervelocity Impact Testing, *ESA CR(P) 4104*, January 1997.

Canning, T.N., A. Seiff, and C.S. James, Ballistic range Technology, *AGARDograph 138*.

Charters, A.C., Development of the high velocity gas dynamics guns, *International Journal of Impact Engineering*, Vol. 5, pp. 181-203, 1987.

Chhabildas, L.C., J.E. Dunn, W.D. Reinhart, and J.M. Miller, An impact technique to accelerate flier plates to velocities over 12 km/s, *International Journal of Impact Engineering*, Vol. 14, pp. 121-132, 1993.

Chhabildas, L.C., L.N. Kmetyk, W.D. Reinhart, and C.A. Hall, Enhanced Hypervelocity Launcher – Capabilities to 16 km/s, *International Journal of Impact Engineering*, Vol. 17, pp. 183-194, 1995.

Combs, S.K., C.R. Foust, M.J. Gouge, and S.L. Milora, Acceleration of small, light projectiles (including hydrogen isotopes) to high speeds using a two-stage light gas gun, *Journal of Vacuum Science & Technology*, Vol. 8, Num. 3, pp. 1814-1819, 1990.

Combs, S.K., S.L. Milora, C.R. Foust, C.A. Foster, and D.D. Schuresko, Repeating pneumatic hydrogen pellet injector for plasma fuelling, *Review of Scientific Instruments*, Vol. 56, Num. 6, pp. 1173-1178, 1985.

Combs, S.K., Pellet injection technology, *Review of Scientific Instruments*, Vol. 64, Num. 7, pp. 1679-1698, 1993.

Crozier, W.D., and W. Hume, High Velocity Light Gas Gun, *J. of Appl. Phys.*, 28, 1957.

De Cecco, M., and D. Pavarin, Computer based control and diagnosis of a two stage light-gas gun by means of pressure recordings, *10th Symposium on Development in Digital Measuring Instrumentation*, 17-18 Sept. 1998.

De Cecco, M., and D. Pavarin, Projectile hypervelocity measurement by means of back-scattering technique, *10th Symposium on Development in Digital Measuring Instrumentation*, 17-18 Sept 1998.

Francesconi, A., D. Pavarin, M. Antonello, and F. Angrilli, Feasibility study of a 15 mm high-shot-frequency hypervelocity launcher for impact testing, *XVI Congresso Nazionale AIDAA*, Palermo, 24-28 Sept 2001.

Frattolillo, A., S. Migliori, G. Angelone, M. Capobianchi, C. Dommo, G. Ronci, and D.K. Griffin, Acceleration of large size deuterium pellets to high speed using a small two-stage pneumatic gun, *Review of Scientific Instruments*, Vol. 70, Num. 5, pp. 2355-2364, 1999.

Grosch, and J.P. Riegel, SWRI Development and optimization of a ‘micro’ two stage light gas gun, *International Journal of Impact Engineering*, vol.14, pp.1315-324, 1993.

Jakhlakov, Ju., MBR facility. *Presentation on the 15th IADC session*, Houston, USA, 1997.

Keaton, P.W., *et al.*, A hypervelocity microparticle impacts laboratory with 100 Km/s projectiles, Los Alamos National Laboratory, internal report.

Kibe, S., T. Yamamoto, and M. Katayama, Development of Conical Shaped Charge and Remaining Problems, *50th International Astronautical Congress*, Amsterdam, October 1999.

Kim, K., Electromagnetic railgun hydrogen pellet injector – progress and prospect, Internal report, Fusion Technology and Charged Particle Research Laboratory, University of Illinois.

Lambert, M., Shielding against orbital debris – a comparison between different shields, ESA EWP 1740, 1993.

Persico, Principles of particle accelerators, W.A. Benjamin, INC New York, 1968.

Riedler, W., F. Schafer, M. Herrwerth, S. Hiermaier, and E. Schneider, Shape Effects in Hypervelocity Impact On Semi-Infinite Metallic Targets, *Proc. Of the 18th Meeting of the Inter-Agency Space Debris Coordination Committee*, June 13-16, 2000, Colorado Springs.

Seigel, A.E., The theory of high speed guns, *AGARDograph 91*, 1965.

Septier, A., Focusing of charged particles, vol.1, Academic Press, NewYork, 1967.

Stilp, A.J., and V. Hoher, Aeroballistic and impact physics research at EMI, *International Journal of Impact Engineering*, vol.17, pp.785-805, 1995.

Stilp, A.J., Review of Modern Hypervelocity Impact Facilities, *Int. J. of Impact Engng.*, 5, 1987.

Terada, F., Specification of NASDA Two Stage Gas Gun, *15th IADC WG3*, December 1997.

Toewer, M.M., *et al.*, Hypervelocity Testing Using An Electromagnetic Rail Gun Launcher, *International Journal of Impact Engineering*, vol.5, pp.635-644, 1987.

Walker, J.D., D.J. Grosch, S.A. Mullin, A hypervelocity fragment launcher based on an inhibited shaped charge, *International Journal of Impact Engineering*, Vol. 14, pp. 763-774, 1993.

Weldon, W.D., Development of Hypervelocity electromagnetic gun, *International Journal of Impact Engineering*, vol.5, pp.671-679, 1987.

5 Numerical Modelling

The development and application of numerical models to simulate hypervelocity impacts on spacecraft structures and materials is an important element of PWG's activities. Following an introduction to the modelling approach, this chapter describes the models currently in use by the PWG, and the benchmark scenarios defined to validate them. Other activities covered in the chapter include:

- The development of material models for Nextel and Kevlar epoxy resin
- The simulation of hypervelocity impacts on pressure vessels
- A hybrid particle – finite element method to simulate debris impact problems

5.1 Introduction

In order to perform numerical simulation of fast transient events innovative numerical methods have been under development since the early 50s. These so called Hydrocodes or Wave propagation codes allow the study of the time-resolved progression of acoustic and shock wave propagation due to impact, penetration or detonation in fluids and solids.

In 1952 the first hydrocode (HEMP) was developed by Mark L. Wilkins [Wilkins, 1999]. Having the name from its original application to pure fluid dynamic problems or to situations where the hydrostatic pressure dominates the material strength by orders of magnitude, hydrocodes are often misinterpreted as being not suitable for structural design.

This class of codes is fundamentally based on a spatial and time discretisation of the impacting bodies into small elements to which the first principles or conservation equations for mass, momentum and energy are applied over small time steps. This technique was a departure from the standard implicit finite element methods that solved equilibrium conditions using, for example, the minimum of potential energy. In the hydrocodes, the first principles of physics are applied together with an equation of state (EOS) to give the relationships between pressure, density and internal energy. This provides a complete set of equations governing hydrodynamic behaviour. Since many of the early hydrocodes were applied to the study of atomic detonations, the very high pressures involved negated the need to incorporate material strength. For this reason, the term “Hydrocodes” was applied to this class of codes. This name was kept even after the incorporation of material strength. A step that was realised in a way that the stress tensor was calculated as a sum of the hydrostatic pressure given in the EOS and the deviatoric stress expressed by a stress rate tensor.

The following paragraphs identify some basic aspects of hydrocodes in general as well as some of the specific limitations and advantages of different hydrocodes that are applied for protective design purposes.

5.1.1 Spatial Discretisation

The standard approach to solve partial differential equations for any engineering problem is to discretise the domain of interest through a grid of nodes connected together. Depending on the interpolating scheme used to determine the values of the variables between the nodes, the most common numerical grid-based methods are denoted as finite element, finite difference or finite volume. Such techniques allow two different ways to describe material motion in space. Either body fitted co-ordinates (Lagrangian grid) or a grid fixed in space (Eulerian grid) can be used. Traditionally, Lagrangian grids are mainly used in structural dynamics, while Eulerian grids are more common for fluid dynamics.

The conservation equations of mass, momentum and energy In the Lagrangian and Eulerian description are expressed as follows:

LAGRANGE**EULER**

Mass:

$$\dot{\rho} + \rho \frac{\partial u_i}{\partial x_i} = 0 \qquad \dot{\rho} + \rho \frac{\partial u_i}{\partial x_i} + u_i \frac{\partial \rho}{\partial x_i} = 0 \qquad [5.1-1 \text{ \& } 5.1-2]$$

Momentum:

$$\dot{u}_i = f_i + \frac{1}{\rho} \frac{\partial \sigma_{ji}}{\partial x_j} \qquad \dot{u}_i + u_j \frac{\partial u_i}{\partial x_j} = f_i + \frac{1}{\rho} \frac{\partial \sigma_{ji}}{\partial x_j} \qquad [5.1-3 \text{ \& } 5.1-4]$$

Energy:

$$\dot{e} = f_i u_i + p \dot{V} + \frac{1}{\rho} S_{ij} \dot{\epsilon}_{ij} \qquad \dot{e} + u_i \frac{\partial e}{\partial x_i} = f_i u_i + p \dot{V} + \frac{1}{\rho} S_{ij} \dot{\epsilon}_{ij} \qquad [5.1-5 \text{ \& } 5.1-6]$$

The form of the two sets of equations differs because of the additional terms needed to define variable fluxes in space in an Eulerian frame of reference. A Lagrangian frame of reference is material centred and does not require the extra terms. Therefore, from a computational point of view, additional derivatives have to be calculated in the Eulerian formulation, but this is not the most relevant difference for the application of the equations to hypervelocity impact phenomena.

The equations can be numerically solved through a grid of nodes, approximating the geometry of the problem. In a Lagrangian solution, the nodes are joined with the material elements and move according to the local velocity. Therefore, the grid has to be placed only in the region occupied by the material at the beginning of the problem, as its future evolution will be represented through the movement of nodes. On the other hand, in an Eulerian model the grid is fixed in space, so that it has to be placed also in the void space regions where the material is foreseen to move over the course of the calculation. This requires a larger number of nodes compared to an equivalent Lagrangian model with the same resolution, and a consequent increase of the computation time. This difference becomes significant in the representation of typical spacecraft protection systems, where the space occupied by the shielding plates is much smaller than the void space among them.

Another advantage of Lagrangian models is that material and boundary interfaces can be directly defined by node arrays at their initial position, so that they will be continuously defined over successive relative motion. This is not possible in Eulerian models, as interfaces are continuously re-defined as the material advances through the fixed grid. At some point after the initial condition, some of the cells composing the material interfaces may become re-defined as “mixed” cells, i.e., containing more than one material (or void). The distinction of the interface boundary can become diffused as the resolution of the interface is limited by the dimension of the mixed cells. Of course, increasing the resolution can reduce such uncertainties, but again at the price of higher computation time.

History-dependent material models, particularly useful in the simulation of hypervelocity phenomena, can be directly implemented in a Lagrangian model, where the nodes are always attached to the same material point. Eulerian models cannot keep the history of the material, as it flows through the cell boundaries and the nodes relate at each cycle to a different material point. Internal state variables can be created to transport history information with the material, but their accuracy diminishes when they mix and again a higher computation time is required.

The major drawback of Lagrangian grids is that they can undergo large distortions or mesh entanglement when representing high material deformation. In particular, the simulation of hypervelocity impacts would typically result in numerical problems leading to the termination of the calculation at a very early stage if the grid degeneration and entanglement were not resolved. This problem is obviously absent in fixed Euler grids.

A possibility to generally overcome distortion problems is to rezone the grid before it becomes excessively distorted. A new grid is created to mesh the actual geometry, and the variable values at the new nodes are calculated through interpolation of the old ones. However, such operation can be very time-consuming and require extensive user intervention. In any case, rezoning was shown to be inadequate to handle the extremely high strain-rate, large deformation involved in hypervelocity impacts, even if performed with a very high frequency.

Another option to avoid the problems of grid distortion is to remove the cells reaching a selected geometric strain value, high enough to ensure a negligible residual strength of the removed material, but still not causing degeneration (typically between 100% and 300%). Such a technique (erosion) allows for the representation of the target perforation and/or crater formation, but not the evolution of independent fragments that result during the process of perforation of, for example, multi-wall shields. The erosion algorithm would remove most of the fragments generated during the impact of the outer shield leading to an inaccurate loading of the inner shield. In some codes, the option exists to transform the eroded cells into free nodes conserving their mass and velocity, but this option was shown to give unsatisfactory results because of its own diffusiveness and the neglect of the hydrostatic pressure term.

Another advantage of Eulerian models is the ability of simulating diffusion and mixing problems. This is not possible with Lagrangian models, as each cell contains only one material type and flow across the cell boundary is not allowed.

Some hydrocodes use a method in which Lagrangian and Eulerian grids are coupled in order to treat problems where the structural response to fluid type loads is of interest.

Numerical simulation of hypervelocity impacts requires a code that is able to describe very large deformations as well as strong density gradients including phase change of material. The expanding fragment clouds behind a bumper shield are of major interest to assess the shield. Thus, the simulation must be able to describe the fragment cloud as accurately as possible; in particular its expansion velocity, density and fragment distribution.

In an attempt to solve this problem, attention has recently focused on the so-called “meshless” methods (**Figure 5.1-1**). The basic idea is to represent the continuum bodies through an array of Lagrangian nodes that are not physically connected by a grid, but whose relative motion is

controlled by interpolating functions. The lack of a grid clearly removes the distortion problem affecting the standard Lagrangian techniques while providing most of the advantages found in the Eulerian method.

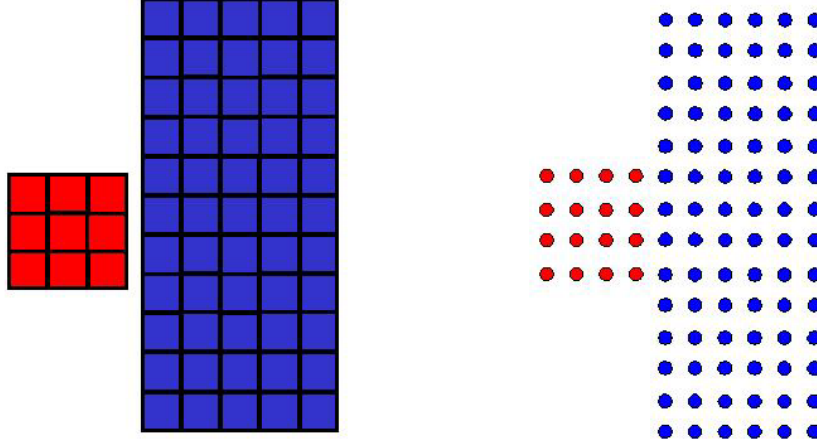


Figure 5.1-1: Grid based and meshless discretization of an impact situation.

Smoothed Particle Hydrodynamics (SPH) has shown to be, up to now, the most promising meshless method for application to hypervelocity impact simulation. First invented by Astrophysicists [Monaghan, 1983; Benz, 1989] in the 70's, the SPH method was expanded to include structural mechanics in the late 80's [Libersky, 1995] by including deviatoric stress and material strength. The physical description of material behaviour in the SPH method is similar to that in standard hydrocodes. Algorithms for the mathematical formulation of material strength, failure and related variables can be easily transformed from other codes. The primary difference is in the SPH method for the discretisation of mass. Instead of nodes and elements, this method uses free movable points of fixed mass, so called particles, interacting with each other via an interpolation function.

For example, the value of a function $u(\vec{x})$ and its spatial derivation $\nabla u(\vec{x})$ at the location of a particle i are approximated in the SPH formalism by the use of N neighbour particles j as:

$$\langle u(\vec{x}) \rangle = \sum_i u(\vec{x}_i) W(\vec{x} - \vec{x}_i, h) \frac{m_i}{\rho_i} , \quad [5.1-7]$$

$$\langle \nabla u(\vec{x}) \rangle = - \sum_i u(\vec{x}_i) \nabla W(\vec{x} - \vec{x}_i, h) \frac{m_i}{\rho_i} . \quad [5.1-8]$$

A typical interpolation function W , also called the kernel function, and its derivatives W' and W'' are shown in **Figure 5.1-2** together with an interpolation scheme for a SPH particle.

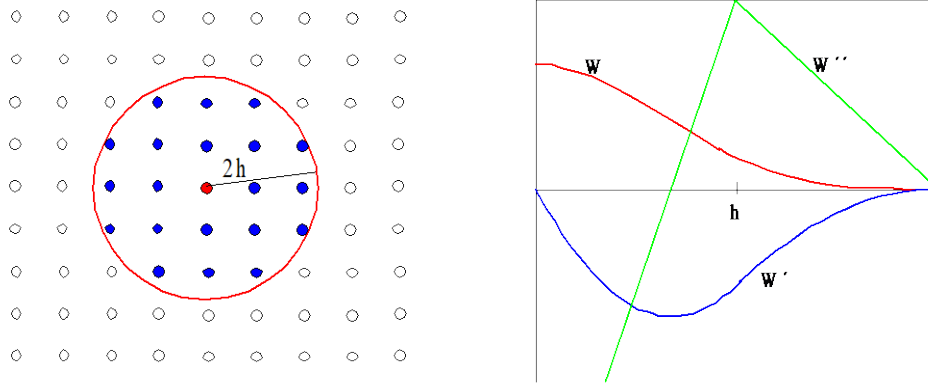


Figure 5.1-2: Particle interaction and interpolation function W with first and second derivative

The above equations allow the description of the conservation of mass, momentum and energy in terms of interpolation sums as:

$$\frac{d\rho_i}{dt} = \rho_i \sum_j \frac{m_j}{\rho_j} (u_i^\beta - u_j^\beta) W_{ij,\beta} \quad [5.1-9]$$

$$\frac{du_i^\alpha}{dt} = - \sum_j m_j \left(\frac{\sigma_i^{\alpha\beta}}{\rho_i^2} + \frac{\sigma_j^{\alpha\beta}}{\rho_j^2} \right) W_{ij,\beta} \quad [5.1-10]$$

$$\frac{de_i}{dt} = \frac{\sigma_i^{\alpha\beta}}{\rho_i^2} \sum_j m_j (u_i^\alpha - u_j^\alpha) W_{ij,\beta} \quad [5.1-11]$$

With the notations $W_{ij} = W(\bar{x}_i - \bar{x}_j, h)$ and $W_{ij,\beta} = \partial W_{ij} / \partial x_i^\beta$.

A problematic aspect of SPH is the existence of instabilities in the method itself which result in large velocity oscillations of single particles. Swegle *et al.*, 1995, and Balsara, 1995, demonstrated and analysed the instabilities leading to particle clumping. Improvements have been shown through the use of conservative smoothing [Guenther, 1994] and kernel renormalisation [Johnson, 1996].

It is supposed that the instability problem within SPH has a single root cause: the inability of SPH to accurately interpolate when the particles are unevenly spaced and sized [Dilts, 1999]. In mathematical terms, the SPH equations are not consistent, in that the derivative approximations do not necessarily converge to the continuum values as the average particle size and spacing go to zero [Belytschko, 1996].

The problems in SPH can also be described as being due to a lack of nodal completeness and integrability of the approximations to spatial derivatives. The corrective techniques of Guenther and Johnson and others restore various levels of nodal completeness for the first derivative approximations by satisfying reproducing conditions. They also prevent numerical instability to

an extent. However, Belytschko *et al.*, 1998, concluded that the corrected derivative approximations are not truly complete because of the lack of integrability.

To some extent, these fundamental problems can be fixed by means of the moving-least-squares (MLS) interpolants [Lancaster, 1981], which are also used in Finite-Element Methods [Nayroles, 1983] and in Element-Free Galerkin Methods [Belytschko, 1994], and which were re-introduced in a way such that a generic SPH code can take advantage of them [Dilts, 1996].

Alternatively, the corrective smoothed particle method (CSPM) proposed by Chen *et al.*, 1999 & 2001, like the MLS method, is a mathematically sound correction. However, CSPM is based on a Taylor series expansion of the kernel estimate and is not as computationally complex as MLS. The CSPM is capable of approximating derivatives of any order and has shown to not only remove tensile instability but also enhanced solution accuracy over the entire domain, especially near and on boundaries.

Currently the following hydrocodes, which provide meshless methods for hypervelocity impact simulations, are widely used within the hypervelocity analysis community:

- ANSYS AUTODYN, ANSYS, Inc., Various formulations
- EPIC, Alliant Techsystems, Kernel Renormalisation
- EXOS, University of Texas, hybrid particle-finite element formulation
- MAGI, Air Force Research Laboratory, Kernel Renormalisation
- PAMSHOCK, Engineering Systems International, Various formulations
- SOPHIA, Ernst-Mach-Institute, Moving Least Squares
- SPHINX, Los Alamos National Laboratory, Moving Least Squares

From the above description, both grid-based (Lagrange or Euler) and meshless methods show some problems and limitations in the simulation of hypervelocity impacts. Consequently, it is not possible at present to identify the most suitable discretisation technique from a general point of view. The choice should then be performed on a case-by-case basis, depending on the characteristics of the problem to be analysed (impact velocity, material properties, geometry, etc.).

5.1.2 Time Integration Scheme

The time discretisation in hydrocodes uses an explicit integration scheme provided by a forward differential quotient. An explicit time integration is needed if stress waves and shocks are an important part of the solutions. This is the case for any kind of transient events like impact or penetration phenomena.

Explicit schemes need an upper time step limit as introduced by Courant-Friedrich-Levy [Courant, 1928]. Basically, the time step is calculated from the speed of sound in each cell and its geometrical dimensions. The upper time step limit for the whole system is controlled by the element with the minimum ratio of geometric size s_{min} to speed of sound c_{max}

$$\Delta t = \frac{s_{min}}{c_{max}} \quad [5.1-12]$$

This means that both high grid resolutions and high velocities result in short time steps and thus in high computational costs. The limit guarantees numerical stability and accuracy. It is comparable to convergence criteria used in implicit schemes.

Additional time step reductions are identified by the stability analysis of von Neumann. They take into regard material compressibility and artificial viscosity [v. Neumann, 1950].

5.1.3 Equations of State

A simple example for an equation of state (EOS) for solid materials is the linear EOS where the hydrostatic pressure is calculated from the material's bulk modulus and the ratio of actual density ρ to reference density ρ_0 .

$$p = K \left(\frac{\rho}{\rho_0} - 1 \right) \quad [5.1-13]$$

In order to calculate shock phenomena, the shock Hugoniot of a material must be defined and implemented to the EOS. Examples are the Mie-Grüneisen type equations and tabular data like the SESAME library published by the Los Alamos National Laboratories.

Depending on the impact velocity and the involved materials hypervelocity impact can include shock induced melting or vaporisation. If the resulting effects are of interest the equation of state must represent the related changes of phase. The Tillotson EOS is an example of a popular EOS which includes the capability to model shock induced changes of phase (solid to gas transition). For low pressures it is equivalent to the Mie-Grüneisen shock Hugoniot EOS and for very high pressures it converges to the Thomas-Fermi theoretical EOS.

A comparison of different equations of state (Mie-Grüneisen shock, Tillotson, SESAME) applied to hypervelocity impact is given in [Hayhurst, 1998].

5.1.4 Deviatoric Stress Rate and Strength Models

Most current structural dynamics hydrocodes have, in addition to the standard fluid dynamic modelling capability, material strength modelling capability as well by incorporating the complete stress tensor, $\sigma^{\alpha\beta}$, into the conservation equations. Thus, an additional equation is necessary to compute the deviatoric part, $\dot{S}^{\alpha\beta}$, of the total stress tensor, $\sigma^{\alpha\beta}$:

$$\sigma^{\alpha\beta} = S^{\alpha\beta} - p \delta^{\alpha\beta} \quad [5.1-14]$$

The deviatoric stress rate, $S^{\alpha\beta}$, may for instance be calculated using the Jaumann formulation which is objective in terms of rigid body motions:

$$\dot{S}^{\alpha\beta} = S^{\alpha\beta} \dot{R}^{\beta\gamma} + S^{\gamma\beta} \dot{R}^{\alpha\gamma} + G \left(\dot{\epsilon}^{\alpha\beta} - \frac{1}{3} \delta^{\alpha\beta} \dot{\epsilon}^{\delta\delta} \right) \quad [5.1-15]$$

where G is the shear modulus and

$$\dot{\varepsilon}^{\alpha\beta} = \frac{1}{2} \left(\frac{\partial u^\alpha}{\partial x^\beta} + \frac{\partial u^\beta}{\partial x^\alpha} \right) \quad [5.1-16]$$

$$\dot{R}^{\alpha\beta} = \frac{1}{2} \left(\frac{\partial u^\alpha}{\partial x^\beta} - \frac{\partial u^\beta}{\partial x^\alpha} \right) \quad [5.1-17]$$

give the tensors of strain rates and rotation rates.

Calculating the deviatoric stresses from strains delivers the full stress tensor and thus offers the possibility to implement yield or failure criteria of any kind.

The fact that many materials behave very different under dynamic loading compared to quasi static loading conditions demands rules to describe this strain rate dependency mathematically. There are several approaches to be found in the literature [Johnson, 1983; Zerilli, 1987; Steinberg, 1980]. A very common method is the Johnson-Cook model [Johnson, 1983] where the dependency of the yield stress σ_y on strains ε , strain rates $\dot{\varepsilon}$ and temperature T is described as:

$$\sigma_y = (A + B \varepsilon_p^n) \left[1 + C \ln \left(\frac{\dot{\varepsilon}_p}{\dot{\varepsilon}_0} \right) \right] (1 - T^{*m}) \quad [5.1-18]$$

The material parameters A , B , n , C and m must be derived by dynamic material tests. With the room temperature T_{Room} and the melting temperature T_{Melt} the homologous temperature is defined as

$$T^* = (T - T_{Room}) / (T_{Melt} - T_{Room}) \quad [5.1-19]$$

5.1.5 Failure Criteria

Material failure models are needed to describe the limitations of material strength. Hydrocodes generally provide maximum tensile or compressive stresses or strains, strain rates, maximum hydrodynamic pressure (to describe spallation) or fracture toughness as failure criteria. Under hypervelocity impact conditions a shock wave travels into the projectile and the target. By the reflection along free surfaces it is converted into tensile waves that are strong enough to produce spallation in the affected materials.

Therefore, a stress or hydrodynamic pressure criteria should be used. Examples and comparison of different criteria are shown in [Hayhurst, 1998].

5.2 Validation of Hydrocodes

In order to validate hydrocodes for application to hypervelocity impact, several reference cases of HVI have been established and accepted by the PWG. Codes are validated if they are able to predict the known hole sizes in bumpers, fragment cloud shapes and velocities, and crater sizes or perforation of backwalls.

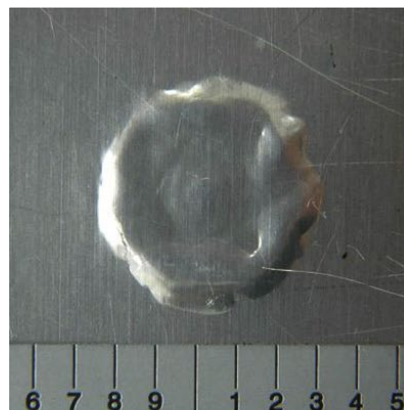
5.2.1 Definition of Benchmark Cases

Six benchmark test cases have been defined for validating hydrocodes. All the cases cover aluminium shields only. Two cases address Whipple shields at two velocities typical of Light Gas Gun (LGG) experiments with aluminum projectiles. Two cases address Whipple shields for two projectile densities representative of meteoroids at typical LGG speeds. The last two cases address the more complex configuration of Double Bumper Shields. One test was performed with a LGG while the last case was an oblique impact test performed with Shaped Charges.

5.2.1.1 Whipple Shield (Al projectile)

Fully documented work in: Piekutowski, A.J., Poormon, K.L., Christiansen, E.L. and Davis, B.A. *Performance of Whipple shields at impact velocities above 9 km/s*. International Journal of Impact Engineering, **38**, pp. 495-503 (2011).

- Projectile: 2017-T4 aluminium sphere 2.713 mm diameter, 7.09 km/s, normal impact (shot line perpendicular to target surface)
- Bumper: 6061-T6 aluminium 0.597 mm thick
- Spacing: 46.69 mm
- Backwall: 2219-T87 aluminium 1.483 mm thick
- Damage description: 15.0 mm-dia. Central spall with several open cracks at edges



7.09 km/s (Pass)

Shot No. 4-2012

Figure 5.2-1: Image of rear wall back surface damage including attached spall.

5.2.1.2 Whipple Shield (Al projectile > 9 km/s)

Fully documented work in: Piekutowski, A.J., Poormon, K.L., Christiansen, E.L. and Davis, B.A. *Performance of Whipple shields at impact velocities above 9 km/s*. International Journal of Impact Engineering, **38**, pp. 495-503 (2011).

- Projectile: 2017-T4 aluminium sphere 2.601 mm diameter, 9.29 km/s, normal impact (shot line perpendicular to target surface)
- Bumper: 6061-T6 aluminium 0.597 mm thick
- Spacing: 46.69 mm
- Backwall: 2219-T87 aluminium 1.466 mm thick
- Damage description: Bulging with a 3.05 mm x 3.56 mm spall and partial spall ring.



9.29 km/s (Fail)

Shot No. 8-3288

Figure 5.2-2: Image of rear wall back surface damage including attached spall.

5.2.1.3 Whipple Shield (Alumina projectile)

Fully documented work in: *To be published in* Miller, J.E., Davis, B.A., Deighton, K.D. and McCandless, R.J. *Rear Wall Perforation in Whipple Shields for Low- and High-Density Particles*. The 2nd International Orbital Debris Conference Proceedings, (2023).

- Projectile: Al₂O₃ (alumina) sphere 2.52 mm diameter, 6.62 km/s, normal impact (shot line perpendicular to target surface)
- Bumper: 6061-T6 aluminium 0.29 mm thick (hole size 3.6 mm-dia.)
- Spacing: 45.0 mm
- Backwall: 2219-T87 aluminium 1.07 mm thick
- Damage description: 124.8 mm² hole, max damage size 19.6 mm

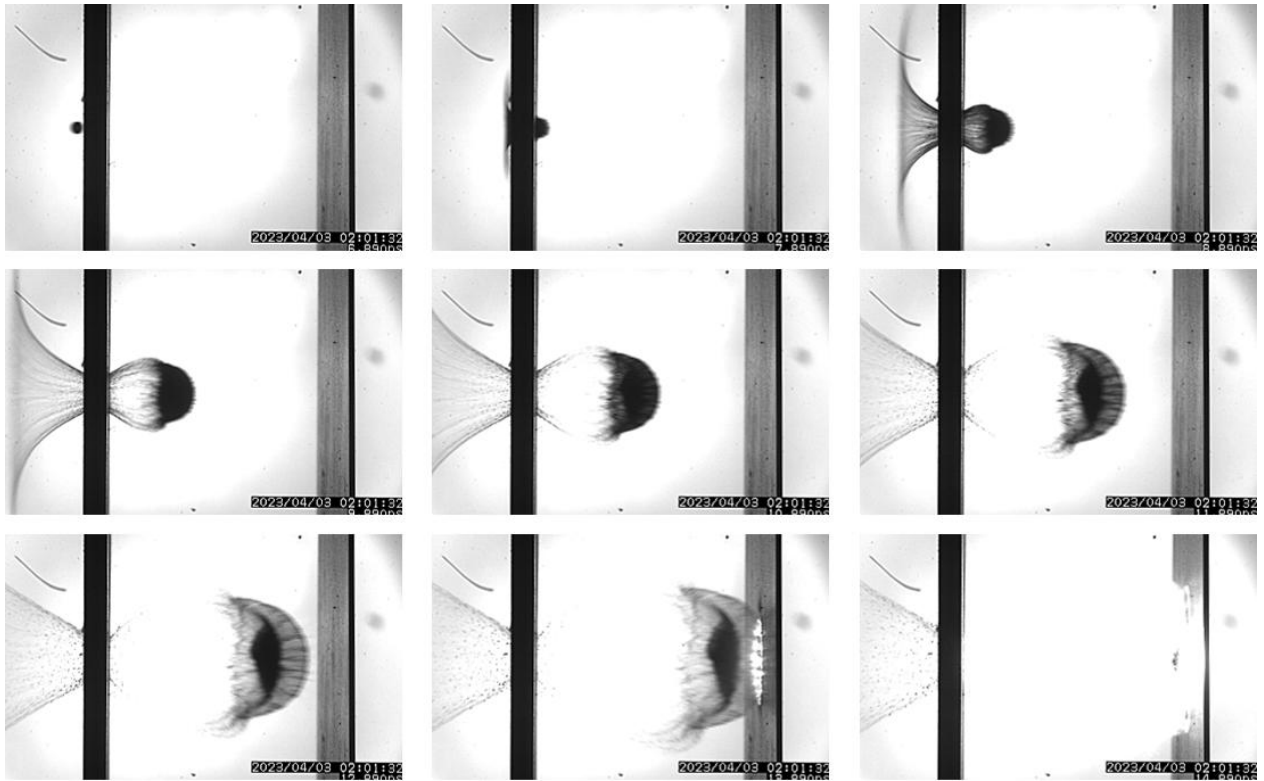


Figure 5.2-3: Debris cloud at 1 μ s interframe rate

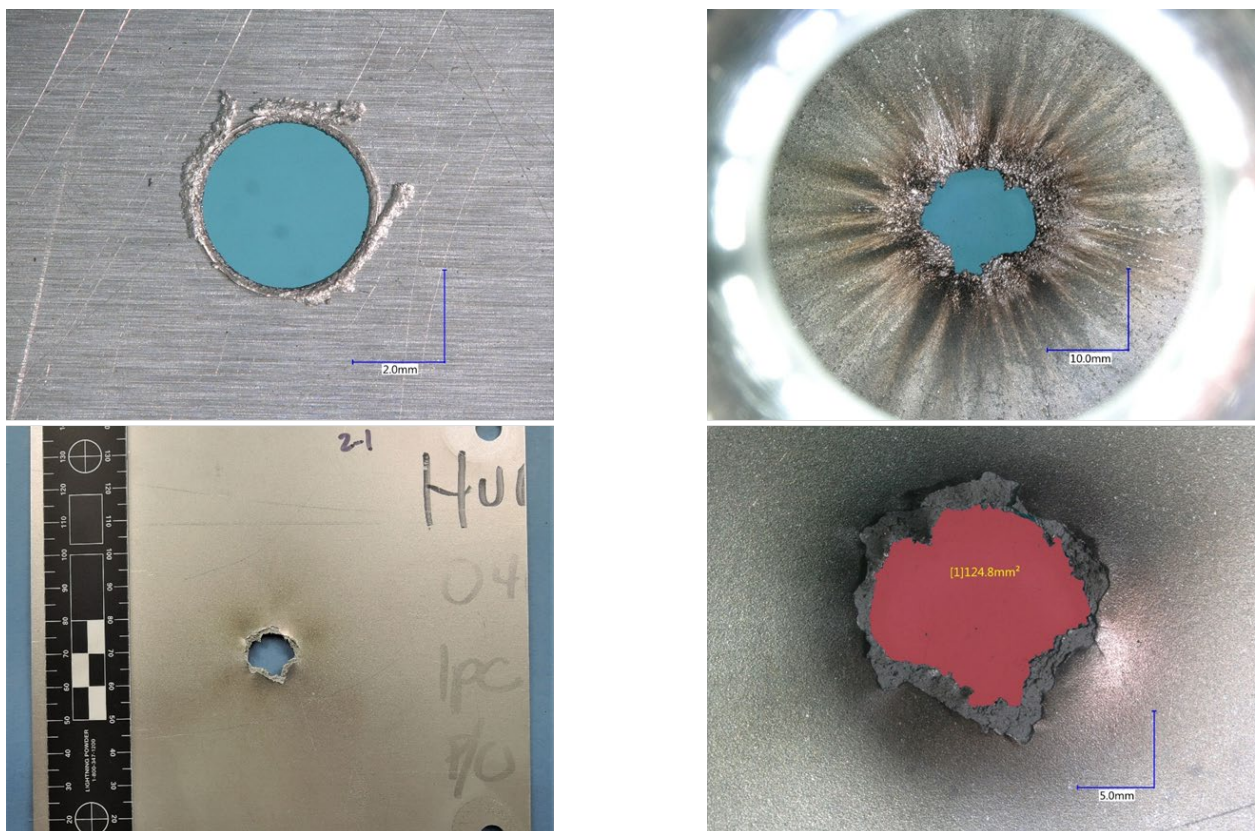


Figure 5.2-4: Image of front wall and rear wall (front and back surface) damage

5.2.1.4 Whipple Shield (Nylon projectile)

Fully documented work in: *To be published in* Miller, J.E., Davis, B.A., Deighton, K.D. and McCandless, R.J. *Rear Wall Perforation in Whipple Shields for Low- and High-Density Particles*. The 2nd International Orbital Debris Conference Proceedings, (2023).

- Projectile: Nylon sphere 2.75 mm diameter, 6.49 km/s, normal impact (shot line perpendicular to target surface)
- Bumper: 6061-T6 aluminium 0.29 mm thick (hole size 3.6 mm-dia.)
- Spacing: 15.0 mm
- Backwall: 2219-T87 aluminium 1.07 mm thick
- Damage description: 19.4 mm² hole, max damage size 13.9 mm

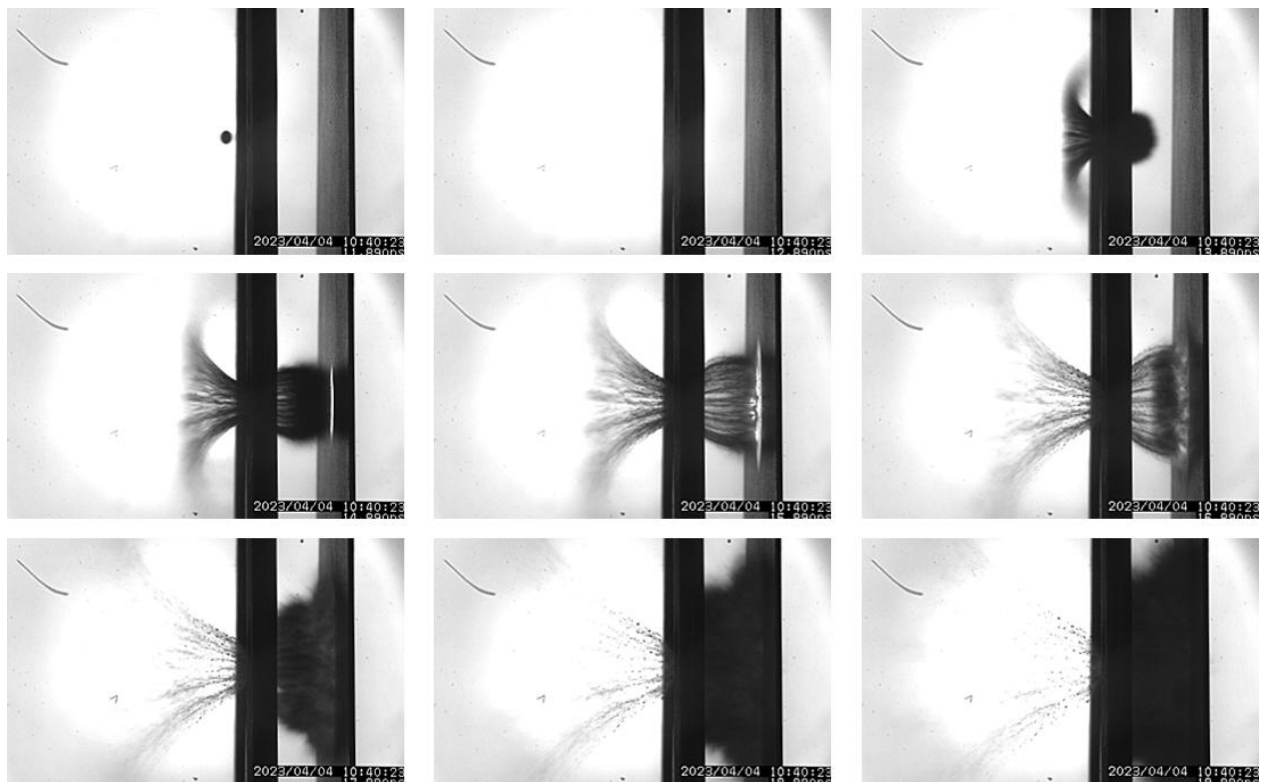


Figure 5.2-5: Debris cloud at 1 μ s interframe rate

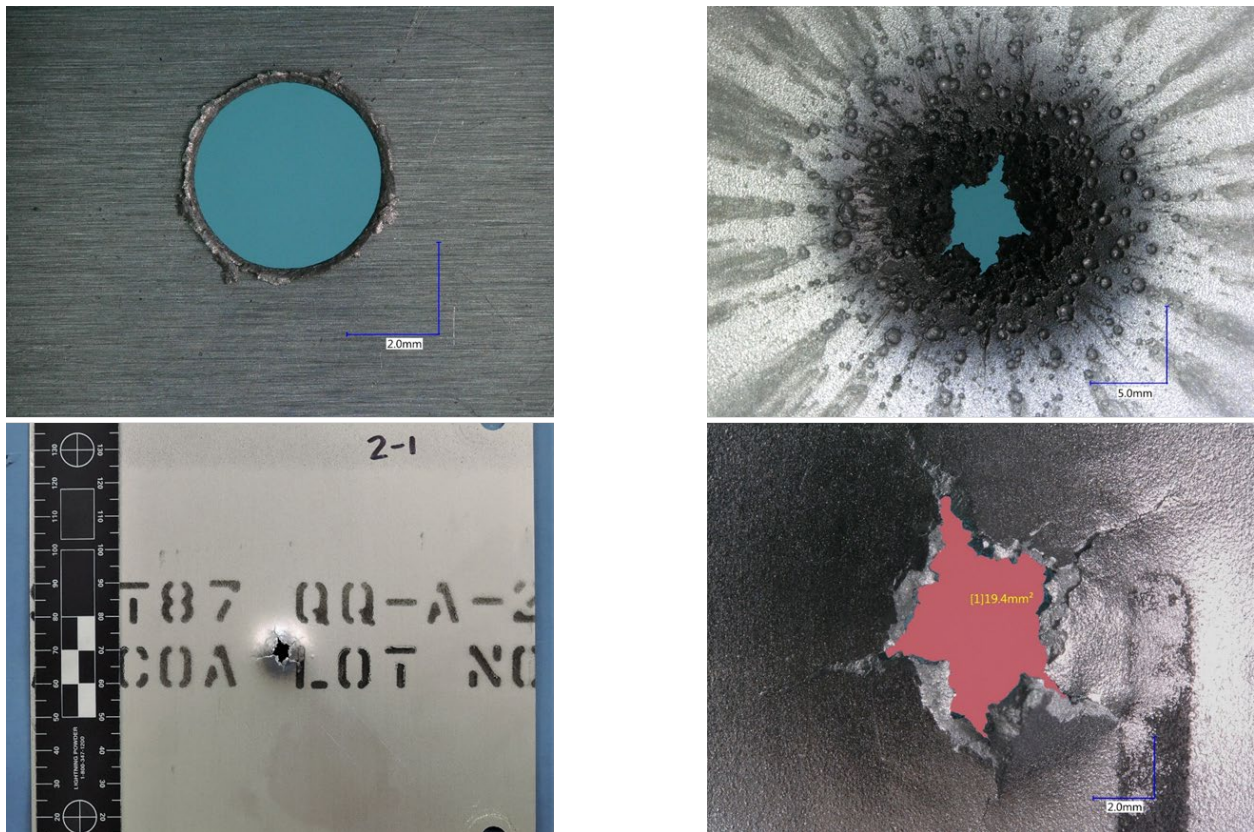


Figure 5.2-6: Image of front wall and rear wall (front and back surface) damage

5.2.1.5 Double Bumper Shield (8 km/s)

- Projectile: 1100 aluminium sphere 4 mm diameter, 8.0 km/s, normal impact (shot line perpendicular to target surface)
- First bumper: 2024-T3 aluminium 0.8 mm thick
- Spacing: 60 mm
- Second bumper: 2024-T3 aluminium 0.5 mm thick
- Spacing: 60 mm
- Backwall: aluminium 3.2 mm thick made of: 0.8 mm 2024-T3 + 0.15 mm adhesive + 3.10 mm AlMg₃.

5.2.1.6 Double Bumper Shield (11 km/s, Oblique Impact)

- Projectile: 99.9% pure aluminium 1.1 gram, length / diameter ratio 4.3, 11.2 km/s, oblique impact : 45 degrees
- First bumper: 6061-T4 aluminium 2.5 mm thick
- Spacing: 60 mm
- Second bumper: 6061-T4 aluminium 2.5 mm thick
- Spacing: 60 mm
- Backwall: 2219-T851 aluminium 5 mm thick

5.2.2 Validation Results

Members of the PWG are currently undertaking a programme of validation for different hydrocodes. Results from this will be presented here in a future issue of the Protection Manual.

5.2.2.1 NASA

5.2.2.1.1 Whipple Shield (Al projectile)

5.2.2.1.2 Whipple Shield (Al projectile > 9 km/s)

5.2.2.1.3 Whipple Shield (Alumina projectile using CTH from Sandia National Laboratory)

Fully documented work in: *To be published in* Miller, J.E., Davis, B.A., Deighton, K.D. and McCandless, R.J. *Rear Wall Perforation in Whipple Shields for Low- and High-Density Particles*. The 2nd International Orbital Debris Conference Proceedings, (2023).

The simulation of the benchmark case of 5.2.1.3 has been performed using CTH from Sandia National Laboratory. The simulation has been performed in a three-dimensional problem space; however, symmetry has been assumed along the central axis of the shield at the impact point. This symmetry assumption allows for a fourth of the total problem volume to be assessed. From the symmetry boundaries, the analyzed space is 3.6 cm in each orthogonal direction (7.2 cm total width because of the symmetry assumption) and from 0.5 cm in front and 6.0 cm behind the front of the shield in the flight direction. This problem domain is discretized into cells that are 0.1 mm on each side. To assist numerical stability during debris cloud expansion, the problem domain is filled with $0.12 \mu\text{g}/\text{cm}^3$ of a helium ideal gas at about 4 K, which translates into about a 1 Pa backfill. The non-symmetry boundaries are assumed to have an outflow and extrapolated pressure condition, which allows mass to flow out but not into the mesh while maintaining pressure (equivalent to an atmosphere). Materials are tracked down to at least $10^{-4} \text{ g}/\text{cm}^3$ (about a tenth of an atmosphere) before being discarded to improve time step stability; meanwhile, the backfill is tracked down to $10^{-7} \text{ g}/\text{cm}^3$. Simulations are carried out to 30 μs .

As alumina is commonly used by NASA to represent high-density meteoroids, material models that are developed using very high-pressure measurements are favored over models like the Mie-Grüneisen model that assumes a constant specific heat and temperature independent Grüneisen coefficient. To this end, the Al_2O_3 sphere is modelled with the SESAME B601 tabular equation-of-state (EOS). At the speeds attained on a two-stage, light-gas guns, the shear properties are more important than at normal meteoroid impact speeds; therefore, hydrodynamic shear properties are not assumed. That said, the model is kept simple because the stresses at impact in the normal use case is well above the material's strength capability, so a constant yield surface at a yield strength of 2.6 GPa is used. A Poisson's ratio of 0.22 is used to relate the bulk modulus to the other moduli. The material melting temperature, the temperature that shear strength goes to zero, is taken as 2,007.5 K. The fracture stress is taken as -2.6 GPa, which is the point at which void is introduced in the cell to relieve stress in the material to 0.6 of the fracture stress.

The shield is also anticipated to see very high stresses for the normal use case; therefore, both the front and rear wall are modelled with a tabular EOS like the alumina. For the aluminum walls

the SESAME 3700 model is used for the EOS. For Al6061 the tabular EOS is scaled ($\sigma = \text{table density/material density}$) to 2.703 g/cm^3 , and for the Al2219 the tabular EOS is scaled to 2.82 g/cm^3 . For these alloys, the material pressure is determined from $P(\rho, T) = P_{\text{Table}}(\sigma \rho, T)$ and the internal energy is determined by $E(\rho, T) = \sigma E_{\text{Table}}(\sigma \rho, T)$.

For both the bumper and the rear wall, the Johnson-Cook model is used to define the yield surface (yield strength as a function of strain, strain rate and temperature). For the bumper, the Johnson-Cook parameters are $A_{JO}=266.8 \text{ Mpa}$, $B_{JO}=126.8 \text{ Mpa}$, $C_{JO}=0.015$, $M_{JO}=1$, $N_{JO}=0.26$ with a fracture stress of -361 Mpa . The same Johnson-Cook parameters for the rear wall are $A_{JO}=274.0 \text{ Mpa}$, $B_{JO}=432.8 \text{ Mpa}$, $C_{JO}=0.015$, $M_{JO}=1$, $N_{JO}=0.26$ with a fracture stress of -517 Mpa . For both materials the Poisson ratio and melting temperature are taken as 0.33 and 800 K, respectively.

The simulations have been run using the exact projectile and shield parameters as discussed in 5.2.1.3. An image showing the evolution of the simulated debris cloud overplotted on the captured debris cloud images as shown in **Figure 5.2-3** is shown in **Figure 5.2-7**. In this sequence of images, the simulation's half-plane, density contour (reflected on one symmetry axis) is shown from 10^{-3} g/cm^3 to 10 g/cm^3 ; although, densities down to 10^{-4} g/cm^3 are shown because the plot is not clipped at the bottom of the density scale. As the experimental view is not flat, the simulation is shown at the mid-point of the shield in the view.

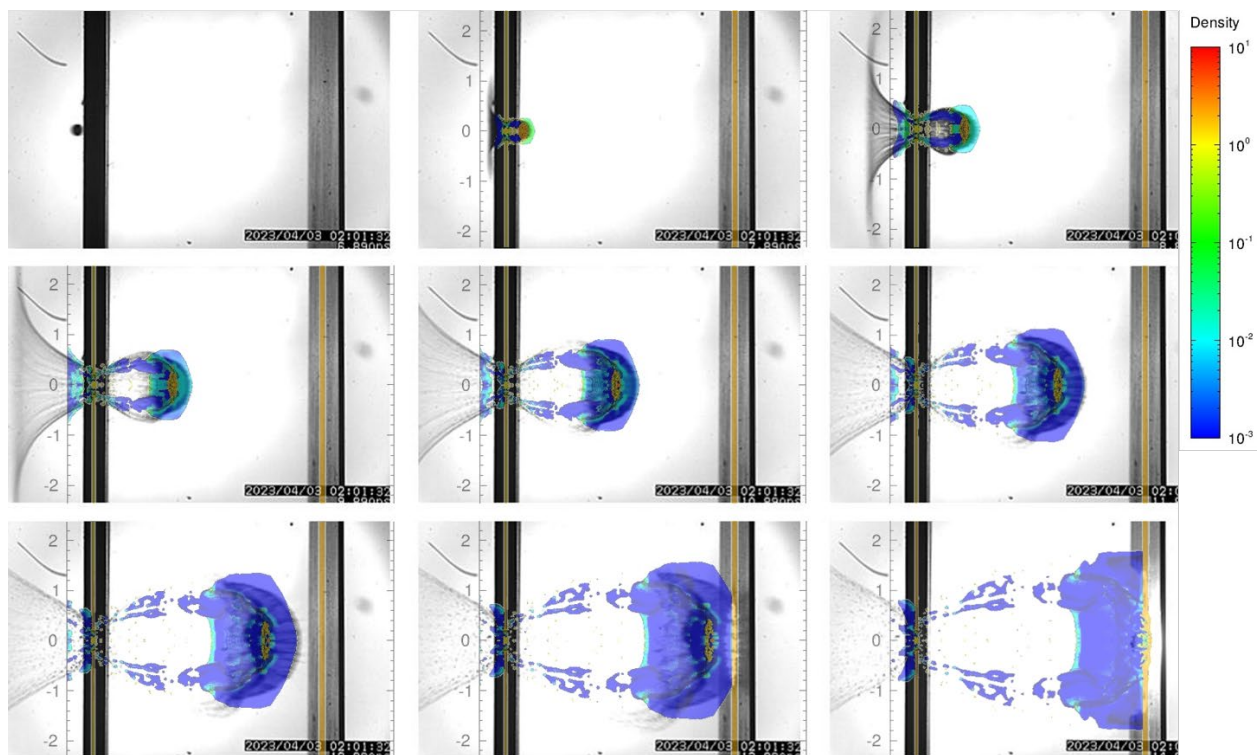


Figure 5.2-7: Comparison of the simulated debris cloud evolution with obtained videographs at $1 \mu\text{s}$ interframe rate

As can be seen in **Figure 5.2-7**, the general characteristics of the debris cloud are captured, speed and general spread down to about 10^{-2} g/cm^3 , but the lowest density portion, 10^{-4} g/cm^3 to 10^{-3} g/cm^3 , does expand more in the simulation than is actually observed. While this could be a topic for future development, the impact of that low of a mass of material on a structural wall is believed to be negligible, and the modelling of the more massive portion of the debris cloud

evolution is deemed sufficient. The movement of the debris cloud through the rear wall is tracked out to 30 μs , and the resulting simulated damage to the rear wall is shown in **Figure 5.2-8** as viewed from the front surface of the rear wall. As with the debris cloud, the image shows the density contour from 10^{-3} g/cm^3 to 10 g/cm^3 for the rear wall surface, but in this rendering, the simulation is reflected across both of the symmetry planes to give the flat face view. The density contour shows the average density in the top cell that is at least half full of the material; therefore, when the material moves out of the cell due to its motion, the density drops to half of its original value and produces the ring type structures shown in the image. Each ring measures 0.1 mm of deflection albeit not necessarily plastic deformation. The width of the outer ring of perforation is 17.6 mm, which compares favorably to the measured 19.6 mm in 5.2.1.3.

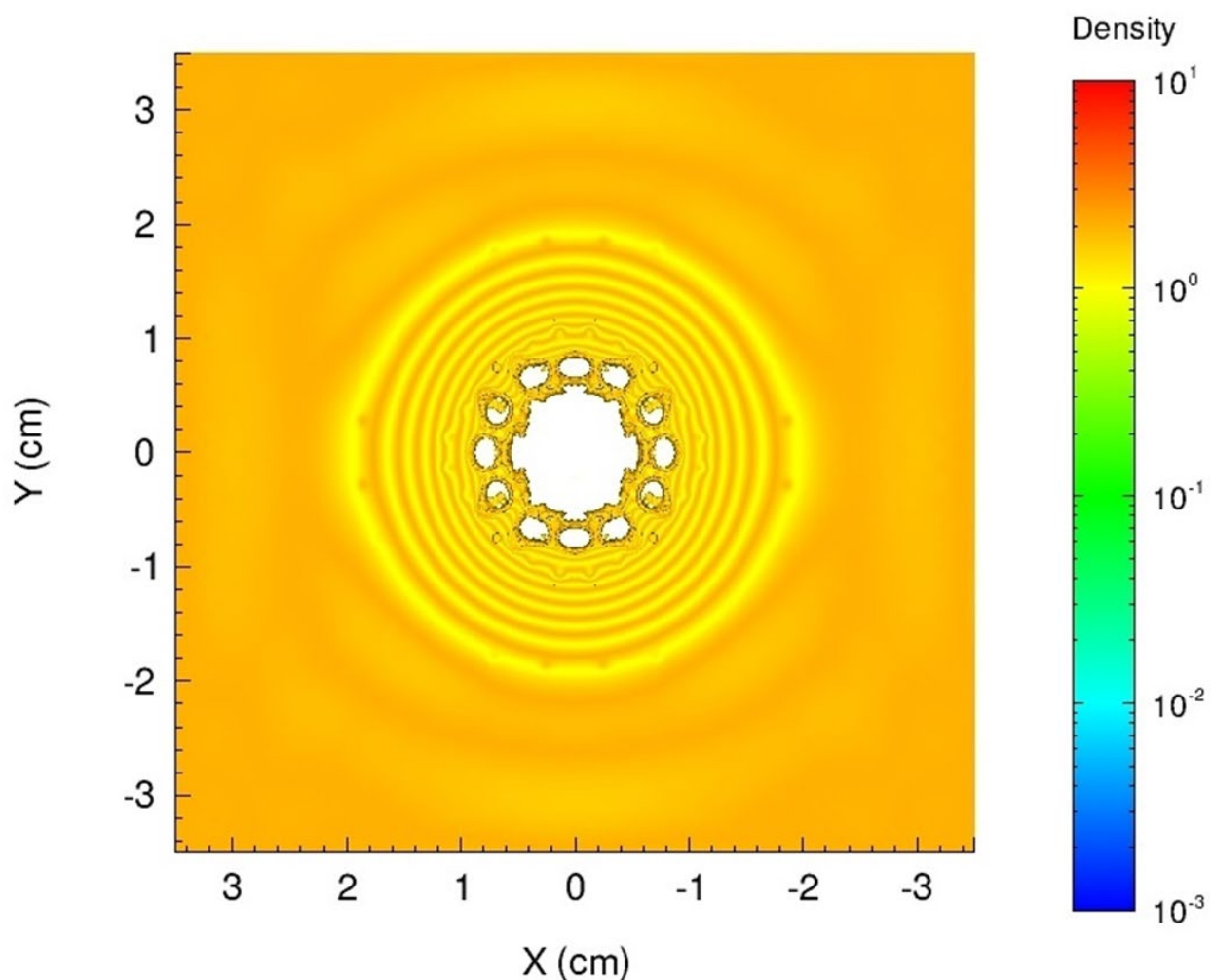


Figure 5.2-8: Density contour of the simulated damage at the front surface view of the rear wall

Arguably the more important damage measurement is the open area of the hole, which would dictate how much fluid behind the shield would escape or how much the internal components are exposed to the space environment. A comparison of the simulated and experimental back surface of the rear wall is shown in **Figure 5.2-9**. This image shows side by side comparisons of the experimental and simulated rear wall, and as can be seen the measured 124.8 mm^2 area of the hole compares very favorably to the simulated hole area of 122.8 mm^2 . The key qualitative difference is the spall ring was completely removed along with the central crater in the experiment, but portions of the spall ring remained intact in the simulation.

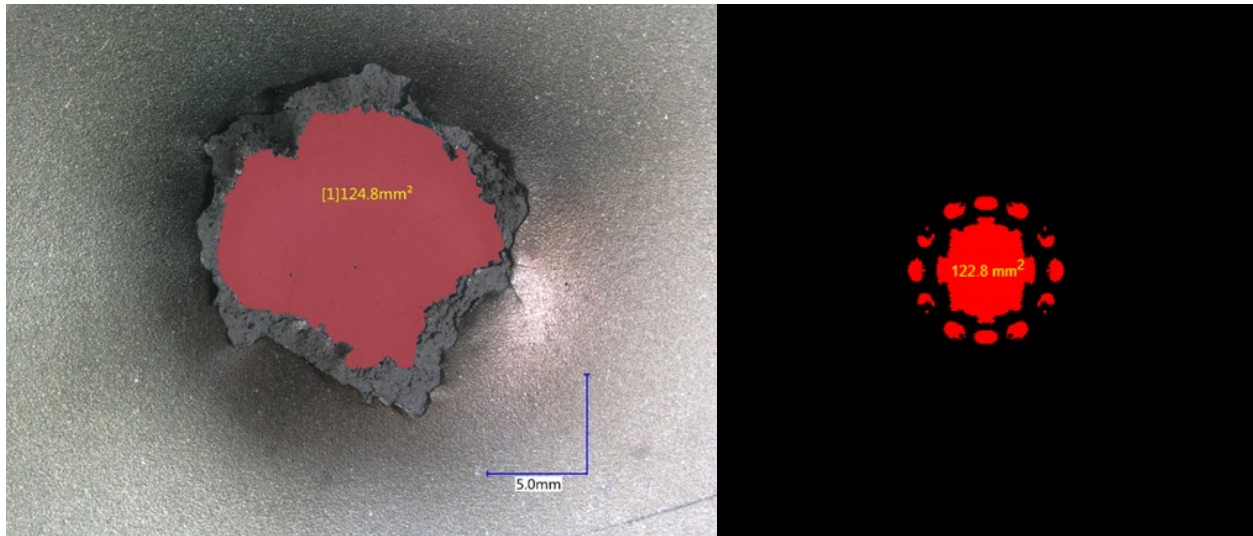


Figure 5.2-9: Comparison back surface rear wall hole from experiment and simulation

5.2.2.1.4 Whipple Shield (Nylon projectile)

Fully documented work in: *To be published in* Miller, J.E., Davis, B.A., Deighton, K.D. and McCandless, R.J. *Rear Wall Perforation in Whipple Shields for Low- and High-Density Particles*. The 2nd International Orbital Debris Conference Proceedings, (2023).

The simulation of the benchmark case of 5.2.1.4 has been performed using CTH from Sandia National Laboratory. The simulation has been performed in a three-dimensional problem space; however, symmetry has been assumed along the central axis of the shield at the impact point. This symmetry assumption allows for a fourth of the total problem volume to be assessed. From the symmetry boundaries, the analyzed space is 3.6 cm in each orthogonal direction (7.2 cm total width because of the symmetry assumption) and from 0.5 cm in front and 3.5 cm behind the front of the shield in the flight direction. This problem domain is discretized into cells that are 0.1 mm on each side. To assist numerical stability during debris cloud expansion, the problem domain is filled with $0.12 \mu\text{g}/\text{cm}^3$ of a helium ideal gas at about 4 K, which translates into about a 1 Pa backfill. The non-symmetry boundaries are assumed to have an outflow and extrapolated pressure condition, which allows mass to flow out but not into the mesh while maintaining pressure (equivalent to an atmosphere). Materials are tracked down to at least $10^{-4} \text{ g}/\text{cm}^3$ (about a tenth of an atmosphere) before being discarded to improve the time step stability; meanwhile, the backfill is tracked down to $10^{-7} \text{ g}/\text{cm}^3$. Simulations are carried out to 30 μs .

As Nylon is commonly used by NASA to represent volatile meteoroids like ice, material models that are developed using very high-pressure measurements are favored over models like the Mie-Grüneisen model that assumes a constant specific heat and temperature independent Grüneisen coefficient. To this end, the Nylon sphere is modelled with the SESAME 7300 tabular equation-of-state (EOS). At the speeds attained on a two-stage, light-gas guns, the shear properties are more important than at normal meteoroid impact speeds; therefore, hydrodynamic shear properties are not assumed. That said, the model is kept simple because the stresses at impact in the normal use case is well above the material's strength capability, so a constant yield surface at a yield strength of 62.4 Mpa is used. A Poisson's ratio of 0.4 is used to relate the bulk modulus to the other moduli. The material melting temperature, the temperature that shear strength goes

to zero, is taken as 487.4 K. The fracture stress is taken as -63.0 Mpa, which is the point at which void is introduced in the cell to relieve stress in the material to 0.6 of the fracture stress.

The shield is also anticipated to see very high stresses for the normal use case; therefore, both the front and rear wall are modelled with a tabular EOS like the alumina. For the aluminum walls the SESAME 3700 model is used for the EOS. For Al6061 the tabular EOS is scaled ($\sigma = \text{table density/material density}$) to 2.703 g/cm³, and for the Al2219 the tabular EOS is scaled to 2.82 g/cm³. For these alloys, the material pressure is determined from $P(\rho, T) = P_{\text{Table}}(\sigma \rho, T)$ and the internal energy is determined by $E(\rho, T) = \sigma E_{\text{Table}}(\sigma \rho, T)$.

For both the bumper and the rear wall, the Johnson-Cook model is used to define the yield surface (yield strength as a function of strain, strain rate and temperature). For the bumper, the Johnson-Cook parameters are $A_{JO}=266.8$ Mpa, $B_{JO}=126.8$ Mpa, $C_{JO}=0.015$, $M_{JO}=1$, $N_{JO}=0.26$ with a fracture stress of -361 Mpa. The same Johnson-Cook parameters for the rear wall are $A_{JO}=274.0$ Mpa, $B_{JO}=432.8$ Mpa, $C_{JO}=0.015$, $M_{JO}=1$, $N_{JO}=0.26$ with a fracture stress of -517 Mpa. For both materials the Poisson ratio and melting temperature are taken as 0.33 and 800 K, respectively.

The simulations have been run using the exact projectile and shield parameters as discussed in 5.2.1.4. An image showing the evolution of the simulated debris cloud overplotted on the captured debris cloud images as shown in **Figure 5.2-5** is shown in **Figure 5.2-10**. In this sequence of images, the simulation's half-plane, density contour (reflected on one symmetry axis) is shown from 10⁻³ g/cm³ to 10 g/cm³; although, densities down to 10⁻⁴ g/cm³ are shown because the plot is not clipped at the bottom of the density scale. As the experimental view is not flat, the simulation is shown at the mid-point of the shield in the view.

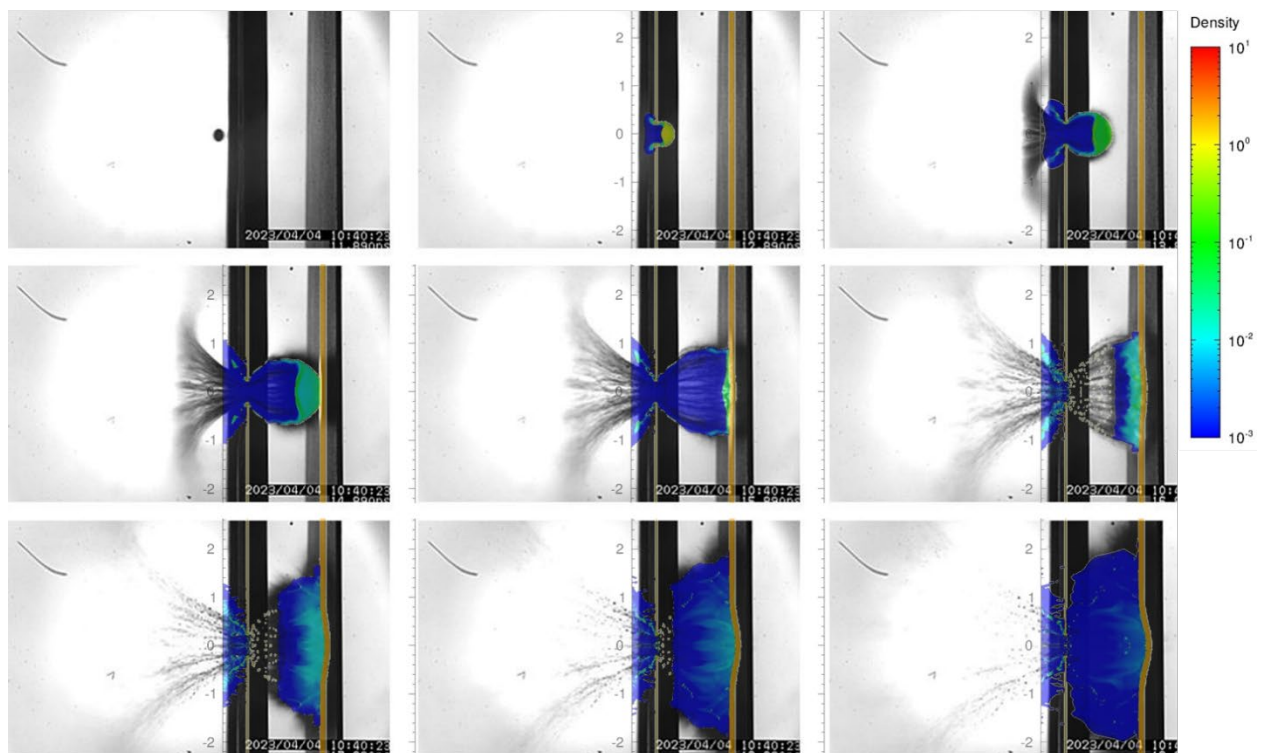


Figure 5.2-10: Comparison of the simulated debris cloud evolution with obtained videographs at 1 μ s interframe rate

As can be seen in **Figure 5.2-10**, the general characteristics of the debris cloud are captured, speed and general spread, albeit the shield gap is small and a only a few frames are available of the debris cloud prior to it interacting with the rear wall. The movement of the debris cloud through the rear wall is tracked out to 30 μs , and the resulting simulated damage to the rear wall is shown in **Figure 5.2-11** as viewed from the front surface of the rear wall. As with the debris cloud, the image shows the density contour from 10^{-3} g/cm^3 to 10 g/cm^3 for the rear wall surface, but in this rendering, the simulation is reflected across both of the symmetry planes to give the flat face view. The density contour shows the average density in the top cell that is at least half full of the material; therefore, when the material moves out of the cell due to its motion, the density drops to half of its original value and produces the ring type structures shown in the image. Each ring measures 0.1 mm of deflection albeit not necessarily plastic deformation. The width of the largest crack is 13.1 mm, which compares favorably to the measured 13.9 mm in 5.2.1.4.

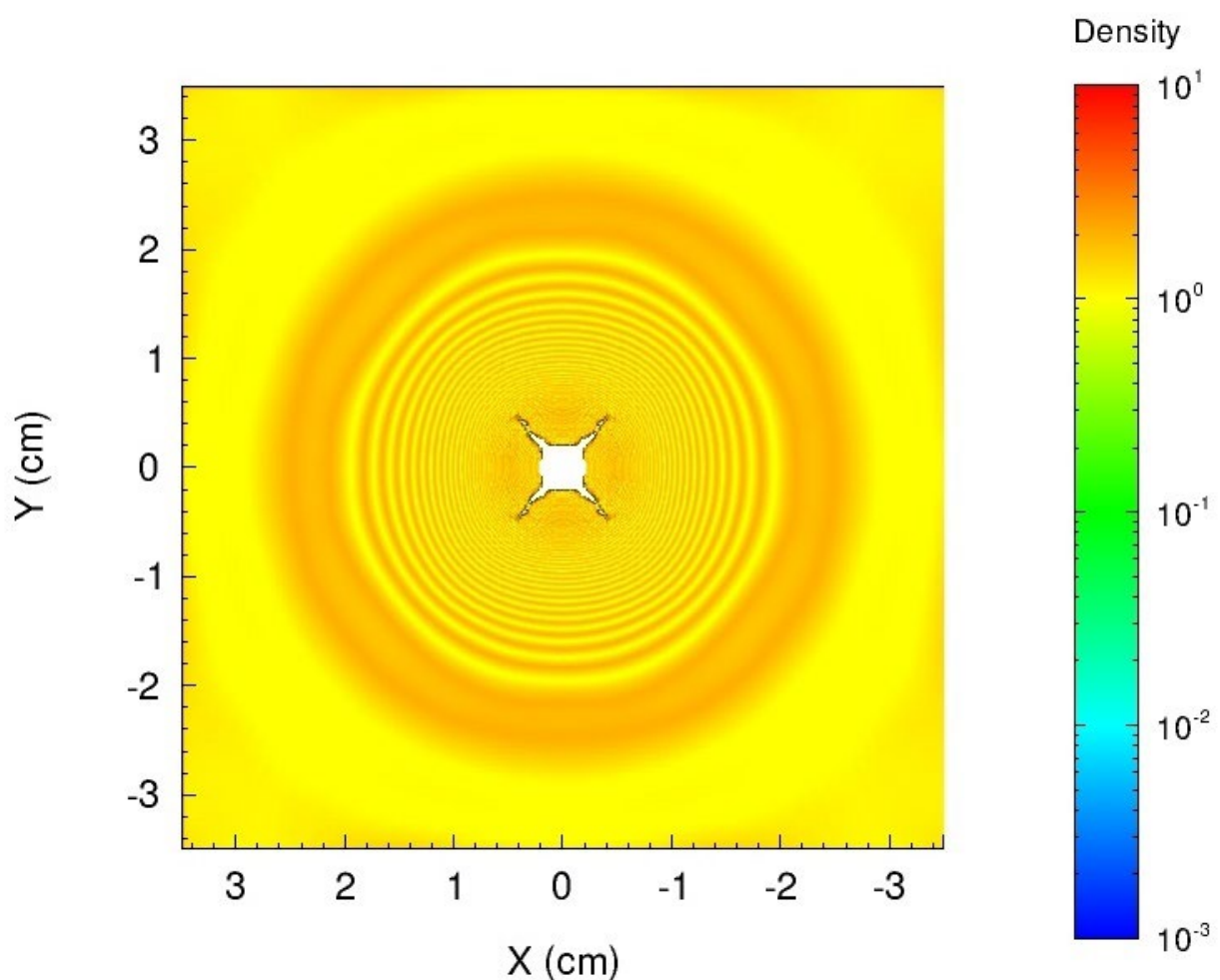


Figure 5.2-11: *Density contour of the simulated damage at the front surface view of the rear wall*

Arguably the more important damage measurement is the open area of the hole, which would dictate how much fluid behind the shield would escape or how much the internal components are exposed to the space environment. A comparison of the simulated and experimental back surface of the rear wall is shown in **Figure 5.2-12**. This image shows side by side comparisons of the experimental and simulated rear wall, and as can be seen the measured 19.4 mm^2 area of the hole compares very favorably to the simulated hole area of 16.1 mm^2 . Although the hole in the

simulation is smaller at 30 μ s, it is possible with much longer run times hole areas will come into closer agreement; however, regardless of that quantitative difference, qualitatively it can be seen that the simulation closely captures the general characteristics of the perforation.

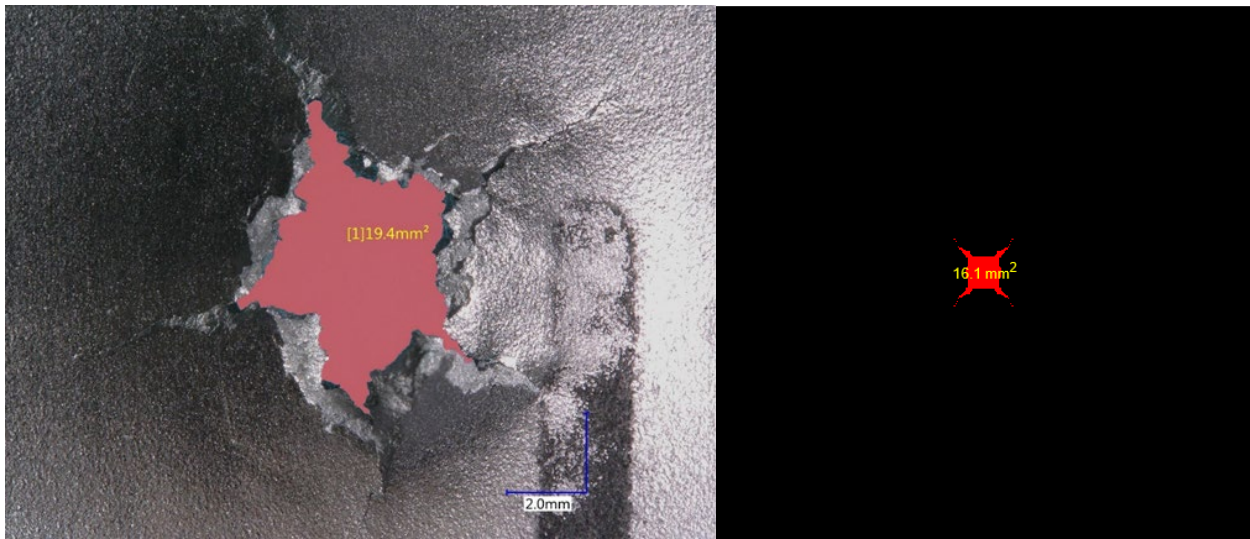


Figure 5.2-12: Comparison back surface rear wall hole from experiment and simulation

5.3 Codes Used by the PWG

5.3.1 ROSAVIAKOSMOS

With its advanced launching technology and hydrocodes, the Russian Federal Nuclear Center (VNIIEF-RFNC) is well placed to conduct combined experimental (see Section 4.4.3) and theoretical research. The facility utilises modern numerical KERNEL and EGAK hydrocodes [Bashurov, 1992, 1997]. The 3-D code KERNEL is based on the SPH-method and has a variety of EOS for modelling of gases, elastic-plastic behaviour of solid bodies and two-phase flows. The Kernel code is assigned to perform numerical simulation of the following problems:

- Hypervelocity impact of single projectiles to mono- and multi-layered barriers as well as barriers consisting of distanced sheets.
- Penetration of deformable bodies into semi-infinite media.
- Detonation of HE and combustible mixtures.

The integral-differential code EGAK is intended for numerical modelling of 2D flows of compressible multi-component media with large deformations.

The EGAK code is being evaluated against the test cases quoted above [Ioilev, 1998].

5.3.2 NASA

NASA uses a variety of hypervelocity impact simulation techniques, including the CTH code from Sandia National Laboratory, Impetus- γ SPH from IMPETUS-Afea through its North American distributor CertaSim, and EXOS developed at the University of Texas. NASA is involved in validating the codes with available test data (light gas guns and inhibited shaped charge launcher). NASA then uses the validated code to obtain insight in expected impact damage at conditions not tested. For instance, shield performance against non-spherical projectiles in untested orientations, obliquities and speeds and for meteoroids at speeds greatly in excess of what is achievable in terrestrial facilities.

5.3.3 ALENIA

Alenia Aerospazio and University of Rome “La Sapienza” have gained experience in HVI numerical simulation using hydrocodes [Faraud, 1998]. The planned activity includes the calibration of hydrocodes, the study of normal and oblique impacts on triple wall systems, with the extrapolation of the experimental results to higher impact velocities.

The Aerospace Department of University of Rome “La Sapienza” is performing numerical simulations of hypervelocity impacts using the hydrocode AUTODYN, developed by Century Dynamics.

All the simulations performed in the hypervelocity regime involve the use of the SPH (Smoothed Particle Hydrodynamic) processor. SPH is a gridless method particularly suitable for the simulations of very large material deformations and expansions occurring in hypervelocity impact phenomena.

As the SPH technique has not been sufficiently validated yet for structural problems, and the AUTODYN SPH processor is still a Beta version, a part of the research activity regards the code calibration. This is achieved by simulating hypervelocity experiments available in the literature involving different geometries, materials and impact velocities, and tuning the numerical parameters in order to obtain a good agreement with the experiments.

A second part of the analysis is concerned with the applications of numerical simulations to the design of space structures.

In particular a research program in co-operation with Alenia Aerospazio exists for the simulation of hypervelocity impacts against the space debris shields of the European modulus Columbus on the International Space Station [Palmieri, 1998]. The numerical results are compared with the Light Gas Gun (LGG) hypervelocity impact tests performed at Ernst Mach Institute (Freiburg, Germany). For the moment the analyses were performed only on three aluminium wall shielding systems, due to the lack of hypervelocity behaviour models for other materials used of interest such as Kevlar and Nextel. The simulations were conducted by considering a wide range of parameters, such as spatial resolution, material models, discretisation technique, artificial viscosity coefficients and the smoothing length of the SPH algorithm. A comparison was also performed between the results obtained with AUTODYN and the PAMSHOCK code, developed by ESI.

Another ongoing research co-operation with Ernst Mach Institute regards the numerical and experimental study of hypervelocity impacts on pressure vessels.

Future activity to be carried out as part of the co-operative effort with Alenia Aerospazio, concerns the:

- extrapolation of the impact data into higher velocity regimes not achievable in the laboratory due to limitations of the LGG technology,
- simulations of experiments performed with different techniques such as shaped charges,
- introduction of materials as Kevlar and Nextel by using recently developed material models, and the
- characterisation of the shape effects.

5.3.4 JAXA

JAXA has carried out a series of hypervelocity impact analyses by using AUTODYN-2D. Some of the results were compared with two-stage light gas gun experimental results in the lower velocity region; the numerical results were discussed with reference to NASA's ballistic limit curve [Shiraki, 1997a, 1997b]. The debris and stuffed Whipple bumper shield except for the back wall were modelled by the multiple material Eulerian solver, while the back wall was modelled by the Lagrangian solver, and the interfaces between Lagrangian and Eulerian solvers were taken into account by the Lagrange/Euler interaction capability.

The numerical analysis method was extended to the tests by the inhibited conical shaped charge. The simulated debris by the inhibited CSC was modelled by the multiple material Eulerian solver [Shiraki, 2000].

5.3.5 NAL/CRC

As part of NAL/CRC's modelling initiatives, Katayama *et al.*, 1993, proposed the interactive rezoning method of AUTODYN-2D's Lagrangian solver in order to simulate the debris cloud formation and impact on the back wall of the Whipple shield, and demonstrated its effectiveness.

NAL conducted a series of hypervelocity impact tests by using the rail gun (ISAS), two-stage light gas gun (Tohoku Univ.) and the powder gun (Kyoto Univ.). Numerical analyses were performed using AUTODYN-2D's Eulerian solver to optimise the material models for the Whipple bumper shield and simulated debris. After that, the damage of the back wall was estimated by the interactive rezoning method of AUTODYN-2D's Lagrangian solver, and it was shown that the numerical results had good agreement with the experimental results [Katayama, 1995]. It was also ascertained that the multiple material Eulerian solver provides comparable results, although it required much more CPU time, but with significantly less manpower [Katayama, 1997].

The numerical method by the multiple material Eulerian solver to simulate the inhibited conical shaped charge was proposed and its effectiveness was demonstrated by comparing with the experimental results. The simulation includes the jet formation, the jet travelling and the jet penetrating into the target [Katayama, 1998]. The method was enhanced by using the Lagrange/Euler interaction capability of AUTODYN-2D to simulate the inhibitor deformation and its delayed jet trapping [Katayama, 2000a, 2000b].

5.3.6 CDL

Hydrocode modelling activities at Century Dynamics Ltd, UK (the developers of AUTODYN) are well covered in the literature (e.g., Hayhurst, 1995, 1996, 1997, 1998, 1999, and 2001).

The AUTODYN code has been evaluated against impact test results on Whipple and double bumper shields in the velocity range from 3.1 to 11.0 km/s [Hayhurst, 1998]. It has been found that all the hypervelocity impact test cases considered for this work have been successfully simulated.

Other UK groups are also actively engaged in using or developing hydrocodes [McDonnell, 1993; Campbell, 1996, 1997].

5.4 Development of Material Models for Nextel and Kevlar Epoxy Resin

ESA has funded a research project under contract No. 12400/97/NL/PA(SC) to develop and define advanced material models and data for Nextel and Kevlar/Epoxy under hypervelocity impact conditions. The work was carried out by the Ernst-Mach-Institut (EMI), Century Dynamics Ltd (CDL) and TNO Prins Maurits Laboratorium (TNO).

The AMMHIS project [Hiermaier, 1999] was particularly concerned with the materials used in the spacecraft shielding configuration shown in **Figure 5.4-1**, this being a shielding configuration for the European Columbus module of the ISS.

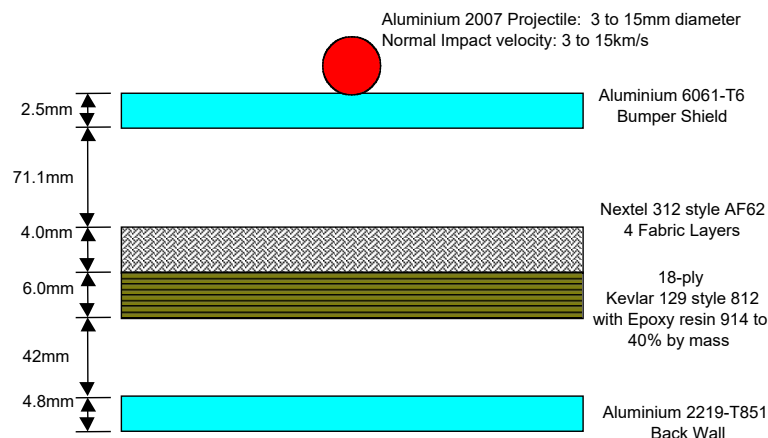


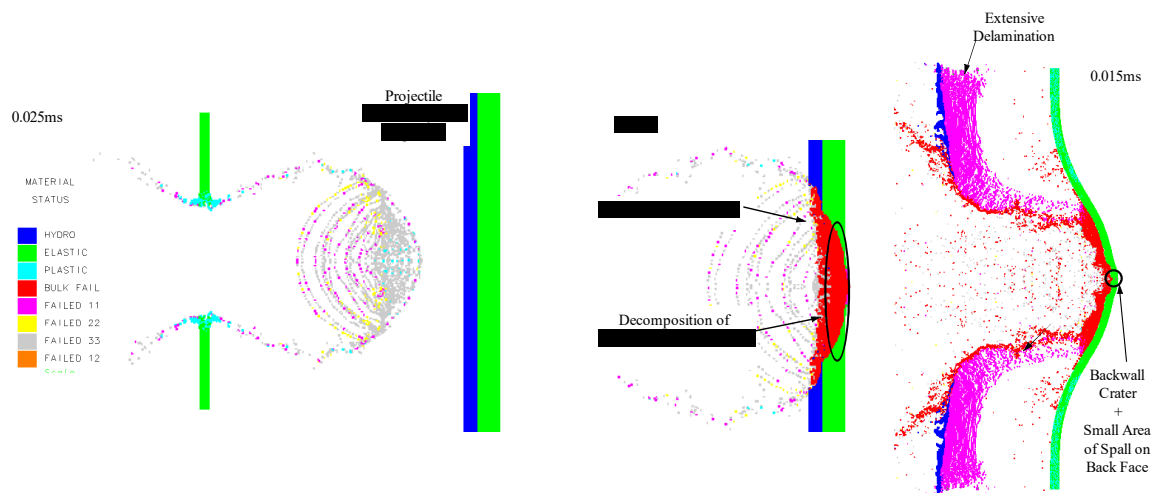
Figure 5.4-1: Spacecraft shielding configuration for the Columbus module.

The developed numerical model describes the material behaviour of Nextel and Kevlar/Epoxy under highly dynamic loading. The hypervelocity impact of aluminium projectiles up to 15 mm in diameter and normal velocities in the range of 3 km/s to 15 km/s were considered. In order to make numerical simulations of a hypervelocity impact on the reference configuration possible in terms of computation times, a macroscopic continuum model for the involved materials had to be developed. Existing experimental work performed by EMI showed that the failure patterns after a normal impact are mostly circular. Thus, initially a two dimensional axisymmetric model would be able to describe the performance of the shield under normal impact. The large deformations occurring in any hypervelocity impact are best discretized by meshless methods. Therefore, the AUTODYN SPH solver was used to model the projectile and bumper shields. The backwall was modelled with the Lagrange solver and coupled to the SPH particles through contact logic.

A co-ordinated and combined strategy of simulations and physical testing was developed that allowed a model to be derived that is able to describe the complex material response. A combination of static compression tests under rigid and reactive confinement, one- and two-dimensional tension tests, wave propagation tests and two kinds of flyer impact tests were conducted. This wide range of experiments was required to gain an understanding of, and information about, the material behaviour under dynamic loading conditions. Due to the experimentally observed behaviour of Nextel and Kevlar/Epoxy, a new orthotropic hydrocode

model was developed. This was necessary because pressure inside these materials depends on deviatoric strain components as well as volumetric strain. Non-linear effects, such as shock effects, can be incorporated through the volumetric straining in the material. Thus, a basis was found to couple the anisotropic material stiffness and strength with shock effects, associated energy dependence and compaction. The developed model includes orthotropic material stiffness, a non-linear equation of state and material compaction within a unified formulation. No known model has been developed with this combination of capabilities before. Details of the model are available in Hayhurst, 1999, together with initial simulations, on the above reference configuration, using the model. The developed AMMHIS material model is able to predict the main aspects of the shielding material response as illustrated in **Figure 5.4-2**. Calculated shielding damage in the first bumper and in the Nextel and Kevlar/Epoxy layers correlates well with experimental results. In terms of the backwall damage, the model is able to reproduce closely the ballistic limit observed experimentally.

Subsequently the model has been incorporated into AUTODYN-3D and simulations of oblique and 3D normal impacts have been performed [White, 2001]. In this work conducted for Alenia Spazio the model was used to assess the ballistic limit across a range of projectile masses and impact velocities. Aluminium spherical projectiles of diameter range 12mm to 17mm and impact velocities of 3 to 11 km/s were simulated and compared with the analytical ballistic limit curves. Validation against 10 light gas gun tests at the lower velocity range was also performed. A limited range of oblique impact cases were performed for aluminium projectiles and a simulation to compare with the ISCL (Inhibited Shaped Charge Launcher) test conducted at SwRI was performed. A summary of the more recent work has also been published [Hayhurst, 2001].



AUTODYN-2D SPH Simulation, Key Features of Material Response During Impact

Figure 5.4-2: AUTODYN-2D Simulation using the AMMHIS model.

5.5 Simulation of HVI on Pressure Vessels

5.5.1 CNES Simulations

The main question addressed by CNES in their simulations is: under what conditions can a hypervelocity impact on a composite high-pressure tank lead to a burst or a leak?

Thus, the aim of the study managed by EADS Launch Vehicles with INSA Toulouse is to determine the driving parameters of the tank and of the projectile, and to identify the different domains of behaviour using a modelling approach [Salomé, 2001].

5.5.1.1 The High Pressure Tank

Mechanical Characteristics

- Titanium liner ($e = 0.9$ mm)
- Carbon / epoxy composite overwrapping
- Useful volume 50 to 180 litres

Fluid Characteristics

- Helium initial pressure up to 31 Mpa
 remaining pressure during orbit life: 3 Mpa
- Xenon initial pressure up to 18 Mpa
 decreasing to 0 during the orbit life

5.5.1.2 The Numerical Simulation

A SPH (Smooth Particle Hydrodynamic) code is used.

Composite Modelling

A transverse isotropic composite material (filament winding) is considered, so, the elastic stiffness matrix comprises five independent coefficients:

- in-plane Young modulus (longitudinal)
- transverse Young modulus through the thickness
- shear modulus in the (t, l) plane
- two Poisson coefficients

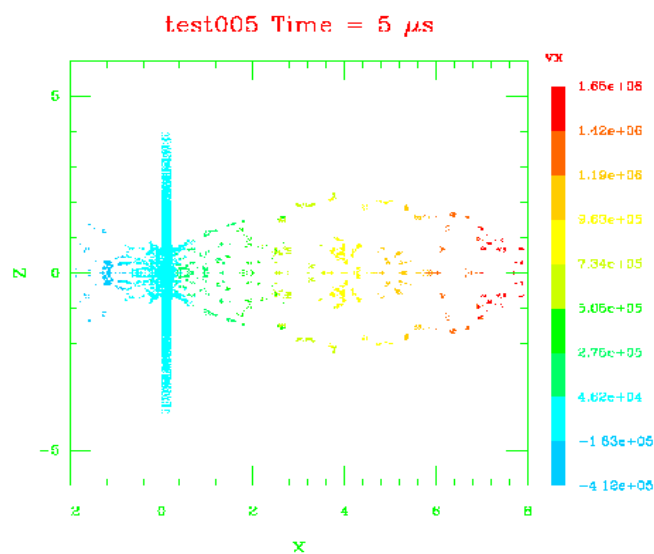
Projectile

- Aluminium sphere $0.1 \text{ mm} < \Phi < 5 \text{ mm}$
- Velocity $5 \text{ km/s} < V < 20 \text{ km/s}$

Target

- 7-liter Stainless steel liner (spherical) overwrapped with carbon/epoxy (sample for future tests)
- liner thickness: 1mm
- composite thickness: 3.4mm
- 3 configurations of gas storage conditions were analysed:
- helium at 3 and 30 Mpa
- xenon at 15 Mpa

Preliminary SPH code validation 2D/3D in-plane and axisymmetric configurations



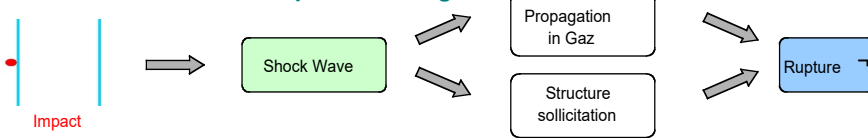
$\Phi = 5$ mm, $V = 5$ km/s, Aluminium plate ($e = 2$ mm)

Figure 5.5-1: 3D axisymmetric simulation

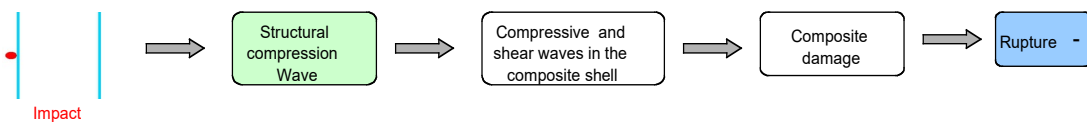
5.5.1.3 Damage Scenarios

Three damage scenarios which can lead to the burst rupture of the tank have been identified:

Scenario 1 : Shock wave in the pressurised gas



Scenario 2 : Compressive and shear waves in the composite shell



Scenario 3 : Damage of the back wall by the debris

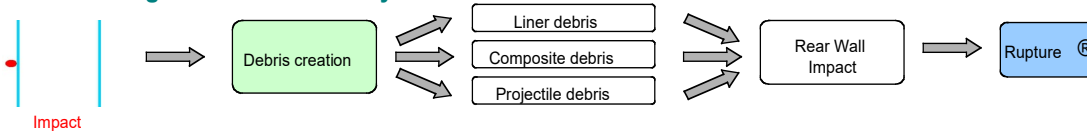


Figure 5.5-2: Tank rupture scenarios

1. Shock wave in the pressurized gas: The pressure peak of this strong shock wave is proportional to the initial pressure in the tank and can reach up to 1 Mbar ($\sim 10^{11}$ Pa). Starting from the impact area, the shock wave is transmitted to the gas by the fragment cloud and propagates into the fluid and can reach the opposite side of the tank. It also goes along the tank wall. Thus, all the structure is subjected to very high loads which can be higher than the design burst characteristics of the tank.
2. Compressive and shear waves in the tank shell: Upon impact, the liner and the composite shell are subjected to large deformations and high stresses. These lateral compression waves can be damped in the liner. However, they may reach the opposite side and result in locally exceeding the material strength by a resonance process. Moreover, interference phenomenon can occur into the composite and induce detrimental damage whereas the composite material has low performance in compression.
3. Damage of the rear side by fragments: A fragment cloud is generated by the impact from the projectile, the metallic liner and the composite shell. The cloud propagates with a velocity up to 1.4 times the initial velocity of the projectile. The fragments are decelerated in the gas and in some conditions their kinetic energy can be decreased down to 0. However, some of them can reach the opposite side of the tank with sufficient energy to induce cratering and perforation with generation of new debris and possible catastrophic failure.

A fourth scenario, similar to a fatigue failure, also has to be considered.

5.5.1.4 Results

Various simulation cases were done and the analysis has been performed in 5 steps:

- determination of the perforation threshold
- estimation of the hole diameter and of the residual energy transmitted to the gas
- determination of the energy threshold beyond which the critical pressure is reached (80 Mpa in the case here)
- determination of the angle of the pressure cone (piston effect)
- evaluation of the damages on the opposite side of the tank

Sensitivity of the Model

The sensitivity analysis of the model to several parameters (pressure loads in the shell before impact, characteristics of the composite) shows that:

- the hole and the damaged area diameters are not very dependent of the initial loads in the shell
- the damaged area diameter can be increased of about 30% with respect to the limit load characteristics of the composite

Helium Tank

Figure 5.5-3 and Figure 5.5-4 are cross sections of the tank showing the shock wave within the gas.

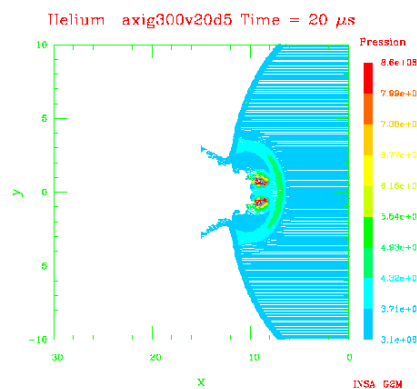


Figure 5.5-3: Helium 30 Mpa

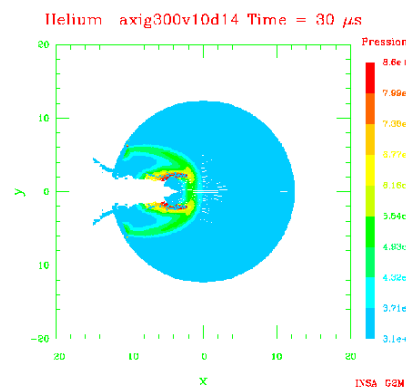


Figure 5.5-4: Helium 300 Mpa

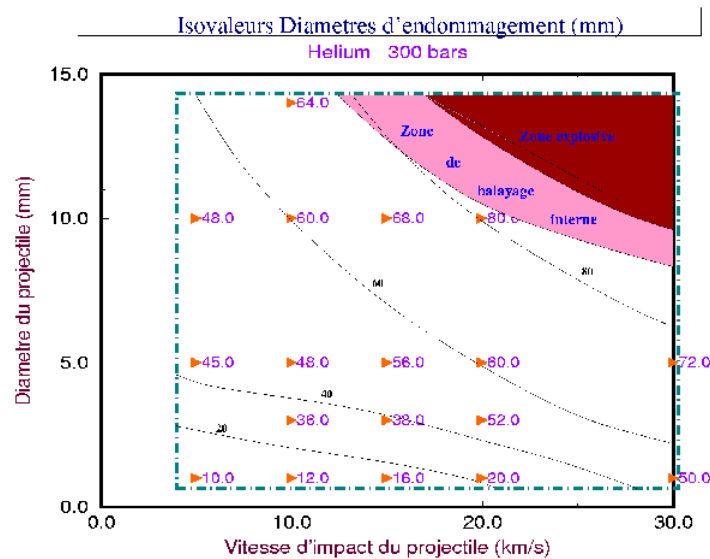


Figure 5.5-5: Phase diagram – Helium 30 Mpa

This shows that the explosive domain is reached for projectile with a diameter above 10 mm. The failure scenario is the scenario (1) due to the pressure shock wave in the gas. The pressure value of 80 Mpa corresponding to the limit load characteristic of the composite seems to be representative of the rupture threshold of the tank.

The scenario (2) is obtained for smaller projectiles with slower velocity.

Xenon Tank

Figure 5.5-6 and **Figure 5.5-7** present the results for Xenon configurations.

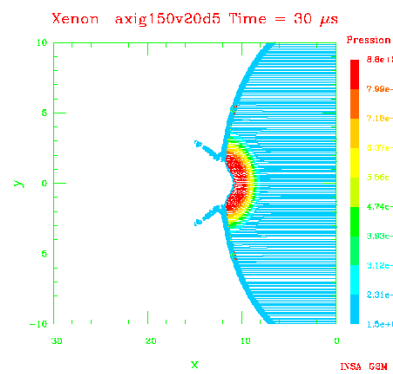


Figure 5.5-6: Xenon – 15 Mpa

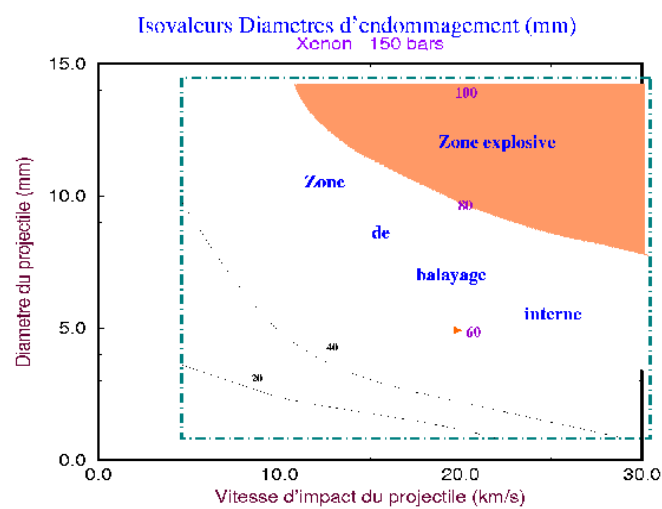


Figure 5.5-7: Phase diagram – Xenon 15 Mpa

5.5.1.5 Conclusion

The first results obtained by the numerical modeling performed with SPH code provide a good idea of the high pressure composite tank under hypervelocity impact.

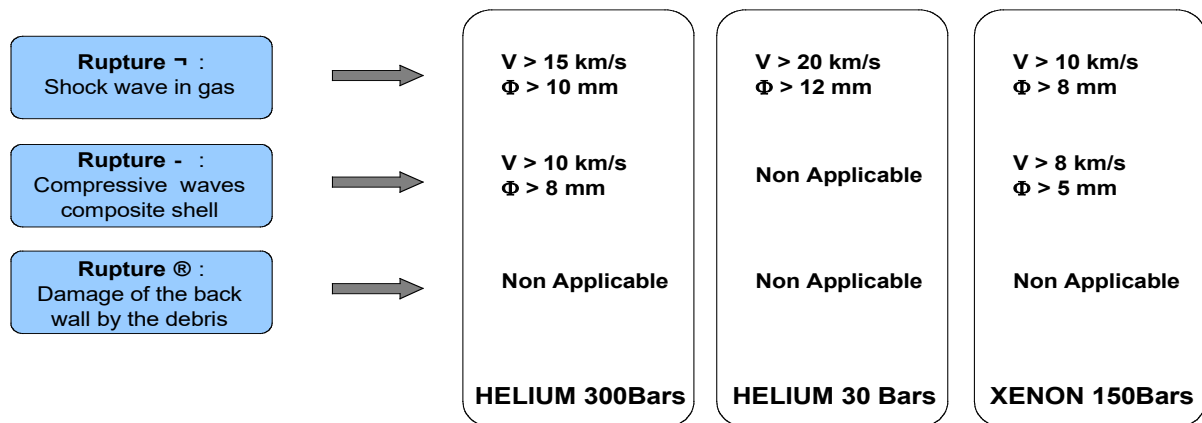


Figure 5.5-8: Results of HVI simulation on pressure vessels

The bigger the tank is, the lower are the effects of the internal shock wave in the gas. The effects of the fragments on the rear wall of the tank will decrease too.

The initial gas pressure is of a major importance. The higher the pressure is, the more important the kinetic energy transfer is. Then, the risk of over-pressure in the tank is increased. Nevertheless, the fragments are slowed down and the risk of damaging the back wall is reduced.

The use of Xenon leads to possible explosive regime more critical compared to the helium case. But the effect of the fragment cloud is less dangerous.

No detrimental effect has been foreseen due to Xenon loading in a super critical state.

Careful consideration must be given to the fourth scenario, which takes place during a lapse of time not covered by the runs performed. After the tank shell is perforated, the gas pressure will decrease slowly, typically in a few seconds, which is a long time compared to the duration of the phenomena in the tank (up to few tens of microseconds). Thus, a perforated tank will withstand a pressure close to its initial value before the impact.

The higher the pressure is the more critical this scenario is.

The next step of the study will be to perform hypervelocity impacts on real samples to get improved input data related to the composite. Further on, the SPH code will be used to simulate the behaviour of the 70 litres test pressure vessel. In parallel, the test facility will be defined and a test plan will be issued.

5.5.2 ESA Simulations

Hypervelocity impact on pressure vessels, as used for many different applications in and around spacecraft, was investigated by experimental and numerical means at EMI under ESA contract 10556/93. Of specific interest was the fragment cloud inside the vessel and the shock wave in the gas. Both have significant influence on the failure mode of the vessel. In the worst case a catastrophic rupture would lead to fragmentation of the vessel and related threat to nearby personal, structures and devices.

In the case of a hypervelocity impact on gas-filled vessels, there is a significant influence of the gas pressure on the formation of the fragment cloud [Hiermaier, 1999b]. Therefore, a simulation of this kind of impact must of course also describe the gas and its interaction with the fragment cloud. This can be done in different ways. Commonly, a fluid, like a pressurised gas, would be described by an Eulerian grid. This would, however, require the use of a single Eulerian grid for the whole system. A coupled Euler-Lagrange or Euler-SPH method would need some type of polygon to describe the interaction zone between solid material and the fluid. Due to the fragmentation of the impacting sphere and the target material it is impossible to use standard polygon type interaction capabilities between Eulerian and Lagrangian or SPH methods. Based on ESA / EMI's experience with other hypervelocity impact simulations the whole system was described using SPH particles. The disadvantage of this is that the SPH method is computationally much more expensive than standard Lagrangian or Eulerian methods.

For the simulation of a 5.2 km/s impact on a vessel filled with gas pressurised to 1.05 Mpa AUTODYN-2D was used. The aluminium material model consisted of a Johnson-Cook strength model and a Tillotson equation of state, whereas air was described via an ideal gas EOS. The vessel casing away from the penetration zone was described using shell elements. For the penetrated front wall SPH particles were applied.

Fragment cloud photographs from experiments, and the corresponding numerical simulation, are presented in **Figure 5.5-9**. At 10 kPa near-vacuum pressure, the well-known undisturbed drop-like cloud shape is formed. In the center of the cloud's leading edge, a large fragment particle is visible in the 25 μ s picture. Experimental work and simulations showed that this large central fragment originates from the center of the spherical projectile. At later stages of the impact process, a gray fog-like dust becomes visible behind the leading edge of the cloud. This dust is most likely due to a small amount of ablation products which are generated from the interaction of the hypervelocity fragments with the residual atmosphere in the target chamber.

Compared to the 1.05-Mpa experimental results the SPH simulation shows very similar phenomena. After the initial formation of a drop-like fragment cloud a spike is built out in the front centre area of the bubble. Bigger fragments are less decelerated in the whole cloud and build additional spikes in the outer regions. The individual fragments initiate shock waves in the surrounding gas. From **Figure 5.5-9** it is visible that the numerical simulation represents very well the expansion of the radial gas shock wave.

The simulation shows quite good agreement with the experiments concerning the bubble shape and velocities, as also shown in **Figure 5.5-9**. The spike formation starts at approximately 20 μ s in the simulation. The resulting jet-like tip grows very similar to the experimentally observed process. One big fragment on the center axis and about five smaller ones in the outer front region characterise the cloud's appearance from then on.

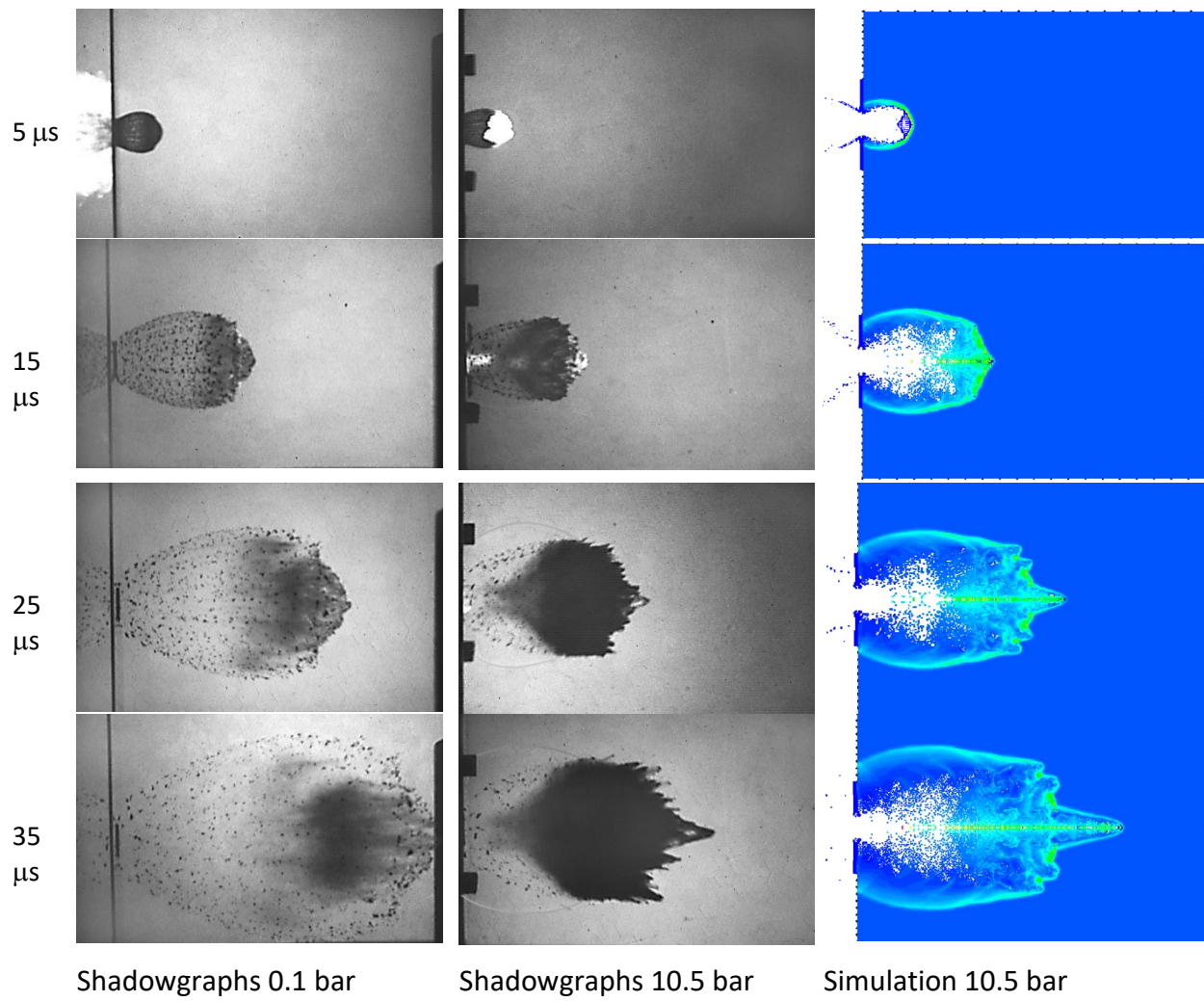


Figure 5.5-9: Shadowgraph pictures of fragment cloud at different pressures and numerical results

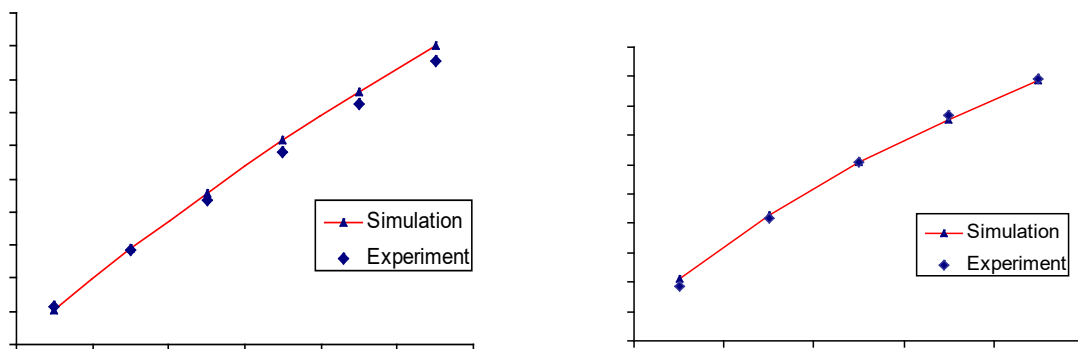


Figure 5.5-10: Position of centre tip fragment and radial expansion of the shock wave in gas

5.6 Simulation of Orbital Debris Impact Problems using a Hybrid Particle – Finite Element Method

The orbital debris hazard to the International Space Station (ISS) and other space structures has focused a significant research effort on the problem of spacecraft shielding design. To date shield design work has relied primarily on experimental hypervelocity impact research, with impact simulation playing a limited role. However, a number of factors suggest that future design work will place increased emphasis on the use of simulation. Experimental studies using light gas guns and inhibited shaped charge launchers are at present unable to investigate the entire projectile velocity and kinetic energy range of interest. The increased use of composite materials (in both shielding and aerospace structures) and the introduction of multi-layered shields have greatly expanded the number of experiments required to fully investigate each shielding design problem. Finally, the increased availability of high performance and massively parallel computing hardware will expand the range of design problems which can be investigated through simulation.

Despite these strong motivations, progress in the application of impact codes to spacecraft shielding design problems has been relatively slow. The most important reason is that the numerical methods embodied in traditional continuum Lagrangian and Eulerian codes are not well suited to address certain non-continuum physics associated with the shielding design problem. Most recent work simulating orbital debris impact effects has employed either pure particle or mixed particle-continuum methods, since only particle-based kinematic schemes offer both an efficient solution to the debris propagation problem and an entirely general representation of contact-impact. Work based on pure particle methods has encountered difficulties with accurate modelling of material strength effects, and other complications. It appears that some mixed or hybrid particle-continuum method will prove most effective in meeting the need for fundamental improvements in simulation-based design of orbital debris shielding.

In the hybrid formulation of Fahrenthold & Horban, 1999 & 2001, particles and finite elements are used simultaneously but not redundantly to represent different physical effects. The particles are used to represent all inertia effects as well as the thermomechanical response of the medium in compressed states. The particle centre of mass co-ordinates in the reference configuration define Lagrangian finite elements, which are simultaneously employed to represent interparticle forces associated with tension and elastic-plastic shear. Damage variables are introduced as internal states for the finite elements, and evolve with the material history to represent the loss of tensile and shear strength and stiffness under thermomechanical loading. Element failure due to spall, melting, accumulated plastic strain or other physical criteria results in the loss of interparticle forces associated with element shear and tension, so that particles unassociated with any intact elements are free to flow under contact-impact loads. No mass or energy is discarded at element failure, and no rezoning is required to model the transition from an intact to a fragmented medium. This hybrid modelling technique avoids the tensile instabilities and numerical fracture problems which arise with some pure particle methods, the use of slidelines and penalty forces which characterise pure Lagrangian finite element methods, and the mixed material thermodynamics and numerical diffusion which are features of Eulerian techniques. As indicated in the example which follows, this hybrid particle-element methodology can be effectively applied in the simulation of rather complex three-dimensional debris shielding problems.

Figure 5.6-1 through **Figure 5.6-5** show the results of a three-dimensional simulation of ESA benchmark case number 4, a dual plate aluminium shield problem. Parameters of the simulation are listed in **Table 5-1**. The use of a hybrid numerical technique allows for completely general characterisation of contact-impact effects, and at the same time accurate modelling of strength effects such as plastic deformation and fragmentation. Work in progress is extending application of the method to more complex shielding designs.

Simulation Parameters	
Projectile diameter (aluminium cylinder)	0.5062 cm
Projectile length	2.2046 cm
First bumper thickness (aluminium plate)	0.25 cm
Second bumper thickness (aluminium plate)	0.25 cm
Wall thickness (aluminium plate)	0.50 cm
Bumper-to-bumper spacing	6.00 cm
Bumper-to-wall spacing	6.00 cm
Impact velocity	11.0 km / sec
Impact obliquity	45 degrees
Equation of state type	SESAME 3719
Number of particles	4,269,067
Total simulation time	150 microseconds
Wall clock time	56.8 hours
Number of processors (SGI Origin)	256

Table 5-1: Simulation Parameters, ESA Benchmark Case Number 4

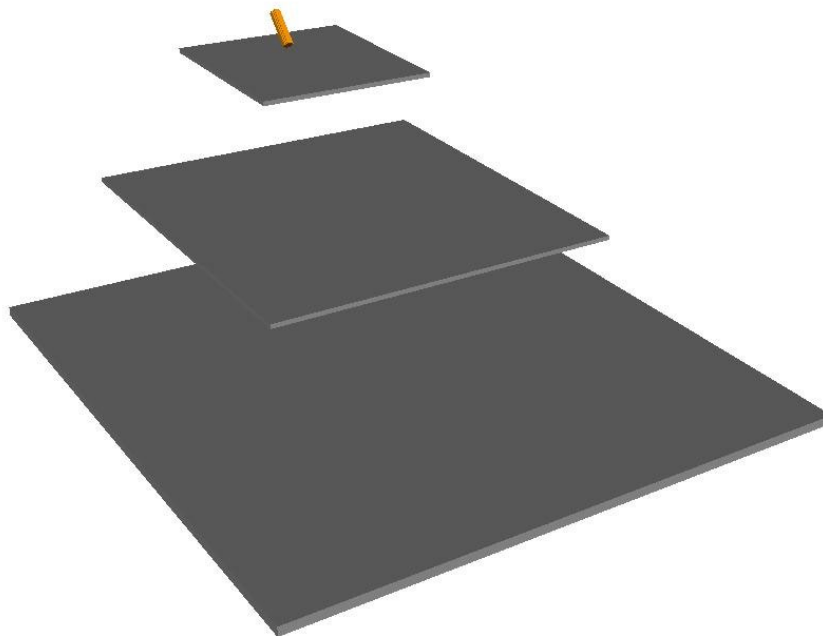


Figure 5.6-1: ESA Benchmark Case Number 4

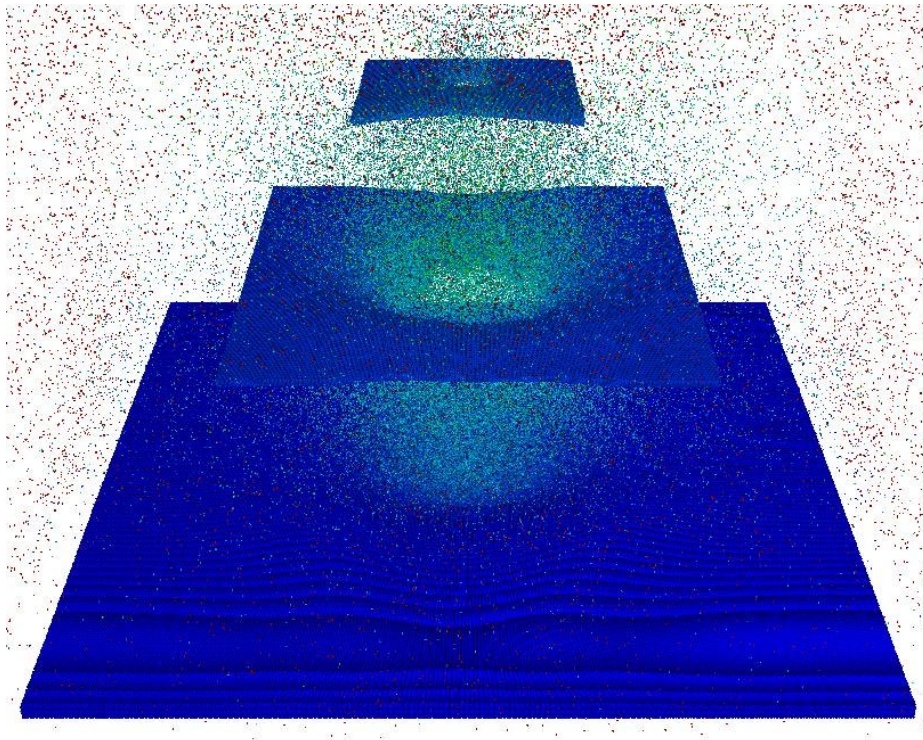


Figure 5.6-2: Particle Plot at 150 Microseconds

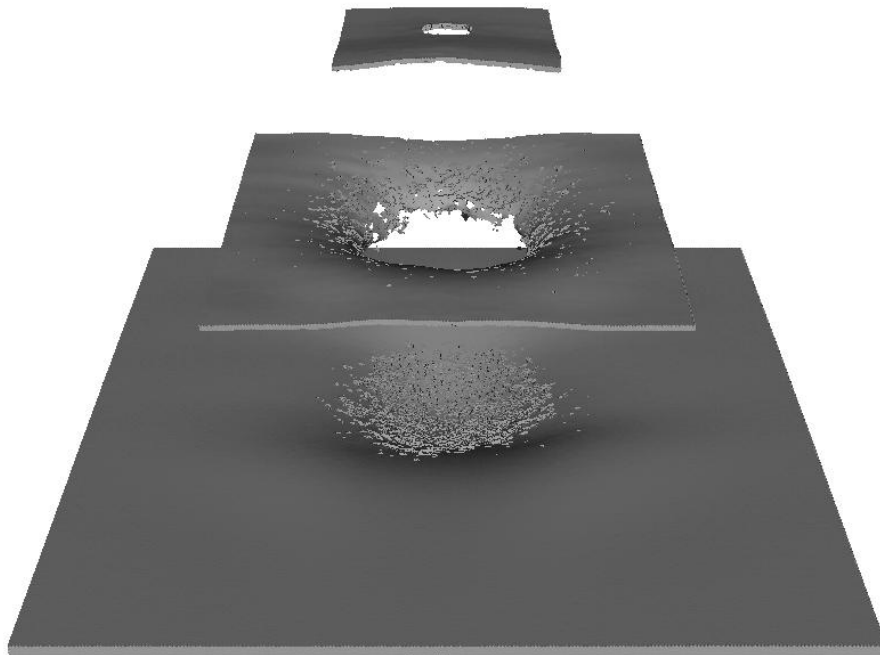


Figure 5.6-3: Element Plot at 150 Microseconds

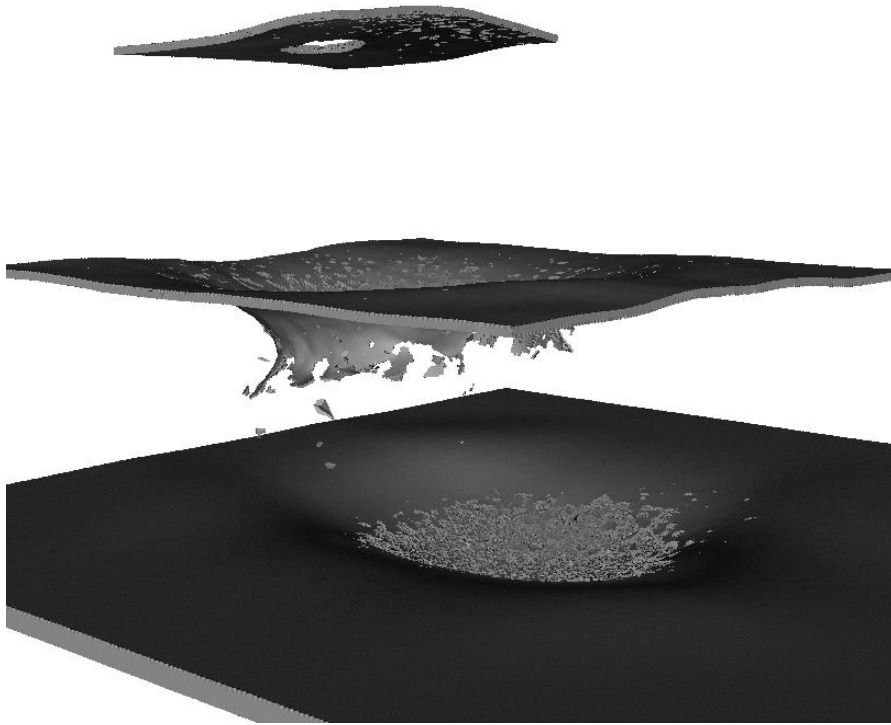


Figure 5.6-4: Element Plot at 150 Microseconds, Alternate View

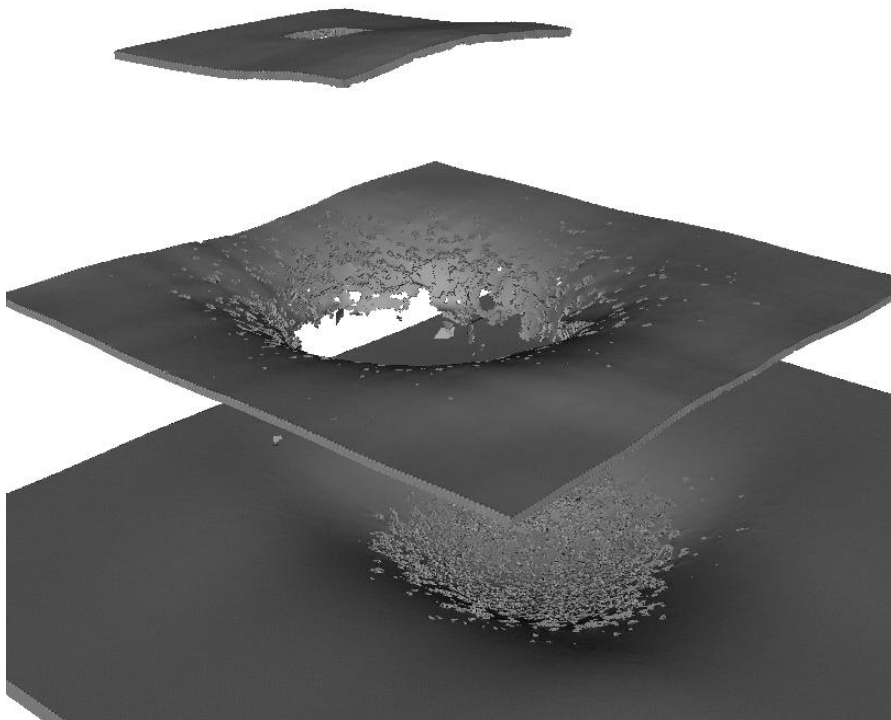


Figure 5.6-5: Element Plot at 150 Microseconds, Alternate View

5.7 References

- Balsara, D.S., Von Neumann Stability Analysis of Smooth Particle Hydrodynamics – Suggestions for Optimal Algorithms, *Journal of Computational Physics*, 121, pp. 357-372, 1995.
- Bashurov, V.V., and N.A. Skorkin, Perforation Problems and Methods of Numerical Simulation, in *Numerical Methods of Continuous Media Mechanics*, pp.17-20. Krasnoyarsk, USSR, 1992.
- Bashurov, V.V., G.V. Bebenin, A.G. Ioilev, *et al.*, Experimental Modelling and Numerical Simulation of High- and Hypervelocity Space Debris Impact to Spacecraft Shield Protection, *Int. J. Impact Engng.*, 21, 1997.
- Bashurov, V.V., G.V. Bebenin, and A.G. Ioilev, Numerical simulation of rod particles hypervelocity impact effectiveness at various attack angles, *Int. J. Impact Engng.*, 21, 1997.
- Belytschko, T., Y.Y. Lu, and L. Gu, Element-Free Galerkin Methods, *Int. J. Num. Meth. Eng.*, 37: 229-256, 1994.
- Belytschko, T., Y. Krongauz, D. Organ, M. Fleming, and P. Krysl, Meshless Methods: An Overview and Recent Developments, *Comp. Meth. Appl. Mech. Eng.*, 139: 3-47, 1996.
- Belytschko, T., Y. Krongauz, J. Dolbow, and C. Gerlach, On the completeness of meshfree particle methods, *Int. J. Num. Meth. Engng.*, 43, pp.785-819, 1998.
- Benz, Smooth Particle Hydrodynamics: A Review, Harvard-Smithsonian Center for Astrophysics, Preprint No. 2884, 1989.
- Campbell, J., and R. Vignjevic, Development of Lagrangian hydrocode modelling for debris impact damage prediction, *Int. J. of Impact Engng.*, Vol. 20, 1997.
- Campbell, J., and R. Vignjevic, Lagrangian hydrocode modelling of hypervelocity impact on spacecraft, *Advances in Computational Methods for Simulation*, pp 95-101, 1996.
- Campbell, J., and R. Vignjevic, Modelling Hypervelocity Impact in DYNA3D, *3rd Int. Conf. on Dynamics and Control of Structures in Space*, London, May 1996.
- Campbell, J., and R. Vignjevic, Numerical Simulation of Hypervelocity Impact on Spacecraft, *3rd Int. Conf. on Computational Structures Technology*, Budapest, August 1996.
- Chen, J.K., J.E. Beraun, and C.J. Jih, Completeness of Corrective Smoothed Particle Method for Linear Elastodynamics, *Computational Mechanics*, Vol. 24, No. 4, pp. 273-285, 1999.
- Chen, J.K., J.E. Beraun, and C.J. Jih, A Corrective Smoothed Particle Method for Transient Elastoplastic Dynamics, *Computational Mechanics*, Vol. 27, No. 3, pp. 177-187, 2001.
- Courant, Friedrichs, and Levy, Über die partiellen Differentialgleichungen der mathematischen Physik, *Mathematischen Annalen*, 100, pp 32-74, 1928.

Dilts, G., Moving-Least-Squares-Particle Hydrodynamics 1: Consistency and Stability, *Int. J. for Num. Meth. In Engng.*, 44 (8), pp.1115-1155, 1999.

Fahrenthold, E.P, and B.A. Horban, A hybrid particle-finite element method for hypervelocity impact simulation, *Int. J. of Impact Engng.*, Vol. 23, pp 237-248, 1999.

Fahrenthold, E.P., and B.A. Horban, An improved hybrid particle-finite element method for hypervelocity impact simulation, *Int. J. of Impact Engng.*, Vol. 26 (2001), pp 169-178.

Faraud, M., R. Destefanis, D. Palmieri, and M. Marchetti, SPH Simulations of Debris Impacts Using Two Different Computer Codes, *Int. J. of Impact Engng.*, 23, pp.249-260, 1998.

Feldstein, V.A., E.P. Buslov, N.G. Panichkin, V.I. Semenov, V.G. Kozlov, V.P. Romanchenkov, A.K. Myshonkov, A.M. Pautkin, and V.G. Sokolov, Method of ballistic limit curves calculation for shielding constructions protecting space vehicles from high velocity impacts of meteoroids or space debris, *50th International Astronautical Congress*, Amsterdam, October 1999.

Guenther, C., D.L. Hicks, and J.W. Swegle, Conservative Smoothing Versus Artificial Viscosity, Sandia Report SAND94-1853, Albuquerque, NM 87185, 1994.

Hayhurst, C., H. Ranson, D. Gardner, and N. Birnbaum, Modelling of microparticle hypervelocity oblique impacts on thick targets, *Int. J. of Impact Engng.*, Vol. 17, 1995.

Hayhurst, C., R. Clegg, and I. Livingstone, SPH technique and their application in high velocity and hypervelocity normal impacts, TTCP WTP 22nd Annual General Meeting Hydrocode Workshop, Banff, Canada, April 10-15, 1996.

Hayhurst, C., and R. Clegg, Cylindrically symmetric SPH simulations of hypervelocity impacts on thin plates, *Int. J. of Impact Engng.*, Vol. 20, 1997.

Hayhurst, C.J., and I.H.G. Livingstone, Advanced Numerical Simulations for Hypervelocity Impacts – AUTODYN Simulations, ESTEC Contract 12469/97, ESA CR(P) 4218, August 1998.

Hayhurst, C.J., S.J. Hiermaier, R.A. Clegg, W. Riedel, and M. Lambert, Development of Material Models for Nextel and Kevlar-Epoxy for High Pressures and Strain Rates, *Intl. J. Impact Engng.*, 23, pp.365-376, 1999.

Hayhurst, C.J., I.H.G. Livingstone, R.A. Clegg, R. Destefanis, and M. Faraud, Ballistic Limit Evaluation of Advanced Shielding Using Numerical Simulations, *Intl. J. Impact Engng.*, 26 pp.309-320, 2001.

Hiermaier, S.J., W. Riedel, C.J. Hayhurst, R.A. Clegg, and C.M. Wentzel, Advanced Material Models for Hypervelocity Impact Simulations (AMMHIS), ESA contract 12400/97/NL/PA(SC), EMI Report No. E 43/99, 1999.

Hiermaier, S.J., and F. Schäfer, Hypervelocity Impact Fragment Clouds in High Pressure Gas – Numerical and Experimental Investigations, *Int. J. Impact Engng.*, Vol. 23, Nr. 1, pp. 391-400, 1999.

Ioilev, A., V. Tarasov, Y. Yanilkin, and I. Sviridova, Advanced Numerical Simulations for Hypervelocity Impact: Preliminary ESA benchmark simulations using EGAK code, 1998.

Johnson, G.R., and W.H. Cook, A Constitutive Model and Data for Metals Subjected to Large Strains, High Strain Rates and High Temperatures, *7th Int. Symposium on Ballistics*, Den Haag, 1983.

Johnson, G.R., R.A. Stryk, and S.R. Beissel, SPH for High Velocity Impact Computations, Submitted for Publication in *Computer Methods in Applied Mechanics and Engineering*.

Johnson, G.R., and S.R. Beissel, Normalized Smoothed Functions for SPH Impact Computations, *Int. J. Num. Meth. Engng.*, 39, 2, pp. 725-741, 1996.

Katayama, M., T. Aizawa, S. Kibe, and S. Toda, A Numerical Simulation of Hypervelocity Impact of Space Debris against the Whipple Bumper System, ESA SD-01, *Proc. Of First European Conference on Space Debris*, Darmstadt, April 1993.

Katayama, M., S. Kibe, and S. Toda, A Numerical Simulation Method and its Validation for Debris Impact against the Whipple Bumper Shield, *International Journal of Impact Engineering*, Vol. 17, 1995.

Katayama, M., S. Toda, and S. Kibe, Numerical Simulation of Space Debris Impacts on The Whipple Shield, *Acta Astronautica* Vol. 40 No. 12, 1997.

Katayama, M., A. Takeba, S. Toda, and S. Kibe, Numerical Simulation of Jet Formation by Shaped Charge and its Penetration into Bumpered Target, ESA SP-393, *Proc. Of Second European Conference on Space Debris*, Darmstadt, March 1997.

Katayama, M., S. Toda, and S. Kibe, Numerical Study on Density and Shape Effects of Projectiles for Hypervelocity Impact, ESA SP-393, *Proc. Of Second European Conference on Space Debris*, Darmstadt, March 1997.

Katayama, M., A. Takeba, S. Toda, and S. Kibe, Analysis of Jet Formation and Penetration by Conical Shaped Charge with the Inhibitor, HVIS 1998, *Int. J. of Impact Engng.*, Vol.23, pp.443-454, 1999.

Katayama, M., S. Kibe, and T. Yamamoto, Numerical and Experimental Study on the Shaped Charge for Space Debris Assessment, *Acta Astronautica*, Vol.48, No.5-12, pp.363-372, 2001.

Katayama, M., and S. Kibe, Numerical study of the conical shaped charge for space debris impact, Hypervelocity Impact Symposium, Galveston, Texas, USA, Nov. 6-10, 2000, to be published in a volume of *Int. J. of Impact Engng.*, Vol.26, (2001).

- Lancaster, P., and K. Saulkaskas, Surfaces Generated by Moving Least Squares Methods, *Math. Comp.* 37: 141-158, 1981.
- Libersky, L.D., A.G. Petschek, T.C. Carney, J.R. Hipp, and F.A. Allahdadi, High Strain Lagrangian Hydrodynamics, *J. Comp. Phys.* 109: 67-75, 1995.
- McDonnell, J., D. Gardner, and P. Newman, Hydrocode Modelling in the study of space debris impact crater morphology, ESA-SD-01, 1993.
- Monaghan, J.J., Shock Simulation by the Particle Method SPH, *J. of Comp. Phys.* 52, S. 374-389, 1983.
- Nayroles, B., G. Touzot, and P. Villon, Generalizing the Finite Element Method: Diffuse Approximation and Diffuse Elements, *Comp. Mech.*, 10: 307-318, 1983.
- Palmieri, D., M. Marchetti, R. Destefanis and M. Faraud, Hypervelocity Debris Impacts on Space Structures: Hydrocode Simulations and Experimental Validation, *IAF 98 Congress*, Melbourne, Australia, IAF-98-I.5.10, Sep. 1998.
- Palmieri, D., M. Marchetti, R. Destefanis and M. Faraud, Orbital debris impacts against spacecraft multiple shield: comparison of hypervelocity experiments and hydrocode simulations, *Proceeding of the SUSI 98 Conference*, Thessaloniki, Greece, pp. 331-340, 1998.
- Randles, P.W., and L.D. Libersky, Smooth Particle Hydrodynamics: Some recent improvements and applications, *Computer Methods in Applied Mechanics and Engineering*, 139, pp. 375-408, 1996.
- Romanchenkov, V., G. Menshikov, L. Zinchenko, and V. Sokolov, The engineering numerical model for ballistic limit curves calculation in the high velocity range, Hypervelocity Shielding Workshop, Galveston, Texas, 8-11 March 1998.
- Salomé, R., V. Albouys, C. Le Floc'H, D. Sornette, and J.P. Vila, High Pressure Tank Behaviour under an Hypervelocity Impact, *Proc. Of Third European Conference on Space Debris*, SP-473, Vol. 2, pp 621-627, 2001.
- Scheffer, U., and S. Hiermaier, Improving a SPH code by alternative interpolation schemes, Fachtagung Baustatik/Baupraxis, Aachen, 18./19.3.1999.
- SESAME, Report on the Los Alamos Equation of State Library, LANL-83-4, Feb. 1983.
- Shiraki, K., F. Terada, N. Noda, and M. Katayama, Hydrocode Simulation for the JEM Pressurized Module Structure Performance for Space Debris Impact, *7th International Space Conference of Pacific-Basin Societies*, Nagasaki, July 1997.
- Shiraki, K., F. Terada, and M. Harada, Space Station JEM Design Implementation and Testing for Orbital Debris Protection, *Int. J. of Impact Engng.*, Vol. 20, pp.723-732, 1997.

Shiraki, K., Projectile Shape Effects for Hypervelocity Impact on Space Debris Protection Shield, *Memoris of the Graduate School of Engineering Kyushu University*, Vol. 60, No. 1, 2000.

Steinberg, D.J., S.G. Cochran, and M.W. Guinan, A Constitutive Model for Metals Applicable at High Strain Rate, *Journal of Applied Physics*, 51, p. 1498, 1980.

Swegle, J.W., D.L. Hicks, and S.W. Attaway, Smooth Particle Hydrodynamics Stability Analysis, *Journal of Computational Physics*, 116, pp. 123-134, 1995.

Tillotson, Metallic Equations of State for Hypervelocity Impact, GA-3216, General Atomic, San Diego, CA, July 1962.

v. Neumann, J., and R.D. Richtmeyer, A Method for the Numerical Calculation of Hydrodynamic Shocks, *J. Appl. Phys.*, 21, pp.232-237, 1957.

White, D.M., Columbus Shielding Validation using AUTODYN, Century Dynamics Ltd report R192:03 for Alenia Spazio, Sept. 2001.

Wilkins, M.L., *Computer Simulation of Dynamic Phenomena*, Springer, 1999.

Zerilli, F.J., and R.W. Armstrong, *Journal of Applied Physics*, 61, p. 1816, 1987.

6 Recommendations and Requirements for Impact Protection of Spacecraft

This chapter summarizes recommendations and requirements for the protection of spacecraft against space debris and meteoroid impacts. The information is presented in two sections. Section 6.1 identifies recommendations and requirements that have been published in various guidelines and standards; section 6.2 contains guidance based on the experience of members of the IADC Protection Working Group.

6.1 Guidelines and Standards

6.1.1 Europe

The “European Code of Conduct for Space Debris Mitigation” [anon., 2004a] has been developed co-operatively amongst responsible space agencies in Europe to identify debris mitigation practices which will serve to minimize the impact of space operations on the orbital environment that will be encountered by future space systems. The document specifies measures for the design and operation of a space system that will avoid or minimize the generation of space debris and proposes measures to protect a space system from the hazard posed by space debris. The document also defines the process to be followed. With respect to the application of specific mitigation measures in conjunction with the more general safety requirements relevant to the project or related activities.

The application of the Code of Conduct for Space Debris Mitigation is voluntary and should be applied by the European Space Agency, by national space agencies within Europe and their contractors. It is also recommended for application by any other space project conducted in Europe, or by a European entity acting outside Europe, including operators. The Code of Conduct contains provisions that may be given binding effect by means of legal instruments between contracting parties.

The measures in the Code of Conduct are defined in terms of what must be accomplished, rather than in terms of how to organize and perform the necessary work. In terms of impact protection measures, the following is stated:

A space debris risk assessment should be included in the space debris mitigation plan.

Some recommendations for impact protection are also contained in a support document to the Code of Conduct [anon., 2004b]. This aims to direct those involved in the management, design, operation, and mission control to appropriate sources of information and tools to assist in implementing the Code of Conduct. With respect to impact protection, the support document provides the following recommendations:

Measures should be investigated and applied in order to ensure the survivability of space systems with respect to debris and meteoroid impacts (for example, shielding) and to decrease the probability that such impacts occur (for example, performance of avoidance maneuvers).

Practices related to the connection and positioning of nominal and redundant devices (for example, an equipment and related system routing) should be optimized to maximize survivability from particle impacts.

If the risk due to a collision between a space system and space debris exceeds initial project criteria, the space project should implement appropriate additional protection measures (for example, shield augmentation, redundancies, collision avoidance) to reduce this risk.

If the risk of damage due to a collision between a space system and space debris exceeds project criteria, the space project should assess the risk and implement maneuvers if necessary (for example, avoidance and/or attitude maneuvers).

6.1.2 Europe – ESA

The European Space Agency has published a document that defines a minimum set of requirements for the limitation of space debris, in particular in the LEO and GEO protected areas, and a minimum set of risk reduction measures in the case of re-entries of space-systems or their components into the Earth's atmosphere [anon., 2008]. The document is currently used as an ESA applicable standard for ESA space projects. It contains management requirements, design requirements, and requirements on the space project prime contractor. There are no requirements specifically relating to spacecraft impact protection.

6.1.3 International Organization for Standardization

In 2003, the International Organization for Standardization (ISO) initiated the development of a series of spacecraft engineering standards for space debris mitigation. The purpose of these voluntary standards is to transform internationally agreed debris mitigation guidelines, such as those published by IADC, into a set of measurable and verifiable requirements together with detailed methods and processes to enable compliance. The standards aim to reduce the growth in space debris by ensuring that unmanned spacecraft and launch vehicle orbital stages are designed, operated and disposed of in a manner that prevents them from generating debris throughout their orbital lifetime. The top-level standard in the series, ISO 24113, specifies all of the primary debris mitigation requirements. It is due to be published in its 4th edition in 2023. Detailed procedures and practices to achieve compliance with the requirements in ISO 24113 are contained in a series of lower-level implementation standards.

In the 2019 edition of ISO 24113 two high-level requirements were introduced relating to space debris / meteoroid impact risk assessment. One of these is concerned with calculating the risk

that an impact will cause a spacecraft to break-up before its end of life. The other requirement deals with assessing the risk that an impact will prevent a spacecraft from performing a successful disposal. To help engineers demonstrate compliance with these requirements, one of the lower-level standards, ISO 16126, provides impact risk assessment procedures and supporting information for quantifying the survivability of unmanned spacecraft against space debris and meteoroid impacts. Efforts have been made to keep the content of the standard consistent with documents prepared by the IADC Protection Working Group, including this Protection Manual. Another of the implementation standards, ISO 11227, describes a test procedure to quantify the amount of ejecta released when external surfaces of a spacecraft are impacted by debris or meteoroids. The purpose of this standard is to assist with choosing better surface materials, i.e., ones that are less likely to cause contamination of the space environment. It should be noted that ISO standards are generally reviewed every 5 years. Important amendments are anticipated for the next editions of each of the above-mentioned standards.

6.1.4 Russia

Industrial Standard OST 134-1031-2003

The Industrial Standard defined includes general recommendations and requirements to OS protection against space debris particles. The list of elements sensitive to meteoroidal and industrial particles impact is determined. Main spacecraft protection measures to be used are described, values for OS resistance to meteoroidal and industrial particles impact are determined. The requirements to the OS design documentation are specified. Currently the Industrial Standard is under consideration and will be amended.

6.1.5 United Nations

The Scientific and Technical Subcommittee of the United Nations Committee on the Peaceful Uses of Outer Space (UNCOPUOS) recommends the following impact protection measure [anon., 1999]:

Spacecraft designers should consider incorporating implicit and explicit protection concepts into their space vehicles.

6.1.6 U.S. – Government

In order to satisfy the objective of selecting a safe flight profile and operational configuration, the U.S. Government Orbital Debris Mitigation Standard Practices [anon., 2001] requires that “Programs and projects will assess and limit the probability of operating space systems becoming a source of debris by collisions with man-made objects or meteoroids”. In this regard, one of the Mitigation Standard Practices states the following:

3-2. Collision with small debris during mission operations: Spacecraft design will consider and, consistent with cost effectiveness, limit the probability that

collisions with debris smaller than 1 cm diameter will cause loss of control to prevent post-mission disposal.

6.1.7 U.S. – NASA

To limit future debris generation, NASA Procedural Requirements (NPR) 8715.6 [anon., 2007a] requires each program and project to conduct a formal assessment of the potential to generate orbital debris during deployment, mission operations, and after the mission has been terminated. NASA-STD 8719.14 [anon., 2007b] serves as a companion to NPR 8715.6 and provides each NASA program and project with specific requirements and assessment methods to assure compliance with the NPR. NASA-STD 8719.14 is used for orbital debris assessments for all payloads, launch vehicle orbital stages, and released objects as required by NPR 8715.6.

With respect to collisions with small size debris (less than 10 cm in diameter), NASA-STD 8719.14 contains the following requirement:

Requirement 4.5-2. Limiting debris generated by collisions with small objects when operating in Earth or lunar orbit: For each spacecraft, the program or project shall demonstrate that, during the mission of the spacecraft, the probability of accidental collision with orbital debris and meteoroids sufficient to prevent compliance with the applicable post mission disposal requirements is less than 0.01 (Requirement 56507).

This requirement limits the probability of spacecraft being disabled and left in orbit at end of mission, which would contribute to the long-term growth of the orbital debris environment by subsequent collision or explosion fragmentation.

An evaluation process is defined to help determine (1) if there may be a significant vulnerability to meteoroid or orbital debris impact, (2) which components are likely to be the most vulnerable, and (3) what simple design changes may be made to reduce vulnerability. This process involves use of the Debris Assessment Software (DAS), as per the following requirement:

For operations in Earth orbit, DAS shall be used to determine whether damaging impacts by small particles could reasonably prevent successful post mission disposal operations (Requirement 56523).

DAS estimates the probability that meteoroid or orbital debris impacts will cause components critical to post mission disposal to fail. This evaluation may point to the need for a more detailed assessment (possibly involving the use of the NASA BUMPER II model), as specified by the further requirement:

If this estimate shows that there is a significant probability of failure, a higher-fidelity analysis shall be used to guide any redesign and to validate any shielding design (Requirement 56524).

Finally, NASA-STD 8719.14 advises that there are many mitigation measures to reduce the probability that collisions with small debris will disable the spacecraft and prevent successful post mission disposal. These measures use the fact that the debris threat is directional (for orbital debris, highly directional) and that the directional distribution can be predicted with confidence. Design responses to reduce failure probability include addition of component and/or structural shielding, rearrangement of components to let less sensitive components shield more sensitive components, use of redundant components or systems, and compartmentalizing to confine damage.

6.1.8 Japan – JAXA

The Japan Aerospace Exploration Agency registered JMR-003 “Space Debris Mitigation Standard”, which has compliance with IADC Guidelines and ISO 24113, has the recommendation for protection design.

5.5.2 Prevention of spacecraft damage caused by on-orbit collisions

(3) Collision with protectable tiny debris. The probability that a spacecraft is damaged by impact of tiny debris to preclude disposal actions (including disposal maneuver, venting residual propellants, and prevention of rupture of batteries) shall be estimated. Critical components including cables exposed to the outer space shall be identified, and if necessary, their functions should be protected by shielding materials, redundant design, or installation behind the rigid materials. The allowable probability shall be determined adequately corresponding to the characteristics of mission, considering the technology to estimate the collision probability and the available protection design. Refer to JERG-2-144-HB001 for the methodology to estimate collision probability and protection design.

JMR-003C is supported by JERG-0-002 “Handbook to support JMR-003” which provide technical rational of the requirements, tailoring guides, detail technical data, and candidate procedure to comply with the requirements. Also, JERG-0-002-HB001 “Space Debris Mitigation Design & Operation Manual for Spacecraft” provides design and operation measures and procedures for spacecraft. Assessment procedure specifically to the debris impact are defined in JERG-2-144 “Micro-debris Impact Survivability Assessment Procedure” (published in 2011). Also, JERG-2-144-HB001 “Space Debris Protection Design Manual” was published in 2009. The purpose of this document is to specify a procedure of a space debris impact risk assessment. The manual contains results of hypervelocity impact experiments and numerical simulations of some components frequently used in an unmanned spacecraft.

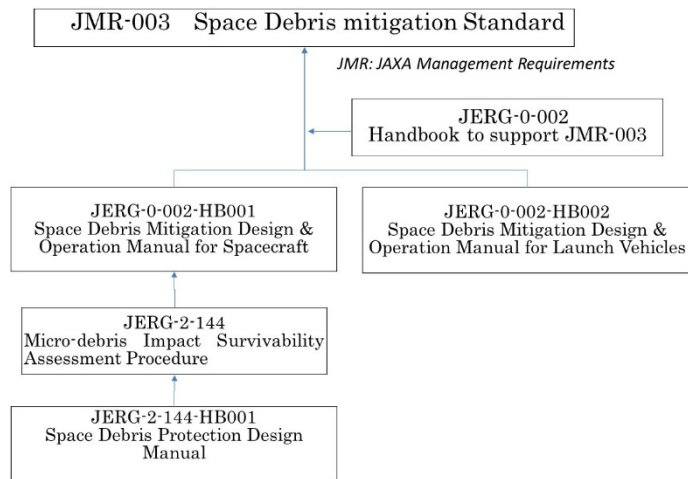


Figure 6.1-1: JAXA document system related to space debris impact assessment.

6.2 IADC Protection Working Group

6.2.1 Spacecraft Design and Operations

An impact risk analysis of a spacecraft may have to be iterated several times before the survivability requirement of the spacecraft is satisfied. This process can necessitate making various changes to the design of the spacecraft. In particular, the IADC Protection Working Group recommends that one or more of the following modifications should be considered:

- Enhance the protection of those surfaces that are most vulnerable to impact, e.g., by altering properties such as thickness, or changing materials, or adding shielding
- Reduce the area of the most vulnerable surfaces
- Relocate critical items away from the most vulnerable surfaces
- Protect sensitive external equipment through the use of shadowing
- Compartmentalize the interior
- Increase redundancy of vulnerable items
- Determine if “redundancy within an item” is better than “redundancy of an item”
- Determine if redundant items should be collocated or distributed
- Include automatic systems to isolate damage (e.g., automatic isolation valves, self-sealing bladders)
- Include an impact sensor network to detect impacts and guide operators in resolving any anomalies that might result
- Adjust flight attitude to reduce M/OD risk
- Include the capability to perform safe-mode operations

6.2.2 Shielding Design Considerations

As noted above, the impact protection of vulnerable spacecraft surfaces can be improved either by enhancing the design of existing panels, walls, etc. or by adding layers of shielding. In the event that shielding is added, the IADC Protection Working Group recommends that the shields should satisfy the following design criteria:

- Be affordable
- Impose minimum weight penalty
- Be amenable to simple design and construction
- Provide a 'second hit' capability, i.e., minimize the sacrificial aspects
- Reduce secondary ejecta and spall
- Ideally, when impacted, prevent the creation of more debris (e.g., by trapping any resulting ejecta or spall)
- Provide a means of melting and/or vaporizing meteoroid and debris particles over a large range of projectile mass, size and velocity
- Provide a degree of thermal and radiation protection
- Be resistive to the effects of atomic oxygen (only necessary for spacecraft in or crossing low Earth orbit)
- Be capable of surviving the normal launch and in-orbit vibration environments
- Meet spacecraft system requirements such as having a conductive external surface, electrically grounded to the spacecraft structure and acceptable thermo-optical properties
- When impacted, any resulting debris, spall or dust from the shield should not cause subsequent failures of spacecraft equipment or unacceptable deterioration in performance (jamming of mechanisms, coating of optics, etc.)
- Avoid interfering with the normal operation of the spacecraft such as deployment sequences, observation and taking measurements, communication and telecommand, etc.

6.3 References

anon., Technical Report on Space Debris, Scientific and Technical Subcommittee of the United Nations Committee on the Peaceful Uses of Outer Space, A/AC.105/720, 1999.
http://www.unoosa.org/oosa/natact/sdnps/sd_nps_docsidx.html

anon., U.S. Government Orbital Debris Mitigation Standard Practices, 2001.

Anon., European Code of Conduct for Space Debris Mitigation, Issue 1.0, 2004a.

anon., Support to Implementation of the European Code of Conduct for Space Debris Mitigation, Issue 1.0, 2004b.

anon., General Requirements on Space Systems for the Mitigation of Human-Produced near-Earth Space Pollution, GOST R25645.167-2005.

Anon., NASA Procedural Requirements for Limiting Orbital Debris and Evaluating Meteoroid and Orbital Debris Environment, NASA Procedural Requirements (NPR) 8715.6B, Feb 2017.

anon., Process for Limiting Orbital Debris, NASA Technical Standard, NASA-STD-8719.14C, 2021.

anon., Requirements on Space Debris Mitigation for ESA Projects, European Space Agency, Annex 1 to ESA/ADMIN/IPOL(2008)2, 2008.

anon., Space Debris Protection Design Manual, JERG-2-144-HB, 2014

ISO 24113:2019, Space Systems – Space Debris Mitigation Requirements

ISO 11227:2012 & Amd 1:2021, Space systems – Test Procedure to evaluate Spacecraft Material Ejecta upon Hypervelocity Impact.

ISO 16126:2014, Space systems – Assessment of Survivability of Unmanned Spacecraft against Space Debris and Meteoroid Impacts to ensure Successful Post-Mission Disposal.

7 Mass Optimization of Meteoroid/Space Debris Protection Systems

This chapter provides information regarding the optimization of protection systems against micrometeoroids and space debris. The optimization is based on the risk assessment described in Chapter 2, ballistic limit equations described in Chapter 3 and design equations. In order to perform a mass optimization, design equations must describe the mass of the protection system as a function of all optimization parameters. Optimization algorithms are employed to determine systems which meet the safety requirements with the least possible mass.

7.1 Introduction

The application of the BLEs to spacecraft design, has to be performed with generic (non MMOD related) requirements that should be included in the design of the shielding. These requirements are constraints for the integration of the MMOD shielding into the design of the spacecraft. Usually, these requirements are provided by the spacecraft design integration team.

Typical requirements:

- Mass allocation for the MMOD protection system as a percent of the spacecraft mass.
- Volume and clearance requirements, such as under an ascent shroud.
- Material restrictions based on the specific type of spacecraft.
- Thermal constraints, such as coatings on MMOD shields and/or integration of body-mounted radiators.
- Avoiding design complexity (finding easier to implement shielding solutions).

The design optimization of the MMOD shielding has to include the constraints of the specific spacecraft. These constraints are different for manned and unmanned spacecraft.

7.2 Optimization of Protection Systems

The optimization problem is characterized by strong non-linearities even for simple spacecraft geometries. Various local mass minima are present in the optimization problem. This must be considered when selecting an appropriate algorithm.

As shown in **Figure 7.2-1**, an optimization algorithm has to change the configuration with respect to the used optimization strategy. For each configuration risk assessment must be performed.

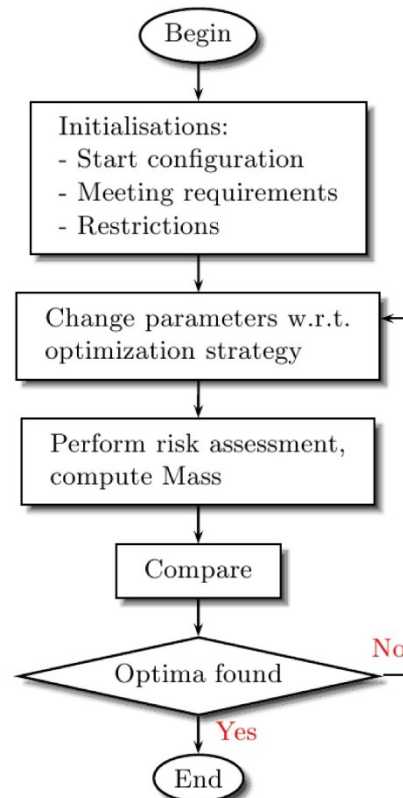


Figure 7.2-1: Optimization Algorithm

7.2.1 Optimization Algorithm

The optimization of protection systems is multidimensional, highly non-linear and constrained. Naturally there are several local minima (that must not constitute an optimized system). An algorithm must find the global minimum to determine the best possible system. In other words, an algorithm must be able to leave a local optimum during the optimization instead of finding just this local point. As optimization is a well described mathematical problem it is not addressed here in detail. Instead, a brief description of possible optimization strategies is given.

Searches for minima could be established by simply run an exhaustive search. It employs a lattice on the search space and evaluates the objective function at every grid point. The best value is selected within the accuracy of the grid size. The obvious disadvantage of this approach is the computational effort. Another approach could be the Monte-Carlo method that checks the objective function at a defined number of random points of the search space. A more advanced concept is the employment of a genetic algorithm.

In order to minimize the computational effort, it is possible to combine different optimization concepts. If the vicinity of global optimum is determined by one algorithm another algorithm that only converges into this optimum might be used. An example of a combination between a genetic algorithm and a sensitivity analysis is given in **Figure 7.2-2**.

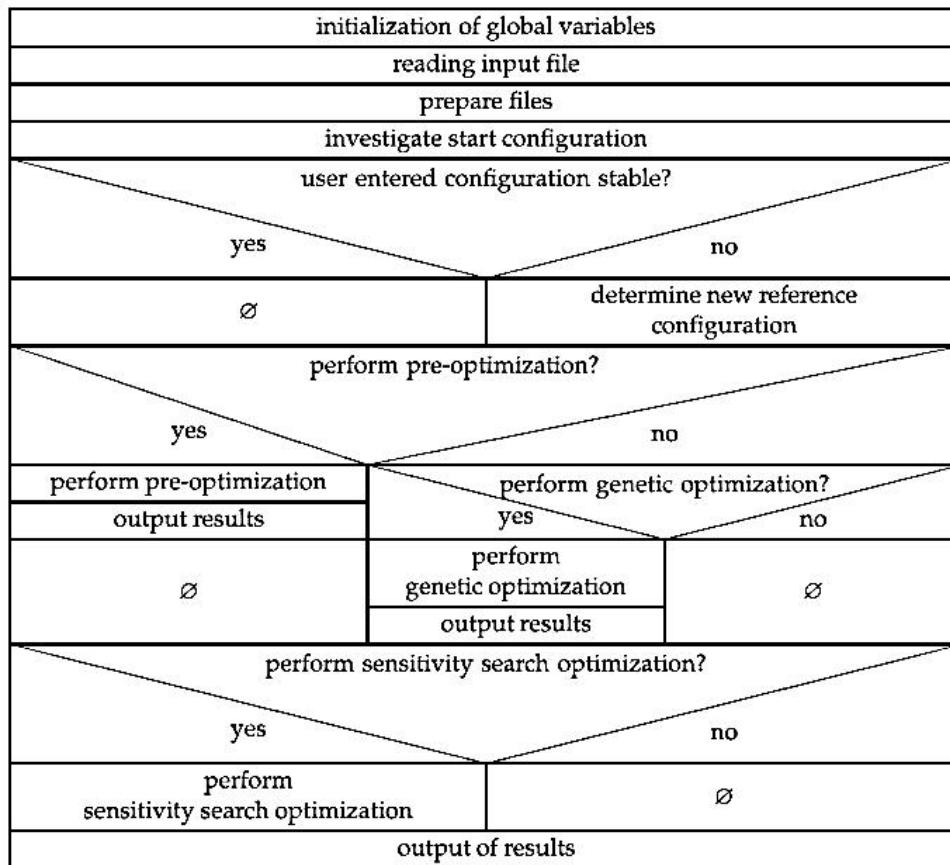


Figure 7.2-2: Structural diagram of a combined genetic algorithm/sensitivity analysis optimization process

7.2.2 Optimization Criteria and Restrictions

The optimization criteria for a protection system may be to find a protection scheme, having minimum additional mass in order to:

- provide a required probability of no penetration,
- provide a required probability of no failure of certain components.

A different approach might be to find an arrangement of components within a spacecraft such that the probability of no failure is a maximum value.

Restrictions result from other requirements or system aspects, which have to be taken into account by the design of the protection structure. These may influence the material selection and the allowable wall thicknesses. The available space for the spacecraft within the launcher will restrict the allowable spacing.

7.3 Ballistic Limit Equations for Optimization

In order to perform a sensible optimization, the ballistic limit equations used in the process must meet general qualities:

- All optimization variables must be included
- A large range of validity must be given

The first point is necessary because an optimization variable that does not exist will not have any impact on the performance and thus is optimized to zero or a lower bound. In order to ensure an optimization not only in a small valid range of parameters determined by the used BLE, the equations should describe the whole range of possible configuration.

Exemplary a brief discussion of considerations concerning BLEs for a single and double wall system follows. Starting from a single wall the ballistic limit equation should be able to calculate the critical particle diameter when the wall thickness approaches zero. On the other end of the range it should determine infinite particle size with the thickness approaching infinity. For a double wall configuration the BLE should converge into the single wall equation for either the spacing or the shield thickness approaching zero. An infinite particle size should be determined for a backup wall thickness approaching infinity.

Within the ballistic limit equations described in Chapter 3 there are some which have been proven to be suitable for optimization. The Christiansen/Cour-Palais equations for single wall systems [Christiansen, 1993] take all optimization variables into account.

The present available equations for Whipple wall systems are not suited for optimization. With the modification by Reimerdes made in an ESA/ESTEC technology study and additional work [Wohlers, 2003], [Reimerdes, 2006] modified Cour-Palais/Christiansen equations are given for double wall structures allowing optimization.

7.3.1 Optimization Variables

The optimization variables that must be taken into account by the BLE are:

- Back wall thickness
- Shield thickness (first, second...)
- Spacing
- Back wall material
- Shield material

Taking different materials into account is currently not possible since available BLE are only valid for certain materials (e.g. aluminium).

7.3.2 Other Parameters

In order to make sensible calculations of the number of penetrations other parameters should be present in the ballistic limit equations.

- Material of the impacting particle (density)
- Velocity of the impacting particle
- Angle of impact
- Shield Configuration
- Impact of multilayer Insulation

Here it must be stated that available BLE do not take all these parameters into account. For future development, the influence of the impacting particle shape should also be considered.

7.4 Mass Design Equations

For a protection system that should be optimized an adequate description of the mass with all parameters, which are variable during the optimization process, is essential. Generally the parameters are:

- Back wall thickness and shield thickness
- Surface area of the protection system
- Back wall density and shield density
- Spacer between back wall and shields (design, number, weight)
- Fasteners (design, number, weight)

The next sections show an exemplary mass analysis for a single wall system and a double wall system (Whipple shield).

7.4.1 Single Wall Mass Analysis

A single wall is of course the simplest protection system. Therefore the mass analysis is straightforward given by

$$m_{w,i} = \rho_i A_i t_{w,i} \quad [7.4-1]$$

7.4.2 Double Wall Mass Analysis

A simplified analysis for a Whipple shield, as shown in Figure 7.4-1, is feasible by summarizing the masses of back walls, shields, spacers and fasteners. It is assumed that the surfaces of back walls and shields are equal. For curved surfaces this is only an approximation. The spacing is typically at least one order of magnitude smaller than the spacecraft diameter. Therefore the approximation causes only small errors. The total mass is herewith given by:

$$m = \sum_i A_i (\rho_{w,i} t_{w,i} + \rho_{s,i} t_{s,i}) + f(S) \quad [7.4-2]$$

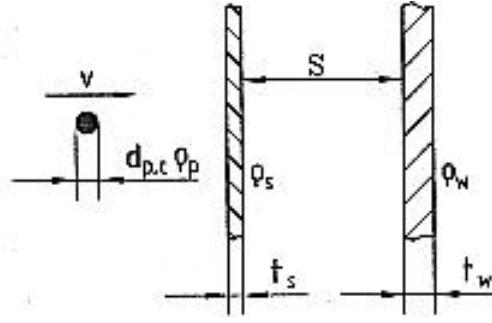


Figure 7.4-1: Whipple Shield

In this equation the effect of the spacing S on the spacer mass is not quantified. When the spacing is increased the mass of the supporting structure for the shielding will naturally rise. The additional mass depends very much on the design of the supporting structure. It is influenced by many parameters like cable ducts, antenna mountings etc. In order to perform analysis in preliminary design a simplified approach is given in this paragraph. This approach can be further developed during the design process. **Figure 7.4-2** shows a simplified spacer design. There are three main requirements that influence the design of the supporting structure:

1. A minimum eigenfrequency is required.
2. Launch loads must not result in plastic deformations.
3. Thermal loads (in orbit) have to be endured.

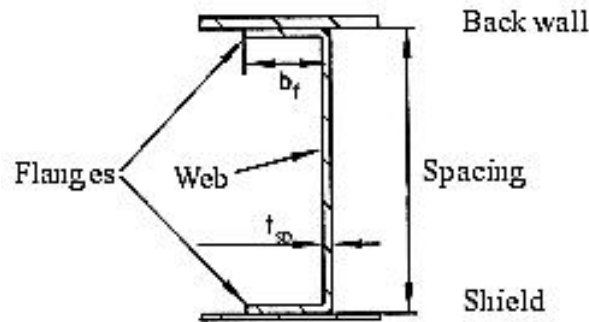


Figure 7.4-2: Spacing

7.4.2.1 Spacer Mass Function

Employing the above mentioned load cases led to a simple equation for the spacer mass depending on the spacing and the shield mass:

$$m_{spacing} = m_{shield} \left(K_{m1} + K_{m2} \frac{S}{10} \right) \quad [7.4-3]$$

The constants K_{m1} and K_{m2} depend on the design of the spacer and the connections. For a preliminary design, **Table 7-1** gives values for these constants. These values must be used with the spacing S given in cm. If the design of the spacer is available, these values should be adapted to it.

K_{m1}	0.5
K_{m2}	0.75-1.25

Table 7-1: Coefficients of spacer mass function

7.5 Benchmark calculations

The optimization approach is applied to the simple box generic spacecraft as defined for validation of damage prediction tools in section 2.3.7. Two shield configurations are investigated:

- single wall design;
- double wall design.

As the optimization is done using a genetic algorithm, the computation is not deterministic and each run provides different results. This indicates that there are many local optima and it is hardly possible to find always the global optimum. The results given here are the best ones (giving lowest mass) selected from several computations.

In order to concentrate on the optimization process and not on the proper implementation of environment models (which may become very complex, leading to non-unique results), the simple environment models, defined for the space station in the document [NASA SSP-30425, Rev. B, 1994] were applied here.

7.5.1 Definition of the Optimization Runs

Spacecraft Geometry:

The generic spacecraft geometry chosen is the simple cubic box (**Figure 7.5-1**) with edge length of 1 m (see also section 2.3.7).

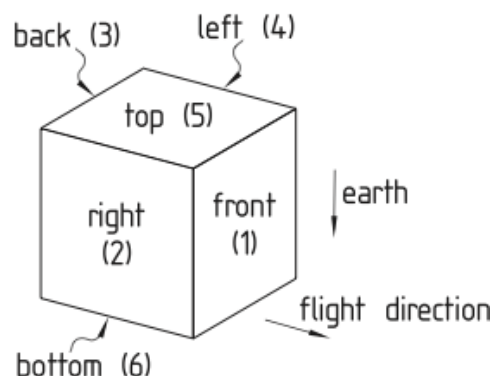


Figure 7.5-1: Geometry of the box

Environment Models:

- Orbital Debris: NASA debris 91 [NASA SSP-30425, Rev. B, 1994]

- Debris density: 2.8 g/cm³
- $S=70$, $p=0.05$, $q=0.02$
- Meteoroid: from [NASA SSP-30425, Rev. B, 1994]
 - Meteoroid density: 1.0 g/cm³ (for all particle masses)
 - Average velocity: 19 km/s

Mission Parameters:

- Altitude: 400 km
- Inclination: 51.6 deg
- Launch: 2002
- Duration: 1 year
- Number of impacts with penetration: $N \leq 0.001$
- Probability of no penetration: $p_0 = 0.999$

Material properties:

- Al 6061-T6 for single wall and for bumper shields:
 - Density: 2.713 g/cm³
 - Brinell hardness: 95
 - Speed of sound: 5.1 km/s
- Al 2024-T3 for rear wall in double wall structures:
 - Density: 2.77 g/cm³
 - Yield strength: 47 ksi

Ballistic Limit Equations:

- single wall equation given in [Christiansen, 1993]
- double wall equations given in [Reimerdes, 2006]

7.5.2 Optimization Results

Optimization is done for single wall and for double wall configurations using MDPOPT, which is a combination of the optimization tool ILBOPT (genetic algorithm at RWTH Aachen) and the damage prediction code MDPANTO.

7.5.2.1 Single Wall Results

Three different computations are performed:

1. no optimization, wall thickness equal for all faces
2. manual optimization, equal relative number of impacts for all faces
3. genetic optimization, thickness of left (2) and right face (4) are forced to be equal.

The results are presented in **Table 7-2**.

Face/ t_w [mm]	no optimization	manual optima.	genetic algorith
front	12.10	21.65	15.86
left, right	12.10	11.80	10.55
back	12.10	2.77	3.87
top	12.10	6.28	6.81
botton	12.10	2.68	3.92
mass [kg]	197.0	154.6	140.0
	100.0%	78.5%	71.1%

Table 7-2: Optimization Results-Single Wall Design**7.5.2.2 Double Wall Results**

Two different computations are performed:

1. All faces equal, but shield thickness, back-wall thickness, and spacing optimized (see **Table 7-3**)
2. Genetic optimization, left and right face are forced to be equal (see **Table 7-4**).

Face	Shield [mm]	Back Wall [mm]	Spacing [mm]
all	0.72	1.88	108.5
		mass [kg]:	58.5

Table 7-3: Optimization Results-Double Wall Design: All Faces equal

Face	Shield [mm]	Back Wall [mm]	Spacing [mm]
front	0.79	2.31	99.1
left, right	0.79	1.68	90.7
back	0.40	1.00	62.6
top	0.40	1.52	79.3
botton	0.40	1.15	67.8
		mass [kg]:	46.6
			79.7%

Table 7-4: Optimization Results-Double Wall Design

7.6 References

Christiansen, E. L.,: Design and Performance Equations for Advanced Meteoroid and Debris Shields, International Journal of Impact Engineering, 1993

Wohlers W., Reimerdes, H.-G.: Analytical Optimization of Protection Systems, International Journal of Impact Engineering 29, 2003

Reimerdes, H.-G., et. al: Modified Cour-Palais/Christiansen damage equations for double wall structures, International Journal of Impact Engineering, 2006

8 List of Acronyms

AOCS	Attitude and Orbit Control System
ASI	Italian Space Agency
ATV	Autonomous Transfer Vehicle (ESA)
BAS	Blast Accelerating System
BLC	Ballistic Limit Curve
BLE	Ballistic Limit Equation
CDL	Century Dynamics Limited
CEG	Centre d'Etudes de Gramat (CNES, France)
CFRP	Carbon Fibre Reinforced Plastics
CISAS	Center of Studies and Activities for Space (Italy)
CNES	Centre National d'Etudes Spatiales
CRC	(Century Research Center: Old company name) Solutions Corporation
CNSA
CSA	Canadian Space Agency
CSC	Conical Shaped Charge
ECSS	European Cooperation for Space Standardization
EDMS	European Space Debris Safety and Mitigation Standards
EMI	Ernst Mach Institute
EOS	Equation of State
EPF	Equation of Projectile Fragmentation
ESA	European Space Agency
ESI	Engineering Systems International
ESTEC	European Space Research and Technology Centre

EVA	Extra Vehicular Activity
FEAC	Field Emission Array Cathode
FEI	Flexible External Insulation
FMECA	Failure Modes Effects and Criticality Analysis
GEO	Geosynchronous Orbit
GFI	Ground Fault Interruption
GUI	Graphics User Interface
HC	HoneyComb
HE
HST	Hubble Space Telescope
HVI	Hypervelocity Impact
HVL	Hyper Velocity Launchers
IADC	Inter Agency Debris Committee
ISAS	The Institute of Space and Astronautical Science
ISO	International Organization for Standardization
ISS	International Space Station
JAXA	Japan Aerospace Exploration Agency
JEM	Japan Experiment Module
JSC	Johnson Space Center
ksi	1,000psi = 6.895 MPa
LDEF	Long Duration Exposure Facility
LEO	Low-Earth Orbit (generally considered for orbital altitudes up to 2000km above the Earth's surface)
LGG	Light Gas Gun

MBR	Model Ballistic Range (Russia)
MIB	Minimum Impulse Bit
MLI	Multi-Layer Insulation
MMH	MonoMethyl Hydrazine
M/OD	Meteoroid and Orbital Debris
MON	Mixture of Nitrogen Oxides (N ₂ O ₄ plus NO)
MPLM	Mini-Pressurized Logistics Module
MS	Multi-Shock Shield
N ₂ O ₄	Nitrogen Tetroxide
n.a.	Not Available
NAL	National Aerospace Laboratory (Japan)
NASA	National Aeronautics and Space Administration (United States)
NASDA	National Space Development Agency of Japan
Ni-H ₂	Nickel-Hydrogen
PM	Protection Manual
PNF	Probability of No Failure
PNP	Probability of No Penetration
psi	pounds force per square inch (lb _f /in ²)
PWG	IADC Protection Working Group (WG#3 of IADC)
RCC	Reinforced Carbon-Carbon
RFNC-VNIIEF	Russian Federal Nuclear Center VNIIEF
RKA	ROSAVIKOSMOS Russian Aeronautic and Space Agency
SCL	Shaped Charge Launcher

SiC	Silicon Carbide
SPH	Smoothed Particle Hydrodynamics
SRIAS	State Research Institute of Aviation Systems (ROSAVIAKOSMOS)
SWS	Stuffed Whipple Shield (Nextel/Kevlar blanket or “stuffing” intermediate layer within a Whipple shield)
TNO	Netherlands Organization for Applied Scientific Research
TPS	Thermal Protection System
TSNIIMASH	Central Research Institute of Machine Building Russian Space Agency
WG#3	Working Group No.3, same as IADC Protection Working Group
WS	Whipple Shield (2 separate layers of generally aluminium, outer layer called a “bumper”, inner layer is a “rear wall”, gap between is a “standoff”)

9 Notations

d	Projectile diameter [cm]
d_b	Particle diameter at ballistic limit [cm]
d_c	Critical diameter for penetration [cm]
D_c	Cavity diameter [cm]
D_h	Hole diameter [cm]
D_s	Spall diameter [cm]
C	Speed of sound in target [km/s]
H	Brinell hardness of target [BHN]
K_1, K_2	Modified Cour-Palais equation specific characteristic factors
P	Penetration depth [cm]
S	Spacing between 1 st bumper and rear wall [cm]
t	Target thickness [cm]
t_b	Thickness of bumper/shield [cm]
t_{Equiv}	Equivalent aluminium single wall thickness [cm]
t_w	Thickness of rear wall [cm]
V	Impact Velocity [km/s]
V_n	Normal component of impact velocity, $V_n = V \cdot \cos \theta$ [km/s]
ρ_b	Bumper density [g/cm ³]
ρ_p	Particle density [g/cm ³]
ρ_w	Rear wall density [g/cm ³]
ρ_t	Target density [g/cm ³]
θ, α	Impact angle measured from surface normal [deg]
σ	Yield Strength of back-up wall [ksi]
τ	Rear wall yield stress [in lb/inch ²]

In Chapter 5:

c	Sound speed [m/s]
e	Specific internal energy [J/kg]
f	External body force per unit mass [N/kg]
h	Smoothing length [m]
m	Mass [kg]
p	Pressure [Pa]
s	Geometric mesh size [m]
t	Time [s]
u	Velocity [m/s]
x	Spatial coordinate [m]
K	Bulk modulus [Pa]

\dot{R}	Spin Tensor
S	Deviatoric stress tensor
V	Specific volume [m ³ /kg]
W	Kernel weighting function
ε	Strain, Strain tensor
ρ	Density [kg/m ³]
σ	Yield stress [Pa], Total stress tensor

10 Appendix

10.1 Risk Analysis Example: Automated Transfer Vehicle (ATV)

The following sections summarise the results of a meteoroid and orbital debris protection analysis done for the ATV with the ESABASE/DEBRIS analysis tool. The feasibility of different shielding configurations to achieve the target Probability of No Penetration (PNP), and the weight increase induced by the different shield types, was analysed and reported. The complete analysis can be found in [Beltrami, 2000].

10.1.1 Mission Parameters

The calculations were done for the ATV/ISS attached phase using the parameters listed in **Table 10-1**.

Mission Parameters		Analysis Parameters	
Mission duration	135 days attached to the Russian Service Module of the ISS	Solar activity parameter, S	70
Orbital altitude	400 km	Debris mass growth rate	0.05
Inclination	51.6°	Small debris growth rate	0.02
Year	2008	Meteoroid material density	1.0 g/cm ³
Attitude of ATV/ISS	Roll: 0° Pitch: -11.2° Yaw: -6.1°	Space debris material density	2.8 g/cm ³

Table 10-1: Mission and analysis parameters

The applied meteoroid and space debris flux models are those defined for the design of the International Space Station (ISS), as specified in [NASA SSP-30425, Rev. B., 1994].

The ESABASE/DEBRIS impact assessment tool [ESABASE/DEBRIS release 2, 1998] was used to perform the analysis. The full velocity and impact angle distribution, as implicit to the flux models, was considered. The debris flux model used for the calculations was the NASA 91 model, which does not consider flux from elliptical orbits and assumes that all debris moves in circular orbits.

A three-step approach as described by E. Christiansen [Christiansen, 2000] was used to calculate the contribution from those particles that penetrate the augmentation wings attached to the Service Module.

The considered failure mode is the penetration of the inner wall.

10.1.2 ATV Model Geometry

Figure 10.1-1 shows the ESABASE model used in the calculations, including the Russian Service Module and the four augmentation wings attached to the RSM. The model includes the new design, dividing the Avionics Module into two elements with different bumper thickness and

eliminating the Avionics Radiator. All elements excepting the Avionics Module have a Multi-Layer Insulation (MLI) layer added on top of the bumper shield. This figure also shows the vectors corresponding to the tilted attitude described in **Table 10-1**.

Table 10-2 shows the corresponding geometry parameters for each module of the baseline ATV configuration. Note that the Spacecraft part (modules 1 to 6) have a higher back-wall yield strength of 57000 psi compared to 47000 psi in the cargo carrier (modules 7 to 9).

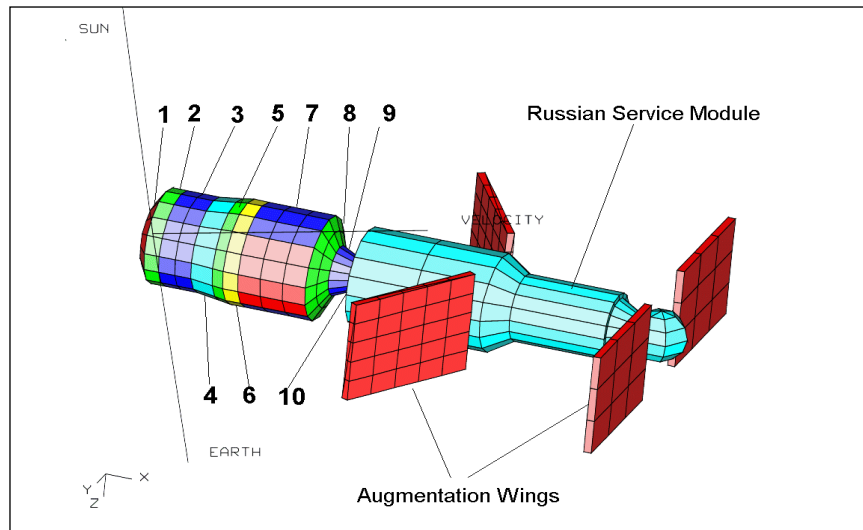


Figure 10.1-1: ATV Geometry

Nr.	ATV element	Area [m ²]	Bumper thickness [cm]	MLI thickness [cm]	Rear Wall thickness [cm]	Spacing bumper-wall [cm]	Back-wall Yield Strength [ksi]
1	Thruster cone (TC)	14.0	0.08	0.022	0.25	4.0	57
2	Lower Thruster Cyl. (LTC)	7.7	0.08	0.022	0.42	9.66	57
3	Upper Thruster Cyl./ Cylindrical panels (UTC)	16.8	0.08	0.022	0.33	9.66	57
4	Lower Avionics module (LAM)	12.1	0.20	-	0.34	10.4	57
5	Upper Avionics Module (UAM)	6.2	0.10	-	0.34	10.4	57
6	Ext. Cylind. (EC)	8.4	0.12	0.022	0.30	12.8	57
7	Pressur. Module Cyl.. (PM)	38.3	0.12	0.022	0.30	12.8	47
8	Cone 2 (C2)	13.2	0.12	0.022	0.25	12.15	47
9	Cone 1 (C1)	5.0	0.12	0.022	0.30	12.8	47
10	RDS system (RDS)	Included in model but not used for risk assessment. The NASA Allocation of PNP = 0.99995 is used instead					

Table 10-2: ATV Geometry

10.1.3 The Stuffed Whipple Shield

In order to improve the protection of the modules, an extra layer is added between the bumper shield and the backup wall of the Whipple shield, thus transforming it into a Stuffed Whipple shield. **Figure 10.1-2** shows the configuration of the Stuffed Whipple Shield used in the calculations.

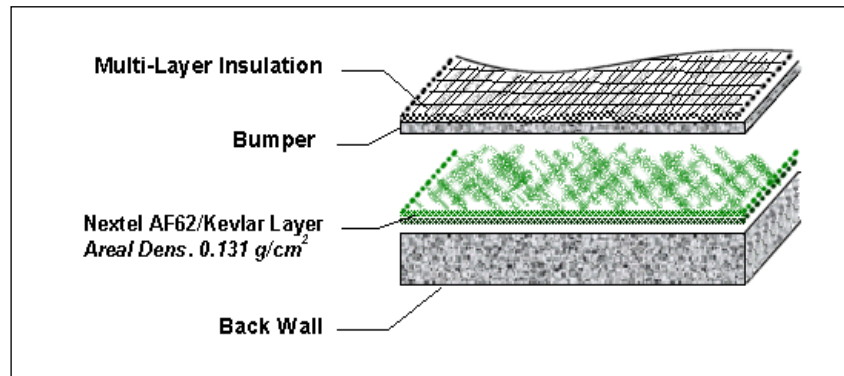


Figure 10.1-2: Configuration of the stuffed Whipple shield

The Multi-Layer Insulation sits on top of the bumper shield. The stuffing consists of two layers, one of Nextel AF62 and one of Kevlar, installed close to the backup-wall. The areal density of the stuffing is 0.131 g/cm^2 . This type of shielding has a low areal density, allowing more modules to be equipped with the extra shielding with a small increase in total weight.

10.1.4 Equations used in the Computation of the PNP for the ATV

Following new tests performed on the actual shield configuration of the ATV, i.e. including the MLI on top of the bumper shield, a Whipple shield equation with a modified parameter was derived and used for the ESABASE/DEBRIS calculations. Also, a new Stuffed Whipple Shield equation was used (see next section). All equations were used without a cut-off for high impact angles.

The Whipple Shield (WS) equation with the modified parameter was used for all subsystems with an MLI layer on top, this being the M/OD shielding in the baseline configuration. The thickness of the MLI is added to the bumper thickness. The previous Whipple Shield equation is used for those modules not equipped with an MLI (the Avionics module).

The Stuffed Whipple Shield (SWS) equation, which consists of the Whipple shield equation with a higher pre-factor, is used for those elements reinforced with a layer of Nextel and Kevlar with a total area density of 0.131 g/cm^2 . For this calculation the thickness of the intermediate Kevlar/Nextel layer is added to the thickness of the back-up wall. The thickness of the MLI is added to the bumper.

The Multi-Shock (MS) equations were used to assess the effect of particles penetrating the Service Module augmentation wings. For this analysis a constant stand-off distance of 40 cm, a total shield areal density of 0.63 g/cm^2 and the real ATV rear wall thickness is used.

The three-step approach described by E. Christiansen [Christiansen, 2000] was used to calculate the contribution from those particles that penetrate the augmentation wings attached to the

Service Module. This contribution is added to the results as a “Correction Factor” (NP_{corr}). In this study the same correction factors as for the previous study [Beltrami, 2000] were used.

10.1.4.1 Whipple Shield and Stuffed Whipple Shield Equation

Low Velocity Region

For $V_n \leq 3$ km/s:

$$d_c = \left[\frac{t_w (\sigma / 40)^{1/2} + t_b}{0.6 (\cos \theta)^{5/3} \cdot \rho_p^{1/2} \cdot V^{2/3}} \right]^{18/19} \quad [10.1-1]$$

Linear interpolation is used between low and high velocity regions.

High Velocity Region

For $V_n \geq 7$ km/s:

$$d_c = \left[\frac{A \cdot t_w^{2/3} (\sigma / 70)^{1/3}}{(\cos \theta)^{2/3} \cdot \rho_p^{1/3} \cdot \rho_b^{1/9} \cdot V^{2/3} \cdot S^{-1/3}} \right] \quad [10.1-2]$$

where A depends on the shield type:

Whipple Shield with MLI on top: $A = 2.9754$

Whipple Shield without MLI: $A = 3.918$

Stuffed Whipple Shield with MLI on top: $A = 5.2002$

10.1.4.2 Multi-Shock Equation (for Calculations with Augmentation Wings)

Low Velocity Region

For $V_n \leq 2.4/(\cos \theta)^{1/2}$ km/s:

$$d_c = 2 \cdot \left[\frac{t_w (\sigma / 40)^{1/2} + 0.37 m_b}{(\cos \theta)^{4/3} \cdot \rho_p^{0.5} \cdot V^{2/3}} \right] \quad \text{with} \quad m_b = t_b \cdot \rho_b \quad [10.1-3]$$

Linear interpolation is used between low and high velocity regions.

High Velocity Region

For $V_n \geq 6.4/(\cos \theta)^{1/4}$ km/s:

$$d_c = \left[\frac{0.358^3 \cdot t_w (\sigma / 40)^{1/2}}{(\cos \theta) \cdot \rho_p \cdot \rho_w^{-1} \cdot V \cdot S^{-2}} \right]^{1/3} \quad [10.1-4]$$

Variables used:

d_c	Critical diameter for penetration[cm]	V	Impact Velocity [km/s]
C	Speed of sound in target [km/s]	S	Spacing between 1 st bumper and back-up wall [cm]
t_w	Thickness of back-up wall [cm]	P	Penetration depth [cm]
t_b	Thickness of bumper/shield [cm]	θ	Impact angle [deg]
ρ_p	Particle density [g/cm ³]	V_n	Normal component of impact velocity $V_n = V \cdot \cos \theta$ [km/s]
ρ_w	Back-up wall density [g/cm ³]	σ	Yield Strength of back-up wall [ksi]
ρ_b	Bumper density [g/cm ³]		
H	Brinell hardness of target [BHN]		

10.1.5 Total Fluxes on the ATV

Figure 10.1-3 and **Figure 10.1-4** show the distribution of the total impact flux for meteoroids and debris over the surface of the ATV in impacts/m²/year for particles larger than $D = 0.01$ cm. The reason for the majority of the debris impacts coming from the sides is that the debris model only includes circular orbits. The shadowing effect of the augmentation wings attached to the Service Module can be clearly seen. The rear part from the Spacecraft section (Upper and lower Avionics Module and Thruster Cylinder) gets hit from the sides by those objects not hitting the wings. These figures do not include the effects of any particles that get through the augmentation wings and hit the ATV, although this was included in the calculations.

Because of the tilted attitude some objects also hit the upper (spaceward) side of the ATV, especially the Cone 2 and the Pressurised Module.

The distribution of the Meteoroid Flux is very different, with most of the objects hitting the upper side of the ATV, while the lower, earthward looking side has almost no flux.

Regarding the numbers shown in these figures, it should be noted that, although the meteoroid impact flux is higher at the minimum size shown of $D > 0.01$ cm, the number of failures caused by debris impacts is much larger than that caused by meteoroids for the given shielding. The reason is that for sizes critical for penetration of the ATV shields, debris fluxes are dominating. According to the reference flux models the directional distribution of impacts, as seen in **Figure 10.1-3** and **Figure 10.1-4**, is the same for all sizes.

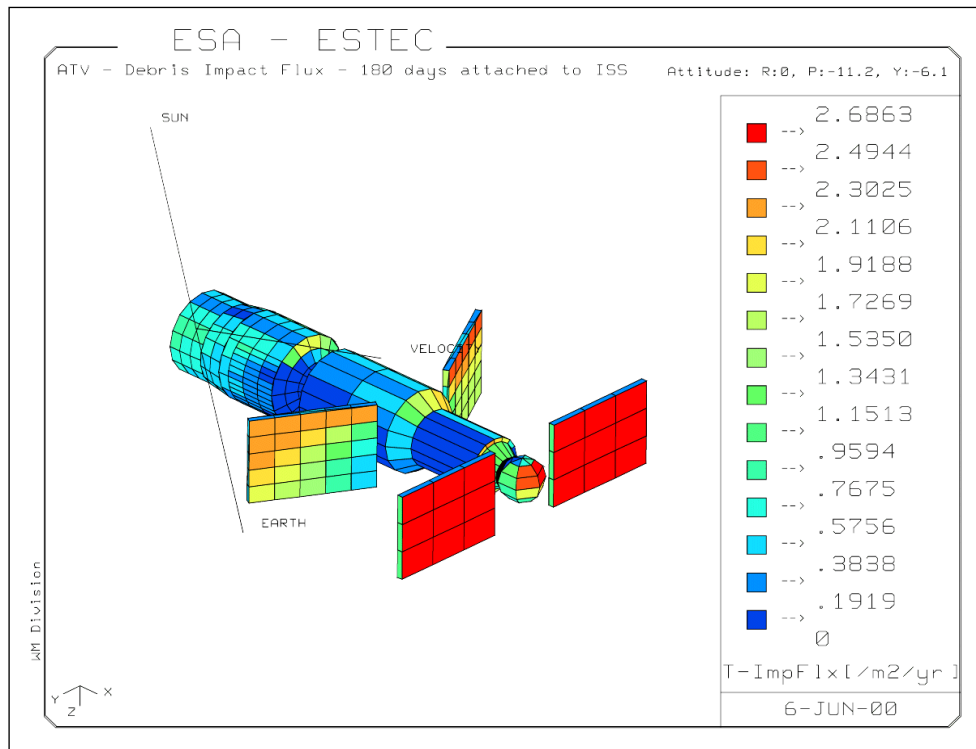


Figure 10.1-3: ATV Debris impact flux

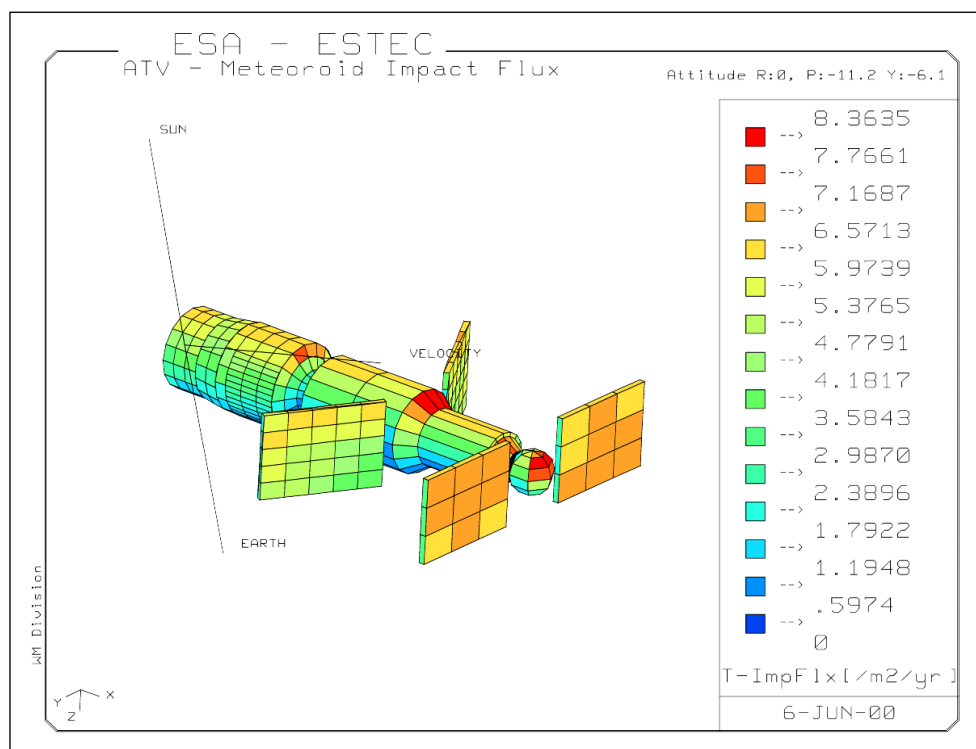


Figure 10.1-4: ATV Meteoroid impact flux

10.1.6 Results

A risk assessment of six different shielding configurations is presented here. For each subsystem in the configurations, the *Number of Penetrations* (NP) and the *Probability of No Penetration* (PNP) are calculated. The Number of Penetrations and the Probability of No Penetration are related by the expression:

$$PNP = e^{-NP} \quad [10.1-5]$$

For each configuration the results of a 135 day mission are given. No allocations for external items or rear flux were included. All calculations were done with the augmentation wings attached to the Service Module and with the ATV in the tilted attitude given in **Table 10-1**. Sigma refers to the yield strength of the back-up wall. The aim of this analysis is to determine what level of protection is necessary to achieve the target PNP of 0.9993 and what weight increase this would produce for the M/OD Protection System.

The tables shown in the next sections present the results for the six configurations, where different modules were equipped with SWS. **Table 10-3** summarises these configurations.

PNP Analysis shielding configurations	
Configuration 1	Baseline – WS in all modules
Configuration 2	SWS in Cone2 and ½ Pressure module
Configuration 3	SWS in Cone2 and ¾ Pressure module
Configuration 4	SWS in Cone2 and Pressure module
Configuration 5	SWS in Cone2, Pressure module, External Cylinder and Thruster Cylinder
Configuration 6	SWS in all modules

Table 10-3: Summary of all shielding configurations

Note that the Pressure module was divided into four parts. This way it was possible to analyse some configurations where only part of it was shielded. **Figure 10.1-5** shows an example corresponding to configuration 2, where only the Cone 2 and ½ of the Pressure Module are equipped with the SWS.

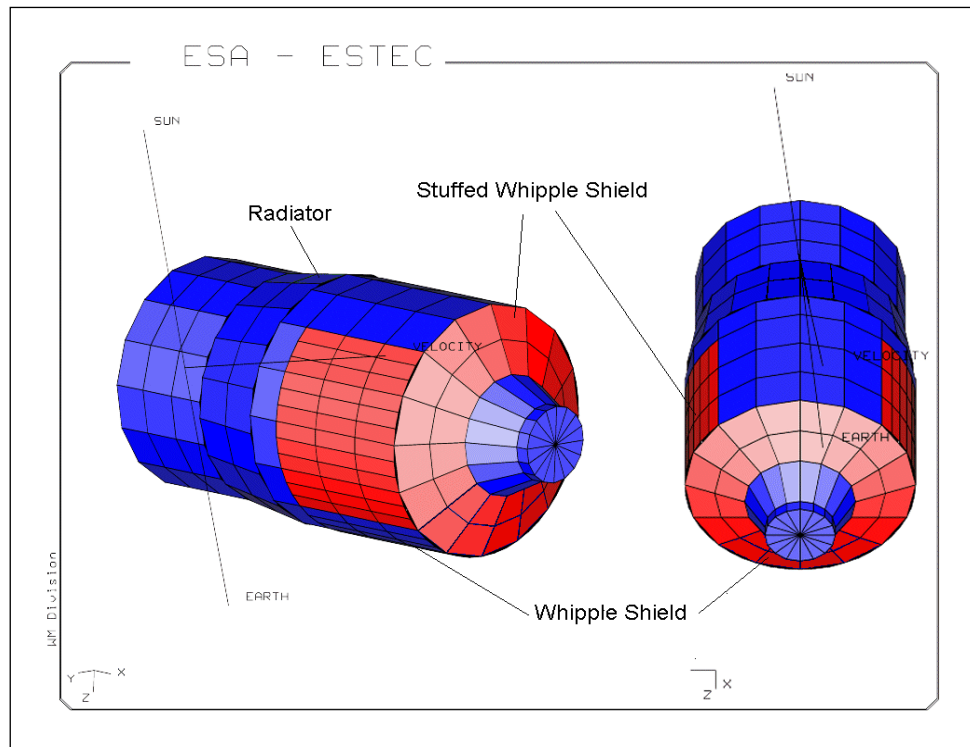


Figure 10.1-5: Example of ATV shielding configuration

10.1.6.1 Configuration 1 - Baseline Configuration (Whipple Shield)

The baseline configuration is a simple Whipple shield in all modules. All modules except the Upper and Lower Avionics module have an MLI on top. The PNP is 0.99815 for 135 days; well below the target PNP of 0.999 for 135 days.

ATV WS + Wings - New equation with high vel. factor = 2.9754 ESA tilt - 135 days - No rear flx. No ext. items								1b
ATV Item	MLI Outside	Shield type	Backwall yield strength [ksi]	Debris	Meteoroids	NP corr	NPTot	PNPtot
Thruster Cone	Yes	WS	57	.156E-5	.446E-4	.000E+0	.462E-4	0.99995
Thruster Cylinder	Yes	WS	57	.890E-4	.851E-5	.908E-6	.984E-4	0.99990
Cylindrical Panels	Yes	WS	57	.276E-3	.364E-4	.359E-5	.316E-3	0.99968
Lower Avion. Module	No	WS	47	.824E-4	.580E-5	.307E-5	.913E-4	0.99991
Upper Avion. Module	No	WS	47	.496E-4	.296E-5	.000E+0	.526E-4	0.99995
Ext m cylinder	Yes	WS	57	.116E-3	.165E-4	.344E-5	.136E-3	0.99986
-Y PM (Left)	Yes	WS	47	.253E-3	.241E-4	.139E-4	.291E-3	0.99971
-Z PM (Up)	Yes	WS	47	.105E-3	.431E-4	.000E+0	.148E-3	0.99985
+Y PM (Right)	Yes	WS	47	.118E-3	.196E-4	.139E-4	.152E-3	0.99985
+Z PM (Down)	Yes	WS	47	.159E-4	.124E-5	.000E+0	.171E-4	0.99998
Cone2	Yes	WS	47	.338E-3	.793E-4	.273E-4	.444E-3	0.99956
Cone 1	Yes	WS	47	.943E-5	.669E-5	.793E-6	.169E-4	0.99998
RDS cylinder	NASA allocation						.375E-4	0.99996
Total 1				.145E-2	.289E-3	.669E-4	.185E-2	0.99815

Table 10-4: Configuration 1 (ATV baseline), 135 days attached to the ISS

10.1.6.2 Config 2 - Stuffed Whipple Shield in Cone 2 and ½ Pressurised Module

In this configuration the Cone 2 and the +Y and –Y sides of the Pressurised Module were reinforced with a SWS. The Weight increase for this configuration is 55 kg including 15% for attachments and 15% for contingencies ($0.131 \text{ g/cm}^2 \times 32.2 \text{ m}^2 + 30 \%$).

ATV + Wings WS/SWS in C2+1/2PM										2b
New equation with high vel. Factor WS => 2.9754 SWS => 5.2002										
ESA tilt - 135 days - No rear flx. No ext. items										
ATV Item	MLI Outside	Shield type	Backwall yield strength [ksi]	Extra Weight incl. 30% Conting. [kg]	Debris	Meteoroids	NP corr	NPTot	PNPtot	
Thruster Cone	Yes	WS	57		.156E-5	.446E-4	.000E+0	.462E-4	0.99995	
Thruster Cylinder	Yes	WS	57		.890E-4	.851E-5	.908E-6	.984E-4	0.99990	
Cylindrical Panels	Yes	WS	57		.276E-3	.364E-4	.359E-5	.316E-3	0.99968	
Lower Avion. Module	No	WS	57		.824E-4	.580E-5	.307E-5	.913E-4	0.99991	
Upper Avion. Module	No	WS	57		.496E-4	.296E-5	.000E+0	.526E-4	0.99995	
Ext m cylinder	Yes	WS	57		.116E-3	.165E-4	.344E-5	.136E-3	0.99986	
-Y PM (Left)	Yes	SWS	47	16.3	.737E-4	.184E-5	.138E-4	.893E-4	0.99991	
-Z PM (Up)	Yes	WS	47		.105E-3	.431E-4	.000E+0	.148E-3	0.99985	
+Y PM (Right)	Yes	SWS	47	16.3	.487E-4	.151E-5	.138E-4	.640E-4	0.99994	
+Z PM (Down)	Yes	WS	47		.159E-4	.124E-5	.000E+0	.171E-4	0.99998	
Cone2	Yes	SWS	47	22.5	.813E-4	.564E-5	.273E-4	.114E-3	0.99989	
Cone 1	Yes	WS	47		.943E-5	.669E-5	.793E-6	.169E-4	0.99998	
RDS cylinder		NASA allocation						.375E-4	0.99996	
Total				55.0	.949E-3	.175E-3	.667E-4	.123E-2	0.99877	

Table 10-5: ATV configuration 2, 135 days attached to the ISS

10.1.6.3 Config 3 - $\frac{3}{4}$ Stuffed Whipple Shield in Cone 2 and Pressurised Module

This configuration is very similar to configuration 2, with the SWS added in the most exposed parts of the cargo carrier. The upper quarter (-Z) of the Pressurised Module also has a SWS, so that all upper $\frac{3}{4}$ of the Pressurised Module and Cone 2 have increased protection. The aim is to protect the upper part of the pressurised module from meteorites and from those objects that are not stopped by the augmentation wings because of the tilted attitude of the ATV. This represents a weight increase of ~71kg including 15% for attachments and 15% for contingencies. ($0.131\text{g/cm}^2 \times 41,9\text{m}^2 + 30\%$).

ATV + Wings WS/SWS in C2+3/4PM									
New equation with high vel. factor WS => 2.9754 SWS => 5.2002									3b
ESA tilt - 135 days - No rear flx. No ext. items									
ATV Item	MLI Outside	Shield type	Backwall yield strength [ksi]	Extra Weight incl. 30% Conting. [kg]	Debris	Meteoroids	NP corr	NPTot	PNPtot
Thruster Cone	Yes	WS	57		.156E-5	.446E-4	.000E+0	.462E-4	0.99995
Thruster Cylinder	Yes	WS	57		.890E-4	.851E-5	.908E-6	.984E-4	0.99990
Cylindrical Panels	Yes	WS	57		.276E-3	.364E-4	.359E-5	.316E-3	0.99968
Lower Avion. Module	No	WS	57		.824E-4	.580E-5	.307E-5	.913E-4	0.99991
Upper Avion. Module	No	WS	57		.496E-4	.296E-5	.000E+0	.526E-4	0.99995
Ext m cylinder	Yes	WS	57		.116E-3	.165E-4	.344E-5	.136E-3	0.99986
-Y PM (Left)	Yes	SWS	47	16.3	.737E-4	.184E-5	.138E-4	.893E-4	0.99991
-Z PM (Up)	Yes	SWS	47	16.3	.456E-4	.329E-5	.000E+0	.489E-4	0.99995
+Y PM (Right)	Yes	SWS	47	16.3	.487E-4	.151E-5	.138E-4	.640E-4	0.99994
+Z PM (Down)	Yes	WS	47		.159E-4	.124E-5	.000E+0	.171E-4	0.99998
Cone2	Yes	SWS	47	22.5	.813E-4	.564E-5	.273E-4	.114E-3	0.99989
Cone 1	Yes	WS	47		.943E-5	.669E-5	.793E-6	.169E-4	0.99998
RDS cylinder	NASA allocation							.375E-4	0.99996
Total				71.2	.889E-3	.135E-3	.667E-4	.113E-2	0.99887

Table 10-6: ATV configuration 3, 135 days attached to the ISS

10.1.6.4 Config 4 - Stuffed Whipple Shield in Cone 2 and Pressure Module

In this configuration the complete Cone 2 and Pressure Module were equipped with SWS. The weight of the extra Kevlar/Nextel Layer is 87.7 kg (including 15% for Attachments and 15% for contingencies ($0.131\text{g/cm}^2 \times 51.5\text{ m}^2 + 30\%$)).

ATV + Wings WS/SWS in C2+PM New equation with high vel. factorWS => 2.9754 SWS => 5.2002 ESA tilt - 135 days - No rear flx. No ext. items									
ATV Item	MLI Outside	shield type	Backwall yield strength [ksi]	Extra Weight incl. 30% Conting. [kg]	Debris	Meteoroids	NP corr	NPTot	PNPtot
Thruster Cone	Yes	WS	57		.156E-5	.446E-4	.000E+0	.462E-4	0.99995
Thruster Cylinder	Yes	WS	57		.890E-4	.851E-5	.908E-6	.984E-4	0.99990
Cylindrical Panels	Yes	WS	57		.276E-3	.364E-4	.359E-5	.316E-3	0.99968
Lower Avion. Module	No	WS	57		.824E-4	.580E-5	.307E-5	.913E-4	0.99991
Upper Avion. Module	No	WS	57		.496E-4	.296E-5	.000E+0	.526E-4	0.99995
Ext m cylinder	Yes	WS	57		.116E-3	.165E-4	.344E-5	.136E-3	0.99986
-Y PM (Left)	Yes	SWS	47	16.3	.737E-4	.184E-5	.138E-4	.893E-4	0.99991
-Z PM (Up)	Yes	SWS	47	16.3	.456E-4	.329E-5	.000E+0	.489E-4	0.99995
+Y PM (Right)	Yes	SWS	47	16.3	.487E-4	.151E-5	.138E-4	.640E-4	0.99994
+Z PM (Down)	Yes	SWS	47	16.3	.126E-4	.117E-6	.000E+0	.127E-4	0.99999
Cone2	Yes	SWS	47	22.5	.813E-4	.564E-5	.273E-4	.114E-3	0.99989
Cone 1	Yes	WS	47		.943E-5	.669E-5	.793E-6	.169E-4	0.99998
RDS cylinder	NASA allocation							.375E-4	0.99996
Total				87.7	.886E-3	.134E-3	.667E-4	.112E-2	0.99888

Table 10-7: ATV configuration 4, 135 days attached to the ISS

10.1.6.5 Config 5 – SWS in Cone 2, Pressure Module, External Cylinder and Thruster Cylinder

This configuration represents one of the possibilities for achieving the target PNP, by adding extra shielding to the Spacecraft (C2, PM, EC) and the Thruster cylinder. This increases weight by 115 kg including 30% for attachments and contingencies and achieves a PNP of 0.99903 for 135 days.

ATV + Wings WS/SWS in C2+PM+ThCyl+EM									
New equation with high vel. factor WS => 2.9754 SWS => 5.2002								7b	
ESA tilt - 135 days - No rear flx. No ext. items									
ATV Item	MLI Outside	shield type	Backwall yield strength [ksi]	Extra Weight incl. 30% conting.[kg]	Debris	Meteoroids	NP corr	NPTot	PNPtot
Thruster Cone	Yes	WS	57		.156E-5	.446E-4	.000E+0	.462E-4	0.99995
Thruster Cylinder	Yes	SWS	57	13.1	.340E-4	.719E-6	.961E-6	.357E-4	0.99996
Cylindrical Panels	Yes	WS	57		.276E-3	.364E-4	.359E-5	.316E-3	0.99968
Lower Avion. Module	No	WS	57		.824E-4	.580E-5	.307E-5	.913E-4	0.99991
Upper Avion. Module	No	WS	57		.496E-4	.296E-5	.000E+0	.526E-4	0.99995
Ext m cylinder	Yes	SWS	57	14.3	.413E-4	.127E-5	.347E-5	.460E-4	0.99995
-Y PM (Left)	Yes	SWS	47	16.3	.737E-4	.184E-5	.138E-4	.893E-4	0.99991
-Z PM (Up)	Yes	SWS	47	16.3	.456E-4	.329E-5	.000E+0	.489E-4	0.99995
+Y PM (Right)	Yes	SWS	47	16.3	.487E-4	.151E-5	.138E-4	.640E-4	0.99994
+Z PM (Down)	Yes	SWS	47	16.3	.126E-4	.117E-6	.000E+0	.127E-4	0.99999
Cone2	Yes	SWS	47	22.5	.813E-4	.564E-5	.273E-4	.114E-3	0.99989
Cone 1	Yes	WS	47		.943E-5	.669E-5	.793E-6	.169E-4	0.99998
RDS cylinder	NASA allocation							.375E-4	0.99996
Total				115.1	.756E-3	.111E-3	.668E-4	.971E-3	0.99903

Table 10-8: ATV configuration 5, 135 days attached to the ISS

10.1.6.6 Config 6 – SWS in all Modules

In this configuration all modules of the ATV were equipped with a Stuffed Whipple Shield. This configuration shows the maximum PNP possible with the actual SWS. The PNP achieved is 0.99934 for 135 days. The weight of the extra Kevlar/Nextel Layer is almost 200 kg (including 15% for Attachments and 15% for contingencies).

ATV + Wings Complete SWS									
New equation with high vel. factorWS => 2.9754 SWS => 5.2002									10b
ESA tilt - 135 days - No rear flx. No ext. items									
ATV Item	MLI Outside	shield type	Backwall yield strength [ksi]	Extra Weight incl. 30% conting.[kg]	Debris	Meteoroids	NP corr	NPTot	PNPtot
Thruster Cone	Yes	SWS	57	23.8	.128E-5	.352E-5	.000E+0	.480E-5	1.00000
Thruster Cylinder	Yes	SWS	57	13.1	.340E-4	.719E-6	.961E-6	.357E-4	0.99996
Cylindrical Panels	Yes	SWS	57	28.6	.974E-4	.288E-5	.345E-5	.104E-3	0.99990
Lower Avion. Module	No	SWS	57	20.9	.576E-4	.179E-5	.310E-5	.625E-4	0.99994
Upper Avion. Module	No	SWS	57	10.6	.296E-4	.699E-6	.000E+0	.303E-4	0.99997
Ext m cylinder	Yes	SWS	57	14.3	.413E-4	.127E-5	.347E-5	.460E-4	0.99995
-Y PM (Left)	Yes	SWS	47	16.3	.737E-4	.184E-5	.138E-4	.893E-4	0.99991
-Z PM (Up)	Yes	SWS	47	16.3	.456E-4	.329E-5	.000E+0	.489E-4	0.99995
+Y PM (Right)	Yes	SWS	47	16.3	.487E-4	.151E-5	.138E-4	.640E-4	0.99994
+Z PM (Down)	Yes	SWS	47	16.3	.126E-4	.117E-6	.000E+0	.127E-4	0.99999
Cone2	Yes	SWS	47	22.5	.813E-4	.564E-5	.273E-4	.114E-3	0.99989
Cone 1	Yes	SWS	47	8.5	.444E-5	.513E-6	.837E-6	.579E-5	0.99999
RDS cylinder	NASA allocation							.375E-4	0.99996
Total				207.6	.528E-3	.238E-4	.667E-4	.656E-3	0.99934

Table 10-9: ATV configuration 6, 135 days attached to the ISS

10.1.7 Conclusions

Figure 10.1-6 shows the PNP results and weight penalties for the six configurations (over the 135 day mission). The mass penalties for the various configurations with extra shielding range from 55 kg to 200 kg (including 15 % for attachments and 15 % for contingencies). To achieve a PNP of 0.999 for the ATV, when attached to the Russian Service Module of the ISS for 135 days, an extra mass of ~115 kg is required.

A comparison of configurations 2 and 3 shows that a reinforcement of the upper side of the Pressure module is important, in order to protect the ATV from meteoroids and from those debris particles not stopped by the augmentation wings.

A comparison between configurations 3 and 4 shows that a reinforcement of the Earth- looking side (-Z) of the ATV modules produces almost no improvement of the PNP. This is because with the modelled attitude of the ISS, almost no particles hit the lower side of the ATV. By leaving the Earth-looking side of the ATV without SWS, 25 % of the extra weight could be spared.

Configuration 5 represents the minimal configuration needed to achieve the target PNP.

The calculations were done without including the contributions from the external items and the rear flux and with the augmentation wings attached to the Service Module. These wings have a significant effect on the protection of the ATV although their effectiveness is greatly reduced if the pitch or roll attitude of the ISS is further increased.

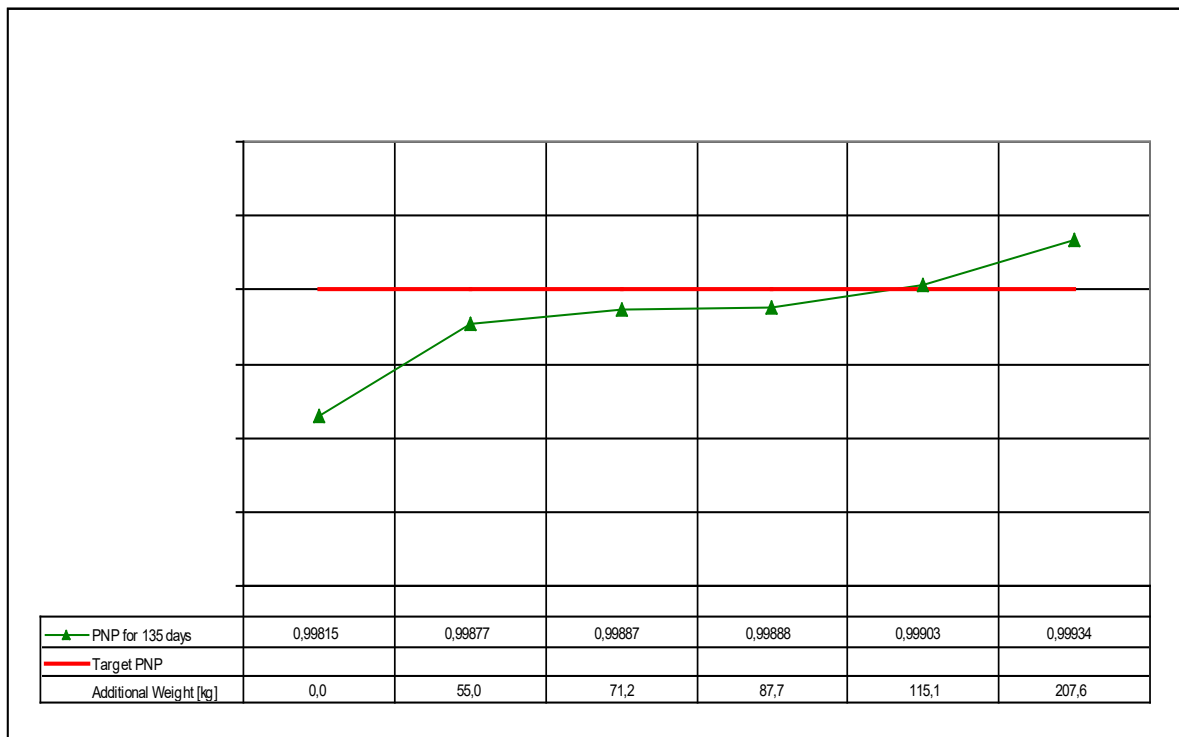


Figure 10.1-6: Summary of the results for all configurations for a 135 day mission

10.2 References

Beltrami, P., and G. Drolshagen, Assessment of the Probability of No Penetration and mass penalty for different shield configurations of the ATV, ESA internal report, ref. EMA/00-058/GD/ATV, June 2000.

ESABASE/DEBRIS release 2, Final Report, *ESA report, CR (P) 4214*, 1998.

NASA SSP 30425, Rev. B, Space Station Program Natural Environment Definition for Design, 1994.